ELECTRONIC PHOTODISSOCIATION SPECTROSCOPY

OF METAL-POLYPYRIDINE COMPLEX IONS

by

SHUANG XU

B.S., Nanjing University, China, 2010

A thesis submitted to the

Faculty of the Graduate School of the

University of Colorado in partial fulfillment

of the requirement for the degree of

Doctor of Philosophy

Department of Physics

2016

This thesis entitled:

ELECTRONIC PHOTODISSOCIATION SPECTROSCOPY

OF METAL-POLYPYRIDINE COMPLEX IONS

by

SHUANG XU

has been approved for the Department of Physics

_____

Professor J. Mathias Weber

_____

Professor W. Carl Lineberger

_____

Date

The final copy of this thesis has been examined by the signatories, and we find that both the content and the form meet acceptable presentation standards of scholarly work in the above mentioned discipline.

Xu, Shuang (Ph. D., Chemical Physics, Department of Physics)

Electronic Photodissociation Spectroscopy of Metal-Polypyridine Complex Ions

Thesis directed by Professor J. Mathias Weber

The properties of many important molecules are only known from condensed phase studies, where the interaction with solvent or other chemical environments masks the intrinsic properties of the solute molecule. Consequently, these intrinsic properties cannot be easily obtained from condensed phase experiments. Spectroscopy of gas-phase molecular ions *in vacuo* is an attractive alternative to spectroscopic studies in the condensed phase. Ions *in vacuo* are isolated systems and free from perturbation inflicted by a chemical microenvironment, such as a solvent or crystal lattice. Consequently, it becomes possible to examine the intrinsic properties of the ions *in vacuo*. Furthermore, gas-phase ions can be trapped, cooled and mass-analyzed, which provides researchers with the opportunity for controlling and selecting ion species and conditions. This thesis comprises my work on photodissociation spectroscopy of several series of metal-polypyridine ions *in vacuo.* These species have been extensively studied in inorganic chemistry because they serve as potential candidates for broad industrial applications and also as prototypical systems to study fundamental scientific questions such as the mechanisms of metal-ligand interaction and chemical reaction. This thesis describes the first investigation of such systems in the gas phase using laser spectroscopy in the visible and UV spectral ranges.

In this work, the gas-phase ions are produced by electrospray ionization. The ions are trapped and buffer-gas cooled in a cryogenic quadrupole ion trap and then undergo mass-selection in a time-of-flight mass spectrometer. The selected ion species are irradiated by a laser pulse with widely tunable photon energy. If photoabsorption leads to dissociation, fragments will be separated and analyzed by a reflectron. The yield of fragment ions is monitored as a function of photon energy and recorded as a photodissociation spectrum. While absorption spectra in

solutions of the species studied here are usually broad and featureless, the photodissociation spectra acquired in the gas phase show new resolved features, often even at room temperature.

Four series of ions were studied and the results are presented in this thesis. The first two are $[Cu(bpy)\text{-}L]^{+}$ and $[Ru(bpy)(tpy)\text{-}L]^{2+}$, where bpy = 2,2'-bipyridine and tpy = 2,2':6',2''-terpyridine, and L represents a variable ligand. The choices for L in the two types of complexes are different, but they both form a series from weakly (*e.g.* N_2) to strongly interacting ligands (*e.g.* Cl, CH_3CN). It is found that the ligand can dramatically shift the molecular orbitals and change the electronic structure of the ion. Another critical element in the ion is the metal. To explore how the metal affects the properties of the ion, the photodissociation spectra of a series of $[M^{II}(bpy)_3]^{2+}$ ions were measured. Here, M represents a transition metal, and in this study, several first-row transition metals and the d^6-column metals are included (Mn, Fe, Co, Ni, Cu, Zn, Ru, Os). The experimental data suggest that the $[M^{II}(bpy)_3]^{2+}$ ions can have significantly different excitation energies, excited-state lifetimes and symmetries. Finally, the complex ion can be generated in microsolvated states by condensing solvent molecules onto the bare ion in the cryogenic ion trap. By experimenting on mass-selected ions solvated by a well-defined number of solvent molecules, it is possible to observe the solvation effect in a stepwise fashion, *i.e.* one solvent molecule at a time. The target ion used in this study is $[Ru(bpy)(tpy)\text{-}OH_2]^{2+}$ and it is found that solvation by only four water molecules already contributes more than 75% of the full solvatochromic shift exhibited in its bulk solution. By comparing the geometry and the spectrum of each solvation stage, the evolution of the solvatochromic shift can be linked to the formation of solvation shells.

Apart from the experimental work, computations based on density functional theory were carried out to provide more ground-state information of the systems. Excited-state calculations were performed using time-dependent density functional theory and are compared with the experimental results. This comparison is used to assign the measured spectra, and to gauge the reliability of the calculations.

To my family.

Acknowledgements

I would like to express my deepest gratitude to the Weber research group. It is a vibrant, friendly and talented group with which I feel so fortunate to spend the past five years of my degree pursuit. In particular, the group leader and my advisor, Professor J. Mathias Weber, is a knowledgeable scientist, patient mentor and considerate friend, who has taught me how to be a diligent researcher, guided me through perplexing technical predicaments, tolerated my brainlessness and indulged my recklessness. I feel blessed to have been able to join his group and embarked on an adventure in ion spectroscopy when I arrived in Boulder bearing only Josephson junctions in my mind. This transition would have been forbidden had I not been lucky to gain the trust and guidance of Professor Weber and the predecessors of my project, Dr. Sydney Kaufman and Casey Christopher. I am also in debt to other group members, Dr. Benjamin Knurr, Michael Thompson, Curtis Beimborn, who work on different projects but have offered tremendous help at times, and James Smith, who often inspires me to rethink many things I have done. I would like to thank the three short-term group members, Luke Long, Martin Meissner and Dr. Jacob Ramsey for having been memorable companions. I will never forget the moments of cheers and laughs in and out of the lab with these wonderful mates.

I must thank the technicians, engineers and other scientists who have worked or talked with me because they are an indispensable source of craft and wisdom. The JILA machine shop, electronic shop and computing group have lent critical help in the construction and maintenance of my hardware and software. Nothing would have been possible without the assistance from these omnipotent technical masters. Thanks also go to the JILA supply office personnel who have processed our frequent purchase requests and kept our experiment running timely. The weekly

meetings with the “supergroup” participated by Professor Veronica Bierbaum, Professor Carl Lineberger, Professor Barney Ellison and their coworkers have been incentive and resourceful. I have received valuable remarks and learned fascinating science in this small community. I am also grateful to the National Science Foundation for supporting my research under Grant CHE-1361814.

Next, I need to acknowledge a special group of people who hardly understand what I am doing but have been forever unconditionally encouraging – my family. As most Chinese families tend to stay close together for cultural and economic causes, I am extremely lucky to have my open-minded parents and grandparents caring and supporting me when I decided to take a long journey to the west. I hope I will be able to repay their solicitude and sacrifice by more than just making them proud. There is no word that is strong enough to express my gratitude to my wife, Dr.-to-be Guoyu Wang, for her constant tender and merry company, and persistent understanding and supporting. We have gone through years of geographical separation and now she is lured aboard my somewhat adventurous journey in America. Although much excitement has come along in the migration, both of us long for a settle-down in the next chapter of our life, which is just around the corner as I graduate. I will have to ensure that she will never regret her choice.

Last but not least, I want to extend thanks to all my previous teachers and friends, who have been a big part in making me who I am. Maybe I should also mention the random people I have encountered in the concert hall, on the trail, at the party, on the soccer field and even on the Internet, who have enriched my life with the different colors and endless joy.

Contents

Lists of Tables

List of Figures

1 Introduction

1.1 Interest in organometallic compounds

Organometallic compounds are essential compounds in many fields of chemistry. They are systems which raise a number of fundamental questions in coordination chemistry, such as the nature of the chelating motif, metal-ligand interaction type and strength, effects of ligand substitution, *etc*. They also bear great significance in practical terms. For example, many organometallic species are found to be important intermediates in synthetic processes; some others are known for their excellent performance as catalysts.

Chemical engineers have devoted tremendous efforts to developing cost-effective synthetic pathways and catalysts, but their methodologies have been largely empirical. In order to modify a chemical reaction to make it follow a desired fashion, *e.g.* lower threshold, higher efficiency, or product selectivity, one needs to understand how the reaction is affected or controlled by all parameters. For decades, research in the field of physical chemistry, or chemical physics, has been dedicated to looking into these chemical problems using the methods of physics. Nevertheless, scientists have not been able to acquire insights with sufficiently fundamental details until recently. Recent advances in experimental and computational methods and techniques have opened many possibilities to investigate a variety of systems, which hopefully will lead to a more thorough understanding of the mechanisms of important chemical processes.

Driven by their potential applications and scientific significance, researchers have been studying organometallic compounds for decades. Most experiments have been performed in condensed phase, *i.e.* in solutions or crystals. The most pursued questions center around

stability, geometry and reactivity. In particular, laser spectroscopy, as a widely deployed experimental method, has collected very useful information regarding the electronic and vibrational structure of a large number of organometallic compounds. Advanced computational methods and capabilities allow for predicting the properties of unknown species. Among the efforts towards more fundamental understanding and more sophisticated exploitation of organometallic compounds, the present work is concerned with the application of laser spectroscopy to selected metal organic ions *in vacuo*. This approach can be expected to uncover new details that cannot be observed in the condensed phase and serve as benchmark for theoretical computations.

1.2 Why *in vacuo*?

Molecules *in vacuo* are isolated and free from short range interactions with solvent or crystal lattice. Therefore, the properties of the system are unperturbed by its chemical environment, which becomes an important advantage when one needs to learn about the intrinsic properties of certain species. Traditional experiments in the condensed phase are often easier from a practical point of view. For example, to measure an absorption spectrum of a compound, one only needs to dissolve it and put the solution in a commercial spectrometer after synthesis and purification. However, there are inevitable drawbacks of working with solutions. First, every solute is subject to solvatochromism once it is dissolved in a solvent. The magnitude of solvatochromic shifts varies from a few to thousands of cm^{-1}, depending on the polarity of the solvent, the specific solute and the different absorption bands. Therefore, to obtain the intrinsic spectrum of a certain species, such shifts need to be corrected. Solvatochromism is just one of

the many side effects caused by the interaction between the solute and the solvent. Another problem in solution is speciation, since many chemical species may coexist in a solution. For example, solvating the ionic compound AB in water may actually lead to a variety of ions in addition to A^+ and B^-, such as AH^+, AOH^+, $A(H_2O)^+$, $A(H_2O)_2^+$, AB_2^- and many more. As a result, a "traditional" UV/vis absorption measurement records the collective response of all existent species, but may not be able to yield a spectrum of just one particular species.

One particular aspect concerning spectroscopy is the peak width. It is desirable to observe well-resolved, sharp spectral features, so that it is possible to assign individual transitions. However, spectra taken in solutions are often broad and featureless, which hinders detailed assignment. One factor causing broadening is thermal excitation, resulting in hot bands, even though experiments on frozen solutions can be used to suppress this effect. An alternative medium that compensates some of the drawbacks of solutions is to use diluted crystals which can be cooled down to very low temperatures. This method has the potential to resolve some of the speciation and temperature issues in solutions but synthesis can be challenging. In addition, it is impossible to grow a crystal without impurities to a size that allows spectroscopic examination, and the phonon modes of crystals are often observed in parallel with other absorption features, adding unwanted components to the spectra. Furthermore, because solvent- or lattice-assisted de-excitation often dominates over the intrinsic dynamics of the system under study, the width of the peak obtained in the condensed phase may not represent the intrinsic photophysical properties of the species in question.

New experimental approaches need to be explored to circumvent the problems mentioned above, and experiments *in vacuo* are a promising alternative. Many techniques can

be applied to ions *in vacuo*, which opens many possibilities of experimental control. For example, buffer gas cooling can be used to cool ions to a temperature as low as the boiling point of the buffer gas. Mass spectrometry is a powerful tool to analyze and select gas-phase ions by mass-charge ratio, nearly eliminating speciation problems. To generate ions in the gas phase, one may choose from a variety of techniques, such as electrospray ionization, laser ablation, electron attachment, *etc*., based on the nature of the ions under study. Certain species are unstable or non-existent in solutions or solids, such as uncommon charge states, radicals, or clusters, but it is possible to produce them *in vacuo*. In summary, experiments on mass-selected, cryogenically prepared ions *in vacuo* can serve as a complement to more conventional measurements, providing researchers with opportunities to study unperturbed, well-defined ionic systems under ideal conditions that are often unavailable in solutions or solids. Many new discoveries have been made since cryogenic ion spectroscopy has been applied to systems that have already been thoroughly studied in more "traditional" experiments.

1.3 In this thesis

The theme of my work is photodissociation spectroscopy applied to electrosprayed, buffer-gas cooled and mass-selected ions. This study focuses on the UV and visible spectral ranges, investigating the electronic states of the ions so prepared. The experimental apparatus is home-built and a large part was designed and constructed as part of my graduate work. The apparatus and the relevant techniques will be described in detail in Chapter 2. The next chapters will introduce studies on several series of metal-polypyridine complex ions. An organometallic complex ion is composed of one or more metal atoms and several ligands. The targets in this

study are chosen specifically to explore the role of the ligands (Chapter 3) and the role of the metal (Chapter 4) by changing one unit (ligand or metal) at a time. Another interesting topic related to these complex ions is microsolvation, where the ion is solvated by only a few solvent molecules. It can be conceived as an intermediate state between the gas phase and the condensed phase. One can perform the experiments *in vacuo* on the solvated systems to explore the role of solvents, and to follow solvation one molecule at a time - one example will be presented in Chapter 5. The last chapter contains concluding remarks and outlooks.

2 Methods

This chapter has been reproduced in part with permission from Shuang Xu, Samer Gozem, Anna I. Krylov, Casey R. Christopher, J. Mathias Weber, *Ligand Influence on the Electronic Spectra of Monocationic Copper–Bipyridine Complexes*, Physical Chemistry Chemical Physics **2015**, 17 (47), pp.31938-31946. Copyright 2015, Royal Society of Chemistry.[1]

2.1 Overview

The goal of the present work is to measure absorption spectra of molecular ions in the gas phase at low temperatures. The whole experiment can be decomposed into three major steps: ion preparation, mass selection and photodissociation spectroscopy, as described in a flowchart shown in **Figure 2.1**. Since the ion source used in the present work is new, it will be described in detail in this chapter.

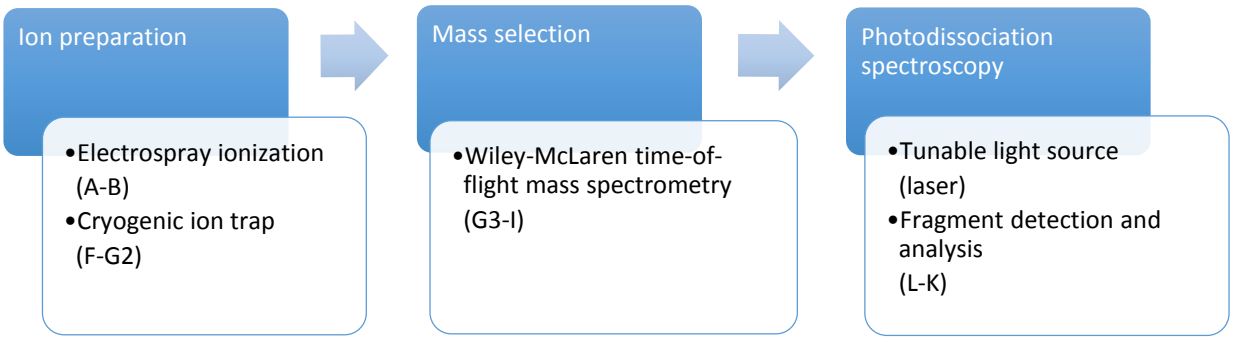

Figure 2.1 This flowchart shows the three major steps of our experiment (main blocks, blue). Listed in the appended blocks (white) are the technologies utilized to implement each step. The letter/number symbols in the parentheses refer to the parts of instrumentation as labeled in **Figure 2.2**.

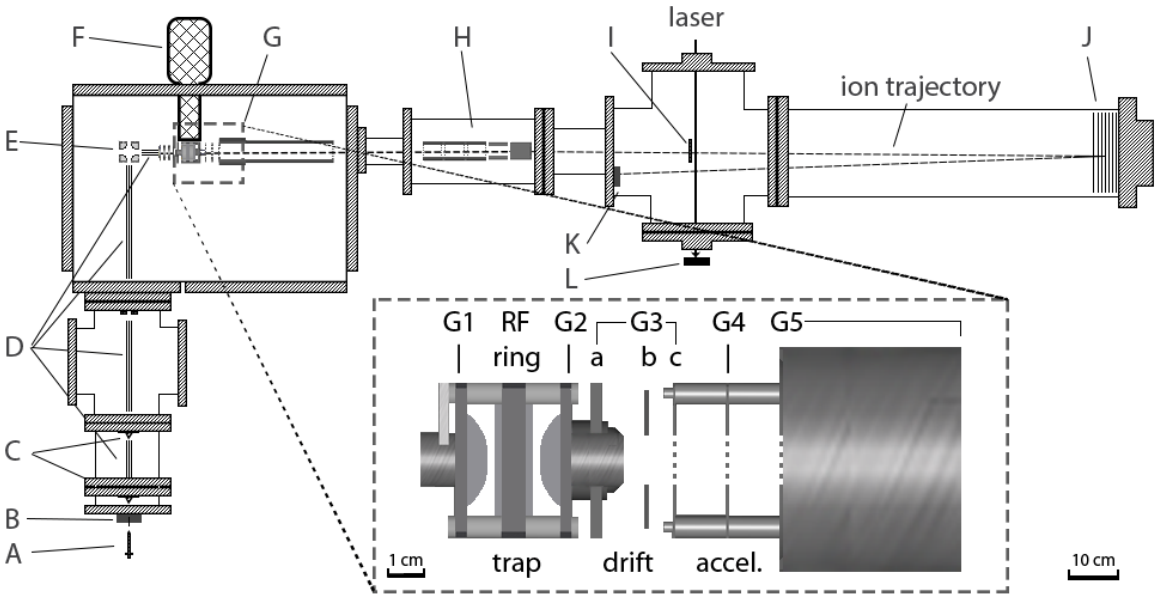

Figure 2.2 Schematics of the experimental apparatus. A - electrospray needle; B - desolvation capillary; C - skimmer; D - octupole ion guide; E - quadrupole bender; F - helium cryostat; G - ion trap and accelerator assembly; H - x-y deflectors and Einzel lens; I - mass gate; J - reflectron; K - microchannel plate; L - pyroelectric joulemeter. The inset zooms in on the trap region. This figure is adapted from Ref.[1]

We use electrospray ionization to prepare ions in the gas phase, then cool the ions to low temperatures in a cryogenic ion trap. Next, we select the ion species of interest by its mass-to-charge ratio using time-of-flight mass spectrometry. Finally, we measure the photodissociation spectrum of the ion species by tuning the wavelength of the laser and monitoring the laser induced change of ion signals (yield of fragments or loss of parent ions). To perform all these functions, the instrumentation encompasses the following major parts, as shown in **Figure 2.2**: the ion source (A-E), the cryogenic ion trap (F-G), the mass spectrometer (G-K) and the laser system. The following paragraph provides a more detailed description of the fundamental

processes from the perspective of ions. Specific technical details are explained in individual sections featuring different parts of the apparatus.

We use electrospray ionization to extract the ions of interest from solution (§2.2.1). After electrospraying, ions enter the first vacuum chamber through a heated desolvation capillary. The ions are accumulated into ion packets in an octupole ion guide and trap in the second differential pumping chamber and then directed by octupole ion guides through the third and the fourth differential pumping stages until they reach the cryogenic ion trap (§2.2.2).

The cryogenic ion trap is a 3-dimensional quadrupole ion trap (Paul trap) and is mounted on the cold head of a closed-cycle helium cryostat. Inside the trap the ions are cooled by collisions with a buffer gas pulse (§2.2.3). The lowest ion temperature that has been achieved in our apparatus is estimated to be around 30 K. After some time (typically 95 ms) for storage and cooling, all ions in the trap are ejected into the accelerator of the time-of-flight mass spectrometer.

Our time-of-flight mass spectrometer consists of an accelerator, a pulsed mass gate and a reflectron, and can be divided into two stages (§2.3). The first stage is between the accelerator and a pulsed mass gate located at the first space focus, and is used for mass selection of the target ions, while the second stage containing the reflectron is for mass anlaysis of the fragments. The mass gate is a device that can either deflect the ions from their normal trajectory (closed mode) or let the ions pass (open mode). It is programmed to be open only at the time when the ions under investigation arrive (§2.3.3). Immediately behind the mass gate is the laser interaction region, where the ions are irradiated by a laser pulse. The laser pulse is timed to intercept the focused and mass-selected ions after they are transmitted through the mass gate. The

wavelength of the laser radiation is widely tunable (220-2500 nm), realized by a combination of a beta barium borate based optical parametric oscillator pumped by an Nd:YAG laser and a frequency conversion stage (§2.5).

We are interested in the absorption spectra of mass selected ions, and we use photodissociation spectroscopy to obtain information on these spectra (§2.4). If an ion is excited by a photon, and fluorescence can be neglected, the absorbed photon energy will be eventually redistributed to the vibrational modes of the ion. When certain conditions (§2.4.2) are met, the vibrationally hot ion can undergo unimolecular decay and fragmentation, resulting in photofragment ions with different mass-to-charge ratios. The photofragment ions are mass-analyzed by the second stage of the mass spectrometer. Here, a reflectron is used to separate the undissociated parent ions and the photofragment ions (§2.3.4). A dual microchannel plate detector is used to detect the ions (§2.3.2).

Typical experimental procedures start with optimizing the parent ion intensity. When the mass gate is kept open, the entire mass spectrum can be used to analyze the components of the ion packet out of the ion trap. The mass spectra have a typical mass resolution ($m/\Delta m$) greater than 2000, enough to distinguish 1/4 atomic mass unit in the mass range we typically work with (mass-to-charge ratio ≤ 500). One can conveniently watch the intensity change of different ions on the mass spectrum when tuning the source and trap parameters and find the optimal combination for the target ion. After maximizing the signal for the target ion, we need to search and optimize the photo-induced signal. This is usually done by fixing the laser at a wavelength that the target is most likely to absorb, then adjusting the laser pulse timing and the ion trajectory to achieve optimal spatial and temporal overlap between the ion packet and the laser pulse, so

that the yield of photofragments or the loss of the parent ions is maximized. Photodissociation spectra are acquired by varying the photon energy and monitoring the photo-induced changes in parent or fragment ion signal as well as the laser pulse energy. Since in this laser system each crystal configuration has a limited tunable range, change of crystals may be necessary to cover the desired spectral range. A full spectrum spanning over a few hundred nanometers is usually a concatenation of several overlapping scans with different crystal configurations (§2.5.3).

Along with our experiments we use the Turbomole[2,3] program suite (v6.2) to perform quantum chemistry computations to assist the interpretation of our experimental results. The methods are based on density functional theory[4] and we will describe the details for each study in its designated chapter.

2.2 Ion preparation

2.2.1 Electrospray ionization source

2.2.1.1 Principle and instrumentation

Electrospray ionization (ESI) is the most suitable method for our experiment because our targets, organometallic ions, are usually soluble but unstable under harsh conditions that often come along with other methods such as laser ablation. ESI was invented as a soft method to extract fragile solute ions from solution[5] and often used with mass spectrometry to analyze the products from the extraction. This approach was first demonstrated by Dole.[6] Fenn developed this method for biological macromolecules in the late 1980s and was awarded the 2002 Nobel Prize in Chemistry.[7] The principle of ESI is based on the fact that the total charge that a droplet of a certain size can carry has an upper limit. If the charge on a droplet exceeds this limit, or in

other words, the size of the droplet falls below the minimum that can carry the resident charge, the droplet will fissure into smaller droplets. The fundamental mechanism is the competition between the surface tension that holds the droplet together and the Coulomb repulsion that tends to break the droplet apart. In 1882, Lord Rayleigh investigated the case of a spherical droplet theoretically. [8] By balancing the two effects, he derived the critical condition known as the Rayleigh limit

$$q^2 = 8\pi^2 \varepsilon \gamma D^3$$

which states that *q*, the charge a spherical droplet with diameter *D* can carry scales with $D^{3/2}$. The prefactor depends on the permittivity of the environment ε and the surface tension coefficient of the solvent γ. However, it has been observed in reality that a charged droplet fissures before reaching the Rayleigh limit because deviation from a spherical shape due to mechanical deformation lowers the maximum charge that the droplet can carry.[9]

A cartoon showing our basic setup together with the microscopic mechanism (positive ion mode in this example) is presented in **Figure 2.3**. The spraying needle for ESI is a commercial assembly (Analytica of Branford). Silica capillary tubing (75 μm ID, 193 μm OD, Polymicro Technologies) is threaded through the spraying needle and extends 1-2 mm out of the needle tip. Dry N_2 gas (30-40 psi) is fed through the hollow space in the spray needle, serving as nebulizing gas around the tip. The solution containing the ions under study is pumped to the spraying needle at a rate of 25-75 μL/h by a syringe pump (New Era, model NE-1000) and flows through the silica capillary tubing to the tip of the spraying needle. The spraying needle assembly is biased with a DC voltage of ±3-4 kV against the counterelectrode, which is the desolvation capillary in our case. At the exit of the silica capillary tubing, a cone-shaped jet known as the Taylor cone is formed

due to the strong electric field at the tip of the spraying capillary[10] (see **Figure 2.3**). Droplets containing a net excess of either positive or negative ions (depending on the polarity of the needle bias) break away from the tip of the Taylor cone and fly towards the desolvation capillary under the effect of the electric field; this process is aided by the nebulizing gas flow. Solvent starts to evaporate and the droplets are shrinking and approaching the Rayleigh limit. Some droplets may already fissure before reaching the desolvation capillary.

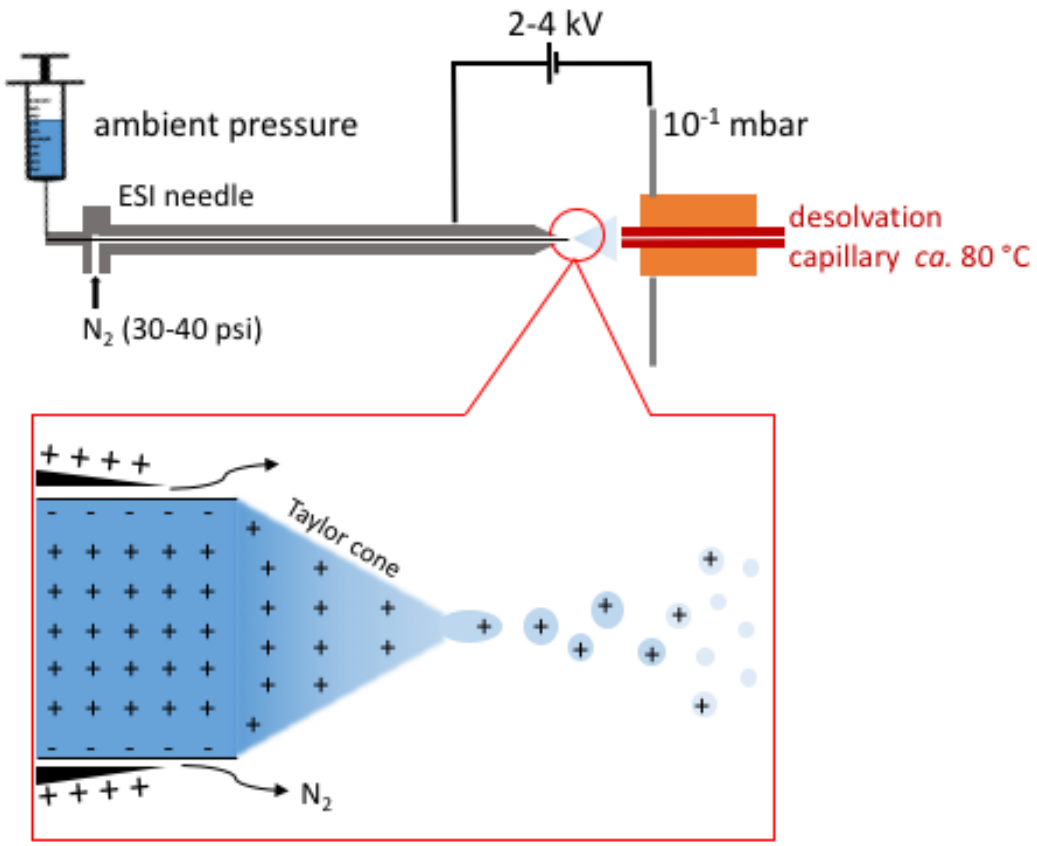

Figure 2.3 Illustration of our ESI setup and microscopic mechanism of the process in positive ion mode (see text).

The desolvation capillary is made of stainless steel and is 58.4 mm long. It has an ID of 0.5 mm and serves as a duct for ions from ambient pressure to the first vacuum chamber (10^{-1} mbar). It is housed in a cylindrical copper mount which is heated to about 80 °C with a cartridge heater (OmegaDyne CSH-1011001, 100 W) to facilitate desolvation inside the capillary. A type K thermocouple and a temperature controller (Omega CN9000A) are used to monitor and regulate the temperature. Because the front end of the desolvation capillary is directly exposed to the spray, it can be coated or even clogged by deposition of the solute over time. This leads to unstable or vanishing ion signals, so it must be cleaned and flushed every few hours to restore the ion signal. The rate of the deposition is proportional to the amount of the solute dispensed per unit time, *i.e.* the syringe pumping rate times the solute concentration. Therefore, the capillary will need to be cleaned more frequently if higher pumping rates or concentrations are used.

2.2.1.2 Performance of ESI

The performance of ESI has two measures – ion beam intensity and stability – and depends on many parameters. This section summarizes my observations from my own practice and discusses some important parameters to be adjusted to optimize the performance of our setup. More general and systematic discussions on ESI can be found in literature.[5,7,9,11–14]

Solvent. As the starting point of ESI, the properties of the solution play an important role. Generally, better performance can be achieved by using solvents with higher volatility, higher polarity and lower viscosity. In most of the experiments in this work, we used pure methanol or a methanol-water mixture (v: $v = 9$: 1). The choice of solvent may be governed by the properties

of the solute or other considerations. For example, if the solute is an oxidant, or if methanol can bind to the ion forming unwanted adducts, acetonitrile may be used in lieu of methanol.

Solute concentration. The proper concentration of the solution for ESI depends on the solute. The typical range we have been working with is 0.5-5 mM. Many organometallic complexes are easy to electrospray. For certain species such as $[Ru(bpy)_3]^{2+}$ (bpy=2,2'-bipyridine) one can use a concentration as low as 50 μM and still obtain good ion beam intensity. This concentration can be a rough guideline for deciding the amount of similar species when they need to be synthesized. Higher concentrations may increase ion beam intensity, but it can accelerate the deposition of solute on the desolvation capillary. Therefore, we prefer low concentrations and will increase the concentration only when the signal can no longer be improved by other parameters but is still insufficient.

Solution pumping rate. Although increasing pumping rates may improve the ion signal, it does more harm than good. Doubling the rate may increase the ion signal by only 30%, but exacerbates the deposition problem on the desolvation capillary and sometimes can cause electric arcing between the ESI electrodes. Therefore, we typically pump the solution no faster than 40 μL/h, except if absolutely necessary.

Nebulizing gas pressure. The pressure of the nebulizing gas is critical to the stability of ESI. The optimal pressure, however,is not significantly influenced by other parameters, and we have been using a value between 38-40 psi for all our experiments.

Electrospray voltage. ESI performance usually is not very sensitive to the magnitude of the electrospray voltage. The choice depends on the polarity of the solvent and the stability of the ions. If the target ions are fragile, lower voltages are favored in order to better preserve the

ions. Typical functioning voltage is around 3 kV, but we have used values throughout the range 2-4 kV.

Position of the spray needle. The spray needle assembly is mounted on a three-axis translation stage with insulators to allow adjusting and optimizing its position relative to the desolvation capillary during operation. The distance between the spray needle and the capillary determines the electric field in between and is typically about 3-4 mm at 3 kV spray voltage. A too short distance can result in arcing and destruction of the target ions.

Temperature of the desolvation capillary. The temperature of the desolvation capillary is set close to the boiling point of the solvent (*ca.* 80 °C, depending on the actual solvent). Lowering the temperature decreases the productivity but is necessary if the target ions are heat sensitive.

2.2.2 Ion guides and pre-trap ion optics

Since the ions are sprayed at ambient pressure, a series of differential pumping stages are needed to reach the high vacuum required for time-of-flight mass spectroscopy (10^{-6} - 10^{-7} mbar). Our apparatus has four differential pumping stages leading to the ion trap and three stages from the ion trap to the flight tube. The pressure, approximate mean free path and pumping device of each chamber when an experiment is running are tabulated in **Table 2.1**.

Table 2.1 Specifications of each differential pumping chamber in operation.

chamber	pressure (mbar)	mean free path (m)	pump
I	1	10^{-5}	65 m^3/h rotary vane pump, Leybold Trivac D65 B
II	0.1	10^{-4}	65 m^3/h rotary vane pump, Leybold Trivac D65 B
III	10^{-4}	0.1	685 L/s turbomolecular pump, Pfeiffer HiPace 700
IV "the trap chamber"	10^{-6}	10	1100 L/s turbomolecular pump, Leybold Turbovac 1000 C
V	10^{-7}	100	230 L/s turbomolecular pump, Pfeiffer TMU261
VII "the flight chamber"	10^{-8}	1000	520 L/s turbomolecular pump, Pfeiffer TMU521

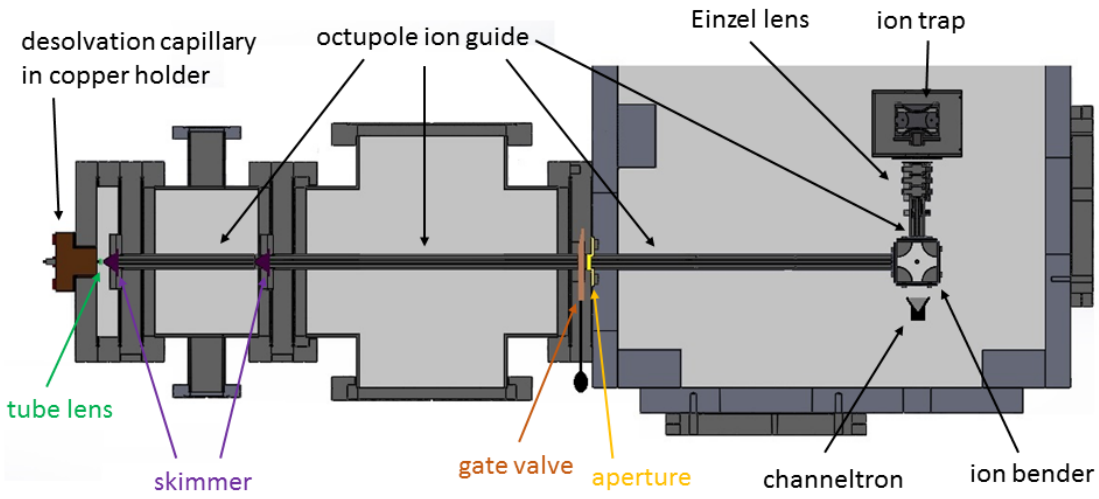

Figure 2.4 Elements from ESI to the ion trap (see text).

The section of the apparatus from the ESI source to the ion trap is provided in **Figure 2.4**. The first two chambers are separated by a stainless steel skimmer (1.5 mm aperture) located about 5 mm downstream from the exit of the desolvation capillary. To maximize the number of

ions entering the skimmer, a small tube lens (3 mm long) is inserted right after the desolvation capillary to focus the ions. Usually a gentle gradient of electric potential is created to limit the ion speed and prevent collision-induced dissociation as the pressures in the first and second chamber are still relatively high.

From the second differential pumping chamber to the ion trap, the ions are guided by a sequence of four octupole ion guides across the chambers. Octupole ion guides are devices that consist of eight metal rods placed in parallel with equal spacing in a circular pattern (see **Figure 2.5**).

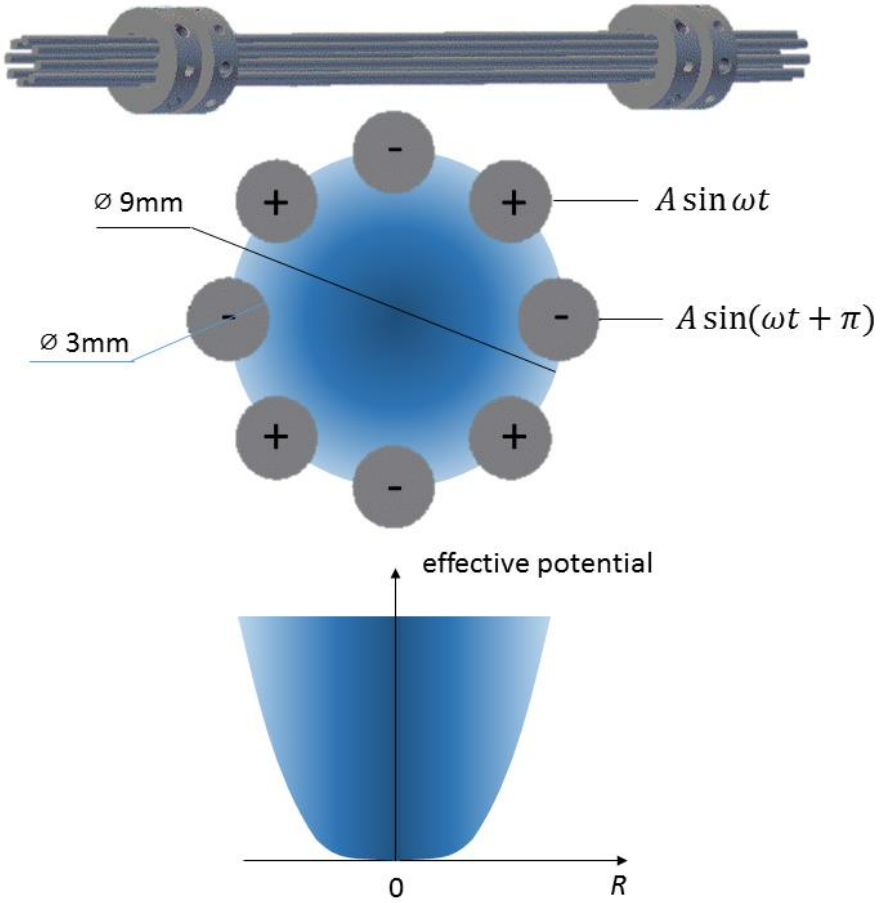

Figure 2.5 Octupole ion guides. All rods have a diameter of 3 mm and placed on a circle of 9 mm in diameter. Adjacent rods are driven by 10 MHz AC signal of opposite phases, forming a radial potential in the cylindrical space.

When each rod is driven with an AC signal (10 MHz) with opposite phase to its neighbor rods, an effective potential is created along the radius, restricting the motion of ions in the cylindrical space surrounded by the rods. The performance of octupole ion guides has been experimentally and theoretically investigated by Tosi, Jones and Gerlich.[15–17]

All of our octupole guides and their AC drivers were built by the machine shop and the electronic shop at JILA. Each rod has a diameter of 3 mm, and all eight rods enclose a cylindrical volume with a diameter of 9 mm, as shown in **Figure 2.5**.

The four octupole guides have different lengths (see **Table 2.2**) and therefore are powered by individual impedance-matched AC drivers. The AC amplitude and DC bias of each octupole can be tuned for the best performance. Typical values of the AC amplitude for each octupole guide are listed in **Table 2.2.**

Table 2.2 Lengths and typical RF amplitudes of all four octupole ion guides.

octupole	I	II	III	IV
length (mm)	139	313	304	39
peak-to-peak amplitude (V)	480	440	240	500

The ions are guided by octupoles in both the second and the third chambers. These two chambers are separated by a skimmer that is identical to the one between the first two chambers. These two skimmers together with the octupole guide in the second chamber act as a pre-trap for ions as shown in **Figure 2.6**.

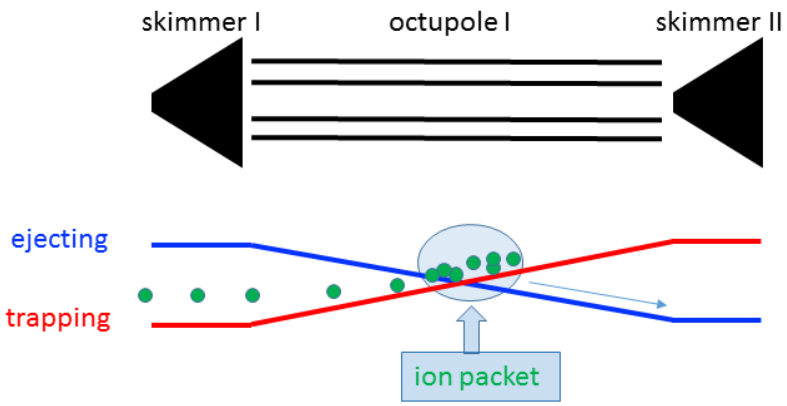

Figure 2.6 The scheme of the pre-trap in the second differential pumping chamber. The skimmers are pulsed to generate loading (red) and unloading (blue) potentials to form ion packets from a continuous flow of ions (green).

The skimmers are pulsed to create trapping and ejection potentials along the axis of the octupole guide to load and unload ions. During the loading period the ions from ESI continuously flow into the octupole guide zone and get trapped by the axial potential, while during the unloading period all trapped ions are released as an ion packet. The purpose of the pre-trap is to prepare ion packets and to prevent ions from entering the cryogenic trap in a continuous flow.

The third and fourth chamber are separated by a gate valve and an aperture with 9 mm ID. Inside the fourth chamber the ions go through the third octupole guide before reaching a home-built quadrupole ion bender, which can deflect the ions by 90 degrees either towards the ion trap or towards a channel electron multiplier (CEM) detector (Sjuts Optotechnik GmbH, KBL 10RS/90) mounted on the opposite side. The purpose of the bender is to separate the neutral gas beam from the first few vacuum stages from the ions. The CEM can be used to detect ions before the trap injection ion optics and to test and troubleshoot the ion source and transmission through the octupole up to this point.

Between the bender and the ion trap, another short octupole guide, a small Einzel lens and an additional aperture are used to inject the ions into the Paul trap.

2.2.3 Cryogenic ion trap

2.2.3.1 Trap setup

Our ion trap and its power supply were purchased from Jordan TOF Products. It is a 3D quadrupole trap, also known as Paul trap. It consists of three electrodes – a central ring electrode and two hyperbolic end caps (G1/2), which are spaced by ceramic rings, as shown in **Figure 2.7**.

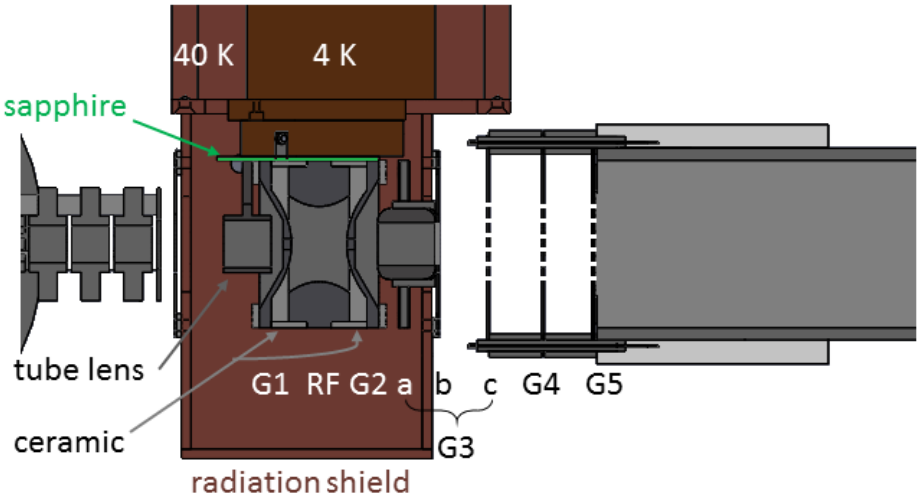

Figure 2.7 Schematic of the ion trap assembly. The trap is mounted on the 4 K cold head of a closed-cycle helium cryostat via a sapphire plate and OFHC copper mounts. A radiation shield attached to the 40 K stage of the cryostat encloses the trap assembly. The acceleration unit (G3-5) of the time-of-flight mass spectrometer is coupled with the ejection ion optics of the trap (G3a).

The trap is mounted on the cold head of a helium cryostat (Sumitomo F-70L, 1.5 Watt at 4.2 K), with three layers sandwiched in between. The layer closest to the trap is a 1-mm-thick

sapphire substrate for electric insulation from the cold head, while maintaining good thermal contact. The other two layers are mounting and adapter plates made of OFHC copper. The trap is enclosed in a radiation shield which is also made of OFHC copper and is electrically grounded. It has dimensions of 66.6 mm × 95.2 mm × 90 mm (length × height × width) and is attached to the 40 K shroud of the cryostat. There is an aperture with 16-mm diameter in both the entrance and the exit wall of the radiation shield. Two tube lenses are used to optimize ion transportation in and out of the trap . At the trap entrance, the tube lens is 12.7 mm long and has an ID of 12.7 mm. The tube lens at the trap (G3-a) exit is 15.2 mm long and has an ID of 11.5 mm, and its upstream end is covered with a fine wire mesh (88.6% transmission). All electric connections inside the radiation shield use gauge 34 magnet wires, except for the ring electrode of trap, which uses gauge 28 to avoid resistive heating since it is driven by high-amplitude radio frequency. All wires inside the radiation shield are wound around the cold head inside the shield. They are wound around the 40 K shroud as well to limit heat flow onto the trap. All cold units are coated with Apiezon N grease to improve thermal contact.

There are two silicon diode temperature sensors near the trap. One (Lakeshore DT-670-CU-1.4L) is embedded in the cold head; the other (Lakeshore DT-670-SD) is attached near the bottom of the trap. Both sensors are used to enable measurement of the temperatures during operation. The temperature of the trap is controlled by a Lakeshore 336 Temperature Controller.

To slow down and cool the ions, the ions are decelerated by the DC voltages on the entrance tube lens and the entrance end cap of the trap. In addition, buffer gas is pulsed into the trap by a general valve (Parker General Valve Series 99) via a ceramic tubing and a notch on the

first ceramic ring. The backing pressure of the buffer gas supply is 40 psi and the average pressure in the chamber is usually kept at several 10^{-6} mbar.

After the ions are cooled in the trap for a certain period of time, they need to be transferred from the trap to the time-of-flight mass spectrometer and accelerated. This is realized by implementing extended electrodes on and outside of the radiation shield (G3-b/c). They are both thin (0.64 mm) plates, each with a 12.7-mm orifice. G3-b is mounted on the heat shield while G3-c is outside the heat shield and coupled with the accelerator units of time-of-flight mass spectrometer (G4/5). These electrodes are driven with the same voltage as the exiting tube lens (G3-a) and act as an elongated lens (G3). The end caps (G1/2) are operated in concert with G3 to create an electric field to eject the ions (see §2.2.3.2 for details).

2.2.3.2 Operation and performance

The operating principle of a quadrupole ion trap is described in detail in the literature.[18,19] In brief, the central ring electrode is driven by a radio frequency (RF) signal with a DC bias, creating an effective 3D potential well inside to trap the ions. The RF amplitude and the DC bias determine the shape of the potential and are adjusted to optimize the ion signal of different species in each experiment. In our setup, the ring electrode is driven with 1 MHz RF by the power supply provided by the trap manufacturer. The DC bias is applied via this power supply as well. The peak-to-peak amplitude of the RF signal is tunable between 0-4 kV.

The operation of the ion trap is somewhat similar to the pre-trap. It can be divided into two steps: injection/trapping and ejection. For a 10-Hz trapping cycle, the ions are trapped for

ca. 95% of the period (*ca.* 95 ms) while ejection takes only a few microseconds. **Figure 2.8** shows the timing scheme of a single trapping cycle.

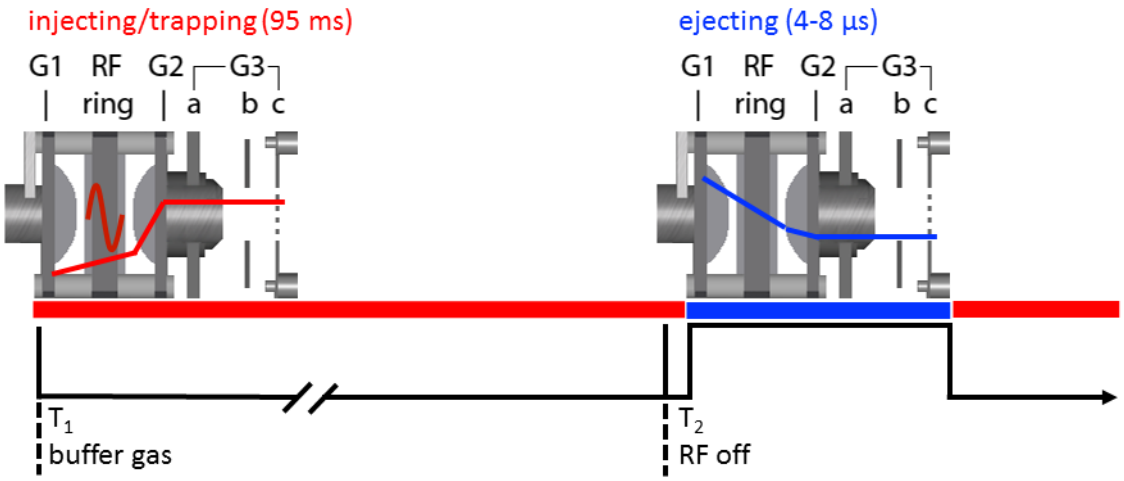

Figure 2.8 Operation of the ion trap on a time axis. At T_1, buffer gas is pulsed into the trap and the injecting period starts with RF on and an uphill potential inside the trap. After *ca.* 95 ms of accumulation, at T_2 a signal is sent to switch off the RF and the trap ejects with a downhill potential. The red and blue lines represent the DC potential energy the ion experience. The actual AC trapping potential (present only during loading) is not shown.

In the following description, we will refer to the electrodes as denoted in **Figure 2.8**. At T_1, the general valve is open to release a short pulse (a few ms) of buffer gas. Meanwhile the RF of the ring electrode is on and electrodes G1/2/3 are biased to create an uphill potential for the incoming ions. The ions are decelerated by the electric field (*ca.* 30 V/cm) and cooled by collisions with buffer gas molecules if the trap is at low temperature. After storing and cooling the ions for *ca.* 95 ms, a trigger pulse is sent to the RF power supply to switch off the RF signal, terminating the loading period. For ejection, the voltage configuration of G1/2/3 is flipped to create a downhill potential (*ca.* 200 V/cm) so that the ions in the trap can be ejected towards the next

stage. This operation is delayed by 0.5-1 μs after the switching off the RF and lasts for 4-8 μs. After the trap is depleted, the RF and the uphill potential inside the trap are resumed to set the conditions for injection in the next cycle. The actual timing scheme is slightly more complex and will be discussed in more detail in §2.6.1.

There are three major factors influencing the ion trapping performance - the RF amplitude, the DC bias and the buffer gas pressure. The optimal combination of these factors depends on the ion species. In general, higher RF amplitudes and buffer gas pressures are needed for ions with greater mass-to-charge ratio. However, such settings can lead to RF induced heating of the ions and and can destroy fragile species. To vary the input amount of buffer gas one can adjust either the duration or the amplitude of the pulse signal that drives the general valve. The only indication of the buffer gas input is the average ambient pressure inside the chamber, which is usually held on the order of 10^{-6} mbar.

The ion cooling efficiency depends on the buffer gas type and pressure as well as the ion storage time. Longer storage times allow better cooling, which is a natural conclusion and can be shown qualitatively by comparing the electronic spectra of crystal violet at 20-Hz cycles (45 ms storage time) vs 10-Hz cycles (95 ms storage time). While the trap temperature is the same (10 K), significant hot bands arise when the storage time is short, as shown in **Figure 2.9**. To ensure that all ions in an ion packet spend the same amount of storage time inside the trap, the packet needs to be formed before it enters the trap. To achieve this goal, a pre-trap is implemented using the skimmers and the octupole guide in the second differential pump stage (see §2.2.2).

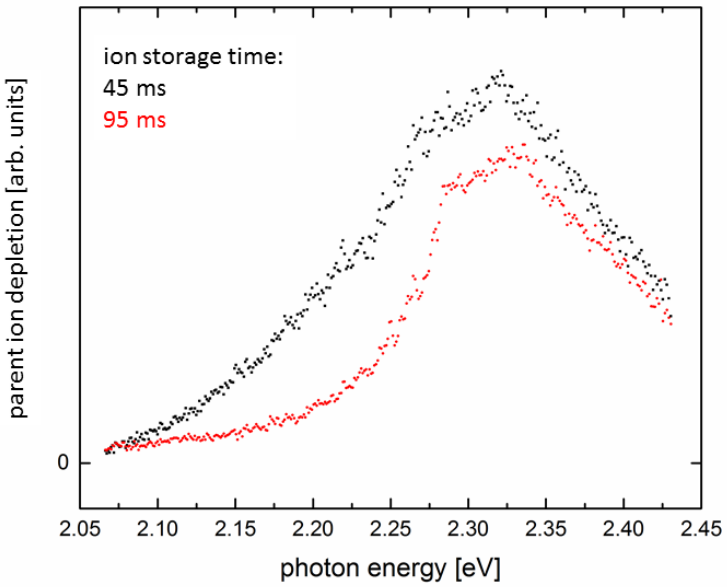

Figure 2.9 The photodissociation spectrum of crystal violet anion with different ion storage times: 95 ms (red) and 45 ms (blue). Ion trap is held is at 10 K in both cases. Significant hot band to the left the rising edge emerges when the storage time is shorter.

The choice of buffer gas is also important when cooling ions. When the trap is cold, it is normally good practice to use a buffer gas that will not condense in the trap. For example, helium is mostly used in our experiment at 10 K. However, there are exceptions when we need to attach messenger tags or solvent molecules to ions in the trap. In such case, nitrogen, deuterium or water vapor is used even if the trap temperature is below the freezing point of the gas (see §2.4.3).

2.2.4 Modifying ions in the trap and the pre-trap

While the ions are cooled in the cryogenic ion trap, they are allowed to interact with buffer gas, providing the possibility of producing new species. Messenger tagging is usually performed in the cryogenic ion trap (see §2.4.3). If solvent vapor is used as the buffer gas, one

may be able to generate solvated species in the gas phase (see Chapter 5). Such processes usually require low temperatures because of the decreasing binding energies as the number of attached solvents grows. However, the lowest possible ion temperature is limited due to the condensation of the buffer gas being used. To alleviate the conflicting requiremens for adduct formation and the target temperature to which the adducts need to be cooled, we can separate these two processes by using the pre-trap to form the adducts first and then transfering the adducts to the cryogenic trap to cool them. For example, in the study of ruthenium complexes (§3.3), the acentonitrile adduct was formed in the pre-trap by leaking acentonitrile vapor into the vacuum chamber containing the pre-trap. Afterwards, we were able to cool the ions in the main trap with temperature held at 30 K. Although this specific acentonitrile adduct was ready to form at room temperature, other adducts may require lower temperatures. Therefore, to broaden the range of species to which this method is applicable, we plan to redesign the pre-trap and to integrate it with a liquid nitrogen cooled dewar and temperature control.

2.3 Mass selection and mass analysis

2.3.1 Reflectron time-of-flight mass spectrometer

The theory of time-of-flight mass spectrometry (ToF-MS) can be easily derived using Newtonian mechanics. Consider a case where an ion with mass-to-charge ratio m/z is accelerated by an electric field with potential difference U. The final speed that the ion acquires will be

$$v = \sqrt{\frac{2U}{m/z}}$$

Suppose the ion flies a distance of L, the total time of flight will be

$$t = \frac{L}{v} = L\sqrt{\frac{m/z}{2U}}$$

Obviously, by measuring the time of flight, one can distinguish ions with different mass-to-charge ratios. However, because the ions are initially spread in a certain volume in space, L and U are not same for all ions, which leads to an uncertainty in the time of flight and impairs the mass resolution. To alleviate this problem, Wiley and McLaren developed a dual stage accelerator which can spatially focus the ions and reduce the uncertainty in t.[20,21]

Our time-of-flight mass spectrometer follows Wiley-McLaren's design and is modified from a commercial angular reflectron ToF-MS (Jordan TOF Products D-850). The acceleration region is inside the trap chamber and immediately follows the ion trap ejection electrodes (see **Figure 2.7**). The accelerator electrodes (G4/5) are coupled with the last ejecting electrode (G3-c) of the ion trap, forming a dual stage accelerator in together. G4 is a metal plate of the same material and dimensions as G3-c except that the orifice is covered by a wire mesh (90% transmission). G5 is a combination of a plate like G4 and a 265-mm-long tube (44.5 mm ID).

After an ion packet is ejected from the trap it drifts through G3 within a few microseconds. When the ion packet reaches the acceleration zone, G4/5 are pulsed to high voltages to accelerate the ions. However, because the ion packet contains ions of different mass-to-charge ratios but they are all ejected by the same electric field, different ions will arrive at the acceleration region at slightly different times.

When the acceleration field is turned on after a certain delay relative to the ejection, some ions have already passed the acceleration zone while some have not arrived yet. Only

those with certain mass-to-charge ratios are in the proper acceleration zone. As a result, the final mass spectrum shows only a window of mass-to-charge ratios.

There is an alternative that allows the mass spectrum to show all components in the trap in a single shot. If the end caps of the Paul trap are used as acceleration electrodes, all ions in the trap will be accelerated at the same time. This scheme also improves the mass resolution owing to the absence of the drifting section. But because the buffer gas is pulsed into the trap and the local pressure inside the trap is estimated to be four orders of magnitude higher than the pressure in the surrounding chamber, the collision rate is much higher. As a result, acceleration from the trap may heat and even dissociate the target ions. Since we are mostly interested in spectroscopy at low temperatures and the resolution of the mass spectrometer is not our priority, this alternative is only used for initial characterization of the mass spectrum at room temperature.

Ions with the same mass-to-charge ratio can be at slightly different places in the acceleration zone when the voltages are pulsed. Using Wiley-McLaren's scheme, the voltages on the accelerator electrodes are configured to spatially and temporally focus the ions at the laser interaction region to maximize the number of ions that can be irradiated. A removable microchannel plate detector is located at the laser interaction region to check the quality of the space focus (see Figure 2.11 in Ref.[22]). For cations we typically use -325 V and -3800 V for G4 and G5, respectively. The power supplies for G4 and G5 are products of FUG (HCN35-6 500). The pulsing switches are Willamette MHVSW-008V for G4 and Behlke GHTS 60 for G5. The Willamette high voltage switch is used with a customized circuit (shown in **Figure 2.10**) to improve the pulse quality.

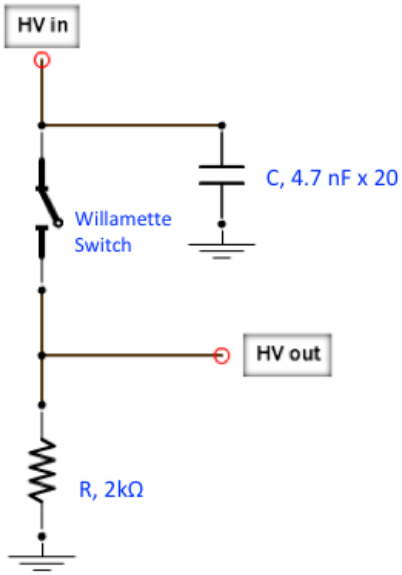

Figure 2.10 Adaptor circuit for the Willamette high voltage switch.

Once the ion packet completely enters the long tube of G5, all acceleration units are pulled to ground potential, so that the ion packet will not experience any electric field when it exits G5. Between the trap chamber and the flight chamber is the fifth differential pumping chamber, which houses a set of ion optics to steer and focus the ion packet. It includes a pair of X-Y deflectors and an Einzel lens, both home-built. The deflectors are two pairs of parallel metal plates (45.7 mm long, 30.5 mm apart) and the Einzel lens is a sequence of three cylindrical electrodes (45.7 mm long, 30.5 mm ID).

In the flight tube, the pressure is at 10^{-7} - 10^{-8} mbar, corresponding to a mean free path of 100-1000 meters, so the ions should not encounter any collisions during their *ca.* 2.5-meter flight. The ions are mass selected by mass-to-charge ratio by a pulsed mass gate (see §2.3.3) so that only the ions of interest can interact with the laser.[23]

At the end of the flight chamber a dual-stage reflectron is installed. The main purpose of the reflectron in our apparatus is to separate the parent ions from charged and uncharged photofragments, but it also improves the resolution of the mass spectrometer (see §2.3.4 and **Figure 2.11**). Because the accelerator focuses the ions to the laser interaction region rather than the detector, the same ions will spread again beyond the laser interaction region and result in a broader peak on the mass spectrum. The reflectron can be used to correct this spreading by refocusing the ions to the final detector as shown in **Figure 2.11(a)**. With this device we can achieve a mass resolution m/Δm up to 2000.

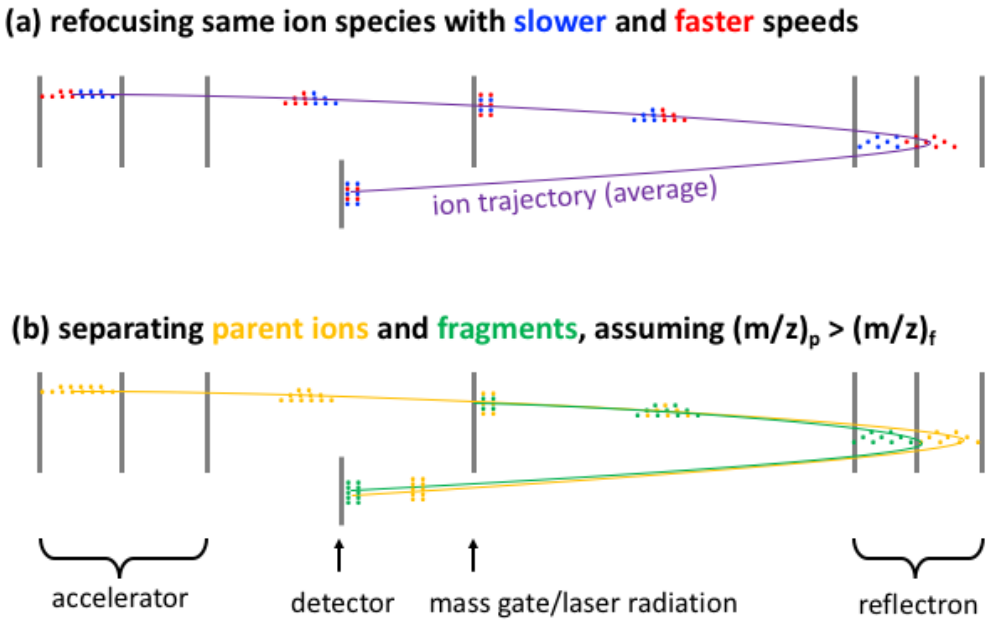

Figure 2.11 The two functions of the reflectron: (a) refocusing the same ion species that have picked up different speeds from the acceleration zone; (b) separating the parent ions and the fragments. Note that the geometry is *not* drawn to scale.

2.3.2 Ion detection

At the end of the ion trajectory we use a 40-mm dual microchannel plate (MCP, Jordan TOF Products, C-726) to detect the ions. The MCP detector is powered by a Bertan 225-05R high voltage power supply through a home-built voltage dividing circuit shown in the left panel of **Figure 2.12**.

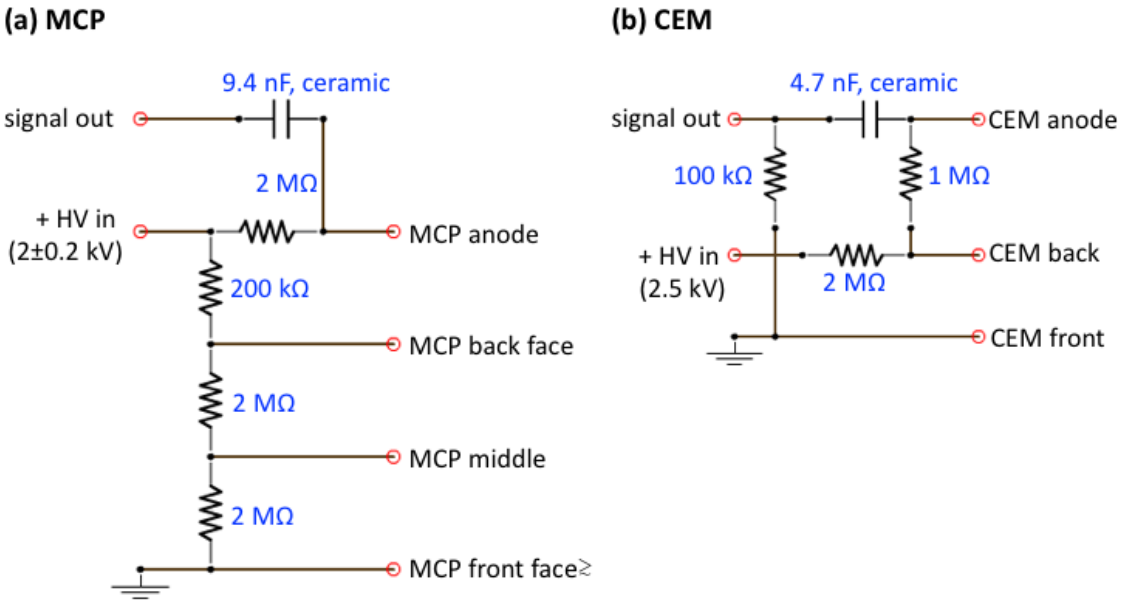

Figure 2.12 Home-built voltage dividers for MCP (a) and CEM (b).

The dual stage MCP has an amplification factor of *ca.* 10^6. The current from the anode is registered as a voltage by an oscilloscope using a 50 Ω terminator. The ion count can be easily estimated from the peak voltage registered on the oscilloscope. For 1 V peak voltage, the current is 20 mA. Dividing the current by the amplification factor and using half its value to estimate an average, the area under a single peak with 20 ns width is approximately 10 mA · 20 ns / 10^6 =

$2 \cdot 10^{-16}$ C. The detection efficiency of an MCP is typically *ca.* 25 %, so this charge pulse corresponds to about 5000 ions, assuming that each ion initially ejects one electron from the MCP surface.

The CEM detector located near the ion bender is driven by a slightly different circuit, shown in the right panel of **Figure 2.12**.

2.3.3 Mass gate

The mass gate is a simplified and more robust version of the design by Stoermer *et al*.[23] It consists of a stack of parallel metal shims with a thickness of 0.5 mm, placed at 5 mm distance to each other. The mass gate is "open" when all shims are at ground potential and "closed" when adjacent shims are biased at *ca.* ±80 V with opposite polarities (see **Figure 2.13**). The positive and negative voltages compensate in the far field, so ions only experience an electric field in the immediate vicinity of the mass gate assembly.

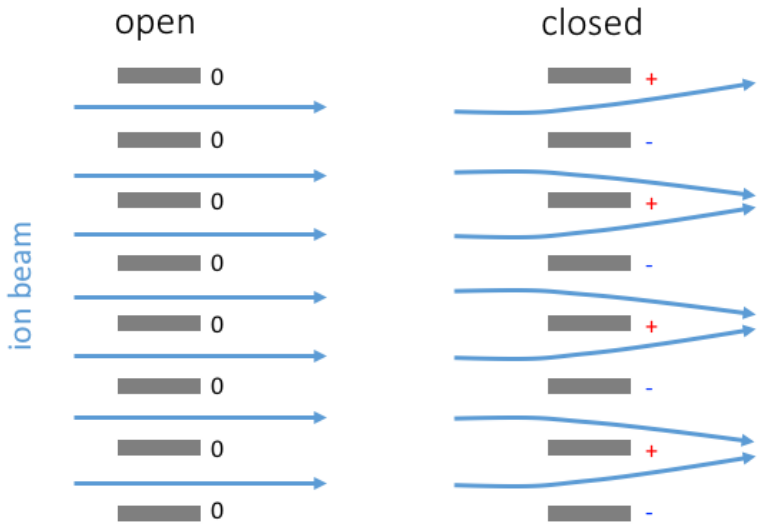

Figure 2.13 Illustration of mass gate in open and closed configurations (*not* to scale).

The mass gate is installed right before the laser interaction region. The mass gate is open for about 300 ns only when the ions of interest arrive, so only these ions will pass the mass gate and enter the laser interaction region. The transmission window can be narrowed down to a single mass peak in the m/z region we typically work at (*ca*. 200-600 u/e). Other ion species are deflected out of the ion trajectory leading to the detector when the mass gate is closed. However, this scheme cannot separate different ions that to have the same mass-to-charge ratio within one atomic unit (*e.g.* HPO_4^- and SO_4^-) or isomers of the same atomic composition (*e.g.* 2/3/4-nitrophenolate). The former situation is rare and often can be avoided by carefully choosing the reagents when preparing the solution, but isomers sometimes present real problems. We try to use pure isomers wherever possible – this equals to a chemical selection before ESI. For example, we purchased the three isomers of nitrophenol to prepare the corresponding nitrophenolate solutions separately. But if isomerization occurs after ESI, we will have no control nor information of the isomers. In this case, spectroscopy becomes necessary to determine the structure of the isomers if possible. Likewise, cluster isomers cannot be selected by pre-ESI chemistry.

2.3.4 Analyzing photofragments

Since the parent ions and the fragments continue to fly after laser irradiation at the same speed, one needs to distinguish between them and analyze the fragment mass. This is realized by using the reflectron as a secondary mass analyzer.

Assume the parent ions with mass-to-charge ratio $(m/z)_p$ will arrive at the MCP detector at time t_p. The corresponding variables for the fragment are noted by the same symbols with

subscript *f*. Let the speed of the parent ions and the fragments before entering the reflectron be v_0 and reflectron voltage be *V*. For simplicity, consider a single-stage reflectron in which the field strength is constant *E* and proportional to *V*. The time that the parent ions spend in the reflectron is

$$t_{p,r} = \frac{2v_0}{\frac{E}{(m/z)_p}}$$

For the fragments

$$t_{f,r} = \frac{2v_0}{\frac{E}{(m/z)_f}}$$

Since the parent ions and the fragments are flying at the same speed v_0 in other sections of the trajectory between the irradiation and the detector, the total time of flight registered on the mass spectrum is then $t_{p,r}$ or $t_{f,r}$ plus the flight time before and after the reflectron, which is the same for both parent and fragment ions. As a result, $(t_{p,r} - t_{f,r})$ is equal to $(t_p - t_f)$, the difference of the total time of flight between the parent ions and the fragments. Mathematically it is easy to obtain

$$(m/z)_f = (m/z)_p - \frac{E(t_p - t_f)}{2v_0}$$

but here E and v_0 are not precisely known and cannot be easily measured. Consequently there is no directly way to calculate $(m/z)_f$. However, one can adjust the reflectron voltage to alter the field strength to *E'* such that the new total time of flight of the fragments t'_f is equal to t_p. Now the fragment ions should appear at the original position of the parent ions on the time-of-flight trace. Following the previous argument, this means that the time spent by parent ions in

the reflectron with the original field and by the fragment ions with the modified field are the same, given by

$$t'_{f,r} = \frac{2v_0}{\frac{E'}{(m/z)_f}} = t_{p,r}$$

Using the equation for $t_{p,r}$ it follows that

$$\frac{(m/z)_f}{(m/z)_p} = \frac{E'}{E} = \frac{V'}{V}$$

where V' is the new reflectron voltage. Now we can calculate the mass-to-charge ratio of the fragment using a simple relationship

$$(m/z)_f = \frac{V'}{V}(m/z)_p \qquad \textbf{Equation 2.1}$$

In brief, one only needs to find a pair of reflectron voltages V and V' that bring the parent ions and the fragments, respectively, to the same time-of-flight, and then use the above equation to calculate the mass-to-charge ratio of the fragments.

Although this is a very convenient way to determine the mass-to-charge ratio of the fragments, it may not apply to all fragments, because $\frac{V'}{V}$ has a limited range of accessible values in practice. If the mass-to-charge ratio of the fragment is too small, the adjusted reflectron voltage V' needs to be very low, which impairs the efficiency of ion detection. There is a minimum value for V' below which ion detection becomes impractical. Note that since the fragments may carry less charge than the parent ions, $(m/z)_f$ can be greater than $(m/z)_p$. But the highest voltage of the reflectron is 4500 V, which imposes an upper limit of the largest $(m/z)_f$ that can be analyzed according to **Equation 2.1**. It is however worth noting that photodissocation spectroscopy can still be performed without identifying the fragments.

The reflectron in our apparatus has two stages and they are biased proportionally – the second stage at voltage V while the first at pV $(0 < p < 1)$. The mathematical description is similar to the single-stage reflectron case as discussed before and the method of analyzing fragments is still valid. The advantage of the two-stage reflectron is that it can refocus the ion beam at an arbitrary position downbeam, *i.e.*, on the MCP detector.

If detecting charged fragments is impossible, neutral fragments may be detected instead. To enable this option another MCP detector is installed behind the reflectron.

2.4 Photodissociation spectroscopy

2.4.1 Concepts

Traditionally, one measures an absorption spectrum by measuring the attenuation of light passing through the sample under study, then calculates the absorption coefficient using Beer's law. However, a minimum number density of absorbers (10^8 cm^{-3} for the most sensitive cavity ringdown experiments) is needed to practically observe this attenuation. In the condensed phase or dense gaseous targets, this minimum number density is usually readily achieved.

With mass selected ions, each ion packet we are able to generate has only 10^3 - 10^5 ions. Even if every ion can absorb a photon, the intensity change for a millijoule laser pulse is on the order of one part per trillion or lower, which is beyond the possibility of detection. Therefore, we employ a less direct method to measure the absorption spectrum – photodissociation spectroscopy.

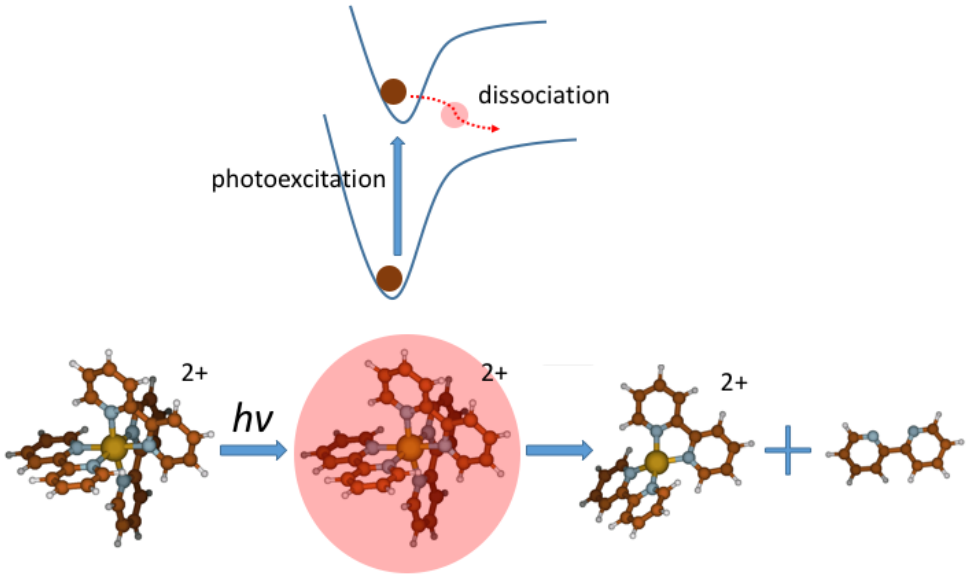

Figure 2.14 Schematic illustration of the photodissociation process. The target ion is excited by a photon to an electronic excited state. After relaxation to the electronic ground state, it becomes vibrationally hot. If a dissociation channel is energetically accessible, the ion will follow this channel and dissociate into fragments.

As illustrated in **Figure 2.14**, when an ion is excited by a photon, the absorbed photon energy can be redistributed to the vibrational modes of the ion. If there is a sufficiently weak bond in the ion, it may be cleaved because the ion is vibrationally hot and ready for unimolecular decay. Once the ion breaks into fragments, we can use the reflectron to separate and analyze the fragments. By scanning the photon energy and monitoring the yield of the fragments, a photodissociation spectrum can be recorded. A spectrum recorded by monitoring the formation of a fragment ion is called photofragment action spectrum. Alternatively, one can monitor the loss of the parent ions. The spectrum recorded in this way is called a parent ion depletion spectrum. Both methods have been used in this work.

In order to apply photodissociation spectroscopy, there are certain conditions to be met. Moreover, since this is an indirect method to measure the absorption, the connection between the yield of photofragments to the actual absorption across section may not be straightforward. To report a photodissociation spectrum as an alternative representation of an absorption spectrum, some assumptions need to be made and the raw data need to be processed accordingly.

2.4.2 Conditions and caveats

The first premise of photodissociation spectroscopy is that the photodissociation process does happen, which is not always the case. It requires that the excited ions have sufficient excess of energy to induce dissociation. This problem is illustrated in **Figure 2.15(a)**. The dissociation threshold is set by the bond dissociation energy to yield fragments plus any potential energy barrier on the path to dissociation. If the energy absorbed through the excitation plus the internal energy prior to absorption cannot overcome this threshold, dissociation will not occur. There are two solutions if this is the case. One is to increase the laser intensity or to use multiple laser shots so that the ions can have the chance of absorbing multiple photons to gain enough energy to dissociate (see §2.4.4). The other is the messenger tagging method as introduced in §2.4.3. By introducing an adduct that is composed of the ion in question and one or more weakly bound molecule(s), such that an energetically accessible dissociative channel is created to enable photodissociation spectroscopy. For a weakly bound tag, it is a reasonable assumption that the spectrum of the original ion remains largely unperturbed. In the present experiment, the generation of such adducts is usually achieved in the ion trap at lower temperatures.

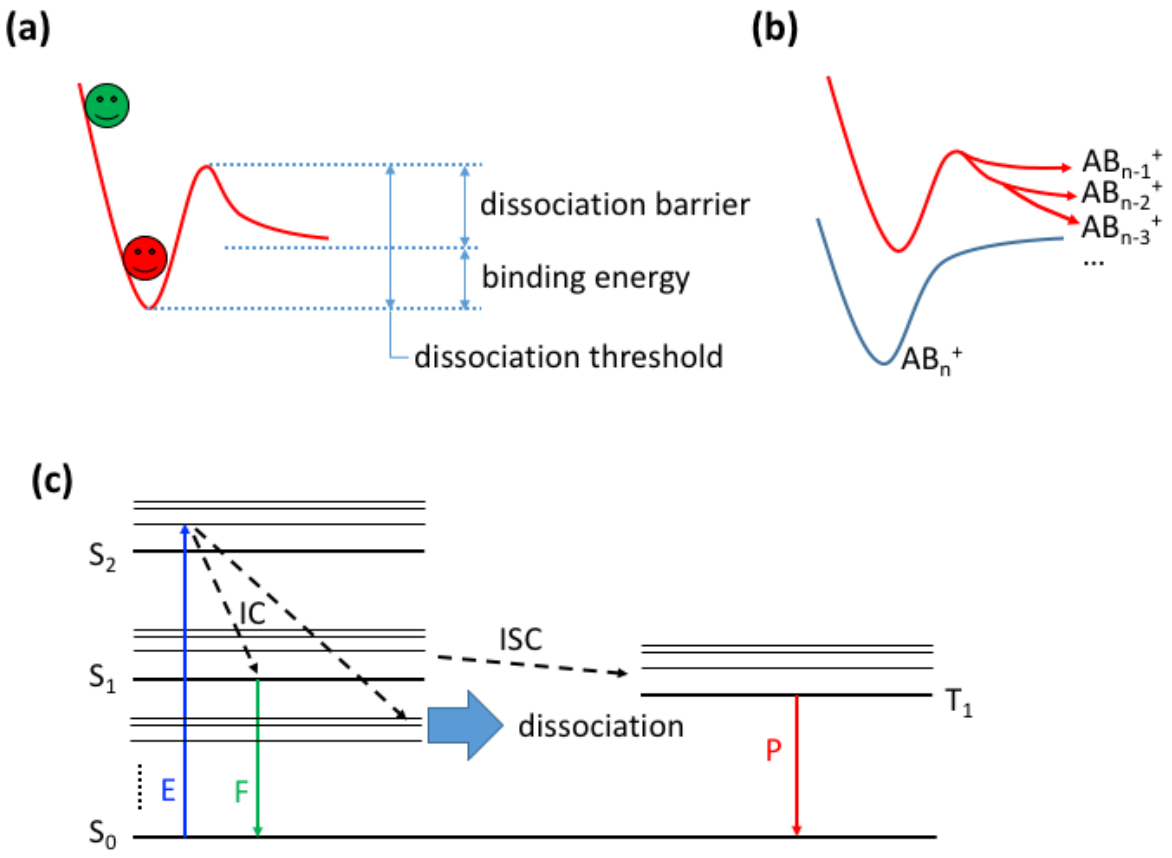

Figure 2.15 Potential problems of photodissociation spectroscopy. The red line is the dissociation curve accessible to the ions in the higher vibrational states of the electronic ground state. (a) The total energy of the ion needs to overcome the dissociation threshold to produce fragments. (b) Multiple photofragments from AB_n^+ ion. (c) Jablonski diagram. S_0 – electronic ground state (singlet); S_1, S_2 – singlet excited states; T_1 – triplet excited state; E – excitation; F – fluorescence; P – phosphorescence; IC – internal conversion; ISC – intersystem crossing.

The next question is, if one is able to take a photodissociation spectrum, to what extent does it represent the actual absorption spectrum of the target? There are several situations where caution should be taken. First, if an ion has more than one dissociation channel, it may have multiple photofragments, as illustrated in **Figure 2.15(b)**. As in practice we are monitoring one photofragment at a time, we need to sum over the yield of all photofragments to obtain the

total spectrum. Since the detection efficiencies for different fragment ions may be different, this may not be feasible. As an alternative, the parent ion depletion spectrum may be better to represent the absorption spectrum if multiple dissociation channels exist. Chapter 5 presents an example of this case.

An ion in the excited state can have different fates, as illustrated by a Jablonski diagram in **Figure 2.15(c)**. Sometimes the ions can release the absorbed energy via non-dissociative channels such as radiative decay. Moreover, even a vibrationally hot ion with sufficient energy may live too long to decay before parent-fragment separation. In this case, neither the depletion spectrum nor the sum of action spectra of all fragments is equal to the absorption spectrum. This brings about the concept of quantum yield. The photodissociation quantum yield Q_{pd} is the ratio of the observed number of dissociation to the number of all excited ions. It can be formulated as

$$Q_{pd} = (1 - Q_{nd})(1 - e^{-\int_{\tau_0}^{\tau} k(E,T,t)dt})$$

where Q_{nd} is the part of non-dissociative decay and depends on the wavelength. When $Q_{nd} \neq 0$, Q_{pd} is less than unity, indicating that the photodissociation spectrum may deviate from the absorption spectrum, unless Q_{nd} is constant over the whole spectral range in question. The second term $1 - e^{-\int_{\tau_0}^{\tau} k(E,T,t)dt}$ accounts for the fact that photodissociation must take place on a finite time scale - from the time when ions are irradiated (τ_0) to the time when fragments are separated from the parent ions, *i.e.* when ions enter the reflectron (τ). The dissociation rate k is a function of the total energy of the excited ion, E, and the ion temperature prior to irradiation, T. In many cases, particularly for ions with few vibrational degrees of freedom, or with energy content far above the dissociation threshold, photodissociation usually occurs within a few tens

of picoseconds. The period $\tau - \tau_0$ is on the order of 10 μs, and the term $1 - e^{-\int_{\tau_0}^{\tau} k(E,T,t)dt}$ can be presumed to be unity in these cases. This may not hold, however, if E is very close to the dissociation threshold. In this case, the photodissociation process may be slow compared to $\tau - \tau_0$ and $e^{-\int_{\tau_0}^{\tau} k(E,T,t)dt}$ becomes significant and reflects an effect called kinetic shift. One can examine whether kinetic shift effects are present by changing the ion speed to vary the time interval $\tau - \tau_0$ and then comparing spectra taken under different settings. If the spectra show intensity differences in the low energy range, a significant kinetic shift is present.

Finally, even if an ion species meets all other conditions for photodissociation spectroscopy and has 100% photodissociation quantum yield upon excitation, the absorption cross section still has to be large enough to produce sufficient amounts of fragments to be detected. One example where this condition is not met will be presented in Chapter 4.

2.4.3 Messenger tagging

As mentioned in §2.4.2, one situation where photodissociation spectroscopy is not feasible is when the bond dissociation energies in the parent ion are too high to achieve dissociation upon excitation with a single photon. For example, in the study of $[Ru(bpy)_3]^{2+}$, the binding energy of a bpy ligand is almost 4 eV, much greater than the energy of visible photons. Therefore, photodissociation is energetically inaccessible for a single-photon process in the visible spectral region. This situation is much more common in infrared spectroscopy because the photon energy is lower. Under such circumstances, a technique known as messenger tagging may be used. One or more molecules can be attached to the target ion to create a weakly bound adduct. These molecules, usually referred to as messenger tags, are usually small and inert, and

they ideally do not alter the spectroscopic properties of the parent ion and can dissociate from the parent ion after the complex absorbs a photon. Typically used messenger tags are Ar, N_2 and D_2.[24,25] Because of the weak interaction between the messenger tag and the target ion, the adduct can only be produced under gentle conditions and in a cold environment. In our experiments, this is done in the cryogenic ion trap by condensing buffer gas molecules to the target ion. We have succeeded in tagging some ions with multiple D_2 and N_2 molecules (see **Figure 2.16**).

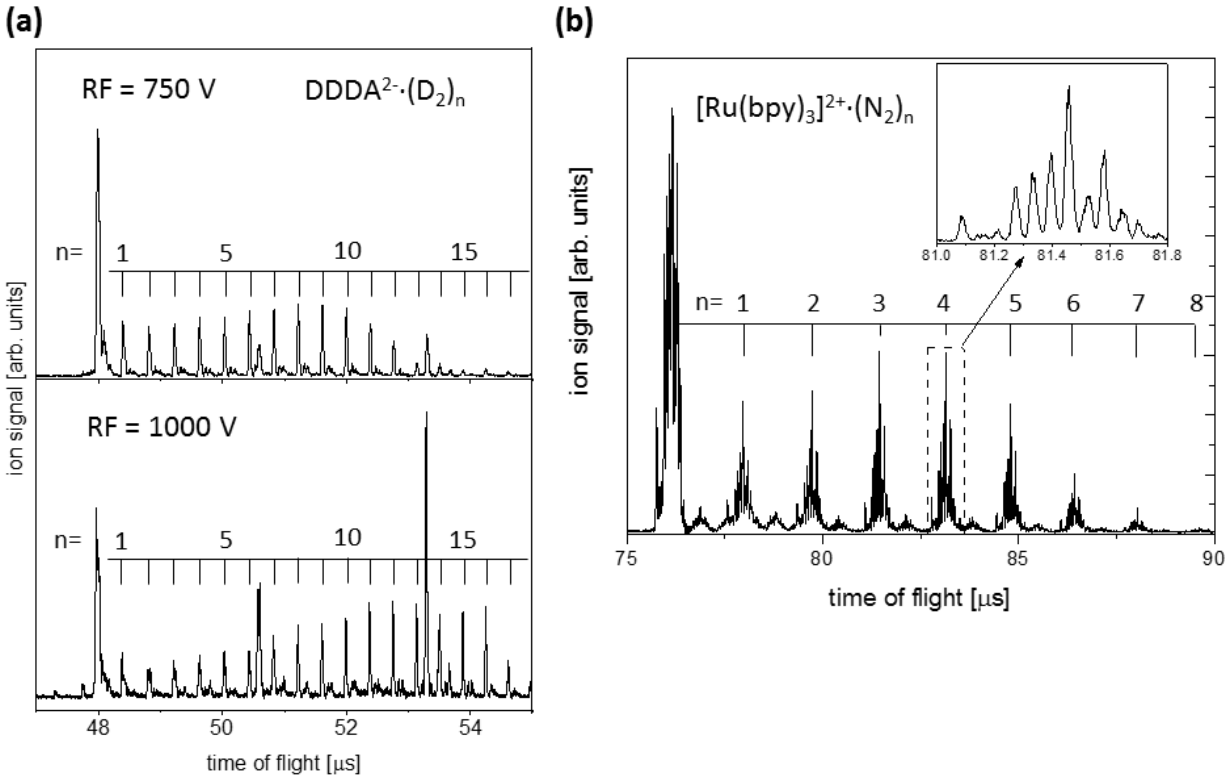

Figure 2.16 Messenger tagging examples. (a) $DDDA^{2-}$ tagged with up to 17 D_2 molecules (trap temperature at 7 K). Different RF amplitudes are favored by different sizes. (b) $[Ru(bpy)_3]^{2+}$ tagged with up to 8 N_2 molecules (trap temperature at 25 K). Inset shows the n=4 adduct and the mass resolution $m/\Delta m \approx 2000$.

Slightly higher RF amplitude and buffer gas input aid the formation of larger adducts, but if these two parameters are significantly increased, the fragile adducts will eventually be destroyed in collisions with the background gas due to RF heating of the stored ions. Shown in **Figure 2.16** are the mass spectra for dodecanedioic acid dianion ($DDDA^{2-}$) tagged with D_2 (trap at 10 K) and $[Ru(bpy)_3]^{2+}$ with N_2 (trap at 25 K). The influence from the RF amplitude to the tagging result is clearly seen for the case of $DDDA^{2-}$.

2.4.4 Multiphoton processes

For species with high dissociation thresholds, absorption of a single photon may not provide sufficient energy to induce dissociation (§2.4.2). If the product of laser intensity and absorption cross section is sufficiently large, the ions may absorb multiple photons and eventually gain enough energy to dissociate. To determine whether this is the case, one can vary the laser intensity and measure the dissociation signal at the same wavelength as a function of the intensity. Fitting the resulting curve with a polynomial reveals how many photons the target has absorbed. If it is indeed a multiphoton process, the data need to be evaluated differently than with single photon dissociation, *e.g.*, the photon number has to be replaced by its square for a two-photon process.

2.5 Laser sources

2.5.1 Overview

The schematics of our entire laser system is depicted in **Figure 2.17**. It consists of a Nd:YAG pump laser (Innolas Spitlight 600), an optical parametric oscillator (OPO, GWU preciScan ULD)

with its frequency upconversion stage (GWU uvScan) and a Sirah Cobra-Stretch dye laser. The visible OPO is pumped by the third harmonic of the pump laser (355 nm) and generates tunable radiation from 415 nm to 2500 nm. The output of the OPO can be used for second harmonic generation (SHG) and sum frequency mixing (SFM) with the fundamental output (1064 nm) of the pump laser to generate UV radiation from 220 to 414 nm. The dye laser is pumped by the fundamental (1064 nm) or the second harmonic (532 nm) of the pump laser. The tuning range depends on the dye in use. The wavelength scan is realized by using a customized LabVIEW user interface to send serial commands to the built-in program provided by the manufacturer. The scan modes are slightly different and will be discussed individually for the OPO and the dye laser in §2.6.2.

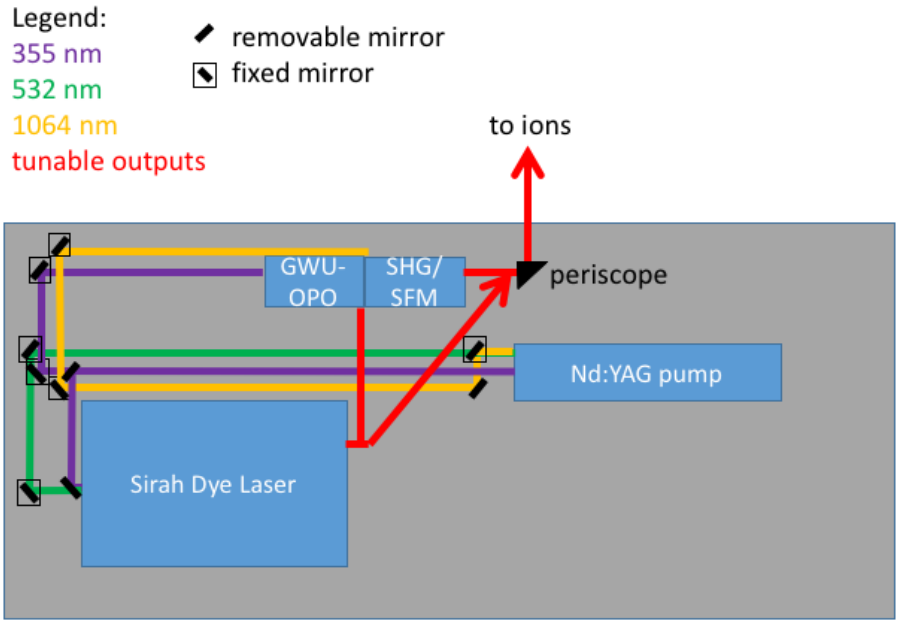

Figure 2.17 Beam diagram of our current laser system (see text).

The laser beams are routed using high reflection mirrors purchased from cvi, LEO and Thorlabs. The final output beam is lifted using a periscope such that it propagates through a CaF_2 window into the chamber at the level of the ion trajectory. During the experiment the laser intensity is monitored by a pyroelectric joulemeter (Coherent J8LP), while other power meters (Coherent PM30 and PM10) are used when calibrating and tuning the power of the system.

2.5.2 Nd:YAG pump

The primary laser source in our system is an Innolas Spitlight 600 pump laser. It consists of a cavity that generates radiation pulses of 1064 nm and additional stages for second (532 nm) and third (355 nm) harmonic generation. The optical structure of the pump laser is shown in **Figure 2.18**. The resonator is formed by a high reflector and an output coupler. Inside the resonator, an Nd:YAG rod pumped by a Xe arc lamp acts as the laser medium. To generate laser pulses, a Pockels cell in the resonator serves as an active Q-switch. The intensity of the output pulse can be changed by adjusting the holdoff voltage and the time delay of the Q-switch. One can also insert a λ/4 wave plate operate the resonator at a fixed Q with disabled Pockels cell for testing purposes. The laser transition is $^4F_{3/2} \rightarrow {}^4I_{11/2}$ in the Nd^{3+} ion at 1064 nm.[26]

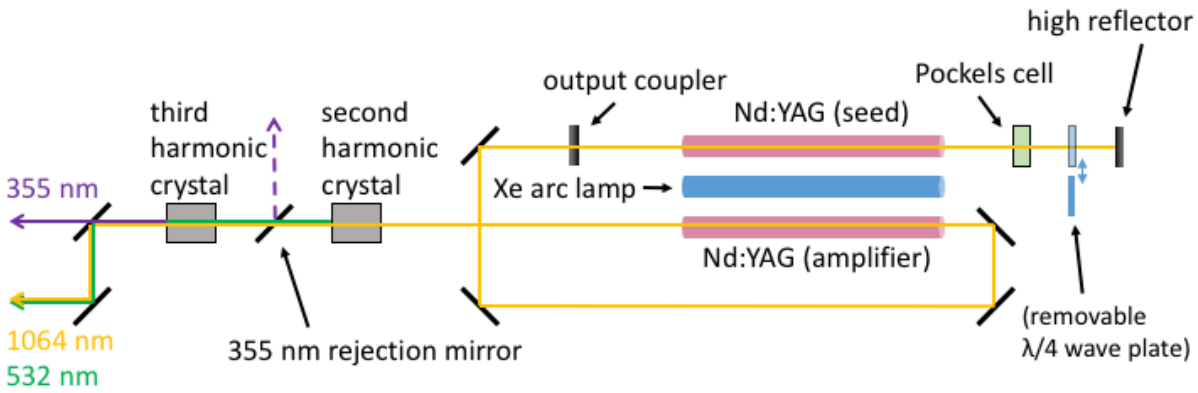

Figure 2.18 Anatomy of Innolas Spitlight 600 Nd:YAG pump laser.

The laser pulse from the resonator is then directed to another Nd:YAG rod, which has been pumped by the same flash lamp at the same time as the first rod, but is seated outside the resonator. The population conversion built up in the second rod amplifies the energy of the original laser pulse to about 600 mJ. The pulse duration is about 5 ns.

In order to pump the visible OPO and the dye laser, shorter wavelengths are needed. The fundamental 1064 nm pulse passes a Type I KD*P (potassium dideuterium phosphate) crystal which doubles the frequency and produces a 532 nm pulse. The power can be optimized by adjusting the crystal angle, and the typical value is 200 mJ/pulse. Now the 532 nm pulse and the residual 1064 pulse propagate collinearly towards a second KD*P crystal where they undergo sum frequency mixing to produce a 355 nm pulse. The energy of the 355 nm pulse is usually 100 to 150 mJ. Each crystal is housed in an oven and held at 70 °C to stabilize the performance of non-linear conversion. In order to separate all the frequency components, a series of dichroic mirrors are used. To prevent the 355 nm beam being back-reflected into the resonator, an additional rejection mirror is placed between the KD*P crystals.

Since a good beam profile and a reasonable power density of the 355 nm pulse are required to optimize the performance of the OPO and avoid damage, we routinely use a photographic film screen to “print” and examine the beam profile, ensuring that the power density is below 0.6 J/cm^2.

2.5.3 OPO and SHG/SFM stage

The OPO is pumped by the third harmonic (355 nm) of the Nd:YAG laser. The pump beam is introduced to the OPO resonator by a periscope. The resonator consists of a Porro prism, a λ/4 wave plate, an output coupler and a Type II beta barium borate (BBO) crystal. The use of the Porro prism and the λ/4 wave plate is to reduce the beam divergence which would result if a simple high reflector was used. The BBO crystal works as the frequency converter that can divide the pump beam into two colors, namely the signal and the idler, observing energy conservation

$$\omega_{pump} = \omega_{signal} + \omega_{idler}$$

where ω_{pump}, ω_{signal} and ω_{pump} are the frequencies of the pump, the single and the idler. By convention, $\omega_{signal} > \omega_{idler}$. The output photons must also observe the conservation of momentum:

$$\vec{\boldsymbol{k}}_{pump} = \vec{\boldsymbol{k}}_{signal} + \vec{\boldsymbol{k}}_{idler}$$

where $\vec{\boldsymbol{k}}_{pump}$, $\vec{\boldsymbol{k}}_{signal}$ and $\vec{\boldsymbol{k}}_{idler}$ are the wave vectors of the pump, the single and the idler. When the BBO crystal is rotated by a precision motor, the wavelength fulfilling the phase matching condition is changed, leading to a tunable output. There are two crystals in the setup, referred to as “blue” and “red”. One of them is chosen at a time depending on the wavelength to be generated. The “blue” crystal is used to generate signal of 415-515 nm and idler of 1140-

2450 nm. The “red” crystal is used to generate signal of 505-710 nm and idler of 710-1190 nm (see **Table 2.3**).

The output from oscillator passes through a UV filter and a quartz compensator to filter the residual pump beam and correct the beam direction of the output. The separation of the collinear signal beam and idler beam is achieved by a Pellin-Broca prism located downbeam.

To generate tunable light in the UV range, an additional stage is installed following the OPO to convert its output to higher frequencies. The GWU uvScan in our setup functions in two modes – second harmonic generation (SHG) and sum frequency mixing (SFM). SHG takes solely the OPO output as input while SFM takes 1064 nm beam from the pump laser in addition.

As shown in **Figure 2.19**, there are two non-linear optical crystals placed in sequence in this stage. The first crystal can be either “UV1” or “UV2”, which is used in accordance with “blue” or “red” crystal, respectively. In either case, the other crystal in the sequence is working as a compensator for the beam walk caused by the frequency converting crystal. The crystal configurations and their according wavelength outputs are shown in **Table 2.3**. Frequency tuning is realized by rotating the crystals using precision motors, same as the OPO.

Table 2.3 OPO and SFM/SHG output ranges in nm.

OPO crystal	signal	idler	SHG	SFM
blue	415-515	1140-2450	220-257	299-350
red	505-710	710-1190	257-354	350-404

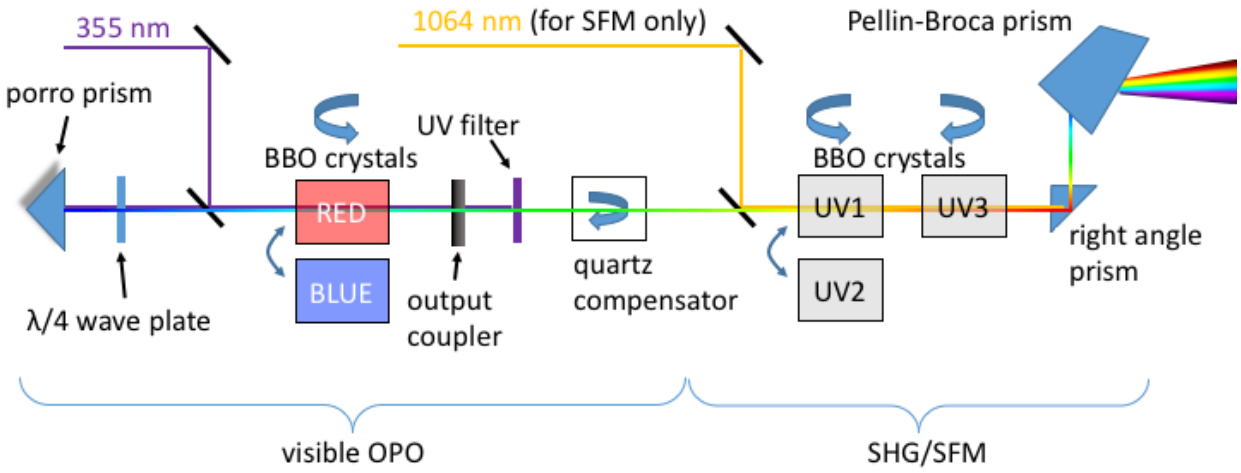

Figure 2.19 Anatomy of the visible OPO and the SHG/SFM stage.

The wavelength calibration of the OPO is performed via a five-point polynomial fitting suite built in the preciScan software. A diffraction grating-based UV-Vis spectrometer (Avantes, AvaSpec-2048- USB2-DT) is used to measure the wavelength. The linewidth is about 5 cm^{-1} and the pulse width is 5 ns. Pulse energies are between 10 and 25 mJ, depending on the wavelength. Calibration of SFM/SHG is done by optimizing the output UV power and using the same built-in polynomial fitting suite.

2.5.4 Dye laser

Dye lasers are known for narrow linewidth and high conversion efficiency, which make it a highly desirable light source for laser spectroscopy. In our experiment, we take advantage of its intense photon fluence to target some ions that have small absorption cross sections or high binding energies. In §2.6.2 we mentioned these as unideal situations, but with sufficient laser

intensity, we have the opportunity to compensate the weak absorption or trigger multiphoton process to overcome these difficulties.

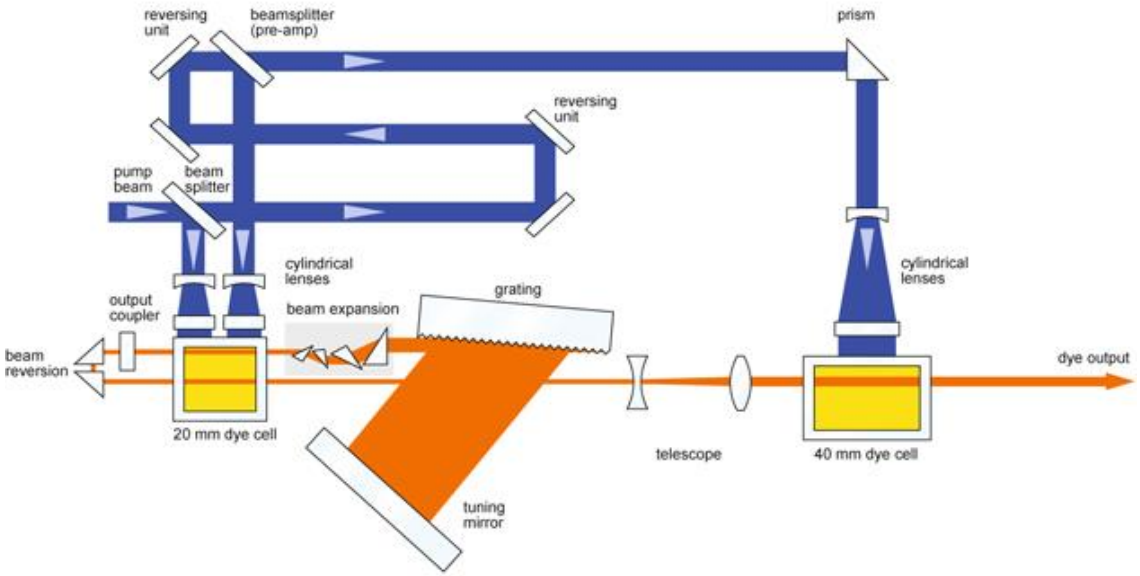

Figure 2.20 The optical schematics of Sirah dye laser (adapted from Sirah Cobra-Stretch dye laser datasheet[27]).

Shown in **Figure 2.20**, our Sirah Cobra-Stretch dye laser has two dye cells serving as the gain medium and the amplifier, respectively. The pump beam is split into the primary pump, the pre-amp and main-amp beams, which are delayed one after another. The primary pump beam excites the dye in the first cell and creates the seed signal. When the pre-amp beam reaches the same cell, the seed signal can be amplified. The wavelength selection is performed by a grating-based monochromator and the linewidth is only a few picometers. The output exits the resonator and then is amplified by the second cell, which is pumped by the main-amp beam.

So far we have used two kinds of dye - Coumarin 307 and Pyrromethene 579. Their specifications are listed in **Table 2.4**. The pump beam is generated by the Nd:YAG pump laser.

Table 2.4 Specifications of the dyes in current study.

dye	Coumarin 307	Pyrromethene 579
pump	355 nm	532 nm
maximum conversion efficiency	30%	53%
tunable range	480-540 nm	566-611 nm

2.6 Operation Control

2.6.1 Timing sequence

The combination of ion trapping, ToF-MS and laser irradiation demands a sophisticated timing sequence for the involving units to act in concert. We use two digital pulse generators (abbreviated “PG”) to control the timing of the experiment. The whole timing scheme is illustrated in **Figure 2.21** and **Table 2.5**, which also contains example values.

Table 2.5 Detailed timing sequence with example values.

controller	channel	event	sync	delay	width[a]	duty cycle[b]
PG 1 (triggered internally at 20 Hz)	T_1	buffer gas	T_0	0	1 µs	1/0/0
	T_2	"RF off"	T_1	45 ms[c]	1 µs	1/0/0
	T_3	flash lamp	T_1	-186 µs[d]	1 µs	-
	T_4	"laser-on"	T_1	0	100 µs[e]	3/1/3
	T_5	"laser-off"	T_1	0	100 µs[e]	3/1/1
	T_8	unload pre-trap	T_1	0	1 µs	1/0/0
RF power supply	T_2'	swtich off RF	T_2	0-1 µs[f]	1 µs	-
	T_2*	ejection	T_2'	0.5 µs	4 µs	-
PG 2 (triggered externally by T_2* at 10 Hz)	A	acceleration	T_2*	6 µs	8 µs	-
	B	oscilloscopes	A	0	1 µs	-
	G	mass gate	A	25 µs	300 ns	-
	E	Q-switch	G	200 ns	1 µs	-

[a] The 1-µs widths are used just for TTL triggering.

[b] The format is written as cycle off (no pulse output)/cycle on/cycles waited to start. Duty cycle is not applicable for RF power supply and PG 2.

[c] 95 ms storage time is realized by 45 ms delay plus the skipped cycle of 50 ms.

[d] The value is set such that the Q-switch is triggered about 215 µs after the flash lamp to catch the best population inversion.

[e] The width of T_4 and T_5 is set to be sufficiently long to perform AND operation with Channel E and B.

[f] Due to the mechanism of how the RF power supply switches off the RF signal, this delay is uncertain. See text for detailed explanation.

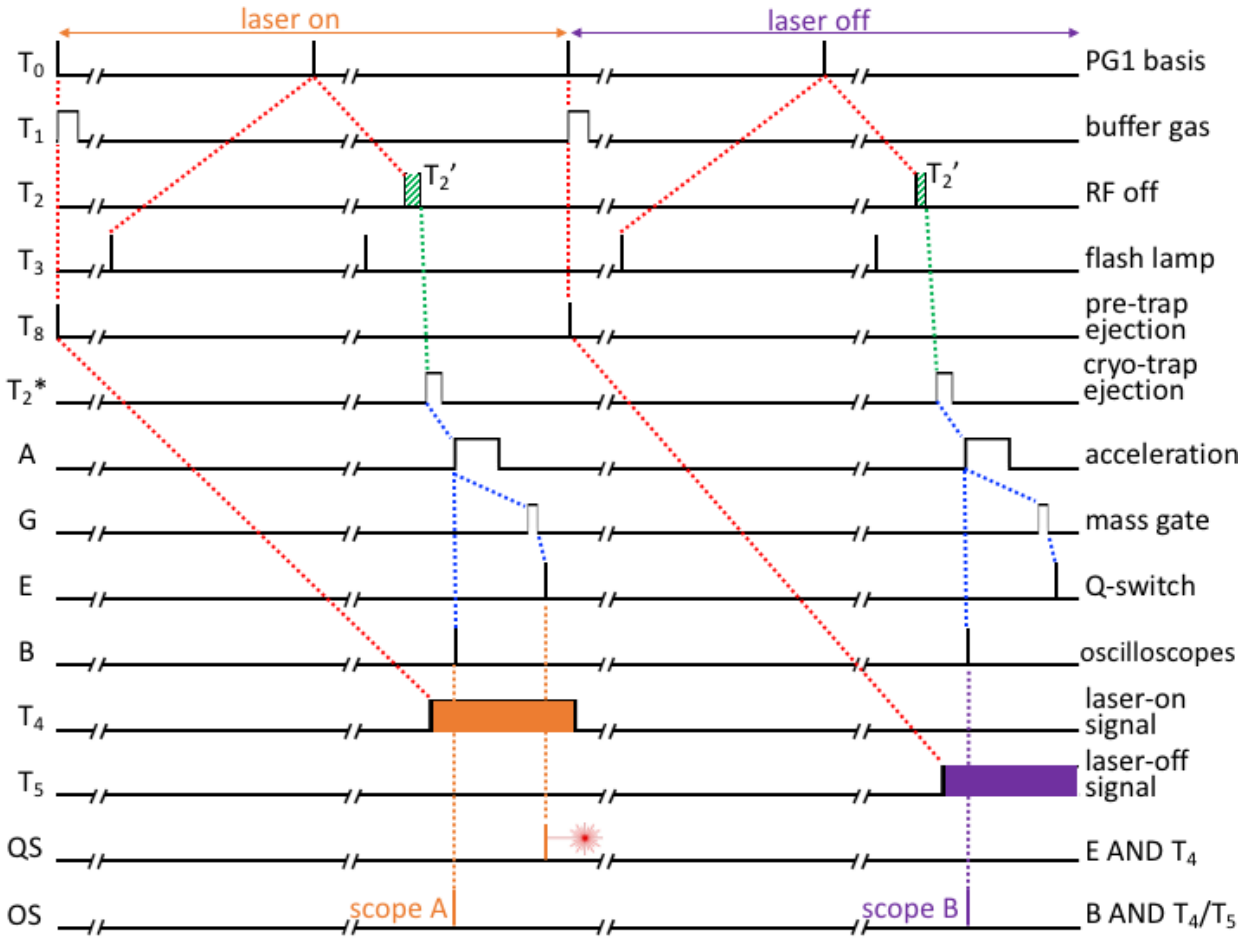

Figure 2.21 The full timing sequence of an experiment with 10 Hz ion source. Pulses with insignificant widths are presented as sticks. Channel numbers are shown on the left and the functions are provided on the right. The diagram shows a full cycle for a single data point, which contains two periods, one with laser on (orange) and the other with laser off (purple). Dotted lines illustrate synchronization hierarchy. Red lines are handled by PG 1; blue by PG 2 (see text). Green lines present the RF power supply and the green shadows indicate the uncertainty of T_2'-T_2. QS is the result of E AND T_4 and the actual trigger of the Q-switch. OS is the trigger for one of the two oscilloscopes in an alternate fashion (see §2.6.2).

Because the flash lamp of the pump laser must be triggered at 20 Hz, it is handled by Channel T_3 of Quantum Composers Model 9618 ("PG 1"), whose fundamental output (T_0) is set to have 20-Hz repetition rate. The generation of ion packets is at 10 Hz (20 Hz if ion cooling is not necessary) and is initiated by the buffer gas pulse on Channel T_1. The pre-trap is triggered by

Channel T_8 to unload the ions. The timing scheme of the main trap has been briefly described in §2.2.3. After an accumulation time of *ca.* 95 ms, Channel T_2 sends a transistor-transistor logic (TTL) signal to the RF power supply of the ion trap. After receiving this signal, the power supply will wait until the RF passes zero from negative and then switches off the RF. Since T_2 may come at any moment during an RF period, the time difference between T_2 and the actual time when RF is switched off, noted as T_2', is uncertain between 0 and 1 μs, shown by the green shadows in **Figure 2.21** on axis T_2. Since the trigger for ion ejection is handled by the power supply too and synchronized to T_2' rather than T_2 (green dotted lines in **Figure 2.21**), the rest of the timing sequence (acceleration, detection, laser pulse, etc.) all has to be referenced to T_2'. Therefore, the TTL output (for ion ejection, noted as T_2*) of the RF power supply is also used to trigger a second pulse generator (Quantum Composers Model 9518, "PG 2") that handles the rest of the timing sequence.

Channel A on PG 2 is synchronized to T_2* and triggers the acceleration of ToF-MS; its delay and width vary with the mass-to-charge ratio of the target ion. For mass selection, the mass gate is triggered by Channel G, which is synchronized to Channel A and tuned to be open only for the target ion species. Channel E triggers the Pockels cell of the pump laser to allow the laser pulse intercept the ion packet in time. Since we need to measure the ion signal with "laser-on" and "laser-off", the laser pulse should be produced at 5 Hz. However, Channel E on PG 2 cannot achieve this on its own, since PG 2 is externally triggered by T_2* at 10 Hz and duty cycle settings will not work. While PG 1 can output 5 Hz pulses using duty cycle settings, the uncertainty of T_2'-T_2 is translated to every channel on PG 1 in respect to the ion packet (see **Figure 2.21**). To circumvent the problem, we use a logic AND gate that takes Channel E and a "laser-on" signal

from PG 1 (T_4). The output will be the right timing owing to Channel E but also the right frequency of T_4 (5 Hz, orange in **Figure 2.21**). This method is also applied to trigger the oscilloscopes. Since two oscilloscopes are required to monitor the laser induced and the background ion signal respectively, the scope triggering (Channel B, 10 Hz) needs to go through the AND gate with T_4 (laser-on) or T_5 (laser-off, purple in **Figure 2.21**) pulse to select the correct oscilloscope (laser-on for Scope A, laser-off for Scope B). The implementation circuit diagram of the AND gate is shown in **Figure 2.22**.

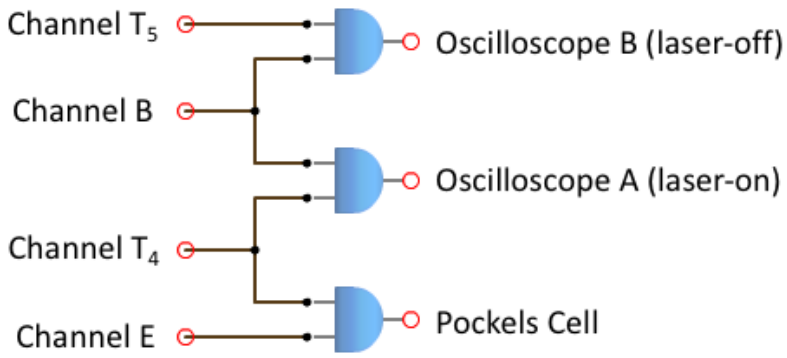

Figure 2.22 AND circuit for triggering pulses.

2.6.2 Data acquisition

To acquire a photodissociation spectrum, we scan the wavelength and monitor the ion signals and laser pulse energy. The scanning schemes are slightly different for the OPO and the dye laser.

The GWU OPO program processes commands remotely sent from a home-written LabVIEW program to perform continuous scans, which means the wavelength changes continuously and samples are collected without stopping the motors. Therefore, in order to keep

the spectral resolution as good as possible, the scan rate needs to be sufficiently slow so that the energy difference of adjacent data points is equal to or less than the linewidth of the laser. For example, in the spectral range around 600 nm (16666 cm^{-1}), with the linewidth being 5 cm^{-1}, the step of the data points should be less than 0.2 nm. Assuming each data point takes about 1.6 s (at 20-Hz repetition rate of the laser), the scan rate should be slower than 8 nm/min. However, in practice all species we have worked with turned out to have absorption bands that are intrinsically much broader, therefore faster scan rates have been applied without loss of information.

For the dye laser, the original control program by the manufacturer is modified and added to our data acquisition and processing modules. Unlike the GWU OPO, the dye laser performs "burst" scans, which means that the wavelength is kept constant for each data point and then driven to the next value for the next data point.

We use two Tektronix TDS 2022 (2-channel, 200 MHz, 2GS/s) oscilloscopes to measure the laser induced ion signal and the background separately. The current from the MCP anode (§2.3.2) is collected using a 50 Ω terminator. The intensity of the laser pulses is measured by a pyroelectric joulemeter (§2.5.1) and the signal is collected by the same oscilloscope that measures the laser induced ion signal (Scope A). The analog input signals at the oscilloscopes are digitized by the oscilloscopes and transmitted to the LabVIEW program via serial ports. For each data point, the wavelength, background signal, laser induced signal and laser intensity, are averaged over 16 or 8 ion shots (samples). Each scan is defined by the boundary wavelengths and the scan rate (OPO) or the step size (dye). After each scan, the raw data are immediately saved and processed according to the choice of action or depletion spectrum by customized modules

built in the LabVIEW program. The processed data are saved as a list of photon energy versus ion signal corrected for photon fluence and background (see §2.6.3).

2.6.3 Data processing

The raw data initially collected by the LabVIEW program consist of ion signals, laser intensity and wavelength. The processing involves background correction and normalization of ion signals to photon number and is automatically performed by the LabVIEW program.and the evaluated spectrum is saved as a separate data file. The operations performed by the program are discussed in this section.

In an action spectrum (see §2.4.2), the intensity of fragment ions, $Y(\lambda)$, actually contains two parts: unimolecular decay of metastable ions, Y_{md}, and photodissociation, $Y_{pd}(\lambda)$. The decay signal from metastable ions is the simply the background fragment signal without laser irradiation and is caused mainly by collisional activation during ion ejection from the trap or during acceleration. Since Y_{md} is measured immediately after every measurement of $Y(\lambda)$, it can be used as the approximate background at the time when $Y(\lambda)$ is measured, and variations of the ion source intensity are minimized this way. A simple subtraction $Y(\lambda) - Y_{md}$ returns $Y_{pd}(\lambda)$.

$Y_{pd}(\lambda)$ is a function of the wavelength λ and proportional to the product of the amount of parent ions P, the photon number $N(\lambda)$, the absorption cross section $\sigma(\lambda)$ and the photodissociation quantum yield Q_d

$$Y_{pd}(\lambda) = P \cdot N(\lambda) \cdot \sigma(\lambda) \cdot Q_d$$

In this equation, the photon number $N(\lambda)$ can be easily derived from the laser intensity $I(\lambda)$ as measured:

$$N(\lambda) = \frac{I(\lambda)}{hc/\lambda}$$

where h is the Planck constant and c is the speed of light. Therefore, $\sigma(\lambda)$ can be represented by

$$\sigma(\lambda) = \frac{hc[Y(\lambda) - Y_{md}]}{\lambda I(\lambda)} \frac{1}{P \cdot Q_d} \qquad \textbf{Equation 2.2}$$

On the right side of **Equation 2.2**, the first term can be calculated directly from raw data, but the second term is difficult to measure in absolute units. Because the reflectron is usually configured to optimize the fragment signal, the intensity of the parent ions cannot be measured simultaneously. In principle, one can use the metastable decay background as a scale of the parent ion $Y_{md} \propto P$, but since Y_{md} is often a small number, normalizing with Y_{md} worsens signal-to-noise. When the ion source is working properly, the yield of parent ion is a stable quantity with random shot fluctuations. Therefore, we assume it to be constant during a single scan (less than 30 minutes). The statistical fluctuations can be smoothed out by averaging over many scans. The photodissociation quantum yield Q_d has been discussed in §2.4.2. Under ideal conditions, Q_d is close to unity. Assuming Q_d is independent on the wavelength, the first term in **Equation 2.2**, denoted as $\sigma'(\lambda)$, is then proportional to the absorption cross section $\sigma(\lambda)$ and can be obtained from the raw data acquired in our experiment, so we can report $\sigma'(\lambda)$ instead of $\sigma(\lambda)$ in our work.

Similarly, for a depletion spectrum, the loss of the parent ion can be linked to the absorption cross section by

$$\sigma(\lambda) = \frac{hc[P - Y_P(\lambda)]}{\lambda I(\lambda)} \frac{1}{P \cdot Q_d}$$

where $Y_P(\lambda)$ is the parent ion signal with the laser on and other symbols are defined as before. The difference in this case is that the "background" parent ion signal P can be measured directly. We then obtain the relative absorption cross section in the limit of small ion depletion

$$\sigma'(\lambda) = \frac{hc[P - Y_P(\lambda)]}{\lambda I(\lambda) P}$$

If the same assumption of Q_d can be made, $\sigma'(\lambda)$ is a good representation of $\sigma(\lambda)$. Normally, because P is a large number and $P - Y_P(\lambda)$ is small, depletion spectra are often noisier than action spectra. If the fraction of the loss of parent ion is significant, the extraction of $\sigma(\lambda)$ is less straightforward. One may use the modified Lambert-Beer law[28]

$$\frac{Y_P(\lambda)}{P} = 1 - \alpha + \alpha e^{-\sigma(\lambda)F(\lambda)}$$

where α is a parameter indicating the overlap between laser and ion packet, and $F(\lambda)$ is the photon fluence. The overlap parameter can be determined by measuring the intensity dependence of the parent ion depletion at the peak of the absorption profile. Chapter 5 will provide a concrete example where this method is deployed.

2.6.4 Baseline and scaling correction

The oscilloscopes used to measure the ion signals have non-zero baseline values. To measure the baseline, the laser beam is blocked before a scan begins and the reading of each channel of the oscilloscopes is recorded and saved. These values will be subtracted from the ion and laser pulse energy measurements to eliminate this artifact.

The oscilloscopes may also have slightly different scaling factors, which can skew large readings. This is a potential problem for depletion spectra as the parent ion signal is usually large.

Therefore, when laser is blocked, the parent ion signals on both oscilloscopes are recorded. The ratio of these two values is calculated and used to rescale the data collected by the two oscilloscopes during the scan.

2.7 References

1. Xu, S., Gozem, S., Krylov, A. I., Christopher, C. R. & Weber, J. M. Ligand influence on the electronic spectra of monocationic copper-bipyridine complexes. *Phys. Chem. Chem. Phys.* **17,** 31938–31946 (2015).

2. Weigend, F. & Ahlrichs, R. Balanced basis sets of split valence, triple zeta valence and quadruple zeta valence quality for H to Rn: Design and assessment of accuracy. *Phys. Chem. Chem. Phys.* **7,** 3297–3305 (2005).

3. Weigend, F., Häser, M., Patzelt, H. & Ahlrichs, R. RI-MP2: optimized auxiliary basis sets and demonstration of efficiency. *Chem. Phys. Lett.* **294,** 143–152 (1998).

4. Parr, R. G. & Yang, W. *Density-Functional Theory of Atoms and Molecules*. *Oxford University Press: New York* (1989).

5. Yamashita, M. & Fenn, J. B. Electrospray ion source. Another variation on the free-jet theme. *J. Phys. Chem.* **88,** 4451–4459 (1984).

6. Dole, M. *et al.* Molecular Beams of Macroions. *J. Chem. Phys.* **49,** 2240 (1968).

7. Fenn, J. B., Mann, M., Meng, C. K. A. I., Wong, S. F. & Whitehouse, C. M. Electrospray ionization for mass spectrometry of large biomolecules. *Science* **246,** 64–71 (1989).

8. Rayleigh, F. R. S. On the equilibrium of liquid conducting masses charged with electricity. *Philos. Mag. Ser. 5* **14,** 184–186 (1882).

9. Hoffmann, E. & Stroobant, V. *Mass Spectrometry: Principles and Applications*. John Wiley & Sons, Ltd. (2006).

10. Taylor, G. Disintegration of water drops in an electric field. *Proc. R. Soc. A Math. Phys. Eng. Sci.* **280,** 383–397 (1964).

11. Blades, A. T., Ikonomou, M. G. & Kebarle, P. Mechanism of electrospray mass spectrometry. Electrospray as an electrolysis cell. *Anal. Chem.* **63,** 2109–2114 (1991).

12. Ikonomou, M. G., Blades, A. T. & Kebarle, P. Electrospray-ion spray: a comparison of mechanisms and performance. *Anal. Chem.* **63,** 1989–1998 (1991).

13. Kebarle, P. & Tang, L. From ions in solution to ions in the gas phase. *Anal. Chem.* **65,** 972A–986A (1993).

14. Kebarle, P. & Verkerk, U. H. Electrospray: from ions in solution to ions in the gas phase, what we know now. *Mass Spectrom. Rev.* **28,** 898–917 (2009).

15. Tosi, P., Fontana, G., Longano, S. & Bassi, D. Transport of an ion beam through an octopole guide operating in the r.f.-only mode. *Int. J. Mass Spectrom. Ion Process.* **93,** 95–105 (1989).

16. Gerlich, D. Inhomogeneous RF fields : a versatile tool for the study of processes with slow ions. *Advances in Chemical Physics: State-Selected and State-To-State Ion-Molecule Reaction Dynamics, Part 1. Experiment* **82** (1992)

17. Jones, R. M. & Gerlich, D. Simple radio-frequency power source for ion guides and ion traps. *Rev. Sci. Instrum.* **68,** 3357–3362 (1997).

18. Dawson, P. H. Ion Storage in three-dimensional, rotationally symmetric, quadrupole fields. I. Theoretical treatment. *J. Vac. Sci. Technol.* **5,** 1 (1968).

19. March, R. E. An Introduction to Quadrupole Ion Trap Mass Spectrometry. *J. Mass Spectrom.* **32,** 351–369 (1997).

20. Guilhaus, M. Principles and instrumentation in time-of-flight mass spectrometry. *J. Mass Spectrom.* **30,** 1519–1532 (1995).

21. Wiley, W. C. & McLaren, I. H. Time-of-Flight Mass Spectrometer with Improved Resolution. *Rev. Sci. Instrum.* **26,** 1150 (1955).

22. Marcum, J. C. Electronic photodissociation spectroscopy of Electrosprayed anions (2011). University of Colorado, Boulder.

23. Stoermer, C. W., Gilb, S., Friedrich, J., Schooss, D. & Kappes, M. M. A high resolution dual mass gate for ion separation in laser desorption/ionization time of flight mass spectrometry. *Rev. Sci. Instrum.* **69,** 1661 (1998).

24. Garand, E., Stipdonk, M. J. Van & Johnson, M. A. Isomer-Specific IR-IR Double Resonance Spectroscopy of D2-Tagged Protonated Dipeptides Prepared in a Cryogenic Ion Trap. *J. Phys. Chem. Lett.* **3**, 1099-1105 (2012).

25. Thompson, M. C., Baraban, J. H., Matthews, D. A., Stanton, J. F. & Weber, J. M. Heavy atom

vibrational modes and low-energy vibrational autodetachment in nitromethane anions. *J. Chem. Phys.* **142,** 234304 (2015).

26. Geusic, J. E., Marcos, H. M. & Van Uitert, L. G. Laser oscillations in nd-doped yttrium aluminum, yttrium gallium and gadolinium garnets. *Appl. Phys. Lett.* **4,** 182–184 (1964).

27. Cobra-Stretch Dye Laser Datasheet. (2015)

28. Schweizer, A. *et al.* Electronic photodissociation spectroscopy of $Au^{4+}{\cdot}Ar_n$, n=0-4: Experiment and theory. *J. Chem. Phys.* **119,** 3699–3710 (2003).

3 The role of the ligands

3.1 Introduction

Ligands play very important roles in organometallic complexes. The properties of ligands, such as their electron affinity, polarizibility, aromaticity and geometry, can profoundly influence the properties of a complex. Different ligands often lead to different complex stability and reactivity, which have been some of the main focuses of study in inorganic chemistry. One of the directions that researchers have been pursuing is to characterize the function of a specific ligand and its influence on the properties of the complex. This is difficult to achieve in the condensed phase, since many other factors influence the behavior of a complex, such as the chemical microenvironment caused by the solvent. In order to systematically investigate ligand influence, one needs systems that have few and controllable variables. One common approach to make a systematic analysis is to alter one single ligand in a complex at a time and observe the change in the properties of the complex.[1–10] But this approach also poses challenges because such experiments usually involve heteroleptic and undercoordinated compounds. Heteroleptic compounds often require delicate syntheses and can undergo speciation processes in solution, even if the syntheses succeed. Undercoordinated compounds are rarely stable in the condensed phase because the open coordination sites are vulnerable to the chemical environment. These difficulties can be avoided if the compound is prepared in the gas phase. As we have introduced in previous sections, solvents and counterions are automatically eliminated in the gas phase. In addition, mass selection allows us to obtain pure samples and interrogate a single species at a time.

Many of the properties are connected with the electronic structures of the compound. A fundamental question in this context is how a ligand modifies the electronic structure of the whole complex. This question can be theoretically approached by ligand field theory, which is capable of explaining some of the important properties, such as spin configuration and color, particularly for homoleptic compounds with high symmetry. Experimentally, the electronic spectra can be measured by applying laser spectroscopy to compounds in the gas phase, thereby excluding any effects related to solvent interaction.

Our focus in this chapter lies on the ligand influence in organometallic ions. We selected a series of compounds with a single variable ligand. The fixed part in the series is ideally stable, non-reactive and well-studied, so that the influence of the variable ligand can be unambiguously tracked. We have looked into two series of complexes.

The first series consists of several copper(I) mono-2,2'-bipyridine (bpy) complexes. They take the form $[\mathbf{Cu}\text{-L}]^+$, where boldface **Cu** represents the fixed part, Cu^I-bpy, and L represents the variable ligand. In this case, L was chosen to be N_2, D_2, H_2O, CH_3OH and Cl, forming a series from weakly to strongly interacting ligands. One major merit of studying this series is that Cu^I is formally a closed-shell metal core so **Cu** does not have d-d bands and its first electronic excitation is a $\pi\pi^*$ transition localized on the bpy ligand (except L = Cl). Consequently, the effects of the additional ligand are expected to be reflected in the $\pi\pi^*$ band of the system. We measured the photodissociation spectrum of $[\mathbf{Cu}\text{-L}]^+$ with different L and examined the influence of L by comparing the spectra.

The second series we studied consists of dicationic ruthenium polypyridyl complexes, denoted as $[\mathbf{Ru}\text{-L}]^{2+}$, where **Ru** = Ru^{II}(bpy)(tpy) and tpy = 2,2';6',2"-terpyridine. L is again the

variable ligand, in this study H_2O, CO_2, CN_3CN and N_2. The complexes based on **Ru** have been extensively studied because they are often involved in catalytic applications, from water oxidation[11,12] and CO_2 reduction[13,14] to nitrogen fixation.[15] This type of complex has a bright absorption band in the visible range that has the character of a metal-to-ligand charge transfer transition. Since **Ru** is an undercoordinate species, the attack of an extra ligand can be expected to alter its properties, which will be important for the function of the complex in catalysis. Therefore, it is imperative to study the electronic structure of $[\mathbf{Ru}\text{-L}]^{2+}$ in aid of understanding fundamental aspects of its function. Note that species like $[\mathbf{Ru}\text{-L}]^{2+}$ are often intermediates and their isolation is often not possible in solution. Our experiment provides the first characterization of these transient ion species without the presence of a chemical environment.

3.2 Copper bipyridine complexes

3.2.1 Background

Copper based compounds have been widely studied because they have many applications in both chemical research and industry and they are relatively inexpensive owing to the large abundance of copper on earth. A recent example for their potential use is their promise as inexpensive water oxidation catalysts, as reported by Barnett *et al*.[17] and Chen *et al*.,[18] but their

photophysics and photochemistry are equally fascinating.[19,20] In particular, complexes containing monovalent Cu^{I} serve as an ideal system to study ligand effects and ligand-ligand interactions because – at least in a qualitative formal charge picture – the metal core is in a closed-shell configuration (d^{10}) and their spectra should therefore be free from complications by transitions between *d*-orbitals. [21–25]

Diimines form a very common group of bidentate metal chelating ligands. Complexes of Cu^{I} and some diimine ligands have found potential applications in solar energy conversion and therefore their electronic structure and photophysical properties are under extensive study.[26–29] Complexes containing 2,2'-bipyridine (bpy) and 1,10-phenanthroline have received more attention because of the basic form of the ligands. In most experimental studies, fully coordinated complexes with a variety of ligands are synthesized and characterized, however, there seems to be a lack of studies of undercoordinated complexes despite of their simplicity.[30–32] This study will focus on mono-bpy complexes of Cu^{I}.

The electronic structure of bpy has been studied for decades.[33–38] It is of C_{2v} symmetry and its ground state is an A_1 state. Therefore, the only optically allowed transitions are those to the A_1, B_1 and B_2 states. The first excited state S_1 (1^1A_2, $n\pi^*$) is not optically accessible due to symmetry restrictions. The transition to the S_2 state (1^1B_1, $n\pi^*$) is very weak, while the transition to the S_3 state (1^1B_2, $\pi\pi^*$) is bright.[38] All these transitions are in the UV spectral region. When bpy is chelated to a metal ion, one would expect that these transitions will be shifted and that the nature of states and their order may be modified. In the simplest case where the metal is a closed-shell ion (Cu^{I} and Zn^{II}), there will be no low-lying d-d bands or charge transfer bands. The n-orbitals involved in the lowest energy excited states of bpy will convert into σ-orbitals to bind

with the metal. The lowest dark transition will therefore have σπ* nature instead of nπ*, but the first bright transition will still be the ππ* band (to the S_2 state). In fact, this reasoning is supported by experiments on $[Zn^{II}(bpy)]^{2+}$. The ππ* transition of $[Zn(bpy)]^{2+}$ in solution was found at *ca.* 32600 cm^{-1},[34] shifted by 3200 cm^{-1} to the red compared to the analogous bpy solution without Zn^{2+}, but the band profile is largely preserved.[39] Therefore, we anticipate similar results for $[Cu^{I}(bpy)]^{+}$ (denoted as **Cu**$^{+}$ in the following). To understand more complicated systems where multiple ligands are present, one may start by asking what happens if another ligand is added to **Cu**$^{+}$. To carry out this study in a systematic fashion, we have examined a series of complexes in the formula [**Cu**-L]$^{+}$, where L is a variable and selectable ligand. By taking advantage of this very simple system in isolation (*in vacuo*), we are able to investigate the role of the additional ligand in detail.

3.2.2 Methods

The instrumentation for the experiment has been described in detail in Chapter 2. To generate a particular [**Cu**-L]$^{+}$ species, we prepared a solution with equal concentration of copper(II) salt and 2,2'-bipyridine in a 1:4 mixture of distilled water and methanol (HPLC grade, EMD Millipore). Copper(II) nitrate hydrate (99.999%, trace metals basis, for L = N_2, D_2, H_2O and CH_3OH) and 2,2'-bipyridine (ReagentPlus grade, ≥99%) were purchased from Sigma-Aldrich, while copper(II) chloride dehydrate (99+%, ACS grade, for L = Cl) was purchased from Alfa Aesar. All chemicals were used without further purification. The concentration was 5 mM, and the solution was pumped to the ESI needle at 25 μL/hr. The spraying needle was held at +3 kV and the desolvation capillary was heated to 70 °C in order to achieve optimal ion intensity.

While [**Cu**-$OHCH_3$]$^+$, [**Cu**-OH_2]$^+$ and [**Cu**-Cl]$^+$ were formed directly in the solution and extracted to gas phase by ESI, [**Cu**-N_2]$^+$ and [**Cu**-D_2]$^+$ were formed in the trap where ambient N_2 or D_2 molecules dock onto **Cu**$^+$. A mass spectrum with mass peaks for **Cu**$^+$, [**Cu**-OH_2]$^+$ and [**Cu**-$OHCH_3$]$^+$ is shown in **Figure 3.1**.

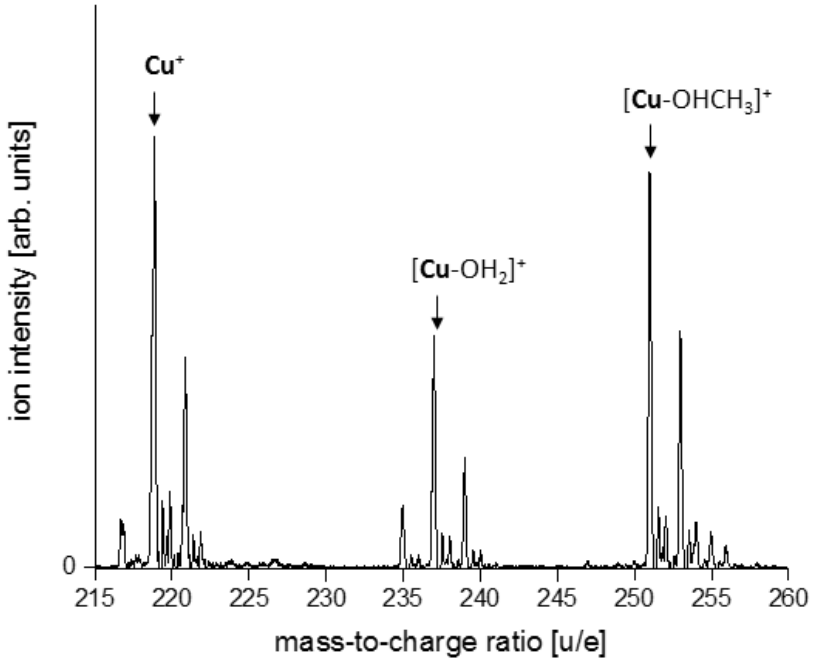

Figure 3.1 Mass spectrum showing the formation of **Cu**$^+$, [**Cu**-OH_2]$^+$ and [**Cu**-$OHCH_3$]$^+$. The arrows point to the ions containing ^{63}Cu only.

We calculated the ground state properties (dissociation thresholds, natural charges, and vibrational frequencies) of the molecules under study with density functional theory[40] (DFT) using the PBE0 functional[41] and def2-TZVP[42] basis sets for all atoms. We also calculated the excitation energies and the respective oscillator strengths for the excited states to aid our assignment of the spectrum. These calculations were performed using the Turbomole suite of programs.[43]

However, our results of the excited states turned out to be unsuitable to describe the experimental observations. Therefore, higher-level calculations using the "equation-of-motion for excitation energies coupled-cluster approach with single and double excitations" (EOM-EE-CCSD)[44,45] were performed by Professor Anna Krylov's group at the University of Southern California.[16]

3.2.3 Results and discussions

3.2.3.1 $[Cu^{I}(bpy)]^{+}$

Before adding the ligand L, it is constructive to obtain some information about **Cu^{+}** itself for comparison. This was feasible because we were able produce this ion by ESI, and the binding energy of Cu and bpy^{+} is estimated to be 415 kJ/mol (34680 cm^{-1}), roughly in the spectral range where we expect the ππ* bands of metal-bpy complexes. The upper panel of **Figure 3.2** shows the photodissociation spectrum of **Cu^{+}** monitoring the yield of bpy^{+} acquired at room temperature. One can immediately notice the resemblance of this spectrum to the fluorescence excitation spectrum of $[Zn^{II}(bpy)]^{2+}$ taken by Kotlicka and Grabowski,[34] shown in the lower panel of **Figure 3.2**.

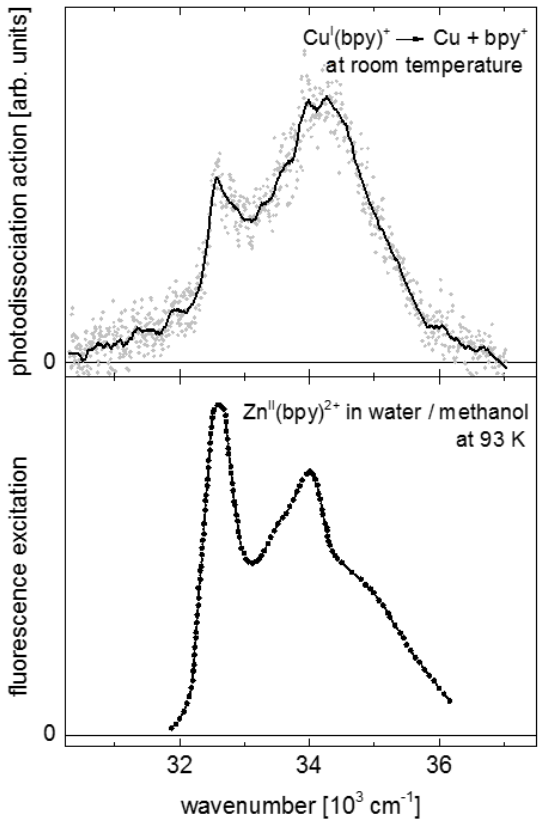

Figure 3.2 The photodissociation spectrum of $[Cu^{I}(bpy)]^{+}$ at room temperature (upper) and the fluorescence excitation spectrum of $[Zn^{II}(bpy)]^{2+}$ at 93 K in water and methanol (lower). In the upper panel, gray dots are raw data and black solid line is 50-point sliding average. The data for $[Zn^{II}(bpy)]^{2+}$ were extracted from the work by Kotlicka and Grabowski.[34]

The positions of the two resolved peaks are almost identical, indicating the same amount of shift compared to the bare bpy as a corroborative trend for d^{10} metal ions. The first peak is found at 32580 cm^{-1}, slightly below the calculated binding energy. Therefore, it is likely that the internal energy stored in the ion at room temperature is a contributing factor to overcoming the dissociation threshold. In fact, upon lowering the trap temperature to 50 K, nearly no photofragments were detected, corroborating this speculation. This may also account for the

difference of the relative peak intensity between **Cu**$^{+}$ and $[Zn^{II}(bpy)]^{2+}$ since the lower-energy peak in the photodissociation spectrum of **Cu**$^{+}$ may have been suppressed due to kinetic effects.

3.2.3.2 L = N_2, D_2, H_2O, CH_3OH and Cl

We first performed DFT calculations for the ground state of all species to glance at the basic properties. Several important properties are summarized in **Table 3.1,** and the geometries are provided in **Figure 3.3**. The results largely meet our expectations. All species are singlets in the ground state except for [**Cu**-Cl]$^{+}$, which is a doublet. The binding energy increases in the order of $N_2 < D_2 < H_2O \approx CH_3OH < Cl$. The charge analysis provides a qualitative picture of the charge distribution. For L = N_2, D_2, H_2O and CH_3OH, the charge on Cu or bpy is fairly close to that in **Cu**$^{+}$, indicating a small polarization effect from the additional ligand, and the ligand L is more or less neutral. In contrast, Cl has a much larger electronegativity and therefore attracts electron density from the copper core. However, the formal charge on Cu is +1.174 and on Cl is -0.512, not quite close to +2 and -1 as one might imagine based on formal charges. One conceivable explanation is that the bpy ligand lends π electron density to the copper core when Cl oxidizes it from the other side. As a result, the net valence on Cu is reduced but a higher valence on bpy is induced, as predicted by the calculation.

Table 3.1 Calculated ground-state properties of the complexes under study (PBE0/def2-TZVP). Binding energies are for the ligand L in [**Cu**-L]$^+$, except for **Cu**$^+$ where the binding energy is given for Cu and bpy$^+$. Partial charges were determined using natural population analysis.[46]

species	Binding energy [kJ/mol]	charge on Cu/ligand L/bpy
^{1}**Cu**$^+$	415	+0.886 / – / +0.114
^{1}[**Cu**-N_2]$^+$	29	+0.918 / -0.081 / +0.163
^{1}[**Cu**-D_2]$^+$	58	+0.850/-0.003/+0.153
^{1}[**Cu**-OH_2]$^+$	106	+0.846 / +0.055/ +0.099
^{1}[**Cu**-$OHCH_3$]$^+$	87	+0.829/+0.066/+0.105
^{2}[**Cu**-Cl]$^+$	247	+1.174 / -0.512 / +0.338

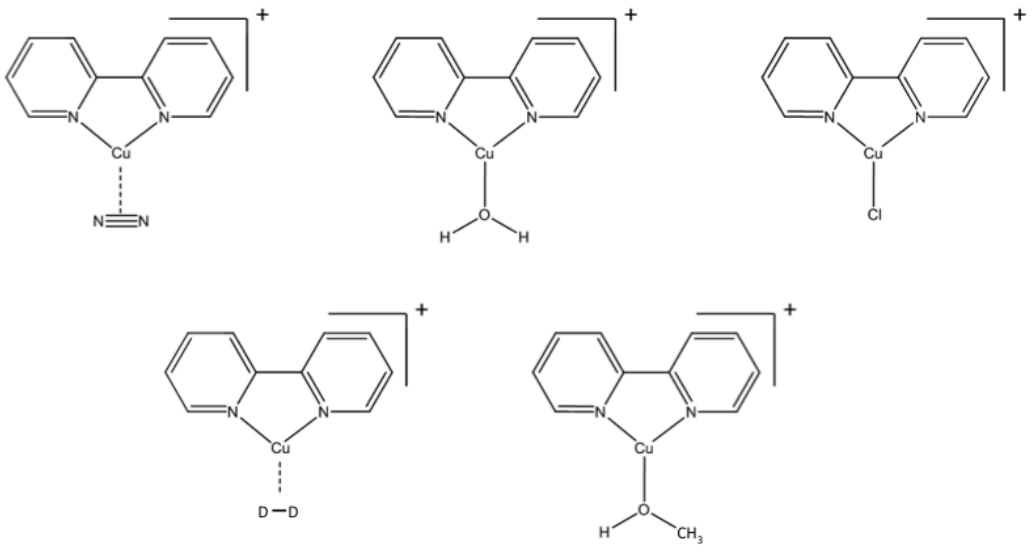

Figure 3.3 The structures for [**Cu**-L]$^+$ (L = N_2, D_2, H_2O, CH_3OH and Cl)

We measured the photodissociation spectra of [**Cu**-L]$^+$ by monitoring the loss of the L ligand. As shown in **Table 3.1**, according to the ground state calculations, the binding energies of the L ligand in all cases are less than 290 kJ/mol (24000 cm^{-1}), allowing dissociation by UV

photons. The loss of the L ligand was found to be the only dissociation channel of these ions when the photon energy was fixed at 33870 cm^{-1} (see **Figure 3.4**).

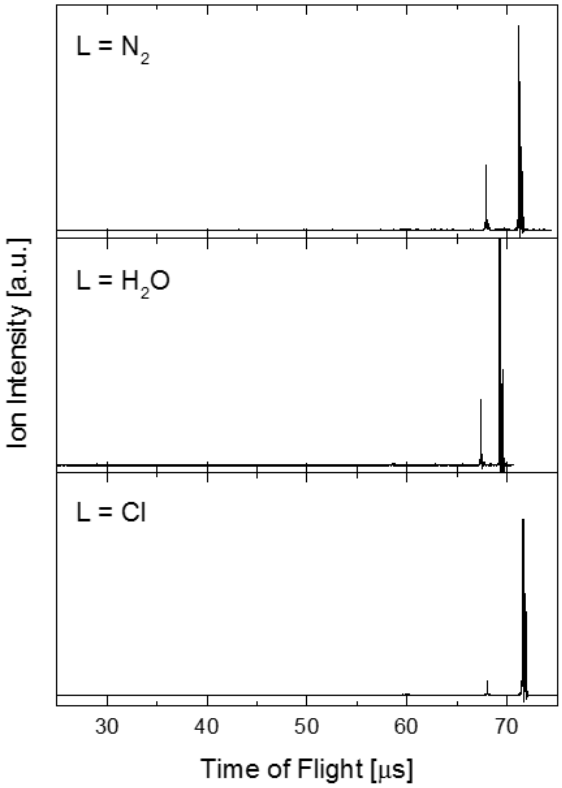

Figure 3.4 Time-of-flight traces for electronic photodissociation of [**Cu**-L]$^+$ complexes at 33870 cm^{-1} (L = N_2, H_2O and Cl). The ion signals on the right represent the parent ions, while the smaller peaks are fragment ion signals. Only one fragment mass is observed in each case.

Figure 3.5 shows the photodissociation spectra for all the species at 250 K trap temperature in the UV region, together with **Cu**$^+$ (room temperature) on the top for comparison. The absorption profile in this spectral range represents the same ππ* transition located on the bpy moiety. All spectra have a discernible peak in the region of 32260 -33070 cm^{-1}. The spectral envelopes are quite distinct with different ligands, but the experimental signatures are broad in all cases.

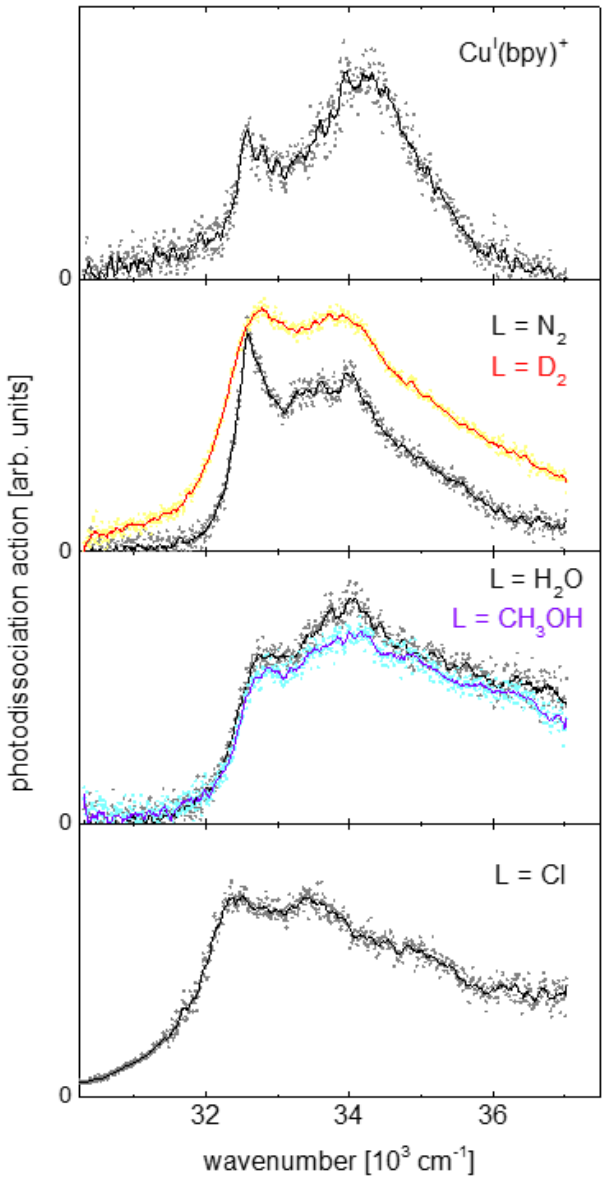

Figure 3.5 Photodissociation spectra at 250 K for L = N_2, D_2, H_2O, CH_3OH and Cl monitoring the loss of L. The spectrum of **Cu**$^+$ at room temperature is included for reference. The data points in the photodissociation spectra are the raw data; the full lines are the same data smoothed by a 10-point sliding average. Spectra in the same panel are rescaled for comparison and do not reflect relative intensity.

Computational description of this series of complexes turned out to be surprisingly difficult. Time-dependent density functional theory (TD-DFT) completely failed to model the electronic spectra. Different functionals including PBE0, B3LYP and BNL[47,48] were used but yielded

inconsistent results. The computed excitation energies were often off by more than 6500 cm^{-1} compared to experimentally observed values. Coupled-cluster calculations using the CC2 model also failed, probably because of a multi-configurational character of the ground state, as evaluated by the D_1 diagnostic proposed by Janssen and Nielsen.[49] Calculations at the EOM-EE-CCSD level of theory yielded better results, but the vertical excitation energies were still consistently 4840 cm^{-1} (0.6 eV) higher than the experiment. Excited state optimization led to small improvements of the excited state energies of the ππ* state. The difference between the adiabatic and the experimental energy for the ππ* state is 3230 cm^{-1}, 3550 cm^{-1}, and 4440 cm^{-1} for L = N_2, H_2O and Cl, still significantly larger than typical deviations of EOM-CCSD, estimated to be at 2400 cm^{-1} (0.3 eV).

The calculations did confirm the ππ* nature of the transition near 32300 cm^{-1}. In addition, a lower-lying dark state was found to exist in all species. This kind of electronic structure is analogous to bare bpy, where a dark nπ* state lies below the bright ππ* state. The only difference is that in the coordination complex the dark state becomes a σπ* state as the bpy binds to the metal core. The computational results are summarized in **Table 3.2**.

Table 3.2 Experimental and computed excitation energies. The experimental energies list the first discernible peaks in each electronic band. Computed energies are determined at the EOM-EE-CCSD/cc-pVTZ level unless indicated otherwise. Computed adiabatic excitation energies are in parentheses. All energies are given in cm^{-1}.

species	experimental	calculated (adiabatic)	term	oscillator strength	type
Cu$^+$	32580				
[**Cu**-N_2]$^+$	– [a]	36537	$^1A_2$	0	σπ*
	32580	37505 (35811)	$^1B_2$	0.047	ππ*
[**Cu**-OH_2]$^+$	– [a]	31940	$^1A_2$	0	σπ*
	– [b]	34763	$^1B_2$	2.9×10^{-4}	MLCT to H_2O
	32830	37827 (37263)	$^1B_2$	0.045	ππ*
[**Cu**-Cl]$^+$	– [b]	9840	$^2B_2$	1.1×10^{-5}	
	– [a]	10485	$^2A_2$	0	
	– [b]	14841	$^2B_2$	2.2×10^{-4}	
	– [b]	15083	$^2B_1$	2×10^{-6}	
	21940	26616 (20487)	$^2A_1$	0.056	CT from Cl to bpy
	– [b]	28068	$^2B_2$	2.4×10^{-5}	
	– [a]	28471	$^2A_2$	0	
	32420	37263 (35972) [c]	$^2B_2$	0.205[c]	ππ*

[a] This transition is symmetry-forbidden.

[b] This band is allowed, but has negligible calculated oscillator strength, and is too weak to be observed experimentally.

[c] These values were computed using EOM-SF-CCSD instead of EOM-EE-CCSD.

In the following paragraphs we will discuss individual cases separately, starting with L = N_2. The spectrum of [**Cu**-N_2]$^+$ shows a clear peak at 32580 cm^{-1}, followed by a plateau which extends shortly beyond 34000 cm^{-1}. Lowering the trap temperature has a dramatic influence on the spectrum. **Figure 3.6** shows the photodissociation spectrum of this ion at 70 K trap temperature. The plateau in the spectrum at higher temperature becomes a sequence of well-

resolved peaks. The leading molecular orbitals involved in the two lowest electronic transitions are plotted in **Figure 3.7**.

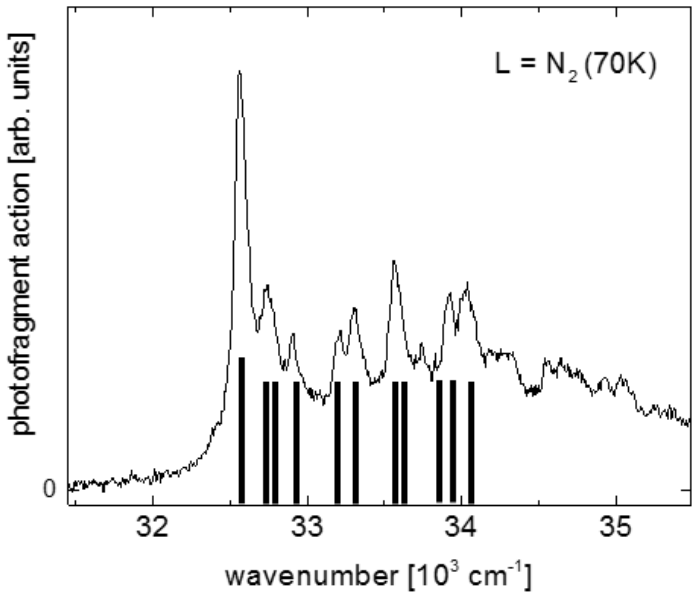

Figure 3.6 Photodissociation spectrum of L = N_2 with trap temperature at 70 K. The photon energy axis is relative to the 0–0 band position of the $\pi\pi^*$ electronic band, which is found at 32580 cm^{-1}. The full line represents experimental data, the stick spectrum shows calculated totally symmetric (ground state) vibrations of [**Cu**-N_2]$^+$ (see also **Table 3.3**). The 0–0 band is marked with a higher intensity for clarity, but we note that we cannot make any quantitative statements on the expected band intensities.

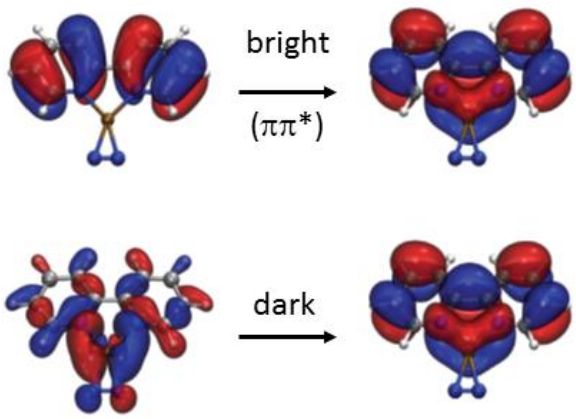

Figure 3.7 Leading molecular orbitals for the two lowest energy transitions in [**Cu**-N_2]$^+$. The upper panel shows the allowed transition to the ππ* state, the lower panel shows the orbitals involved in the (symmetry forbidden) σπ* transition to the dark state calculated 968 cm^{-1} below the bright ππ* state (see also **Table 3.2**).

Since there is only one bright transition in this region, the observed substructure of the absorption band is likely due to vibrational progressions in the Franck–Condon envelope of the electronic band. Considering the already difficult challenge of theoretically describing the electronic structure, Franck–Condon simulations were beyond our computational resources. However, if we assume that the vibrational frequencies in the ground and excited states are not too far apart, we can manually pick out candidates for Franck-Condon active vibrations by inspecting the vibrational modes of [**Cu**-N_2]$^+$ in its ground state, similar to an earlier approach in the study of bpy.[50] Geometry optimization of the ππ* state in bpy (TDDFT with PBE0/def2-TZVP) revealed that the main geometry changes of bpy from its ground state to its ππ* state are the length of the central C-C bond and the CNC bond angle in the rings. Therefore, the totally symmetric vibrations along these coordinates are the most probable contributors to the excited-state vibrational features. The modes identified this way are mainly ring deformation modes and

the energies of these modes are calculated and tabulated in **Table 3.3**. Bending and stretching modes of the CH groups, the N_2 stretch and the Cu-N_2 stretching mode should not be very Franck-Condon active. If we set the electronic band origin at the first peak and mark the Franck-Condon active modes on the energy axis according to their vibrational energies, we are able to qualitatively reproduce the band contour in fairly good agreement with the experimental result, as in **Figure 3.6**. One may also extract the vibrational energies from the experimental data.

Table 3.3 Experimental values were determined by fitting Lorentzian profiles with 100 cm^{-1} full width at half-maximum (which corresponds to the width of the 0-0 band) to the clearly discernible peak features in **Figure 3.6**. The error in these peak positions is ± 10 cm^{-1}. Calculated values are for totally symmetric ground state vibrational modes of [**Cu**-N_2]$^+$ obtained with PBE0/def2-TZVP (harmonic approximation). Additional totally symmetric modes are listed in **Table 3.4**.

experimental [cm^{-1}]	calculated [cm^{-1}]	assignment
179 [a]	170/240	skeletal bipy bending modes
347	381	central C-C stretch
639	673	CNC bending ring deformation
747	783	CCC bending ring deformation
1004 [b]	1055/1098	ring deformation modes
1355 [b]	1318/1326/1366	central C-C stretching modes
1467	1538	CH bend and central CC stretch

[a] This feature is wider than the others and likely combines two unresolved vibrational peaks.

[b] Several of the modes listed could contribute since they have similar character.

If we further lower the trap temperature, nitrogen starts condensing in the trap, hindering the generation of [**Cu**-N_2]$^+$. We were not able to generate a stable ion signal and measure the spectrum at temperatures lower than 70 K using our current setup. The residual width of the

vibrational features comes from the finite temperature, the excited-state lifetime, or a combination of these two contributions.

Since N_2 is chemically inert under most circumstances, one might tend to believe that adding an N_2 molecule as a ligand may not significantly change the electronic structure of the original host. This assumption is corroborated by comparing the spectrum of [**Cu**-N_2]$^+$ and **Cu**$^+$. The peak positions are the same and the spectral profiles are very similar. There is a difference in the relative intensity of the band origin and the rest of the Franck-Condon envelope. However, we were monitoring the loss of N_2 from [**Cu**-N_2]$^+$, and the threshold for this process is much smaller (see **Table 3.1**), therefore the 0-0 band is no longer suppressed by kinetic shift effects that affect the photodissociation spectrum of **Cu**$^+$. One other piece of evidence that supports the above assumption is that the calculated frequencies of the vibrational modes in [**Cu**-N_2]$^+$ and **Cu**$^+$ are very similar. This comparison is based on the calculations of the normal modes of both ions in their ground state, which are listed in **Table 3.4**. The difference of the vibrational frequencies is less than 5 cm^{-1} in most cases.

Table 3.4 Comparison of the calculated vibrational modes in [**Cu**-N_2]$^+$ and **Cu**$^+$. Numbers are given in cm^{-1}.

Cu$^+$	[**Cu**-N_2]$^+$	assignment
195	170	pyridine-Cu-pyridine bend and central C-C stretch
229	240	bipy bend around central C-C bond
- [a]	311	Cu-N_2 stretch
372	381	central C-C stretch
670	673	CNC bending ring deformation
778	783	CCC bending ring deformation
1048	1055	CNC bending ring deformation
1099	1098	CC stretching ring deformation
1143	1143	CH bend
1208	1205	CH bend
1314	1318	central CC stretch and CN stretching ring deformation
1319	1326	central CC stretch and CH bend
1357	1363	central CC stretch and CN stretching ring deformation
1472	1474	CH bend
1532	1538	CH bend and central CC stretch
1636	1637	CH bend and ring deformation
1658	1661	ring deformation
- [a]	2262	N-N stretch in N_2 ligand
3210	3211	CH stretch
3217	3218	CH stretch
3237	3238	CH stretch
3257	3251	CH stretch

[a] These modes involve the N_2 ligand and are not present in **Cu**$^+$.

The spectrum of [**Cu**-D_2]$^+$ resembles that of [**Cu**-N_2]$^+$. Calculations found that the binding energy of D_2 and **Cu**$^+$ is 58 kJ/mol, much higher than N_2 and **Cu**$^+$. The absorption maximum of [**Cu**-D_2]$^+$ is at roughly the same position as that of [**Cu**-N_2]$^+$ but the spectrum of [**Cu**-D_2]$^+$ has different widths. These results imply that D_2 may have a stronger impact on the relaxation dynamics of the

excited state than N_2 does. Consequently, neither N_2 nor D_2 would be useful as tags for undercoordinated metal complexes.

In the case of L = H_2O, lowering the trap temperature also sharpens the spectrum but does not lead to equally well-resolved features as in L = N_2, despite that the trap temperature is at 50 K, lower than for L = N_2 (see **Figure 3.8**).

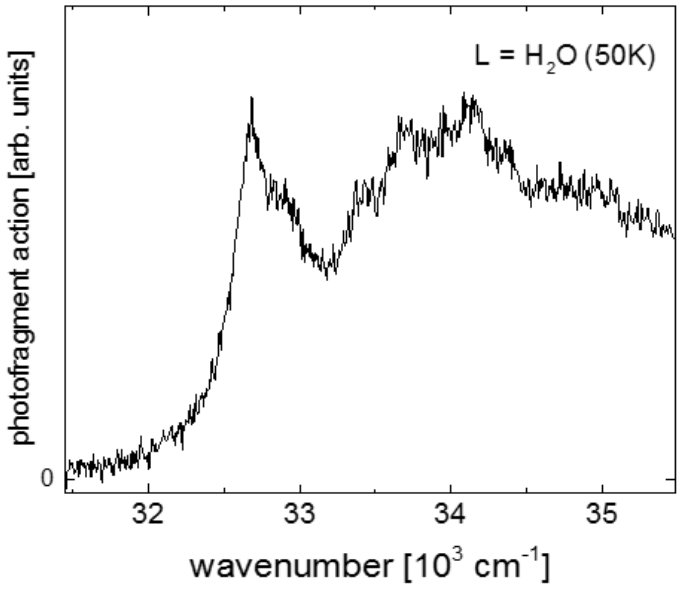

Figure 3.8 Photodissociation spectrum of [**Cu**-OH_2]$^+$ ions (monitoring the loss of water) at 50 K.

It is quite clear though, that the band contour of [**Cu**-OH_2]$^+$ is the similar to that of [**Cu**-N_2]$^+$. The band origin of [**Cu**-OH_2]$^+$ is shifted by 240 cm^{-1} towards higher energies compared to [**Cu**-N_2]$^+$ and **Cu**$^+$, but the major vibrational features can be found at the same distances from the band origin, indicating a very similar Franck-Condon progression. Calculations for [**Cu**-OH_2]$^+$ revealed a weak transition, lying 3065 cm^{-1} below bright $\pi\pi^*$ transition. The main orbitals involved in this transition are plotted in **Figure 3.9**. It has charge transfer character from Cu to

the H_2O ligand and is likely too weak to be observed in our experiment. However, its existence is likely to provide another de-excitation channel and shorten the lifetime of the ππ* state, which can explain the greater spectral width of [**Cu**-OH_2]$^+$ even though the trap temperature in this case is lower.

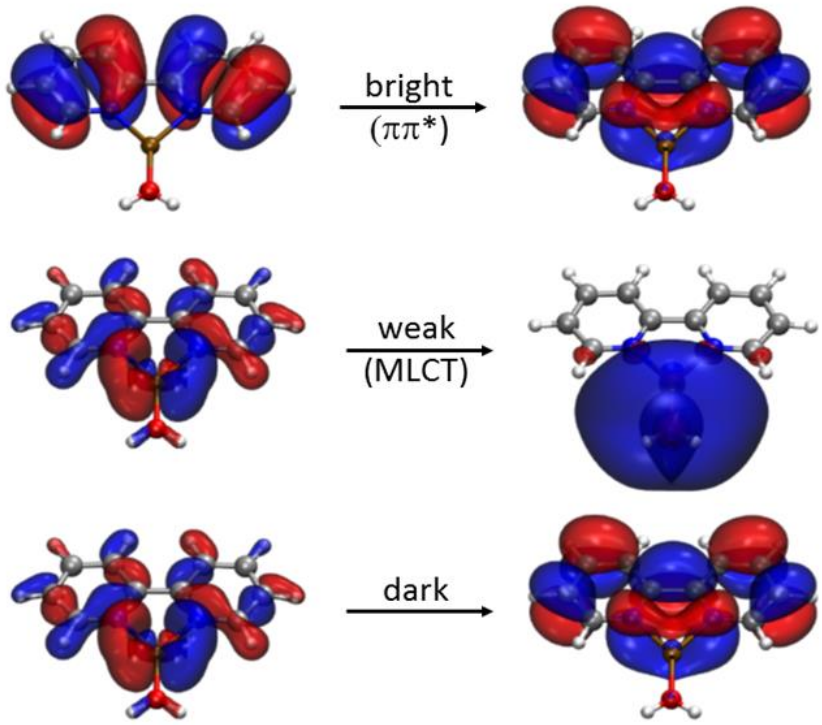

Figure 3.9 Leading molecular orbitals for the lowest energy transitions in [**Cu**-OH_2]$^+$ (see **Table 3.2** for calculated energies).

Since a water/methanol mixture was used for ESI, [**Cu**-$OHCH_3$]$^+$ was formed by the same mechanism as [**Cu**-OH_2]$^+$ but with a smaller ion intensity. Their spectra look almost identical (see **Figure 3.5**). Considering that water and methanol both bind to the metal via the oxygen in the ROH moiety (R = H or CH_3), it appears that the immediate chelating moiety on the ligand dictates its influence on the electronic structure of the complex.

Despite having a much stronger interacting ligand, [**Cu**-Cl]$^+$ shows a very similar profile in the UV region, with the band origin at 32424 cm^{-1}, slightly shifted to the red compared to the others. The substructure also looks similar to the Franck-Condon envelope in [**Cu**-OH_2]$^+$ and [**Cu**-N_2]$^+$. However, an important difference of [**Cu**-Cl]$^+$ is the presence of an unpaired electron. Therefore, its electronic structure is somehow unique among the series. Its ground state is doublet and it exhibits a bright transition in the visible region. **Figure 3.10** shows the full range spectra of [**Cu**-Cl]$^+$ with the trap at room temperature and at 50 K. Interestingly, the visible band exhibits different shapes at the two temperatures. Considering the binding energy of **Cu**$^+$ and Cl is calculated to be 247 kJ/mol, it is likely that the lower energy edge of the visible band is suppressed at the low temperature due to kinetic shift. Both the visible and the UV bands in the cryogenic spectra have significant residual spectral widths, which again supports the assumption that excited-state lifetime is the limiting factor for the width of the observed features.

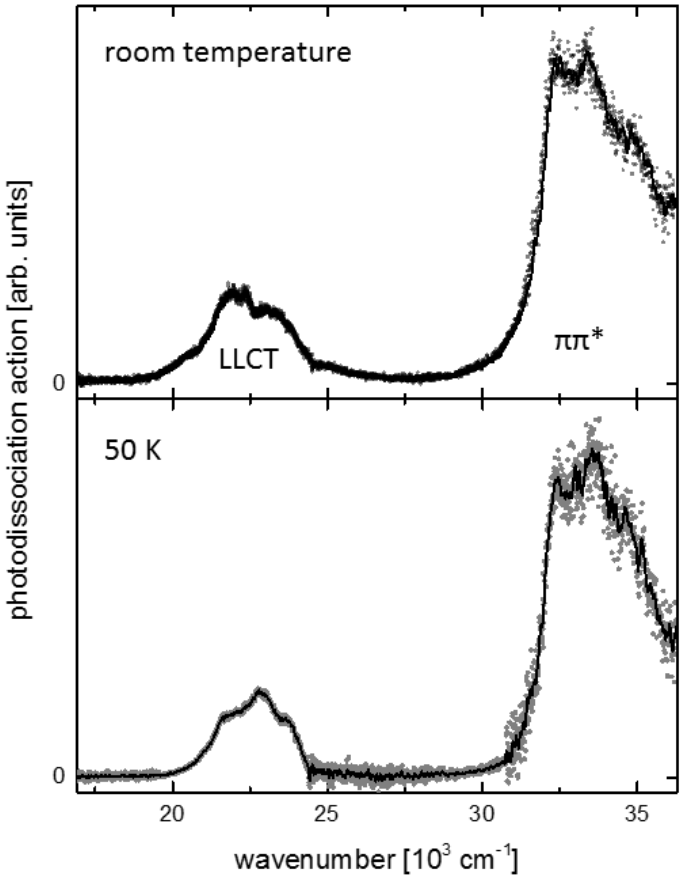

Figure 3.10 Photodissociation spectrum of [**Cu**-Cl]$^+$ ions (monitoring the loss of Cl) at room temperature (top) and at 50 K (bottom). The data points in the photodissociation spectra are the raw data, the full lines are the same data smoothed by 20-point sliding average.

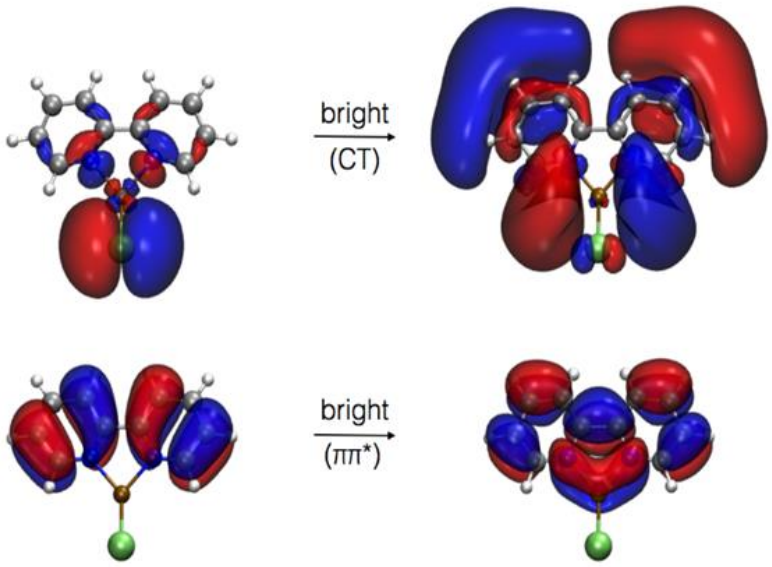

Figure 3.11 Leading molecular orbitals for the two bright energy transitions in [**Cu**-Cl]$^+$ (see **Table 3.2** for calculated energies).

The calculations were able to predict the bright transition in the visible range and identified it as ligand-to-ligand Cl-to-bpy charge-transfer (see **Figure 3.11**). The vertical energy (26616 cm^{-1}) is again *ca.* 4840 cm^{-1} (0.6 eV) higher than the experimental value (21940 cm^{-1}), but there is a large difference (6130 cm^{-1}) between the vertical and adiabatic excitation energies for this state due to a significant excited state relaxation along the Cu-Cl stretching coordinate. The band in the visible spectral range is very broad, and the band origin is less clear, likely because there are several closely lying electronic states calculated to be in the same region (see **Table 3.2**).

3.2.3.3 Summary

We studied the role of the variable ligand L in [**Cu**-L]$^+$ complex ions by photodissociation spectroscopy and computational analysis. Our study has covered species with L = D_2, N_2, H_2O,

CH_3OH and Cl in the visible and UV spectral range. All species show a similar band in the UV with the origin near 32500 cm^{-1}, which is assigned to the B_2 π-π* transition localized on the bpy moiety. Owing to the well-resolved spectrum of [**Cu**-N_2]$^+$ at a low trap temperature, we conclude that the substructure of this band is a Franck-Condon envelope contributed primarily by ring deformation modes of bpy. Excited state lifetime is a dominating factor affecting the width of the observed features and depends on the ligand. N_2 has little influence on the electronic spectrum of **Cu$^+$,** and is less perturbative than D_2. H_2O creates a weakly accessible MLCT state below the bright π-π* transition, which is likely to shorten the excited state lifetime. The striking similarity between the spectra for L = H_2O and CH_3OH suggests that CH_3OH has the same effect. Cl as a ligand alters the electronic structure quite substantially by bringing in multiple lower-lying states, some of which are in the visible region and at least one of them is strong enough to be observed in our experiment. The lifetime decreases from N_2 to H_2O to Cl due to an increasing number of lower lying electronic states that offer efficient de-excitation pathways. All complexes have a symmetry forbidden A_2 state closely below the π-π* state, inherited from bare bpy. While the nature of the ligand does not significantly change the position of the bright π-π* transition, it drastically changes the excited-state dynamics.

3.3 Ruthenium polypyridine complexes

3.3.1 Background

Ruthenium polypyridine complexes form an important group of organometallic compounds. They have found a wide range of applications, *e.g.* in dye-sensitized solar cells,[53–55] or as photo- and electrochemical catalysts for water oxidation and CO_2 reduction.[11,13,14,56–64] One of their characteristic photophysical properties is strong absorption of visible light. For example, tris(bipyridine)-ruthenium(II) has an extinction coefficients of about 14,000 $M^{-1}cm^{-1}$ at 452 nm.[65] The transitions in this region have charge-transfer character and can drive reactions that can be used in artificial photosynthesis. In addition, ruthenium polypyridine complexes also have applications in biochemistry as shape- and enantio-selectively dyes binding to DNA and other biomolecules.[66,67]

Ruthenium coordination complexes have six coordination sites. For many applications of ruthenium polypyridine complexes, only some of the six coordination sites are occupied by the organic polypyridine framework, and one or more sites are open. These open coordination sites afford binding with other ligands, triggering interesting chemistry. For example, it is proposed that the binding of water or CO_2 to an open coordination site is the starting point of a catalytic cycle for water oxidation or CO_2 reduction.[14,68] The interaction with such additional ligands influences the photophysical and photochemical properties of the complex by changing the

electronic structure of the complex, but it is not a trivial task to predict such ligand effects in detail. Experimentally, the biggest difficulty is that complexes formed in this way are rather reactive. They are often unstable with regard to exchanging a particular type of ligand with solvents or other reagents, and purification and isolation may not be even possible. As a result, controlling specific ligands and characterizing a single species is difficult under typical conditions in solution. Therefore, utilization of mass selected ions in the gas phase provides a powerful alternative that allows unprecedented and precise selection of the composition of the complex. Owing to the absence of reaction partners *in vacuo*, many unstable species become accessible in such experiments.

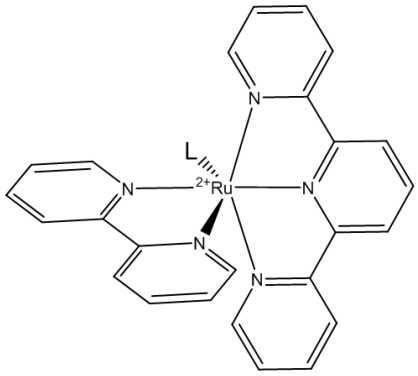

Figure 3.12 Structural template of the complexes under study. The ligand L represents a small molecule (H_2O, CO_2, CH_3CN, N_2).

We have studied a series of ruthenium polypyridine complexes built on the $[(tpy)(bpy)Ru^{II}\text{-}L]^{2+}$ structural template (denoted [**Ru**-L]$^{2+}$), shown in **Figure 3.12**. Five of the six coordination sites of the Ru atom are occupied by 2,2':6',2"-terpyridine (tpy) and 2,2'-bipyridine (bpy), leaving the last coordination site open for coordination to a small molecular ligand L. This structure and its derivatives have been investigated by several other groups recently as an

important prototypical complex for the study of electrochemical and photoelectrochemical catalysis.[69–71] In this work, we made selections of L based on some proposed catalytic cycles in which [**Ru**-L]$^{2+}$ is an important intermediate. The first species, [**Ru**-OH_2]$^{2+}$ (L = H_2O), has been invoked as the starting point of a catalytic circle using **Ru**$^{2+}$ as a water oxidation catalyst.[72] The complex [**Ru**-OCO]$^{2+}$ (L = CO_2) may be an intermediate in CO_2 reduction catalysis where CO_2 is converted to formate.[56] Many of the reactions of Ru^{2+} and similar catalysts have been studied via cyclic voltammetry experiments in acetonitrile solution. Acetonitrile is a very common solvent and frequently used as a displaceable ligand, and it is conjectured that the catalytic cycle is initialized by photon induced ligand substitution of [**Ru**-$NCCH_3$]$^{2+}$ (L = CH_3CN).[62,73] Hence, we included [**Ru**-$NCCH_3$]$^{2+}$ in this study, too. Ruthenium complexes are also known for nitrogen fixation ability. Nitrogen is usually a very inert molecule and is rarely used as a molecular ligand in transition metal chemistry. However, it can bind to suitable undercoordinated transition metal complexes and form a dinitrogen complex. The first isolation of a dinitrogen complex, $Ru(NH_3)_5$-N_2, in 1967[15] inspired the study of many transition metal containing nitrogen-fixing agents, but despite growing interest, there have been relatively few spectroscopic studies on dinitrogen complexes. Inspired by our work on [**Cu**-N_2]$^{+}$, we applied similar experimental conditions and found the existence of [**Ru**-N_2]$^{2+}$ (L = N_2).

3.3.2 Methods

The instrumentation for this experiment is the same as for the others reported in this thesis (see Chapter 2). To generate the [**Ru**-L]$^{2+}$ species, first we need to synthesize the part that is common to all complexes in this series, **Ru**$^{2+}$. The corresponding procedures were found in

literature[70] and adapted to meet our needs. In brief, 0.25 mmol of 2,2'-bipyridine, 2,2':6',2"-terpyridine and $RuCl_3$ were dissolved in 15 mL ethanol and 5 mL water. To the solution 1.25 mmol LiCl and 0.05 mL triethylamine were added and then refluxed for 4 hours at 90 °C. The crude solution was filtered, diluted 1:100 with ethanol, and electrosprayed without further purification. The species with L = H_2O, CO_2 and N_2 were formed in the trap by interaction with water vapor, CO_2 and N_2 in the buffer gas. The lowest temperatures for formation of these complexes are around 180 K (for water and CO_2 adducts) and 70 K (for N_2 adducts), respectively, since the ligand gases freeze out at lower temperatures. The acetonitrile adduct was formed by admitting acetonitrile vapor into the second differential pumping stage where the **Ru**$^{2+}$ complex ion can capture an acetonitrile ligand. Since it was formed outside the cryogenic trap, we were able to lower trap temperatures down to 30 K. The specifications of the chemicals used in this study are listed in **Table 3.5**.

Table 3.5 Chemicals used in the synthesis of **Ru**$^{2+}$.

chemical name	provider	grade
2,2'-bipyridine	Sigma Aldrich	>99%
2,2':6',2"-terpyridine	Alfa Aesar	97%
$RuCl_3$	Alfa Aesar	99.9%
LiCl	Alfa Aesar	99%
triethylamine	Alfa Aesar	99%
ethanol	Decon Labs	100%
acentonitrile	Sigma Aldrich	99.8%

The ground state geometry of each ion under study was calculated using density functional theory[40] (DFT) with def2-TZVP[42] basis sets for all atoms. Two functionals, PBE0[41] and

B3LYP,[74,75] were employed to test the sensitivity of the results to the functional used. Singlet excitation energies were calculated by time-dependent DFT (TDDFT) with the same basis sets and functionals. In order to improve the agreement with the experimental spectra, all predicted transition energies were shifted to lower energies by constant offsets for all species under study. These shifts were -1210 cm^{-1} for B3-LYP and -2420 cm^{-1} for PBE0. Charges were computed using natural population analysis.[46] All computations were performed using the Turbomole program suite.[43]

3.3.3 Results and discussions

3.3.3.1 L = H_2O and CO_2

The *aqua* complex, [**Ru**-OH_2]$^{2+}$, and its derivatives have been studied in the context of water oxidation catalysis as it is proposed to be the initial complex of the catalytic cycle.[68] The ground state geometry optimized by DFT is shown in **Figure 3.13**.

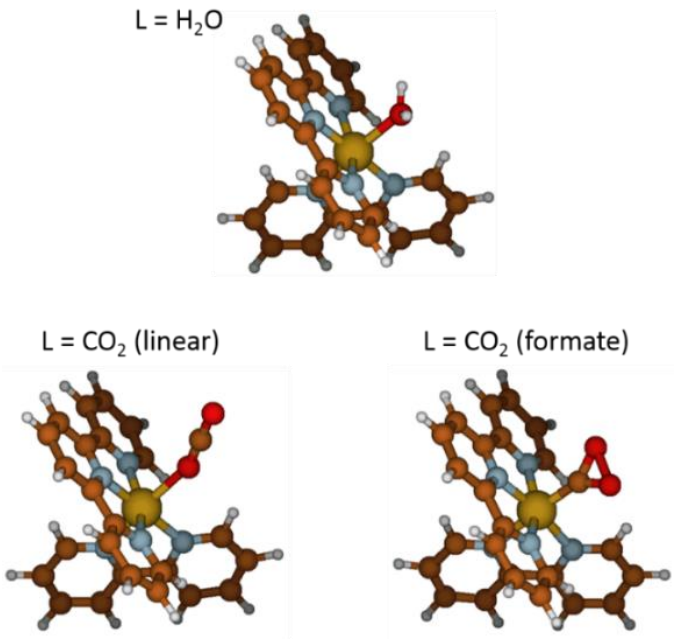

Figure 3.13 Calculated minimum energy structures of [**Ru**-L]$^{2+}$ for L = H_2O and CO_2 (the latter with two different isomers). Carbon atoms are shown in brown, nitrogen in blue, ruthenium in gold, oxygen in red, and hydrogen in white.

The oxygen atom of the water ligand is bonded to the Ru core, forming an angle of 123° between the Ru-O bond and the *aqua* plane, consistent with sp^3 hybridization on the O atom. The CO_2 complex has two stable η^1 isomers, one with the CO_2 ligand binding to the Ru atom through an O atom, the other binding with the C atom to the metal in a metalloformate motif. While this metalloformate motif is very common in metal-CO_2 systems[76] in the context of CO_2 reduction catalysis, here it is calculated to be 444 kJ/mol higher in energy than the end-on isomer. Therefore, we only consider the latter here. However, unlike many other cases, the Ru-O-C angle in this complex is 156° instead of 180°, which could be a result of the sp^2 hybridization of the oxygen atoms in the CO_2 ligand. The remaining lone pair on the O atom may have a very weak

interaction with the nearest CH group on the bpy. The binding energy of the L ligand is 106 kJ/mol for L = H_2O and 39 kJ/mol for L = CO_2.

Table 3.6 Ligand binding energies E_L calculated for [**Ru**-L]$^{2+}$ using the B3-LYP functional.

species	E_L [kJ/mol]
[**Ru**-OH_2]$^{2+}$	106
[**Ru**-OCO]$^{2+}$	39
[**Ru**-$NCCH_3$]$^{2+}$	164
[**Ru**-NN]$^{2+}$	87

The photodissociation spectra of [**Ru**-OH_2]^2 and [**Ru**-OCO]$^{2+}$ at 180 K trap temperature are remarkably similar (see **Figure 3.14**). Both species exhibit broad, partially resolved electronic bands within the ^{1}MLCT envelope. The width of the observed features is likely due to lifetime broadening, which has its origin in the ultrashort intersystem crossing lifetimes that are well known for Ru complexes.[77] Transition energies predicted by TDDFT calculations recover the experimental spectroscopic pattern of both complexes with similar quality (see **Table 3.7**), although at higher energies the calculations for the *aqua* complex are in slightly better agreement with experimental values than in the case of the CO_2 complex.

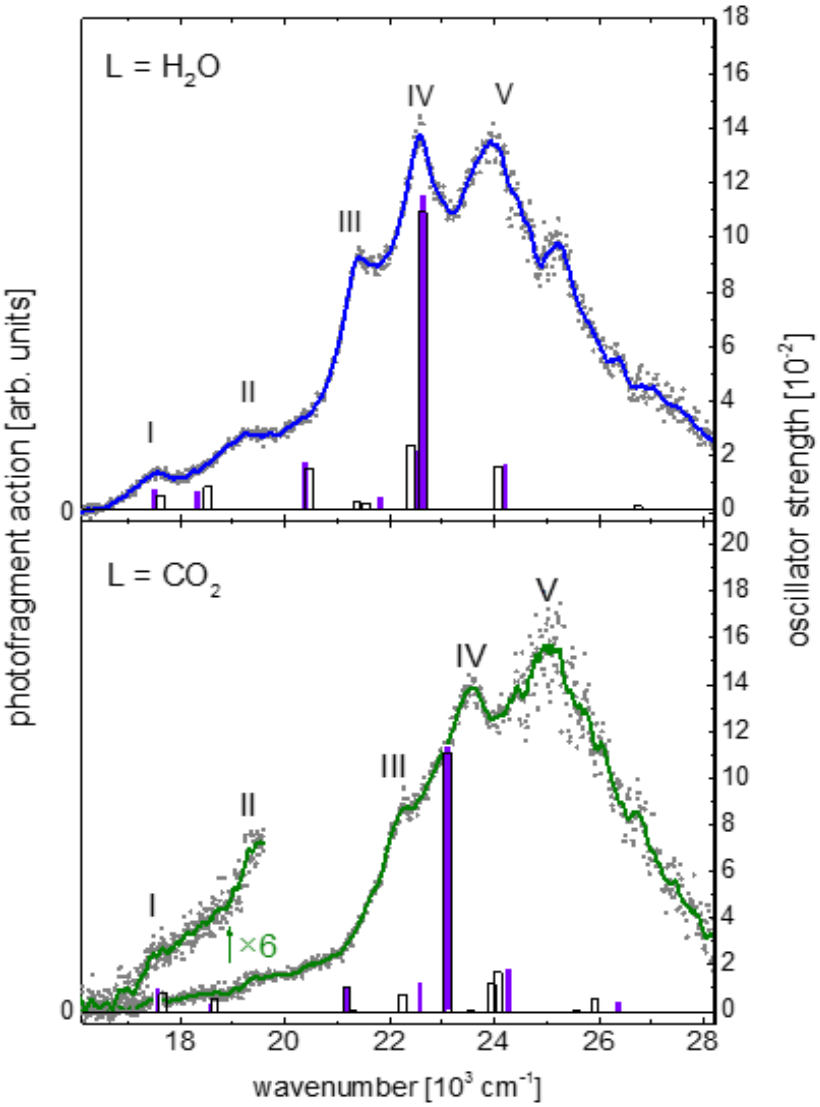

Figure 3.14 Photodissociation spectra of [**Ru**-L]$^{2+}$ with L = H_2O (top) and L = CO_2 (bottom) at 180 K trap temperature. Dots are raw data; full lines are 30-point sliding averages. The resolved features are labeled I through V (see also **Table 3.7**). The vertical columns represent transitions predicted by TDDFT calculations. The calculated transition energies are shifted by -1210 cm^{-1} for B3-LYP (open columns) and -2420 cm^{-1} for PBE0 (filled columns).

Table 3.7 The positions of spectroscopic features observed in the spectra of [**Ru**-L]$^{2+}$ for L = H_2O and CO_2 at 180 K trap temperature, compared to their positions as predicted by TDDFT (B3-LYP functional, shifted by -1210 cm^{-1}). No comparison is made for feature V in each case (see text).

	E_{exp} / E_{calc} [eV] ± 250 cm^{-1}				
feature	I	II	III	IV	V
[**Ru**-OH_2]$^{2+}$	17500 / 17583	19200 / 18551	21370 / 20487	22580 / 21535	23960
[**Ru**-OCO]$^{2+}$	17500 / 17634	19440 / 18631	22340 / 21212	23550 / 22261	25080

The lowest electronic bands (feature I) are found at 17500 cm^{-1} and are assigned to the S_1 state for both complexes (see **Table 3.7**). They are predominantly transitions from the highest occupied molecular orbital (HOMO, Ru based) to the lowest unoccupied molecular orbital (LUMO, tpy based). Feature II, assigned to the S_2 state in each case, is a shoulder at slightly higher energy (see **Table 3.7**). These two features in the spectrum of [**Ru**-OCO]$^{2+}$ are weaker in comparison with those of [**Ru**-OH_2]$^{2+}$. However, note that the calculated binding energy of the CO_2 ligand is even lower than that of the H_2O ligand (see **Table 3.6**), and no kinetic shift effects are observed for [**Ru**-OH_2]$^{2+}$ (to be discussed in Chapter 5, also see Ref.[78]), so we rule out kinetic shift effects for the [**Ru**-OCO]$^{2+}$ complex as well.

The feature next higher in energy is attributed to the S_3 state in both complexes. The two dominant features (IV and V) in both spectra are around the peak of the ^{1}MLCT envelope, which is at *ca.* 23400 cm^{-1} for the *aqua* complex and at *ca.* 24200 cm^{-1} for the CO_2 complex. The higher energy feature (V) in the *aqua* complex has been observed to diminish in relative intensity as solvent molecules are added to the complex, despite the fact that there is no change in the (relatively weak) calculated oscillator strength.[78] Therefore, it can be assumed that feature V is

composed of the weak electronic band calculated in this energy range and the Franck-Condon envelope built on the more intense band (feature IV). The similarity in the calculated and experimental spectra of the *aqua*- and CO_2 complexes suggests that this is the case for both of these species.

Since [**Ru**-OH_2]$^{2+}$ is soluble in water, by comparing the absorption maximum of the aqueous solution and the center position of feature IV and V, its solvatochromic shift in aqueous solution can be determined to be *ca.* -2420 cm^{-1}. A more detailed study of the solvatochromic shift and of solvation effects will be presented in Chapter 5.

It is important to note that kinetic shift effects that would skew the overall shape of the spectrum can be excluded, based on our work on the *aqua* complex.[78] Since the calculated binding energy of the CO_2 ligand is even lower than that of the *aqua* ligand (see **Table 3.6**), we rule out kinetic shift effects for the [**Ru**-OCO]$^{2+}$ complex as well.

3.3.3.2 L = CH_3CN and N_2

The complexes with CH_3CN and N_2 are rather different than the other two in this series. Some of the calculated information is summarized in **Table 3.6**. The acetonitrile and molecular nitrogen ligands have Ru-N-C and Ru-N-N angles of close to 180° (see **Figure 3.15**). Hybridization can explain the ligand alignment in these cases just as in L = H_2O and L = CO_2. Different from water and carbon dioxide, the linear arrangement of acetonitrile and nitrogen ligands is consistent with the sp hybrid orbitals of the binding N atoms in acetonitrile and nitrogen.

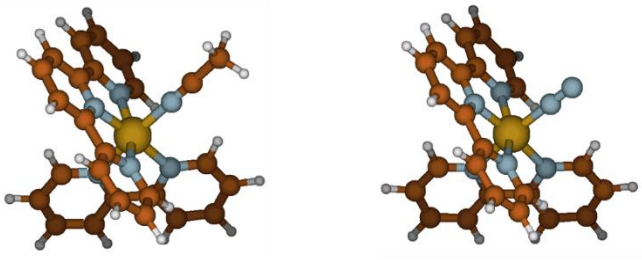

Figure 3.15 Calculated minimum energy structures of [**Ru**-L]$^{2+}$ for L = CH_3CN and N_2 (the latter with two different isomers). Carbon atoms are shown in brown, nitrogen in blue, ruthenium in gold, oxygen in red, and hydrogen in white.

The spectra of [**Ru**-$NCCH_3$]$^{2+}$ and [**Ru**-N_2]$^{2+}$ do not exhibit clearly resolved features like those of [**Ru**-OH_2]$^{2+}$ or [**Ru**-OCO]$^{2+}$ (see **Figure 3.16**), even at cryogenic trap temperatures. The absence of resolved features at low temperatures supports the explanation that the large width of the electronic bands is due to the ultrashort intersystem crossing rather than thermal population, as already invoked for [**Ru**-OH_2]$^{2+}$ and [**Ru**-OCO]$^{2+}$. The calculated spectra for L = CH_3CN and N_2 appear more congested around the most prominent bands than for the other two complexes. The lowest energy excitations are less pronounced than in the spectra of the latter, despite having similar oscillator strengths predicted by calculations. The spectrum of [**Ru**-$NCCH_3$]$^{2+}$ has a peak at 23150 cm^{-1} with a pronounced high-energy tail. The spectra taken at room temperature and at 30 K trap temperature are not very different from each other, although the low temperature spectrum is overall somewhat narrower, most likely due to the suppression of hot bands.

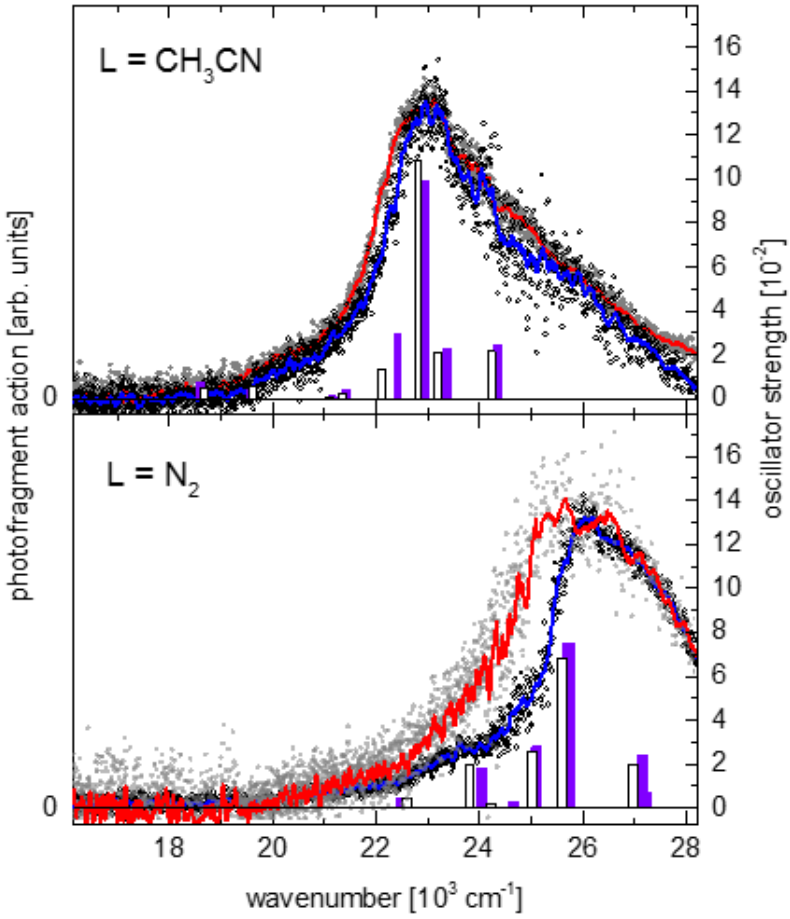

Figure 3.16 Photodissociation spectra of [**Ru**-L]$^{2+}$ with L = CH_3CN (top) and at room temperature (red) and at 30 K trap temperature (blue), and with L = N_2 (bottom) at room temperature (red) and at 70 K (blue). Dots are raw data; full lines are 30-point sliding averages. The vertical columns represent transitions predicted by TDDFT calculations. The calculated transition energies are shifted by -1210 cm^{-1} for B3-LYP (open columns) and - 1210 cm^{-1} for PBE0 (filled columns).

The solvatochromic shift for L = CH_3CN in bulk acetonitrile solution[13] is *ca.* 1050 cm^{-1} to the red, much smaller than for the complex with L = H_2O in aqueous solution[78] (*ca.* 2420 cm^{-1} to the red). This may seem to be counterintuitive, considering that acetonitrile has a much stronger dipole moment than water. However, since the comparison is made between [**Ru**-L]$^{2+}$ and the

solution with L as the solvent, the very first solvent molecule as a ligand has already induced a shift via the interaction with the metal core. In this case, the higher calculated binding energy of CH_3CN to $\mathbf{Ru}^{2+}$ is consistent with the larger dipole moment of CH_3CN. The polarity of the solvent, while important, has a smaller effect on the solvatochromic shift than the interaction strength of a solvent acting as a ligand coupled to the metal center.

The spectrum of $[\mathbf{Ru}\text{-}N_2]^{2+}$ has a broad absorption profile peaking around 26130 cm^{-1} (at 70 K trap temperature), and the only discernible structure is a broad shoulder at *ca.* 23400 cm^{-1}. The room temperature spectrum shows strong hot bands.

The envelopes of the calculated excited states are consistent with the experimentally observed spectra. Interestingly, the calculated energies for the S_1 states are significantly higher than for L = H_2O and CO_2 (18631 cm^{-1} for L = CH_3CN, 21051 cm^{-1} for L = N_2). The calculated oscillator strength for the transition to the S_1 state for L = N_2 is an order of magnitude smaller than for any of the other ligands under study.

Despite the relatively high binding energy of the CH_3CN ligand (calculated to be 164 kJ/mol), there is no indication for kinetic shift effects, judging from the difference between the spectra at room temperature and at 30 K trap temperature. The binding energy of the N_2 ligand is calculated at 87 kJ/mol, ruling out kinetic shift effects.

3.3.3.3 Calculated electronic properties

The binding energy of the ligand L and $\mathbf{Ru}^{2+}$ by calculation lies between 39 and 164 kJ/mol (3260 and 13710 cm^{-1}), well below the spectral range of our spectra. In theory, photo-induced loss of L should be a single-photon process. One can test this assumption by measuring the

fragment yield as a function of laser intensity. **Figure 3.17** shows the results of such measurements. It clearly demonstrates the linear relationship between the fragment yield and the laser intensity, the evidence of a single-photon process. Note that in the case of L = H_2O, saturation effects may be at play for the largest intensities used here.

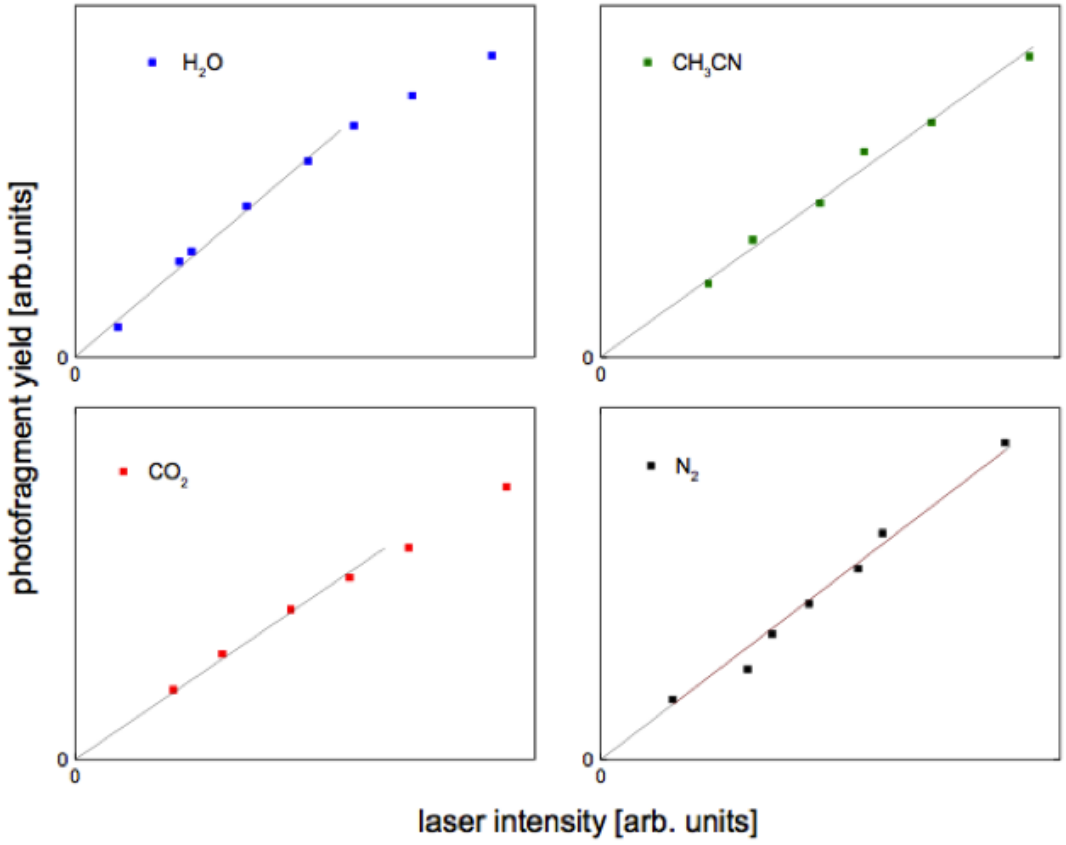

Figure 3.17 Light intensity dependence of fragment ion yield. The laser was set to the wavelength of peak absorption for each species. The full lines show linear fits; their length indicates which data points were included in the fitting. The legend indicates the ligand L.

The charge distributions for the ground state complexes calculated from natural orbitals (see **Table 3.8**) show only few general trends. The small molecular ligands carry only little positive charge in each case. This is not unexpected, since the canonical inorganic chemistry picture

invokes σ donation to the metal and π back donation to the ligand,[79] so the net charge on the ligand may not change much.

Table 3.8 Charge distribution calculated for [**Ru**-L]$^{2+}$ with natural binding orbitals using the B3-LYP functional.

species	charge [e]				
	Ru	L	bonding atom in L / in free molecule	bpy	tpy
[**Ru**-OH_2]$^{2+}$	+0.65	+0.16	-0.86 / -0.92	+0.50	+0.69
[**Ru**-OCO]$^{2+}$	+0.66	+0.09	-0.54 / -0.49	+0.53	+0.72
[**Ru**-$NCCH_3$]$^{2+}$	+0.57	+0.20	-0.34 / -0.32	+0.48	+0.75
[**Ru**-NN]$^{2+}$	+0.54	+0.11	+0.006 / 0	+0.52	+0.83
Ru^{2+}	+0.74	-	-	+0.55	+0.71

The ligands can be polarized by the presence of the central Ru ion, and the polarization is generally stronger for the O-coordinating ligands than for the N-coordinating ligands. The charge on the Ru atom becomes less positive upon chelation, and the O-coordinating complexes have a similar and more positive charge on the Ru atom than the N-coordinating ligands, which are again similar to each other regarding the charge on Ru. The charge on the bpy does not show a systematic variation, but the charge on tpy becomes more positive along the series H_2O < CO_2 < CH_3CN < N_2. Compared to **Ru**$^{2+}$, *i.e.*, the complex without the ligand L, there are only small changes introduced by the O-coordinating ligands, whereas the effect of acetonitrile is somewhat stronger, and N_2 changes the charge on the tpy substantially. The changes in charge distributions cannot be related to simple properties of the small ligands that would be immediately apparent as their origin, such as ionization potential, electric dipole moment or polarizability. We note, however, that the charge on the binding atom of the ligand L is roughly correlated with the charge

distribution on Ru and tpy. The charge on the Ru ion becomes more positive as the charge on the binding atom in the ligand L becomes more negative. In other words, the charge on the binding atom in the ligand stabilizes (or destabilizes) the positive charge on the Ru ion.

TDDFT calculations yielded self-consistent results with B3LYP and PBE0 functionals, as shown by the columns in **Figure 3.14** and **Figure 3.16**. They qualitatively reproduced the spectral envelopes however the absolute values were off by different amounts (as stated in the captions). The character of the transitions is similar for all the complexes under study. The lowest two transitions all are HOMO→LUMO and (HOMO-1)→LUMO, with the HOMO mainly of metal d-orbital character, and the LUMO having π* character on tpy (see **Table 3.9**).

Table 3.9 Calculated selected transition energies (B3-LYP, shifted by -1210 cm^{-1}) sorted by the dominant orbitals involved in the transition.

Species	Calculated transition energy using B3-LYP [cm^{-1}]					
	HOMO → LUMO	HOMO-1 → LUMO	HOMO-2 → LUMO	HOMO → LUMO+1	HOMO-1 → LUMO+1	HOMO-1 → LUMO+2
[**Ru**-OH_2]$^{2+}$	17581	18548	20484	21532	22661	24032
[**Ru**-OCO]$^{2+}$	17661	18629	21210	22500	23065	23952
[**Ru**-$NCCH_3$]$^{2+}$	18710	19597	21371	20161	22823	24274
[**Ru**-NN]$^{2+}$	21048	22581	25000	23790	25565	26935
Ru^{2+}	12742	13629	15403	21371	23548	23871

The transitions at higher energies often involve a mixture of several initial and final orbitals (see §3.3.3.5), but all can be characterized as metal to ligand charge transfer (MLCT) transitions to a π* orbital on tpy and/or bpy. The TDDFT calculations predict for all complexes that one transition has a significantly higher oscillator strength than the other transitions in this energy range. Its dominant character is (HOMO-1) → (LUMO+1). All four species also have charge transfer states from Ru to the small molecular ligand L, but they are mostly calculated to be at

higher energies and have lower oscillator strengths. For example, the lowest MLCT state in the *aqua* complex that involves the *aqua* ligand is calculated at 25003 cm^{-1}, and it does not correspond to an experimentally observed feature. The exception in this series is [**Ru**-OCO]$^{2+}$, where the lowest energy MLCT transition involving the CO_2 ligand is calculated at 21212 cm^{-1}.

Overall, the similarity in the character of the excitations suggests that the changes in the spectra are caused by the differences in the charge distributions and orbital stabilization and destabilization. The role of the binding atom in the ligand L is highlighted by the similarities between spectra for complexes with the same binding atoms (H_2O and CO_2 versus CH_3CN and N_2).

Calculations on the excited states allow a comparison of the properties of the undercoordinated complex **Ru**$^{2+}$ with the different experimentally accessible complexes. The lowest three transitions to LUMO have much lower energies than in the fully coordinated complexes. This can be traced to the MO energies, since the LUMO in **Ru**$^{2+}$ is destabilized by the addition of the ligand L (see **Figure 3.18**).

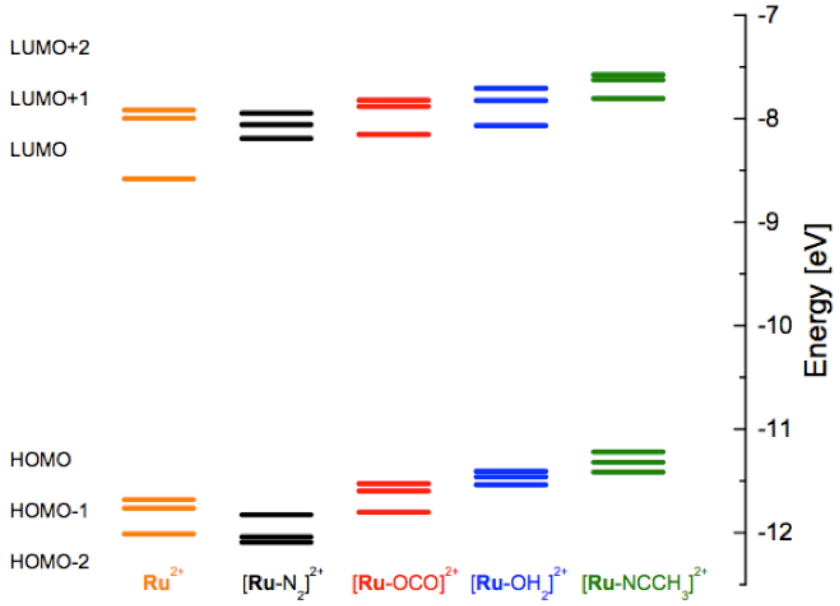

Figure 3.18 Calculated molecular orbital levels for [**Ru**-L]$^{2+}$ and bare **Ru**$^{2+}$.

3.3.3.4 Summary

We have studied the ^{1}MLCT spectra of [**Ru**-L]$^{2+}$ complexes with different small molecular ligands L by cryogenic photodissociation spectroscopy and density functional theory. A comparison of the spectra shows a strong influence of the ligand on the electronic structure of the complex. The *aqua* complex and the complex with L = CO_2 have similar spectra, with several partially resolved electronic bands. In contrast, the complexes with L = CH_3CN and N_2 have much more congested spectra, and different electronic bands cannot be resolved at all, even at trap temperatures down to 30 K. Electronic spectra predicted by TDDFT calculations are in good qualitative agreement with the experimental data. The charge distribution in the complex is on the binding atom of the ligand L is roughly correlated with the charge distribution on Ru and tpy.

Our data for the two complexes for which solvatochromic shift data are available (L = CH_3CN and H_2O) show that the strength of the interaction of a solvent molecule in the role of a coordinating ligand is more important than the polarity of the solvent.

3.3.3.5 Appendix

The excited-state analysis by theory also provided detailed information of each transition, including its character and involved molecular orbitals. The orbitals involved in the prominent transitions are listed in **Table 3.10** through **Table 3.14**, and the contours are plotted in **Figure 3.19** and **Figure 3.23**.

Table 3.10 Lowest energy calculated electronic transition energies and oscillator strengths for L = H_2O (B3LYP functional, not shifted). Only contributions of 10% and greater are shown.

Transition	E [cm^{-1}] / f [10^{-2}]	orbitals (see **Figure 3.19**)	character
1	18793 / 0.53	114 → 115 (96.2%)	d → tpy
2	19761 / 0.85	113 → 115 (95.9%)	d → tpy
3	21696 / 1.15	112 → 115 (66.1%) 114 → 116 (24.5%)	d → tpy
4	22584 / 0.31	114 → 117 (86.8%)	d → bpy
5	22745 / 0.25	114 → 116 (53.1%) 113 → 116 (26.2%)	d → try
6	23551 / 0.005	112 → 117 (91.3%)	d → bpy
7	23632 / 2.37	112 → 116 (92.4%)	d → tpy
8	23874 / 10.9	113 → 116 (56.8%) 113 → 117 (13.1%) 114 → 116 (12.7%) 112 → 115 (11.9%)	d → tpy
9	25245 / 1.61	113 → 117 (69.7%)	d → bpy
10	26213 / 0.01	113 → 122 (40.8%) 114 → 122 (27.0%) 113 → 124 (12.4%)	d → H_2O
11	27987 / 0.13	112 → 122 (64.8%) 112 → 126 (14.2%)	d → H_2O

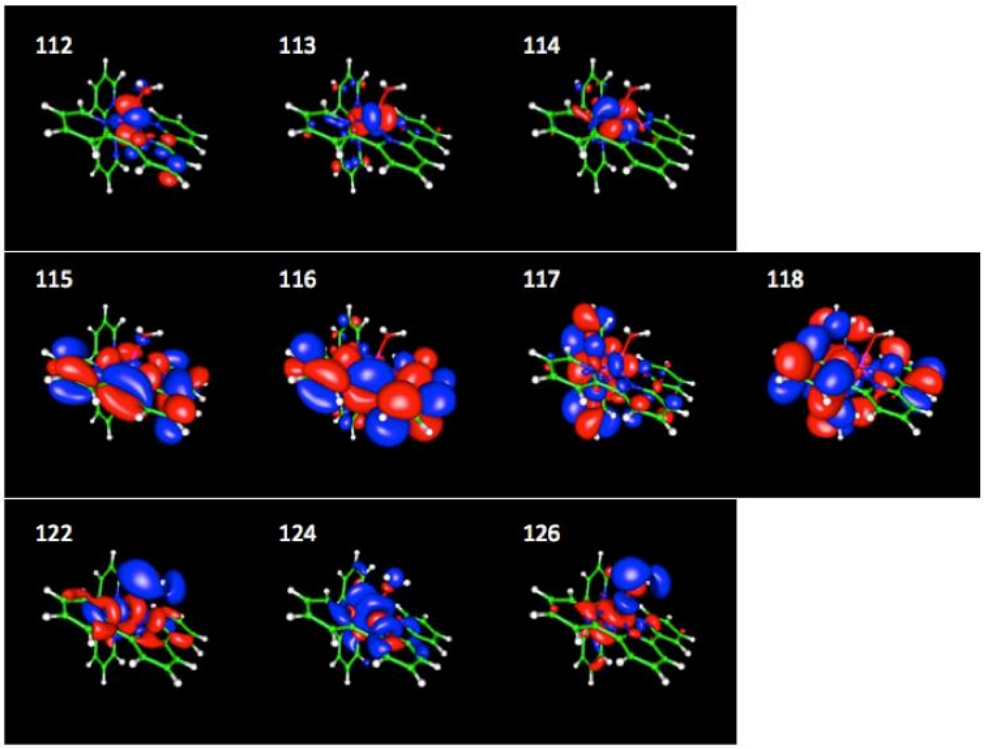

Figure 3.19 Calculated orbitals contributing to transitions for L = H_2O. Orbital numbers are given as mentioned in **Table 3.10**.

Table 3.11 Lowest energy calculated electronic transition energies and oscillator strengths for L = CO_2 (B3LYP functional, not shifted). Only contributions of 10% and greater are shown.

Transition	E [cm^{-1}] / f [10^{-2}]	orbitals (see **Figure 3.20**)	character
1	18873 / 0.78	120 → 121 (92.9%)	d → tpy
2	19841 / 0.53	119 → 121 (91.6%)	d → tpy
3	22422 / 1.05	118 → 121 (52.9%) 120 → 122 (34.1%)	d → tpy
4	22503 / 0.02	120 → 123 (78.2%) 120 → 122 (15.1%)	d → bpy
5	23471 / 0.72	120 → 122 (34.9%) 119 → 122 (23.3%) 119 → 123 (16.8%) 120 → 123 (11.5%) 118 → 121 (11.0%)	d → tpy
6	24116 / 0.03	118 → 123 (29.2%) 120 → 128 (27.9%) 119 → 128 (15.0%) 118 → 122 (10.7%)	d → bpy
7	24277 / 11.0	119 → 122 (73.9%)	d → tpy
8	24761 / 0.02	118 → 123 (37.2%) 119 → 128 (26.2%) 118 → 122 (15.7%)	d → tpy
9	25165 / 1.17	119 → 123 (59.4%) 118 → 128 (20.0%)	d → bpy
10	25245 / 1.68	118 → 122 (70.7%) 118 → 123 (21.1%)	d → tpy
11	26777 / 0.07	120 → 129 (36.8%) 119 → 128 (33.3%)	
12	37100 / 0.55	118 → 128 (50.3%) 118 → 121 (17.6%) 119 → 125 (13.3%)	d → CO_2

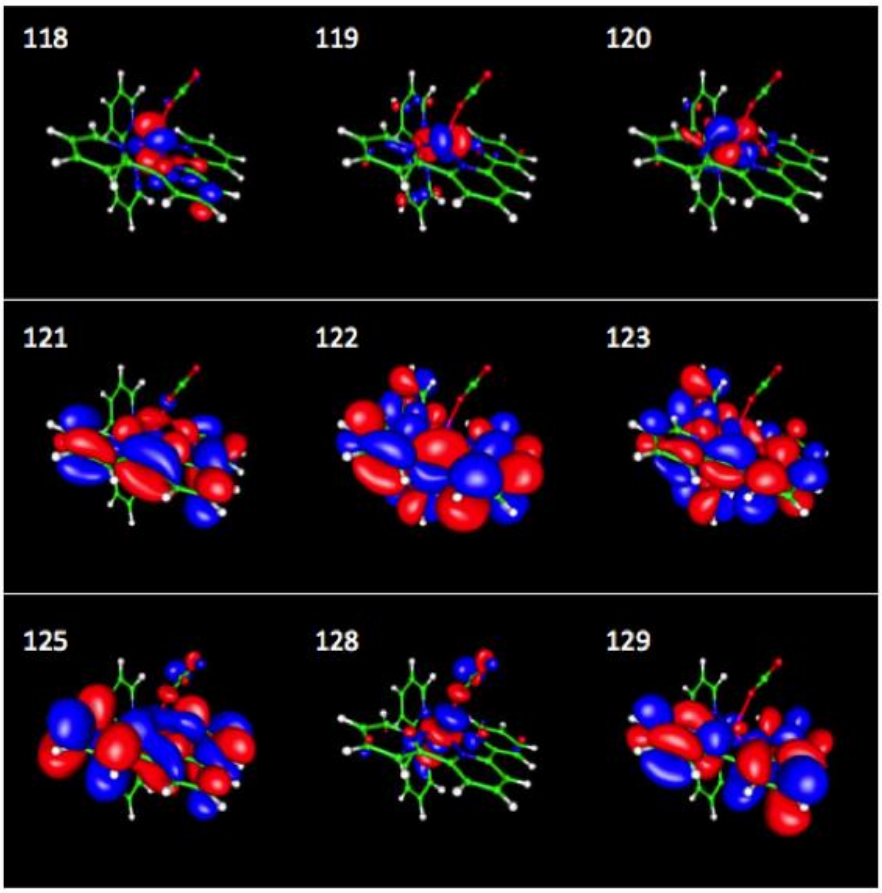

Figure 3.20 Calculated orbitals contributing to transitions for L = CO_2. Orbital numbers are given as mentioned in **Table 3.11**.

Table 3.12 Lowest energy calculated electronic transition energies and oscillator strengths for L = CH_3CN (B3LYP functional, not shifted). Only contributions of 10% and greater are shown.

Transition	E [cm^{-1}] / f [10^{-2}]	orbitals (see **Figure 3.21**)	character
1	19922 / 0.51	120 → 121 (90.8%)	d → tpy
2	20809 / 0.59	119 → 121 (90.8%)	d → tpy
3	22342 / 0.10	120 → 123 (76.1%) 120 → 122 (21.6%)	d → tpy
4	22584 / 0.28	120 → 122 (48.0%) 118 → 121 (38.6%) 120 → 123 (12.0%)	d → bpy
5	23309 / 1.38	119 → 122 (33.7%) 119 → 123 (27.0%) 118 → 121 (23.4%) 120 → 122 (12.6%)	d → tpy
6	23874 / 0.01	118 → 123 (71.2%) 118 → 122 (26.9%)	d → bpy
7	24035 / 10.8	119 → 122 (64.3%) 118 → 121 (12.6%) 120 → 122 (10.1%)	d → tpy
8	24358 / 0.21	118 → 122 (71.3%) 118 → 123 (26.2%)	d → tpy
9	25487 / 0.22	119 → 123 (57.6%) 118 → 121 (20.0%)	d → bpy

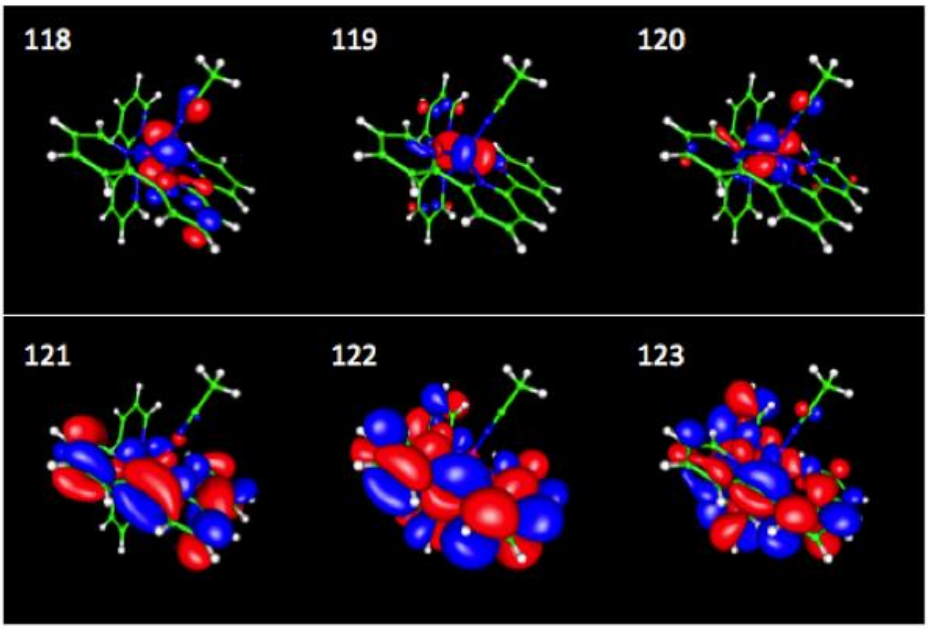

Figure 3.21 Calculated orbitals contributing to transitions for L = CH_3CN. Orbital numbers are given as mentioned in **Table 3.12**.

Table 3.13 Lowest energy calculated electronic transition energies and oscillator strengths for L = N_2 (B3LYP functional, not shifted). Only contributions of 10% and greater are shown.

Transition	E [cm^{-1}] / f [10^{-2}]	orbitals (see **Figure 3.22**)	character
1	22261 / 0.03	116 → 117 (99.1%)	d → tpy
2	23793 / 0.46	115 → 117 (98.6%)	d → tpy
3	25003 / 1.99	116 → 118 (65.7%) 116 → 119 (22.4%)	d → bpy
4	25407 / 0.21	116 → 119 (74.5%) 116 → 118 (22.3%)	d → tpy
5	26213 / 2.56	114 → 117 (65.2%) 115 → 119 (27.3%)	d → tpy
6	26778 / 6.85	115 → 118 (81.2%)	d → bpy
7	27342 / 0.02	114 → 118 (85.7%) 114 → 119 (12.5%)	d → bpy
8	28141 / 1.02	114 → 119 (64.9%) 115 → 119 (12.0%)	d → tpy
9	28165 / 1.97	116 → 119 (46.6%) 114 → 117 (22.1%) 114 → 119 (16.7%)	d → tpy
10	29923 / 0.10	116 → 127 (59.9%) 116 → 124 (15.0%) 116 → 128 (13.1%)	d → N_2

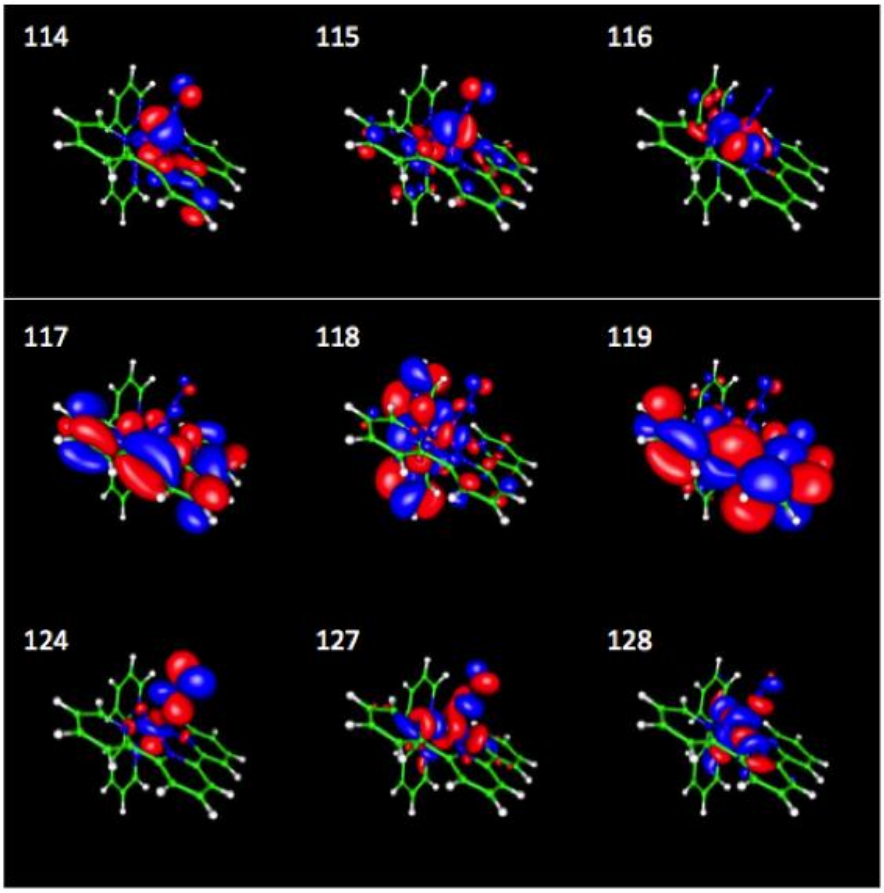

Figure 3.22 Calculated orbitals contributing to transitions for L = N_2. Orbital numbers are given as mentioned in **Table 3.13**.

Table 3.14 Lowest energy calculated electronic transition energies and oscillator strengths for **Ru**$^{2+}$ (B3LYP functional, not shifted). Only contributions of 10% and greater are shown.

Transition	E [cm^{-1}] / f [10^{-2}]	orbitals (see **Figure 3.23**)	character
1	13953 / 0.96	109 → 110 (71.1%) 109 → 113 (13.0%) 108 → 110 (10.7%)	d → tpy
2	14841 / 0.11	108 → 110 (69.1%) 108 → 113 (14.5%) 109 → 110 (14.2%)	
3	16615 / 1.02	107 → 110 (70.3%) 107 → 113 (25.5%)	
4	22584 / 0.22	109 → 111 (80.4%) 109 → 112 (15.7%)	d → bpy/tpy
5	23068 / 0.04	109 → 113 (72.4%) 109 → 110 (12.4%)	d → tpy
6	23471 / 0.11	108 → 113 (72.1%) 108 → 110 (14.8%)	d → tpy
7	23955 / 0.28	109 → 112 (75.2%) 109 → 111 (15.0%)	d → bpy/tpy
8	24761 / 8.56	108 → 111 (81.5%) 108 → 112 (11.7%)	
9	25044 / 3.22	108 → 112 (54.6%) 107 → 113 (25.0%)	
10	25116 / 0.004	107 → 111 (84.3%) 107 → 112 (10.9%)	
11	36374 / 0.12	107 → 112 (76.7%) 106 → 110 (10.9%) 107 → 111 (10.7%)	
12	27020 / 1.56	107 → 113 (40.0%) 108 → 112 (23.0%) 107 → 110 (17.0%)	
13	28149 / 13.27	106 → 110 (81.9%)	
14	29036 / 0.75	105 → 110 (97.5%)	
15	30165 / 0.25	109 → 114 (93.3%)	

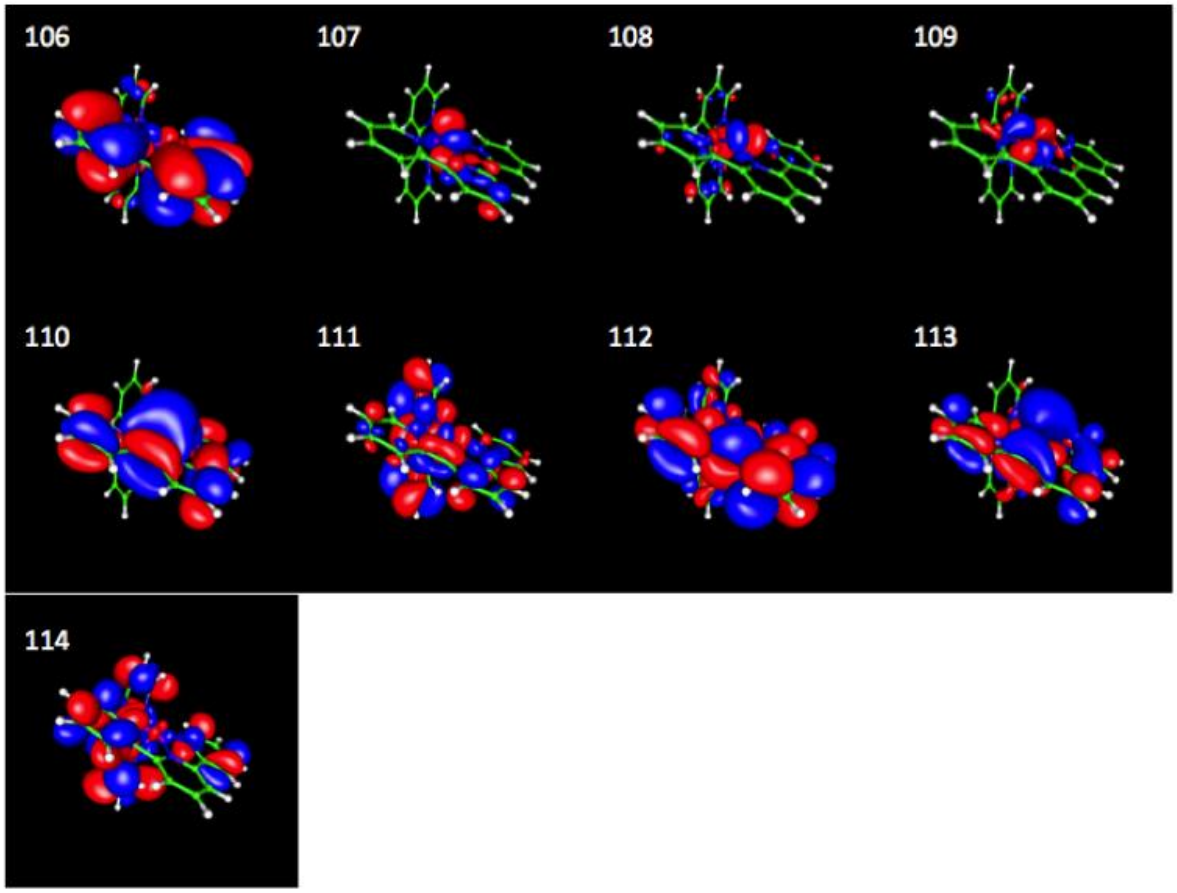

Figure 3.23 Calculated orbitals contributing to transitions for **Ru**$^{2+}$. Orbital numbers are given as mentioned in **Table 3.14**.

3.4 References

1. Rillema, D. P., Meyer, T. J. & Conrad, D. Redox properties of ruthenium(II) tris chelate complexes containing the ligands 2,2'-bipyrazine, 2,2'-bipyridine, and 2,2'-bipyrimidine. *Inorg. Chem.* **22,** 1617–1622 (1983).

2. Crutchley, R. J. & Lever, A. B. P. Comparative chemistry of bipyrazyl and bipyridyl metal complexes: spectroscopy, electrochemistry and photoanation. *Inorg. Chem.* **21,** 2276–2282 (1982).

3. Knoll, J. D., Albani, B. A., Durr, C. B. & Turro, C. Unusually efficient pyridine photodissociation from Ru(II) complexes with sterically bulky bidentate ancillary ligands. *J. Phys. Chem. A* **118,** 10603–10610 (2014).

4. Knoll, J. D., Albani, B. A. & Turro, C. New Ru(II) complexes for dual photoreactivity: ligand exchange and $^1O_2$ generation. *Acc. Chem. Res.* **48,** 2280–2287 (2015).

5. Chen, Y. J., Xie, P., Heeg, M. J. & Endicott, J. F. Influence of the 'innocent' ligands on the MLCT excited-state behavior of mono(bipyridine)-ruthenium(II) complexes: A comparison of X-ray structures and 77 K luminescence properties. *Inorg. Chem.* **45,** 6282–6297 (2006).

6. Bomben, P. G., Koivisto, B. D. & Berlinguette, C. P. Cyclometalated Ru complexes of type $[Ru(II)(N^N)_2(C^N)]^z$: physicochemical response to substituents installed on the anionic ligand. *Inorg. Chem.* **49,** 4960–71 (2010).

7. Madeja, K. & Konig, E. Zur Frage der Bindungsverhältnisse in Komplexverbindungen des Eisen(II) mit 1,10-Phenanthrolin. *J. Inorg. Nucl. Chem* **25,** 377–385 (1963).

8. Spettel, K. E. & Damrauer, N. H. Synthesis, electrochemical characterization, and photophysical studies of structurally tuned aryl-substituted terpyridyl ruthenium(II) complexes. *J. Phys. Chem. A* **118,** 10649–10662 (2014).

9. Bargawi, K. R., Llobet, A. & Meyer, T. J. Synthetic design of MLCT excited states. Ligand-substituted, mono-2,2'-bipyridine complexes of ruthenium(II). *J. Am. Chem. Soc.* **110,** 7751–7759 (1988).

10. Ernst, S. D. & Kaim, W. Energy level tailoring in ruthenium(II) polyazine complexes based on calculated and experimental ligand properties. *Inorg. Chem.* **28,** 1520–1528 (1989).

11. Concepcion, J. J. *et al.* Making oxygen with ruthenium complexes. *Acc. Chem. Res.* **42,** 1954–65 (2009).

12. Concepcion, J. J., Jurss, J. W., Templeton, J. L. & Meyer, T. J. One site is enough. Catalytic water oxidation by $[Ru(tpy)(bpm)(OH^2)]^{2+}$ and $[Ru(tpy)(bpz)(OH_2)]^{2+}$. *J. Am. Chem. Soc.* **130,**

16462–3 (2008).

13. Chen, Z. *et al.* Electrocatalytic reduction of CO_2 to CO by polypyridyl ruthenium complexes. *Chem. Commun.* **47,** 12607–9 (2011).

14. Tanaka, K. & Ooyama, D. Multi-electron reduction of CO_2 via Ru-CO_2, -C(O)OH, -CO, -CHO, and -CH_2OH species. *Coord. Chem. Rev.* **226,** 211–218 (2002).

15. Allen, A. D. & Bottomley, F. Inorganic nitrogen fixation. Nitrogen compounds of the transition metals. *Acc. Chem. Res.* **1,** 360–365 (1968).

16. Xu, S., Gozem, S., Krylov, A. I., Christopher, C. R. & Weber, J. M. Ligand influence on the electronic spectra of monocationic copper-bipyridine complexes. *Phys. Chem. Chem. Phys.* **17,** 31938–31946 (2015).

17. Barnett, S. M., Goldberg, K. I. & Mayer, J. M. A soluble copper-bipyridine water-oxidation electrocatalyst. *Nat. Chem.* **4,** 498–502 (2012).

18. Chen, Z. & Meyer, T. J. Copper(II) catalysis of water oxidation. *Angew. Chemie - Int. Ed.* **52,** 700–3 (2013).

19. Addison, A. W. & Rao, T. N. Synthesis, structure, and spectroscopic properties of Cu(II) compounds. *J. Chem. Soc. Dalt. Trans.* 1349–1356 (1984).

20. Ichinaga, A. K. *et al.* Charge-transer absorption and emission of $Cu(NN)_2^+$ Systems. *Inorg. Chem.* **26,** 4290–4292 (1987).

21. Blaskie, M. W. & McMillin, D. R. Photostudies of copper(I) systems. 6. Room-temperature emission and quenching studies of bis(2,9-dimethyl-1,10-phenanthroline)-copper(I). *Inorg. Chem.* **19,** 3519–22 (1980).

22. Tsuboyama, A. *et al.* Photophysical properties of highly luminescent copper(I) halide complexes chelated with 1,2-bis(diphenylphosphino)benzene. *Inorg. Chem.* **46,** 1992–2001 (2007).

23. Horvath, O. Photochemistry of copper(I) complexes. *Coord. Chem. Rev.* **135/136,** 303–324 (1994).

24. Lazorski, M. S. & Castellano, F. N. Advances in the light conversion properties of Cu(I)-based photosensitizers. *Polyhedron* **82,** 57–70 (2014).

25. McGarvey, J. J., Bell, S. E. J. & Bechara, J. N. Resonance Raman spectra of charge-transfer excited states of copper(I) complexes. *Inorg. Chem.* **25,** 4325–7 (1986).

26. Blake, A. J., Hill, S. J., Hubberstey, P. & Li, W. Copper(I) chelated by 2,9-dimethyl-1,10-phenanthroline and bridged by 4,4'-bipyridine or trans-1,2-bis(pyridin-4-yl)ethene to give discrete dinuclear and polymeric cations. *Dalton Trans.* **2,** 909–915 (1998).

27. Mara, M. W., Fransted, K. a. & Chen, L. X. Interplays of excited state structures and dynamics in copper(I) diimine complexes: Implications and perspectives. *Coord. Chem. Rev.* **282–283,** 2–18 (2014).

28. Renouard, T., Bozec, H. Le, Brasselet, S., Ledoux, I. & Zyss, J. Tetrahedral bipyridyl copper(I) complexes: a new class of non-dipolar chromophore for nonlinear optics. *Chem. Commun.* 871–872 (1999). doi:10.1039/a901972c

29. Siddique, Z. A., Yamamoto, Y., Ohno, T. & Nozaki, K. Structure-dependent photophysical properties of singlet and triplet metal-to-ligand charge transfer states in copper(I) bis(diimine) compounds. *Inorg. Chem.* **42,** 6366–78 (2003).

30. Wilde, R. E., Srinivasan, T. K. K. & Ghosh, S. N. Mono complexes of 2,2'-bipyridine and 1,10-phenanthroline with transition metals. *J. Inorg. Nucl. Chem.* **35,** 1017–1021 (1973).

31. Dwyer, F. P., Gyarfas, H. A. & Goodwin, E. C. Mono- and bis-(2,2'-bipyridine) and (1,10-phenanthroline) chelates of ruthenium and osmium. I. Monochelates of bivalent, tervalent, and quadrivalent ruthenium. *Aust. J. Chem.* **16,** 42–50 (1963).

32. Sone, K., Krumholz, P. & Stammereich, H. Studies on the Coördinate Bond. III. Absorption spectra of mono-α,α'-dipyridyl and mono-o-phenanthroline complexes. *J. Am. Chem. Soc.* **77(3),** 777–780 (1955).

33. Harriman, A. Photophysics of 2,2'-bipyridyl. *J. Photochem.* **8,** 205–209 (1978).

34. Kotlicka, J. & Grabowski, Z. R. The flueorescence of 2,2'-bipyridyl. *J. Photochem.* **11,** 413–418 (1979).

35. Niven, M. L. & Percy, G. C. The infrared spectra of the 2,2'-Bipyridine. *Transit. Met. Chem.* **3,** 267–271 (1978).

36. Gondo, Y. & Kanda, Y. The phosphorescence 2,2'- and 4,4'-bipyridyls. *Bull. Chem. Soc. Jpn.* **38,** 1187–1190 (1965).

37. Dhanya, S. & Bhattacharyya, P. K. Fluorescence behaviour of 2,2'-bipyridine in aqueous solution. *J. Photochem. Photobiol. A Chem.* **63,** 179–185 (1992).

38. Castellucci, E., Salvi, P. R. & Foggi, P. Two-photon exictation spectra of the lowest electronic states of 2,2'-bipyridine. *Chem. Phys.* **66,** 281–291 (1982).

39. Yamasaki, K. Absorptionsspektren von Metallkomplexsalzen des 2,2'-Dipyridyls. I. *Bull. Chem. Soc. Jpn.* **12,** 390–394 (1937).

40. Parr, R. G. & Yang, W. Density-Functional Theory of Atoms and Molecules. *Oxford University Press: New York* (1989).

41. Perdew, J. P., Burke, K. & Ernzerhof, M. Generalized gradient approximation made simple. *Phys. Rev. Lett.* **77,** 3865–3868 (1996).

42. Weigend, F. & Ahlrichs, R. Balanced basis sets of split valence, triple zeta valence and quadruple zeta valence quality for H to Rn: Design and assessment of accuracy. *Phys. Chem. Chem. Phys.* **7,** 3297–3305 (2005).

43. Ahlrichs, R., Bär, M., Häser, M., Horn, H. & Kölmel, C. Electronic structure calculations on workstation computers: The program system turbomole. *Chem. Phys. Lett.* **162,** 165–169 (1989).

44. Krylov, A. I. Equation-of-motion coupled-cluster methods for open-shell and electronically excited species: the Hitchhiker's guide to Fock space. *Annu. Rev. Phys. Chem.* **59,** 433–462 (2008).

45. Bartlett, R. J. Coupled-cluster theory and its equation-of-motion extensions. *Wiley Interdiscip. Rev. Comput. Mol. Sci.* **2,** 126–138 (2012).

46. Reed, A. E., Weinstock, R. B. & Weinhold, F. Natural population analysis. *J. Chem. Phys.* **83,** 735–746 (1985).

47. Livshits, E. & Baer, R. A well-tempered density functional theory of electrons in molecules. *Phys. Chem. Chem. Phys.* **9,** 2932–2941 (2007).

48. Baer, R. & Neuhauser, D. Density functional theory with correct long-range asymptotic behavior. *Phys. Rev. Lett.* **94,** 2–5 (2005).

49. Nielsen, I. M. B. & Janssen, C. L. Double-substitution-based diagnostics for coupled-cluster and Møller–Plesset perturbation theory. *Chem. Phys. Lett.* **310,** 568–576 (1999).

50. De Waele, V., Buntinx, G., Flament, J. P. & Poizat, O. Asymmetric structure for the excited S1 state of 2,2'-bipyridine evidenced by picosecond time-resolved resonance Raman experiments and ab initio calculation. *Int. J. Quantum Chem.* **104,** 794–807 (2005).

51. Leavitt, C. M. *et al.* Isomer-Specific IR-IR Double Resonance Spectroscopy of D_2-Tagged Protonated Dipeptides Prepared in a Cryogenic Ion Trap. *J. Phys. Chem. Lett.* **3,** 1099–1105 (2012).

52. Xu, S., Smith, J. E. T. & Weber, J. M. Ligand influence on the electronic spectra of dicationic ruthenium- bipyridine-terpyridine complexes. *J. Phys. Chem. A* **120,** 2350–2356 (2016).

53. Chen, C., Wu, S., Wu, C., Chen, J. & Ho, K. A Ruthenium complex with superhigh light-harvesting capacity for dye-sensitized solar cells. *Angew. Chemie - Int. Ed.* **118,** 5954–5957 (2006).

54. Gao, F. *et al.* A new heteroleptic ruthenium sensitizer enhances the absorptivity of mesoporous titania film for a high efficiency dye-sensitized solar cell. *Chem. Commun.* 2635–2637 (2008).

55. Wang, P. *et al.* A stable quasi-solid-state dye-sensitized solar cell with an amphiphilic ruthenium sensitizer and polymer gel electrolyte. *Nat. Mater.* **2,** 402–407 (2003).

56. Pugh, J. R., Bruce, M. R. M., Sullivan, B. P. & Meyer, T. J. Formation of a metal-hydride bond and the insertion. Key steps in the electrocatalytic reduction of carbon dioxide to formate anion. *Inorg. Chem.* **30,** 86–91 (1991).

57. Nagao, H., Mizukawa, T. & Tanaka, K. Carbon-carbon bond formation in the electrochemical reduction of carbon dioxide catalyzed by a ruthenium complex. *Inorg. Chem.* **33,** 3415–3420 (1994).

58. Ishida, H., Tanaka, K. & Tanaka, T. Electrochemical CO_2 reduction catalyzed by $[Ru(bpy)_2(CO)_2]^{2+}$ and $[Ru(bpy)_2(CO)Cl]^{+}$. The effect of pH on the formation of CO and $HCOO^{-}$. *Organometallics* **6,** 181–186 (1987).

59. Ishida, H. *et al.* Ligand effects of ruthenium 2,2'-bipyridine and 1,10-phenanthroline complexes on the electrochemical reduction of CO_2. *J. Chem. Soc. Dalt. Trans.* **2,** 2155 (1990).

60. Gersten, S. W., Samuels, G. J. & Meyer, T. J. Catalytic oxidation of water by an oxo-bridged ruthenium dimer. *J. Am. Chem. Soc.* **104,** 4029–4030 (1982).

61. Wasylenko, D. J., Ganesamoorthy, C., Koivisto, B. D., Henderson, M. a & Berlinguette, C. P. Insight into water oxidation by mononuclear polypyridyl Ru catalysts. *Inorg. Chem.* **49,** 2202–9 (2010).

62. Zong, R. & Thummel, R. P. A new family of Ru complexes for water oxidation. *J. Am. Chem. Soc.* **127,** 12802–3 (2005).

63. Yagi, M. & Kaneko, M. Molecular catalysts for water oxidation. *Chem. Rev.* **101,** 21–35 (2001).

64. Blakemore, J. D., Crabtree, R. H. & Brudvig, G. W. Molecular catalysts for water oxidation.

Chem. Rev. **115,** 12974–13005 (2015).

65. Kalyanasundaram, K. Photophysics, Photochemistry and solar energy conversion with tris(bipyridyl)-ruthenium(ii) and its analogues. *Coord. Chem. Rev.* **46,** 159–244 (1982).

66. Sun, Y., Collins, S. N., Joyce, L. E. & Turro, C. Unusual photophysical properties of a ruthenium(II) complex related to $[Ru(bpy)_2(dppz)]^{2+}$. *Inorg. Chem.* **49,** 4257–4262 (2010).

67. Ji, L.-N., Zou, X.-H. & Liu, J.-G. Shape- and enantioselective interaction of Ru(II)/Co(III) polypyridyl complexes with DNA. *Coord. Chem. Rev.* **216–217,** 513–536 (2001).

68. Concepcion, J. J., Tsai, M.-K., Muckerman, J. T. & Meyer, T. J. Mechanism of water oxidation by single-site ruthenium complex catalysts. *J. Am. Chem. Soc.* **132,** 1545–57 (2010).

69. Balzani, V., Juris, A., Ciamician, C. G. & Bologna, I. Photochemistry and photophysics of Ru(II) polypyridine complexes in the Bologna group . From early studies to recent developments. *Coord. Chem. Rev.* **211,** 97–115 (2001).

70. Takeuchi, K. J., Thompson, M. S., Pipes, D. W. & Meyer, T. J. Redox and spectral properties of monooxo polypyridyl complexes of ruthenium and osmium in aqueous media. *Inorg. Chem.* **23,** 1845–1851 (1984).

71. Jakubikova, E. *et al.* Electronic structure and spectroscopy of $[Ru(tpy)_2]^{2+}$, $[Ru(tpy)(bpy)(H_2O)]^{2+}$, and $[Ru(tpy)(bpy)Cl]^{1+}$. *Inorg. Chem.* **48,** 10720–10725 (2009).

72. Liu, F. *et al.* Mechanisms of Water Oxidation from the Blue Dimer to Photosystem II. *Inorg. Chem.* **47,** 1727–1752 (2008).

73. Hecker, C. R., Fanwick, P. E. & McMillin, D. R. Evidence for dissociative photosubstitution reactions of $[Ru(trpy)(bpy)(NCCH_3)^{2+}$. Crystal and molecular structure of $[Ru(trpy)(bpy)(py)](PF_6)_2 \bullet (CH_3)_2CO$. *Inorg. Chem.* **30,** 659–666 (1991).

74. Lee, C., Yang, W. & Parr, R. G. Development of the Colle-Salvetti correlation-energy formula into a functional of the electron density. *Phys. Rev. B* **37,** 785–789 (1988).

75. Becke, A. D. Density-functional exchange-energy approximation with correct asymptotic behavior. *Phys. Rev. A* **38,** 3098–3100 (1988).

76. Benjamin J. Knurr. Structures and Charge Distributions of cluster anions studied by infrared photodissociation spectroscopy (2015).

77. Yoon, S., Kukura, P., Stuart, C. M. & Mathies, R. A. Direct observation of the ultrafast intersystem crossing in tris(2,2'-bipyridine)-ruthenium(II) using femtosecond stimulated Raman spectroscopy. *Mol. Phys.* **104,** 1275–1282 (2006).

78. Xu, S. & Weber, J. M. Absorption Spectrum of a Ru(II)-Aquo Complex in Vacuo: Resolving individual charge-transfer transitions. *J. Phys. Chem. A* **119,** 11509–11513 (2015).

79. Pelikán, P. & Boča, R. Geometric and electronic factors of dinitrogen activation on transition metal complexes. *Coord. Chem. Rev.* **55,** 55–112 (1984).

4 The role of the metal

This chapter has been reproduced in part with permission from Shuang Xu, James E. T. Smith, J. Mathias Weber, *The electronic spectrum of cryogenic ruthenium-tris-bipyridine dications in vacuo*, The Journal of Chemical Physics, **2016**, 145 (2), 024304, Copyright 2016, AIP Publishing[1] and Shuang Xu, James E. T. Smith, J. Mathias Weber, *UV Spectra of Tris(2,2'-bipyridine)-M(II) Complex Ions in Vacuo (M = Mn, Fe, Co, Ni, Cu, Zn)* (under revision).

4.1 Introduction and background – tris(2,2'-bipyridine)-metal complexes

Perhaps not surprisingly, the role of the metal in organometallic compounds is of fundamental importance. For transition metals, the *d*-shell configuration dictates the coordination properties of the metal and its complexes, as different configurations result in different spins, geometries, stabilities and electronic structures. It has been a long pursued topic in inorganic chemistry to characterize the properties of coordination complex as a function of the metal it contains, in order to establish some trend or series based on the metal's place in the periodic table. A commonly adopted strategy is to prepare a series of complexes with the same ligands but an altering metal core. However, exceptions and anomalies are frequent and defy simple and general conclusions. One of the inevitable drawbacks of such traditional experiments is the presence of reaction media, such as the solvent or the crystal lattice. Typical complications caused by these media include changing reaction kinetics, shifting the spectra and adding undesired reactants, and therefore pose great difficulties to observe the intrinsic properties of the target species. Experiments in the gas phase can avoid these complications. We chose to investigate a group of some of the most-studied complexes[2,3] - tris(2,2'-bipyridine)-metal

complexes and obtained unprecedented details of their electronic structure by applying photodissociation spectroscopy to these ions *in vacuo*.

Tris(2,2'-bipyridine)-metal complex ions, denoted $[M(bpy)_3]^{n+}$ (see **Figure 4.1**), are prototypical systems to study fundamental properties such as bonding, stability, steric effects and photophysics.[2,3]

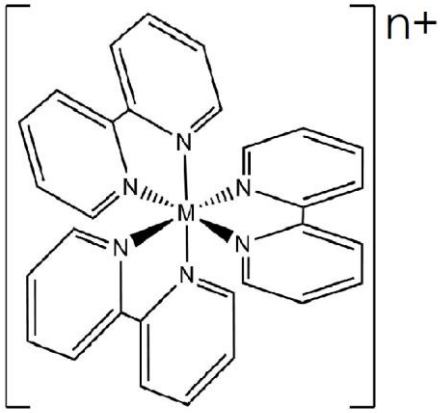

Figure 4.1 General structure of $[M(bpy)_3]^{n+}$ ions.

Among the $[M(bpy)_3]^{n+}$ species, complexes containing a d^6 metal (M = Fe, Ru, Os) have received most attention because of their remarkable extinction coefficients for visible light,[4–24] but complexes involving other kinds of metals[2,3] have been studied as well, particularly with first-row transition metals.[25–36] The earliest spectroscopy experiments on these complexes date back to 1937 and were reported by Yamasaki, who recorded the UV/vis absorption spectra of $[M^{II}(bpy)_3]^{2+}$ (M = Fe, Co, Ni, Cu, Zn) in solutions.[37] He compared the spectrum of free bipyridine in water and that of the chelates and noticed that the spectral envelopes in the UV range were all similar, except that the bands of $[M^{II}(bpy)_3]^{2+}$ were shifted to longer wavelengths compared

to free bipyridine, and that the shift depended on the metal. Such bathochromic shifts were theoretically described by Schläfer as the result of the Stark effect on the ligands due to the charged central metal ion.[38] Nearly three decades later, Palmer and Piper measured the absorption spectra of $[M^{II}(bpy)_3]^{2+}$ (M = Fe, Co, Ni, Cu, Ru) in single crystals using polarized light.[39] They were able to assign the bands in the visible range based on symmetry and polarization, but no information on the UV bands was reported. Several other groups observed a metal dependent splitting in the circular dichroism of $[M^{II}(bpy)_3]^{n+}$ (n = 2, 3) ions in their UV bands.[40,41] The interaction of the bpy ligands, which in the case of D_3 symmetric complexes are equivalent, causes the π-π* bands to split into A_2 and E components.[12,41,42] The resulting splitting of the circular dichroism response was used to determine the chirality of the complex. However, it was realized that the actual assignment of the pair was inconclusive without further theoretical insight.[35,36,43] Despite much previous effort, $[M^{II}(bpy)_3]^{2+}$ complexes have been spectroscopically studied only in solutions or single crystals until recently, and low temperature data are scarce, especially in the UV spectral region.

In this work, we studied the properties of several members of the $[M^{II}(bpy)_3]^{2+}$ family (M = Mn, Fe, Co, Ni, Cu, Zn, Ru, Os) by photodissociation spectroscopy *in vacuo*. We have obtained spectra of these species at low temperature and observe features that are obscured in solution spectra by solvent-solute interaction and hot bands at higher temperatures. Despite cryogenic preparation *in vacuo*, the spectra are still only partially resolved, but they show clear differences for different central metal ions, and the spectra are in qualitative agreement with computational predictions based on time-dependent density functional theory (TDDFT).

4.2 Methods

The instrumentation for the experiment has been described in detail in Chapter 2. To prepare $[M^{II}(bpy)_3]^{2+}$ containing the first-row metals, a divalent metal salt (see **Table 4.1**) is co-dissolved with threefold excess of 2,2'-bipyridine (Sigma-Aldrich, ≥99%) in a 1:9 mixture (by volume) of water and methanol (HPLC grade, EMD Millipore). The solution is used for electrospray without further treatment.

Table 4.1 Metal salts used for production of $[M^{II}(bpy)_3]^{2+}$ in this work. All chemicals were used as received.

metal	salt	source and specified purity
Mn	$MnCl_2$	Alfa Aesa, 97%
Fe	$FeCl_2$	Alfa Aesa, 99%
Co	$CoCl_2$	Sigma-Aldrich, 99%
Ni	NiI_2	Sigma-Aldrich, 99.999%
Cu	$CuCl_2$	Alfa Aesa, +99%
Zn	$ZnCl_2$	Sigma-Aldrich, >98%
Ru	$Ru(bpy)_3Cl_2$	Sigma-Aldrich, 99.95%
Os	K_2OsCl_6	Alfa Aesar, Os 38.7%

$[Ru(bpy)_3]^{2+}$ is generated by electrospraying a solution of $Ru(bpy)_3Cl_2{\cdot}6H_2O$ in water/methanol (1:9) solution . $[Os(bpy)_3]^{2+}$ requires synthesis. The procedures were found in literature[44] and were modified to be compatible with electrospray. In brief, K_2OsCl_6 and 2,2'-bipyridine were mixed in glycerol (Alfa Aesar, 99%+) and refluxed at 240 °C for 1 hour. The green mixture was cooled, diluted with water, then NH_4PF_6 (Alfa Aesar, 99.5%) was added. The resulting solution was filtered to collect the dark green precipitation (mainly $Os(bpy)_3(PF_6)_2$). The solid was dissolved in acetonitrile for electrospray without further purification.

For $[M^{II}(bpy)_3]^{2+}$ where M is a d^6 metal, the binding energy of a bpy ligand is generally so high that photodissociation is energetically forbidden even in the UV region. Therefore, we used N_2 molecules as a messenger tag and measured photodissociation action spectra of $[M^{II}(bpy)_3]^{2+}\cdot N_2$ for these species. This was done by injecting dry N_2 into the 25-K ion trap as the buffer gas. We were able to form adducts with up to 8 N_2 molecules (see §2.4.3, **Figure 2.16**).

For all other species, despite that the bpy biding energy is sufficiently low to allow photodissociation in the UV. However, due to their low absorption cross sections in the visible range,[39] we were not able to produce observable photofragments due to limited laser power and parent ion intensity. Consequently, we were able to register only the UV bands for these species (M = Mn, Co, Ni, Cu, Zn).

We used density functional theory[45] (DFT) with def2-TZVP basis sets[46] for all atoms and the B3-LYP functional[47,48] to calculate the ground state geometry of each species for different multiplicities. Different symmetry restrictions (D_3, C_2) were applied to explore the lowest energy geometry, and these calculations were validated through calculations without symmetry restriction. Excitation energies were calculated by time-dependent DFT (TDDFT[49–51]) with the same basis sets and functionals, assuming that total spin was conserved. Charge analyses were performed using natural population analysis.[52] All computations were done using the Turbomole program suite.[53,54]

4.3 Results and discussions

4.3.1 Computational

We performed the geometry optimization for all species with and without symmetry restrictions. The results are listed **Table 4.2**. Since the calculation without symmetry restriction (C_1) preserves all degrees of freedom in the system, the configuration with minimum energy can be considered as the absolute minimum. If the energy resulting from a certain symmetry-restricted calculation is very close to the minimum energy calculated without symmetry restriction, this is evidence that the ion adopts this symmetry.

Table 4.2 Calculated ground-state energies for the $[M^{II}(bpy)_3]^{2+}$ species in this study (in cm^{-1}) with different symmetries (D_3, C_2, C_1) and spin configurations. The lowest energy for each species is listed in bold font.

M	D_3		C_1	C_2
	low spin	high spin		
Mn	-71740.134 (S=2) -71738.611 (S=4)	**-71741.012**	-71741.013 [a]	
Co	-78046.200	**-78047.370**	-78047.372 [a]	-78047.302 [a]
Ni	-81463.891	**-81463.891**	-81463.892 [a]	
Cu	-85058.364		-85059.299	**-85059.259**
Zn	**-88839.177**		-88839.176	
Fe	**-74807.644**	-74807.559	-74807.647 [b]	
Ru	**-43004.382**	-43001.255	-43004.382 [b]	
Os	**-42889.563**	-42886.958	-42889.562 [b]	

[a] high-spin configuration

[b] low-spin configuration

Following this logic, from **Table 4.2**, we can immediately conclude that all species follow D_3 symmetry in their ground state, except $[Cu(bpy)_3]^{2+}$, which takes C_2 symmetry, probably due

to strong Jahn-Teller distortion as is often the case in other Cu^{II} complexes.[55] This suggests a fundamentally different electronic configuration in $[Cu(bpy)_3]^{2+}$ than in the rest of the series. Indeed, the electronic spectrum of $[Cu(bpy)_3]^{2+}$ appears to be distinct from others both theoretically and experimentally. Therefore, $[Cu(bpy)_3]^{2+}$ is discussed alone in §4.3.2.

For the species with D_3 symmetry, according to experiments by Burstall and Nyholm[56], $[M^{II}(bpy)_3]^{2+}$ takes the highest possible spin multiplicity for M = Mn, Co, Ni, Zn. This observation is corroborated by our DFT calculations as well. Lower spin states of these species are higher in energy compared to the highest possible spin state, except for M = Ni, where the singlet and triplet states are within 0.1 kJ/mol. The opposite is true for M = Fe, Ru, Os, *i.e.* the d^6 metals, and all of their ground states are singlet states. The d^6-metal complex ions are also distinct regarding their complex geometries and binding energies.

Shown in **Table 4.3** are geometric data together with calculated binding energies of the bpy ligand and the charge distribution on the metal. The d^6-metal complex ions have shorter metal-nitrogen bond lengths than the other complexes studied here. The charge on the metal is much lower than in other species, meaning Fe, Ru and Os are significantly reduced by the bpy ligands. More importantly, the binding energy of the bpy ligand in M = Fe, Ru, Os is remarkably higher than that of the others. While for M = Mn, Co, Ni, Cu, Zn, the binding energy lies between 147 and 232 kJ/mol (12100 and 19360 cm^{-1}), which is well below our spectral range in the UV and should not result in kinetic shift effects that could distort the spectral profile, the high binding energy in M = Fe, Ru, Os (> 333 kJ/mol, 27830 cm^{-1}) demands messenger tagging to perform photodissociation spectroscopy. Consequently, we will discuss the d^6 metal complexes in §4.3.4, separate from the other species. The complex with M = Cu is different from all others, since it

has different symmetry. It will therefore also be discussed separately, in §4.3.2. The other complexes (M = Mn, Co, Ni, Zn) will be discussed in §4.3.3.

Table 4.3 Calculated geometric properties and binding energies of $[M^{II}(bpy)_3]^{2+}$.

M	binding energy (kJ/mol)	NN distance (Å)	NCCN dihedral (degrees)	M-N bond length (Å)	charge on M (e)
Mn	204	2.71	10.35	2.29	1.44
Co	194	2.68	5.42	2.18	1.43
Ni	232	2.67	5.61	2.14	1.36
Cu [a]	147	2.67/2.72	4.08/14.3	2.12/2.30	1.38
Zn	166	2.70	7.66	2.21	1.66
Fe	333	2.61	2.28	2.02	0.73
Ru	379	2.64	1.58	2.10	0.55
Os	424	2.62	1.53	2.10	0.80

[a] In C_2 symmetry, the bpy ligand on the C_2 axis has a slightly different structure than the other two bpy ligands. In the Cu entry, the number after the slash belongs to the bpy on the C_2 axis. For the M-N bond length, 2.12 Å is the average bond length of the two M-N bonds of the off-axis bpy ligands.

4.3.2 M = Cu

The ground state of $[Cu(bpy)_3]^{2+}$ is a doublet, similar to many other Cu^{II} complexes. Strong Jahn-Teller distortion of this species results in C_2 symmetry, with two elongated Cu-N bonds on the bpy ligand along the C_2 axis (see **Table 4.2**). The spectrum of $[Cu(bpy)_3]^{2+}$ is broad and almost featureless. The allowed electronic transitions are of A and B symmetry. The TDDFT calculations show that there are a significant number of transitions of similar intensity distributed throughout the observed spectral region. Assuming that broad Franck-Condon envelopes are present for most of the transitions, such a high density of electronic states is almost certain to be responsible

for much of the broadness of the absorption profile. The computed spectrum is able to qualitatively reproduce the experimental spectral profile if the most intense B transition is aligned with the observed peak at 34600 cm^{-1}. This requires a shift of -1610 cm^{-1} of the calculated spectrum, which is applied in **Figure 4.2**. We tentatively assign the peak at 34600 cm^{-1} to the most intense B transition. It has π-π* character and mainly involves the bpy ligand on the C_2 axis. Note that not all transitions in this region are of π-π* character, as some transitions involve orbitals with significant density on Cu. Using the solution spectrum from Yamasaki,[37] the solvatochromic shift in aqueous solution is estimated to be *ca.* 1040 cm^{-1}.

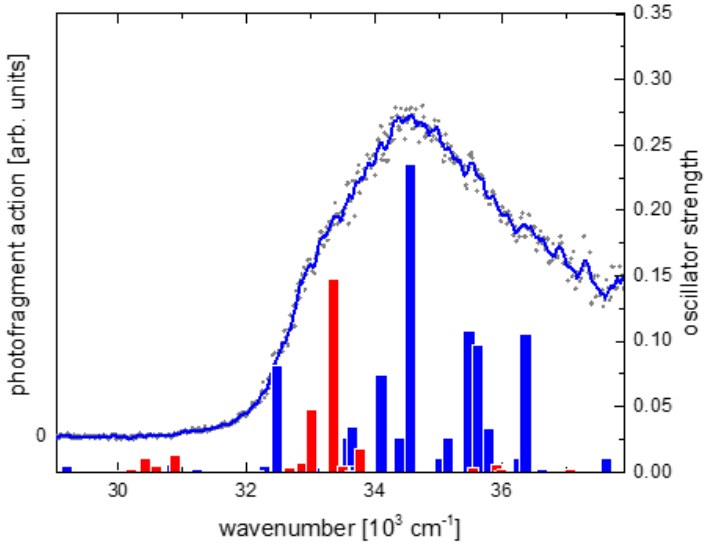

Figure 4.2 Photodissociation spectra for the $[Cu(bpy)_3]^{2+}$. The grey points are raw data; the full lines represent 10-point sliding averages to guide the eye. The vertical bars are calculated A (red) and B (blue) transitions, shifted by -1610 cm^{-1}.

4.3.3 M = Mn, Co, Ni, Zn

These species show D_3 symmetry in the ground state and have similarities regarding the calculated charges on the metal atoms and the binding energies of the bpy ligands. It is therefore conceivable that their electronic structures should also bear significant similarities, which is substantiated by our calculations and experimental observations.

The spectrum of $[Ni(bpy)_3]^{2+}$ displays the most resolved structure among all species in this study. The level of spectroscopic detail in our spectrum exceeds that in the previously reported spectra measured in frozen solutions at 77 K.[35,36] The spectrum shows a prominent peak at 33150 cm^{-1}, followed by a series of smaller peaks. The calculated spectrum is qualitatively consistent with the experimental observations, but needs to be shifted by -2820 cm^{-1} to better match the calculated pattern to the experimental spectrum. The most intense peak in the experimental spectrum is identified as the strongest calculated A_2 transition, which has π-π* character. The substructure of the band closely resembles that of $[(bpy)Cu\text{-}N_2]^+$ except that the peaks are 480 cm^{-1} higher in energy. Based on this similarity, the substructure in $[Ni(bpy)_3]^{2+}$ can be attributed to the Franck-Condon envelope belonging to vibrations on the bpy ligands (mainly ring deformation modes), similar to $[(bpy)Cu\text{-}N_2]^+$ (see **Figure 4.3**, §3.2.3 and Ref.[57]).

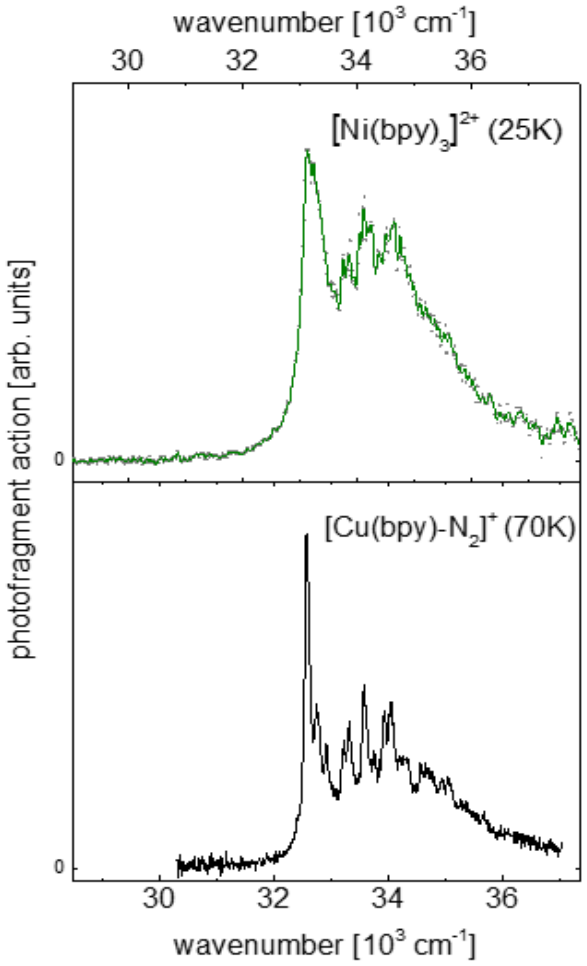

Figure 4.3 Photodissociation spectrum of $[Ni(bpy)_3]^{2+}$ (top) compared to that of $[Cu(bpy)\text{-}N_2]^{+}$ (bottom).[57] Note that the two spectra have slightly shifted wavenumber axes to emphasize their similarity. The points in the upper trace are raw data; the full line is 5-point sliding average to guide the eye.

The main differences between the spectra of $[Ni(bpy)_3]^{2+}$ and $[Cu(bpy)\text{-}N_2]^{+}$ are the peak positions and widths. The vibrational bands in the Franck-Condon progression of the $[Ni(bpy)_3]^{2+}$ spectrum are broader than those in the spectrum of $[Cu(bpy)\text{-}N_2]^{+}$. Since the spectrum of $[Ni(bpy)_3]^{2+}$ was acquired at a lower trap temperature (25 K) than for $[Cu(bpy)\text{-}N_2]^{+}$ (70 K), we can rule out hot bands as a cause of the residual broadening. Note that an important broadening

mechanism in $[Cu(bpy)\text{-}L]^+$complexes is lifetime broadening due to internal conversion to lower lying states.[57] Therefore, the same mechanism may be at play here as well. In fact, our calculations show that there are many more lower lying states in $[Ni(bpy)_3]^{2+}$ than in $[Cu(bpy)\text{-}N_2]^+$, which lends credence to this argument.

Another possible factor contributing to the spectral width is the overlap of multiple bands. Notably, the interaction among the three bpy ligands leads to splitting of their otherwise degenerate π-π* bands into A_2 and E bands, with the E band usually at a lower energy. Although the intensities of the lower lying bands are typically weaker, their Franck-Condon progressions will overlap with the more intense A_2 band envelope and lower the observed contrast of the vibrational structures belonging to the A_2 band. Our TDDFT calculations put the splitting of the A_2 and E bands in $[Ni(bpy)_3]^{2+}$ at *ca.* 400 cm^{-1} and predict an intensity ratio of A_2:E ≈ 2.2. But if this was true, the E transition would be resolved as a separate peak to the red of the prominent A_2 peak. However, our spectrum does not show any partially resolved feature on the low-energy slope of the A_2 peak. We can obtain an estimated upper limit on the A_2-E splitting by the half width of the A_2 peak, *i.e.* 120 cm^{-1}, which is very close to the splitting estimated by Bray *et al.*[35] to be 100 cm^{-1}. This small amount of energy difference leads to more overlapping of the envelopes built on different origins, and thus more severe congestion of the substructures. Both excited state lifetime and A_2-E splitting may contribute to the width of the substructure of the observed bands, but it is likely in the case of $[Ni(bpy)_3]^{2+}$ that the main contribution comes from lifetime broadening, since the low-energy slope of the dominant peak shows no substructure, and it can be fitted with high fidelity by a Lorentzian line shape.

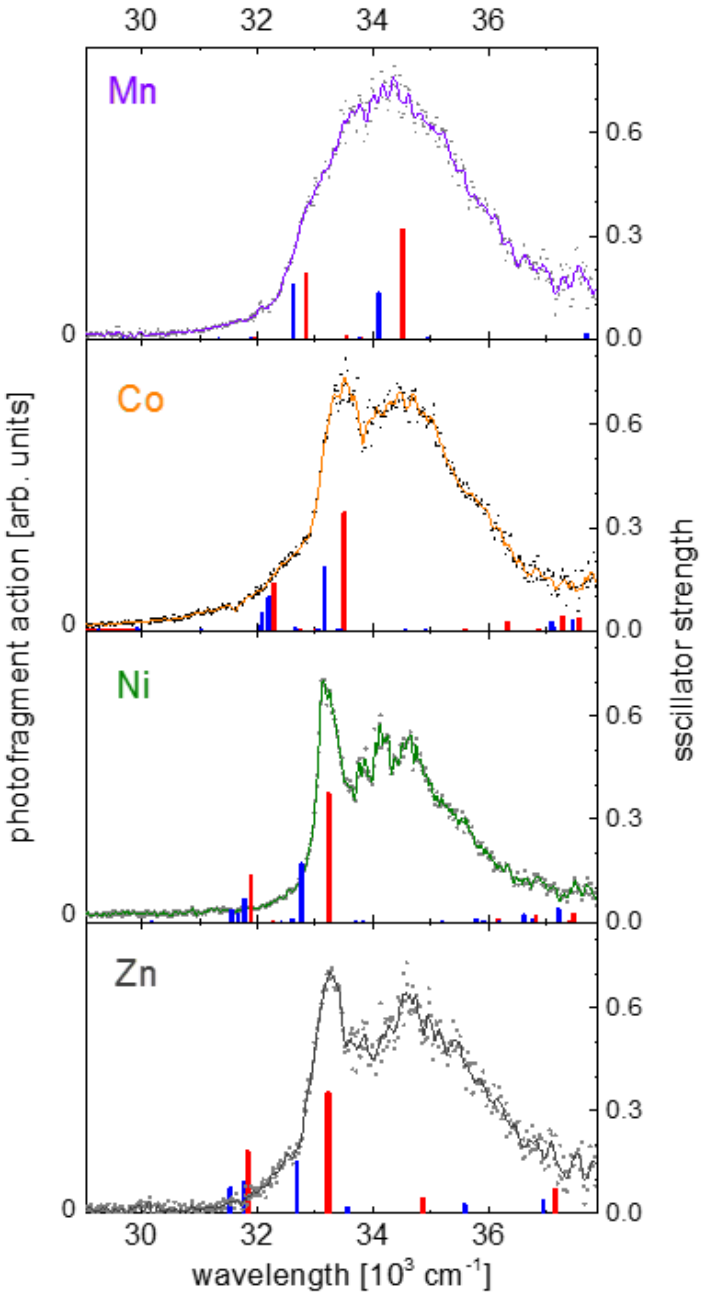

Figure 4.4 Photodissociation spectra of the $[M^{II}(bpy)_3]^{2+}$ complexes studied here (M is noted in the corresponding panel). The grey points are raw data; the full lines represent 10-point sliding averages. The vertical bars are calculated A_2 (red) and E (blue) transitions for each metal; they are shifted by a certain amount to match the experimental results (see text).

The spectra of the complexes with M = Mn, Co, Ni and Zn are shown in **Figure 4.4**, together with our TDDFT calculations. The spectra of $[Co(bpy)_3]^{2+}$ and $[Zn(bpy)_3]^{2+}$ qualitatively resemble

that of $[Ni(bpy)_3]^{2+}$, but they have less resolved substructure. The prominent peaks in these spectra are at similar positions, 33470 cm^{-1} for $[Co(bpy)_3]^{2+}$ and 33230 cm^{-1} for $[Zn(bpy)_3]^{2+}$, close to that of $[Ni(bpy)_3]^{2+}$ (33150 cm^{-1}). Therefore, we assign them to the same A_2 π-π^* band. $[Co(bpy)_3]^{2+}$ and $[Zn(bpy)_3]^{2+}$ also shows extensive features following the A_2 band, which again can be attributed to the Franck-Condon progressions building on the A_2 band. However, the substructures are less distinct compared to $[Ni(bpy)_3]^{2+}$. The calculated spectra need to be offset by -2980 cm^{-1} for $[Zn(bpy)_3]^{2+}$ and -2420 cm^{-1} for $[Co(bpy)_3]^{2+}$ to match experimental and calculated spectra. There are weakly discernible shoulders on the low energy side of the dominant A_2 features for Co and Zn, which we tentatively interpret as experimental signatures of the accompanying E bands. The calculated A_2-E splittings and A_2:E intensity ratios for $[Co(bpy)_3]^{2+}$ and $[Zn(bpy)_3]^{2+}$ are all similar to that calculated for $[Ni(bpy)_3]^{2+}$, but they fit better to the experimental spectra than for $[Ni(bpy)_3]^{2+}$. A more notable and extensive shoulder can be found in the even lower energy region in the spectra of M = Co and Zn but much less so for M = Ni. It is almost 1610 cm^{-1} to the red of the intense A_2 peak, therefore, it is unlikely to be related to the E band. A more plausible candidate for this feature is a set of lower-lying π-π^* states, which is also predicted by the calculations, though the calculated energies are somewhat lower than the position of this shoulder.

If we assume that the width is limited by excited state lifetime, the difference of the spectral width for different species suggests that the lifetime depends on the metal atom, or – more precisely – on the exact electronic structure of the complex. We note that simpler electronic structures (*i.e.*, fewer lower lying states) do not necessarily result in longer lifetimes. An interesting case is $[Zn(bpy)_3]^{2+}$, which contains a d^{10} metal, so its electronic structure does not

allow low-lying *d-d or* MLCT transitions. However, the prominent feature that is observed in the experimental spectrum and assigned to the second A_2 state (the 5th excited state overall) is broader than the analogous feature in the $[Ni(bpy)_3]^{2+}$ spectrum, which belongs to the 22nd excited state. Obviously the sheer number of lower lying states is not as relevant as the coupling to some of them and coupling seems to be dependent on the metal itself. Within our present computational treatment, no simple trend can be found that would explain the different widths of these spectra.

With the gas-phase spectrum, it is possible to calculate the absolute solvatochromic shift in the condensed phase. The solution spectrum of $[Zn(bpy)_3]^{2+}$ in a frozen mixture of methanol and water at 77 K is available from the literature,[32] and comparison with our data shows a solvatochromic shift of *ca.* -830 cm^{-1} for this solvent mixture.

Finally, the $[Mn(bpy)_3]^{2+}$ spectrum has a broad and featureless band in the same range as for all other spectra in this series. No detailed information can be extracted, except a general similarity in the calculated pattern. The calculated spectrum in **Figure 4.4** is shifted by -2420 cm^{-1}, purely for consistency with the treatment of the related species (M = Co, Ni, Zn) in this series. The dominant A_2 and E transitions fall in the same region as everyone else and match the position of the experimentally observed band. Because the calculated spectrum is equally sparse, we assume that the width of the features is caused by even shorter lifetimes compared to the others. This may not be very surprising as $[Mn(bpy)_3]^{2+}$ is a sextet and may have access to many intersystem crossing pathways.

4.3.4 M = Fe, Ru, Os

This group of $[M^{II}(bpy)_3]^{2+}$ species makes up almost half of the literature on tris(bpy)-metal complexes. Unlike the other species in the present work, they have much brighter MLCT bands in the visible region, making their solutions strongly colored. This photophysical property makes them potentially useful as photosensitizers or light harvesting dyes and is the main reason for the attention they have received. Due to the high binding energy of the bpy ligands in these species, we had to resort to N_2 tagging and measured the photodissociation spectra of $[M^{II}(bpy)_3]^{2+}\cdot N_2$. The loss of N_2 from the parent ions is the only significant fragment channel, even in the UV. We will start our discussion with M = Ru, because $[Ru(bpy)_3]^{2+}$ is the most studied complex of the three.

The photodissociation spectrum of $[Ru(bpy)_3]^{2+}\cdot N_2$ throughout the visible and near UV is shown in **Figure 4.5** together with the solution spectrum. Similar to $[Mn(bpy)_3]^{2+}$, the intense A_2 and E transitions with π-π* character predicted by theory in the UV region appear only as a broad and featureless peak (feature IX) at 36100 cm^{-1}. In contrast, in the visible range, the two features that are barely resolved in aqueous solution at *ca.* 22100 cm^{-1} and 23200 cm^{-1} are now two very clear, well resolved bands peaking at 23160 cm^{-1} (feature IV) and 24660 cm^{-1} (feature V). Several shoulders appear at lower energies (features I - III, the onset at about 18700 cm^{-1}), and around 26230 cm^{-1} (feature VI). Some weaker and broader bands (VII, VIII) are observed around 29500 cm^{-1} and 32000 cm^{-1}. These transitions in the visible and near UV have been attributed to MLCT states.[58] The two main peaks in the visible MLCT band show considerable shifts compared to solutions. Features IV and V are shifted by -1060 cm^{-1} and -1460 cm^{-1} in aqueous solution, respectively, and their relative intensities also change. Such differences are not unexpected

because the intensity of hot bands in the solution spectrum is higher, which may lead to changes in the overall peak shapes. The overview spectrum *in vacuo* reported by Kirketerp and Nielsen[15] at room temperature appears more similar to the solution spectra, which supports this argument.

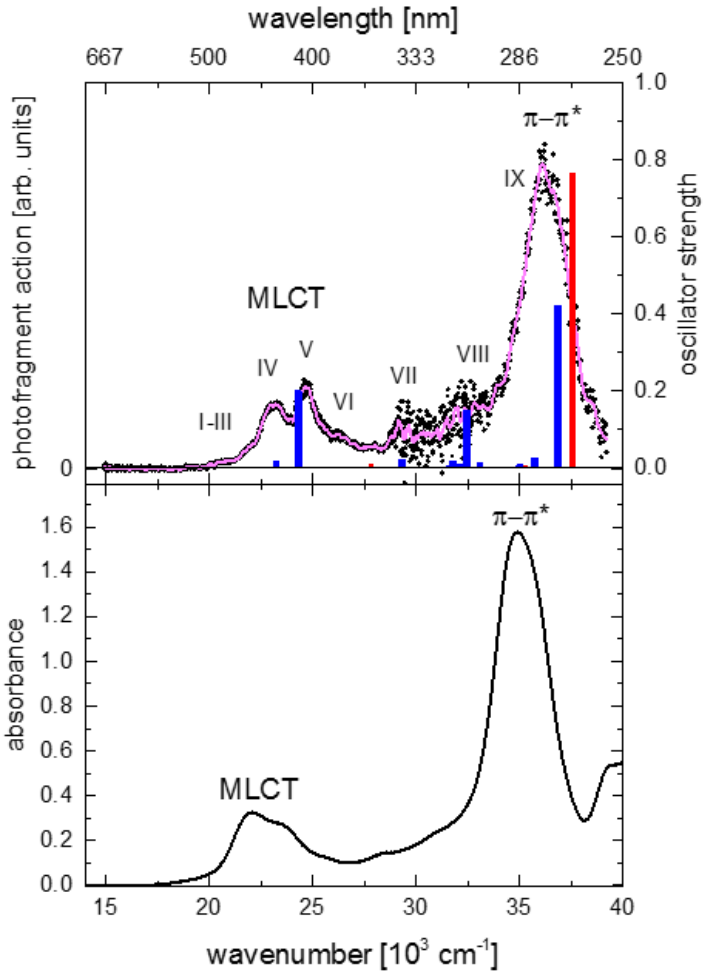

Figure 4.5 Photodissociation action spectrum of $[Ru(bpy)_3]^{2+}\cdot N_2$ at 25 K trap temperature (upper) compared to the UV/vis absorption spectrum of an aqueous solution of $Ru(bpy)_3Cl_2$ (25 μM). The data points in the photodissociation spectrum are raw data; the full line is 30-point slide average. The vertical bars are calculated A_2 (red) and E (blue) transitions; they are shifted by 800 cm^{-1} to the blue to match the experimental results. Distinct features are labeled by Roman numerals as discussed in the text.

Although our TDDFT calculation using B3LYP/def2-TZVP yield a spectral pattern that is qualitatively consistent with the experimental spectrum, the calculated energies are somewhat too low. The calculated spectrum is shifted by 800 cm^{-1} to the blue to match the most intense bands in the experimental spectrum. Using the shifted calculation to aid the assignment of the observed features, we identify the two intense bands IV and V as E transitions, and feature VI tentatively as an A_2 transition. The assignment of features VII and VIII has been controversial. Meyer and coworkers assigned feature VII to an MLCT transition based on molecular orbital arguments,[5] but others speculated that features in this region could be metal centered transitions.[58] Our TDDFT calculations suggest that both features are predominantly MLCT bands. Finally, the most intense feature in the spectrum (IX) can be attributed mostly to two unresolved intense transitions of π–π* character, one of A_2 symmetry and one of E symmetry, similar to the features exhibited in the spectra of other species in this region (see §4.3.3).

The lower-energy features (I-V) are not well represented by our simple approach. Heully *et al.*,[59] who used TDDFT calculations including spin-orbit coupling, were able to provide a simulated spectrum that better matches our result. The effect of the spin-orbit operator on the ground and excited states in the MLCT band region is discussed in Ref.[59] The three highest occupied orbitals in the ground state of $[Ru(bpy)_3]^{2+}$ are metal-centered, two of e symmetry and one of a_1 symmetry. Only those will be significantly affected and mixed by the (atomic) spin-orbit operator, while the spin-orbit splittings on the ligand-centered virtual orbitals are expected to be small. Here, only singlet excited states are considered since direct transitions to the triplet manifold are electric dipole forbidden, and absorption cross sections may be too low for to be

observed. **Figure 4.6** shows more detail of the MLCT bands in the experimental photodissociation spectrum.

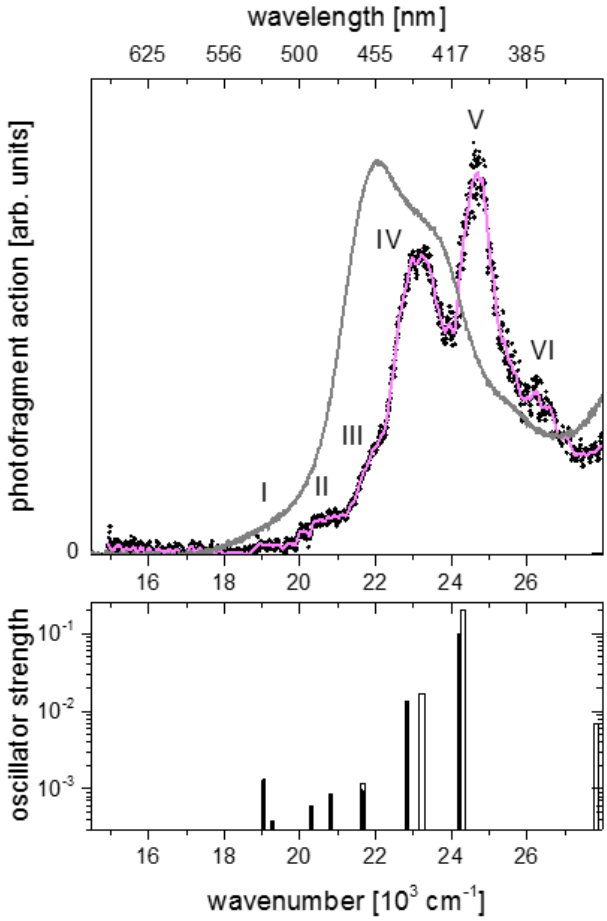

Figure 4.6 Zoom-in onto the MLCT band of the photodissociation spectrum of $[Ru(bpy)_3]^{2+}\cdot N_2$ in **Figure 4.5**. The full grey line is the absorption spectrum in aqueous solution as shown in the lower panel of **Figure 4.5**, scaled to have the same MLCT peak intensity as the photodissociation spectrum. The calculated transitions (lower panel) are displayed as bars (full: Heully *et al.*[59]; open: this work). Both calculated spectra is graphically offset by 800 cm^{-1} to allow easier comparison and assignment. Note the logarithmic scale for the oscillator strength.

Assuming that the onset of the experimental spectrum represents the very first transition, the calculated transitions by Heully *et al.*[59] are about 800 cm^{-1} too low in energy. This is the same

amount of shift that has been applied to our calculations in **Figure 4.5**. Therefore, we show the shifted calculation results by Heully *et al.*[59] as well as our own in the same graph to compare with the experiment in **Figure 4.6**. The lowest energy feature in the experimental spectrum (I) is rather weak and has an onset at *ca.* 18700 cm^{-1}. It rises to a shoulder at 18900 cm^{-1} with a plateau that continues until the photodissociation yield steps up again. We assign this feature to the lowest three dipole allowed states calculated by Heully *et al.*[59] The lowest discernible band in the spectrum is probably dominated by the 2E' transition (the S_2 state) because of its higher oscillator strength. The S_1 state ($1A_2'$) may be slightly lower than 18700 cm^{-1}, based on the difference of 200 cm^{-1} between the S_1 state and the S_2 state, and because it has a much smaller oscillator strength as calculated by Heully *et al.*, we may not be able to observe it. Feature II, beginning at 20100 cm^{-1}, has some substructure and extends up to 21200 cm^{-1}. It can be assigned to a combination of the $3A_2'$ and 6E'states. A shoulder at 21900 cm^{-1} (III) is consistent with the 8E' state, and the two most intense features in the MLCT region can be easily assigned to the 11E' (IV) and the 12E' states (V). Clearly, the calculations taking the spin-orbit coupling into account can describe the low energy region of the electronic spectrum in a much more accurate way than our simple TDDFT calculations do. Unfortunately, no assignment from spin-orbit corrected calculations is available for the higher energy features. Note that in both Heully *et al.*'s[59] and our work, the calculated oscillator strengths for the lower energy transitions relative to the most intense MLCT features are too low by a factor of 10-100, compared to the experiment. The summary of the assignments using calculations with and without spin-orbit coupling presented in **Table 4.4**.

Table 4.4 Transition energies and oscillator strengths for selected calculated excited states (TDDFT with[59] and without spin-orbit interaction) of $[Ru(bpy)_3]^{2+}$ compared to experimentally observed features. Solvatochromic shifts are calculated only for discernible features in both aqueous solution and gas phase spectra.

computational				experimental (this work)		
	state[a]	energy [cm^{-1}]	oscillator strengths	energy [cm^{-1}]	feature[b]	solvatochromic shift, aq. [cm^{-1}]
with spin-orbit coupling (Heully *et al.*[59])	$1A_2'$	18065	$2\cdot10^{-6}$	18900	I	[c]
	2E'	**18242**	**$1.3\cdot10^{-3}$**			
	3E'	18478	$3.8\cdot10^{-4}$			
	$2A_2'$	19197	$2.2\cdot10^{-7}$			
	$3A_2'$	**19487**	**$6\cdot10^{-4}$**	20100	II	
	4E'	19714	$1.7\cdot10^{-5}$			
	6E'	**20007**	**$8.4\cdot10^{-4}$**			
	8E'	**20827**	**$9.6\cdot10^{-4}$**	21900	III	
	$5A_2'$	20844	$2.9\cdot10^{-4}$			
	9E'	21004	$1.3\cdot10^{-5}$			
	$6A_2'$	21842	$6.8\cdot10^{-5}$			
	11E'	**22015**	**$1.3\cdot10^{-2}$**	23160	IV	
	12E'	**23411**	**$1\cdot10^{-1}$**	24660	V	
without spin-orbit coupling (this work)	2E	22429	$1.7\cdot10^{-2}$	23160	IV	-1060
	3E	23507	$2.0\cdot10^{-1}$	24660	V	-1460
	$3A_2$	27014	$6.8\cdot10^{-3}$	26230	VI	-710
	4E	28516	$2.0\cdot10^{-2}$	29500	VII	-1240
	9E	31659	$1.5\cdot10^{-1}$	32000	VIII	-1170
	14E	36066	$4.2\cdot10^{-1}$	36100	IX	-1320
	$8A_2$	36783	$7.6\cdot10^{-1}$			

[a] The state designation follows that given in Ref.[59] Calculated values shown in bold are assigned to the corresponding experimentally observed features.

[b] See **Figure 4.5**.

[c] Cannot be determined due to lack of resolved feature in the solution spectrum.

It is worth questioning whether the presence of the N_2 tag affects the electronic spectrum. Previous work by Nielsen and coworkers established that the presence of an acetonitrile molecule does not have a significant effect on the room temperature spectrum of

$[Ru(bpy)_3]^{2+}$.[60] One may expect that the binding energy of the N_2 tag to $[Ru(bpy)_3]^{2+}$ (calculated to be *ca.* 5 kJ/mol) is smaller than that of acetonitrile, because the latter has a sizeable electric dipole moment. Therefore, it is convincing that the presence of the N_2 tag will not have a significant effect on the spectrum. Since our TDDFT calculations give a reasonable qualitative description of the experimental spectrum, we performed exploratory TDDFT calculations for states up to 30000 cm^{-1} for complexes with and without N_2 tagging. The results are almost identical, confirming that the effects of an N_2 tag on the overall pattern of the electronic spectrum are negligible (see **Figure 4.7**).

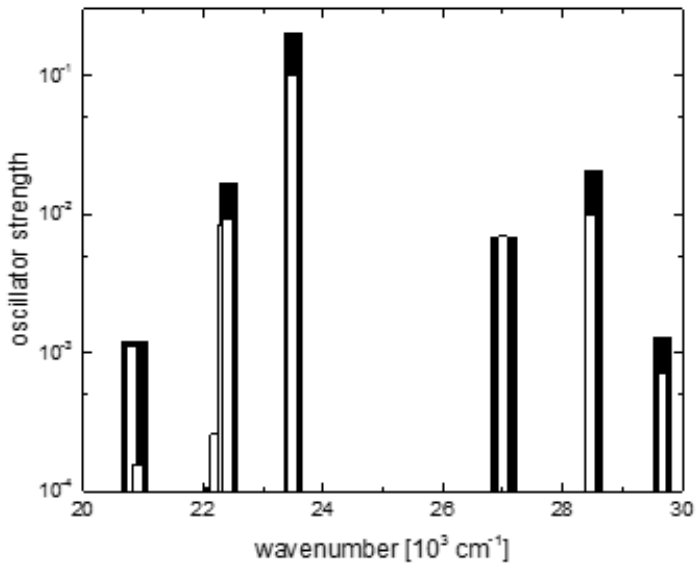

Figure 4.7 Comparison of TDDFT calculations (B3LYP/def2-tzvp) for $[Ru(bpy)_3]^{2+}$ (filled columns) and $[Ru(bpy)_3]^{2+}\cdot N_2$ (open columns).

$[Fe(bpy)_3]^{2+}$. This ion has an electronic structure very similar to that of $[Ru(bpy)_3]^{2+}$, but the transitions are found at lower energies. The full spectrum, shown in **Figure 4.8**, can be also

divided into MCLT and π-π* regions. The calculated spectrum of $[Fe(bpy)_3]^{2+}$ using B3LYP/def2-TZVP is able to qualitatively reproduce the experimental spectral profile. Analogous to the treatment of the $[Ru(bpy)_3]^{2+}$ data, a shift of -3390 cm^{-1} is applied to the calculated spectrum to align the first intense transition to the first prominent feature (II).

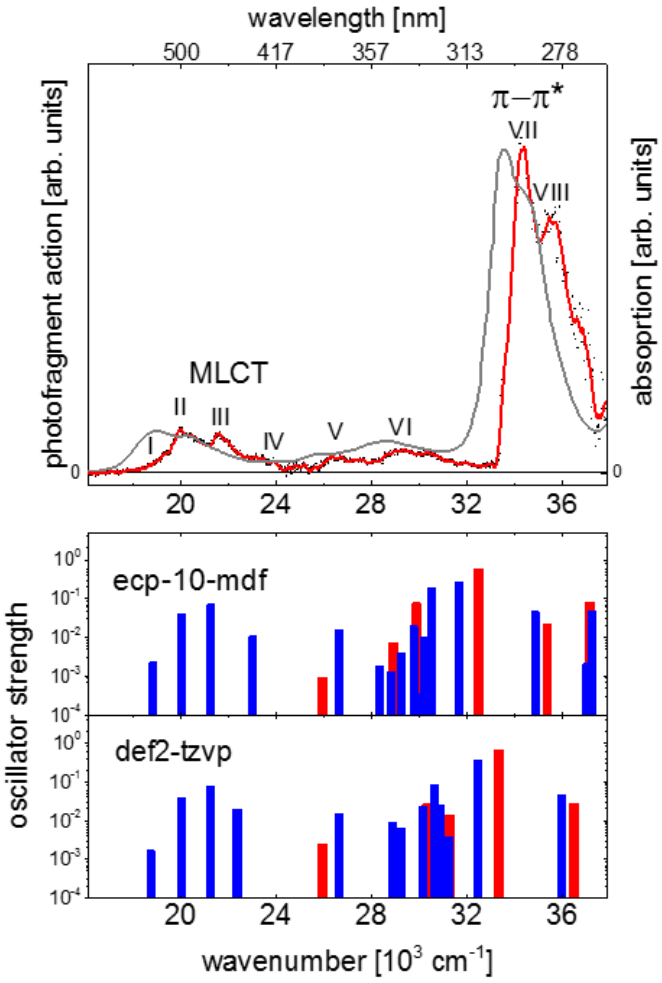

Figure 4.8 Photodissociation action spectrum of $[Fe(bpy)_3]^{2+}\cdot N_2$ at 25 K trap temperature compared to the UV/vis absorption spectrum of its aqueous solution adapted from Ref.[24] (top). The points in the photodissociation spectrum are raw data; the full line is a 20-point sliding average. The lower panel shows A_2 (red) and E (blue) transitions calculated using ecp-10-mdf and def2-tzvp basis sets for Fe. The results are shifted by 3390 cm^{-1} to the red to better match the experimental results. Note the logarithmic scale for the oscillator strength.

Assignments can be made based on the shifted, calculated spectrum as listed in **Table 4.5**. The solvatochromic shift of $[Fe(bpy)_3]^{2+}$ in aqueous solution is calculated by comparing our experimental data with the solution spectrum.[24]

Table 4.5 Transition energies and oscillator strengths for selected calculated excited states (TDDFT without spin-orbit interaction, B3LYP/def2-tzvp) of $[Fe(bpy)_3]^{2+}$ compared to experimentally observed features. Solvatochromic shifts are calculated only for discernible features in both aqueous solution and gas phase spectra.

computational			experimental		
state	energy [cm^{-1}]	oscillator strength	energy [cm^{-1}]	feature[a]	solvatochromic shift, aq. [cm^{-1}]
2E	22153	$2.3 \cdot 10^{-3}$	19300	I	-[b]
3E	23437	$3.6 \cdot 10^{-2}$	19970	II	-1170
4E	24634	$7.5 \cdot 10^{-2}$	21570	III	-1200
5E	25774	$6.8 \cdot 10^{-3}$	23230	IV	-[b]
$4A_2$	29343	$2.5 \cdot 10^{-2}$	26480	V	-580
6E	30044	$1.5 \cdot 10^{-2}$			
11E	34063	$8.2 \cdot 10^{-2}$	29310	VI	-740
14E	35846	$3.6 \cdot 10^{-1}$	34360	VII	-860
$8A_2$	36749	$6.4 \cdot 10^{-1}$			

[a] See **Figure 4.8**.

[b] Cannot be determined due to lack of resolved feature in the solution spectrum.

It should be noted that in the cases of $[Fe(bpy)_3]^{2+}$ and $[Ru(bpy)_3]^{2+}$ calculations using the def2-TZVP basis set attribute the electronic transitions to different types of molecular orbitals, even though the transitions appear to have the same character judging from experimental observation. It is realized that this is simply because the basis set for Fe in def2-TZVP does not apply an effective core potential as it does for Ru. To make the calculations comparable, we used an ecp-10-mdf basis set (for the Fe atom only) and recovered a similar result as for $[Ru(bpy)_3]^{2+}$.

The same shift (-3390 cm^{-1}) needs to be applied to match the low energy region, *i.e.*, the MLCT region of the spectrum. The description of the MLCT bands using the ecp-10-mdf basis set is very similar to the def2-TZVP result, but the energies of the higher transitions are significantly underestimated (see **Figure 4.8**). Unfortunately, higher-level computations considering spin-orbit coupling are currently beyond our computational resources, which prevents more detailed discussions on the MLCT region.

$[Os(bpy)_3]^{2+}$. Our experimental spectrum of $[Os(bpy)_3]^{2+}$ shows less distinct features than for M = Fe and Ru. Because the parent ion intensity of $[Os(bpy)_3]^{2+}\cdot N_2$ was five times lower than those of $[Ru(bpy)_3]^{2+}\cdot N_2$ and $[Fe(bpy)_3]^{2+}\cdot N_2$, the signal-to-noise ratio is worse in this case. It is however clear that the spectral profile in $[Os(bpy)_3]^{2+}$ is different from the spectra of the other two complexes, even though the main bands are found in the same energy regions and are predicted by calculations to have the same overall character (see **Figure 4.9**).

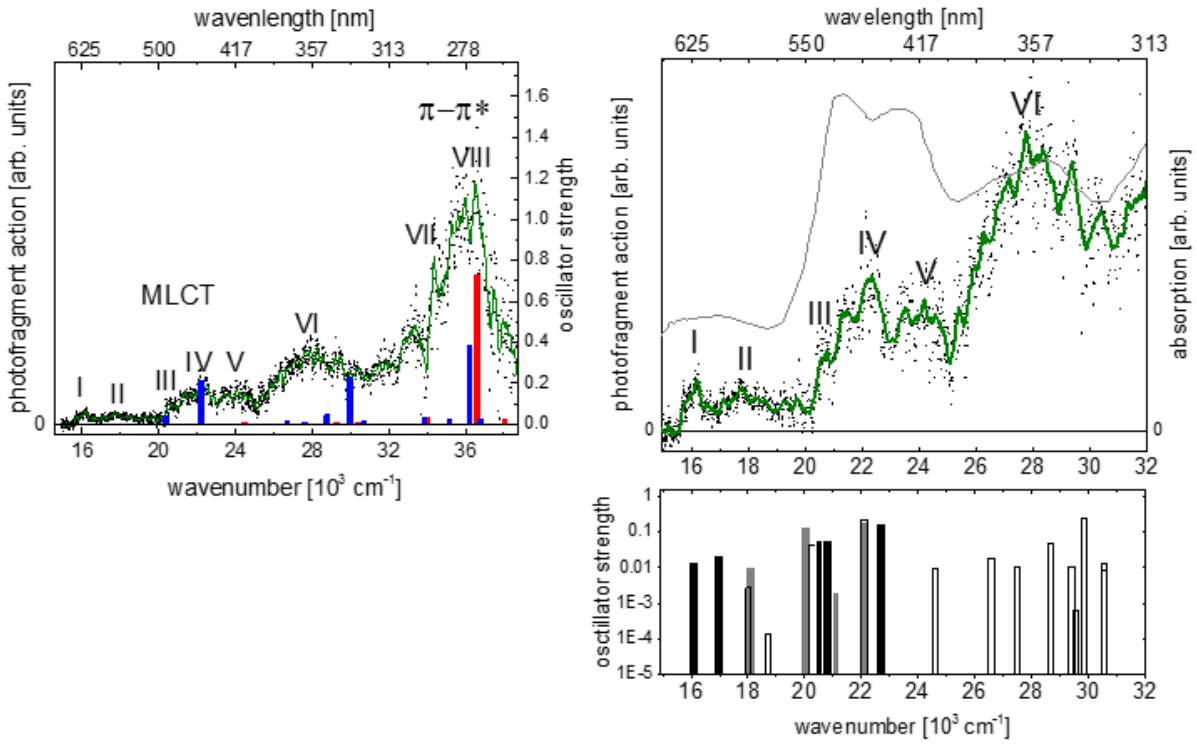

Figure 4.9 Left: Photodissociation action spectrum of $[Os(bpy)_3]^{2+}\cdot N_2$ at 25 K trap temperature with TDDFT calculation using B3LYP/def2-tzvp (unshifted). The data points in the photodissociation spectrum are raw data; the full line is 40-point sliding average. Right: Zoom into the MLCT band (gray points and green line) and comparison with the absorption spectrum (gray line) in acetonitrile solution measured by Shaw *et al.*[61] (upper panel) and calculated spectra (lower panel, full columns: Ronca *et al.*[62]; open columns: this work). The gray columns represent singlet transitions and the black are transitions to the triplet manifold, enabled by spin-orbit coupling. Note the logarithmic scale for the oscillator strength.

We compare our experimental results with our own TDDFT calculations and with computational work including spin-orbit coupling by Ronca *et al.*[62] Our calculation of singlet transitions reproduces several strong transitions but again fails to account for spectral features observed in the lower energy range. The calculations by Ronca *et al.*[62] corroborate our calculations for singlet transitions, but predict more states in the low energy region, which can be assigned to experimental features. Tentative assignments using the same strategy as employed for $[Ru(bpy)_3]^{2+}$ are given in **Table 4.7**.

Table 4.6 Transition energies and oscillator strengths for selected calculated excited states of $[Os(bpy)_3]^{2+}$ (TDDFT with[62] and without spin-orbit interaction) compared to experimentally observed features. Solvatochromic shifts are calculated only for discernible features in both aqueous solution and gas phase spectra.

computational					experimental (this work)	
		state[a]	energy [cm^{-1}]	oscillator strengths	energy [cm^{-1}]	feature[b]
Ronca *et al.* [a]	singlet excitations	**S_1: $1A_2$**	**18083**	**$1.0\cdot10^{-2}$**	17740	II
		$S_{2,3}$: 1E	19373	0		
		$S_{4,5}$: 2E	**20043**	**$1.38\cdot10^{-1}$**	20700	III
		S_6: $2A_2$	21019	$2\cdot10^{-3}$		
		$S_{7,8}$: 3E	**22108**	**$2.06\cdot10^{-1}$**	22310	IV
	spin-orbit coupling	**$ST_{2,3}$: 1E**	**16091**	**$1.5\cdot10^{-2}$**	16140	I
		$ST_{8,9}$: 3E	16962	$2.1\cdot10^{-2}$		
		$ST_{22,23}$: 8E	20527	$6.0\cdot10^{-2}$		
		$ST_{25,26}$: 9E	20785	$5.8\cdot10^{-2}$		
		$ST_{34,35}$: 12E	22672	$1.7\cdot10^{-1}$		
this work - singlet excitations		$1A_2$	18015	$2.7\cdot10^{-3}$	17740	II
		2E	20268	$4.2\cdot10^{-2}$	20700	III
		3E	22094	$2.1\cdot10^{-1}$	22310	IV
		$3A_2$	24610	$9.3\cdot10^{-3}$	24160	V
		8E	29838	$2.3\cdot10^{-1}$	27890	VI
		12E	36110	$3.8\cdot10^{-1}$	36530	VIII
		$7A_2$	36709	$7.3\cdot10^{-1}$		

[a] The state designation follows that given in Ref.[62] Calculated values shown in bold are assigned to the corresponding experimentally observed features.

[b] See **Figure 4.9**.

Spin-orbit coupling is stronger in atoms with higher nuclear charge, such as Os, leading to ultrafast decay channel of singlet excited states into the triplet manifold. As a result, the lifetime of excited states in Os complexes is presumably shorter,[5] which also broadens the spectrum. The

absorption spectrum by Shaw *et al.*[61] was measured in acetonitrile solution and in the visible range. The solvatochromic shift can be determined only for features III-V in our spectrum, and its magnitude is about 930 cm^{-1}.

4.4 Summary

All $[M^{II}(bpy)_3]^{2+}$ species in this study show broad absorption profiles in the UV region from 29000 to 37900 cm^{-1}. The spectra contain multiple π-π* transitions on the bpy ligands in this spectral range. In solution spectra,[37] most $[M^{II}(bpy)_3]^{2+}$ species exhibit only a broad double-peak feature in the UV. Here, we are able to resolve some of the substructures that underlie this feature. The spectra for M = Co, Ni, Zn are very similar, with some variation in the overall width of observed features and with small differences in their absolute positions. The spectra of other species show only a single broad, largely unstructured band. Results from TDDFT calculations are in qualitative agreement with the experimental spectra. The most intense UV transition for each species with D_3 symmetry is of A_2 symmetry, one branch of the π-π* transitions. For most species, the calculated excitation energies are higher than experimental values, which is not unexpected, since the calculations yield vertical excitation energies.

The species containing d^6 metals (M = Fe, Ru, Os) show bright and broad transitions in the visible, which are characterized as MLCT bands. The band energies follow the order Fe > Ru > Os, consistent with our TDDFT calculations. While TDDFT calculations without spin-orbit interaction qualitatively recover the overall spectral profiles, it is necessary to incorporate spin-orbit interaction to interpret the smaller features observed on the low-energy onset of the spectra, at least for M = Ru and Os. Computational work by Heully *et al.*[59] and Ronca *et al.*[62] provides a much

better description of the electronic structures of $[Ru(bpy)_3]^{2+}$ and $[Os(bpy)_3]^{2+}$ in the low energy region.

Since we have only the spectrum in the UV region for all the $[M^{II}(bpy)_3]^{2+}$ species in this work, we summarize the spectral behavior from both experiment and theory in **Table 4.7** only for the π-π* bands.

Table 4.7 Experimental and calculated band positions and other characteristics for complexes with D_3 symmetry.

M	dominant transitions (experimental) [cm^{-1}]		A_2-E splitting in dominant bands [cm^{-1}]		shift of TDDFT [cm^{-1}]	solvatochromic shift of the A_2 peak [b] [cm^{-1}]
	A_2	E	experimental	calculated		
Mn	34350 [a]		-	411	-2420	-
Fe	34360	33880	480	903	-2420	-910
Co	33470	33150	320	347	-2420	-680
Ni	33150	-	-	428	-2820	-680
Zn	33230	32910	320	532	-2980	-660
Ru	36100 [a]		-	717	+800	-1320
Os	36530 [a]		-	599	0	-

[a] The spectrum is broad and the A_2/E transitions cannot be discriminated. The number is the peak location in this case.

[b] shift for aqueous solution[37] relative to values *in vacuo*.

Previous studies have attempted to describe the physical and chemical properties of the complexes as a function of the metal and to form trends along the periodic table. In the past, absorption wavelength has been used as a parameter to describe the interaction strength between the metal and the ligand, based on the argument that stronger interaction leads to a greater shift of the absorption wavelength of the ligand upon chelation.[63,64] For instance, the bathochromic shift of the UV band of the bpy ligand has been used for attempts to describe the

$[M^{II}(bpy)_3]^{2+}$ series along these lines. Modern quantum chemistry methods allow us better describe this interaction and its results, such as geometric parameters and charge distribution. The results of our DFT calculations have been summarized in **Table 4.3**. We cannot observe any simple correlation between these physical properties and our spectroscopy data, or find a simple trend that would reflect the empirical order of stability established by Irving and Williams[65]. The experimental spectra in this work show new spectroscopic details and our results can be used to benchmark existing computational methods and to provide solid assignments of many of the bands observed in $[M(bpy)_3]^{2+}$ complex ions. The observation of Franck-Condon envelopes in many of the complexes studied here highlights the power of cryogenic ion spectroscopy *in vacuo* for the study of metal-organic complexes.

4.5 Appendix

Table 4.8 Calculated energies (E) and oscillator strengths (f) of some of the intense electronic transitions of $[Mn(bpy)_3]^{2+}$ in the region of our spectrum. Only orbitals with contribution greater than 10% are shown (see **Figure 4.10**).

Transition	E [cm^{-1}] / f [10^{-2}]	orbitals
10E	34200 / 15.6	$24a_1$ β → 44e β (27.6%) 44e α → 46e α (20.8%) 43e β → 44e β (17.8%) $25a_1$ α → 46e α (14.4%)
$5A_2$	34440 / 19.1	43e β → 44e β (43.2%) 44e α → 46e α (31.7%) $24a_1$ β → $23a_2$ β (13.5%)
16E	35730 / 13.5	43e β → $23a_2$ β (62.0%) 44e α → $23a_2$ α (31.7%)
$9A_2$	36130 / 32.1	$24a_1$ β → $23a_2$ β (59.1%) $25a_1$ α → $23a_2$ α (27.1%)
20E	40000 / 5.6	44e α → $24a_2$ α (20.2%) 43e α → $23a_2$ α (18.3%) 43e β → $24a_2$ β (16.2%)
$11A_2$	40250 / 7.8	$25a_1$ α → $24a_2$ α (36.8%) $24a_1$ β → $24a_2$ β (32.4%)

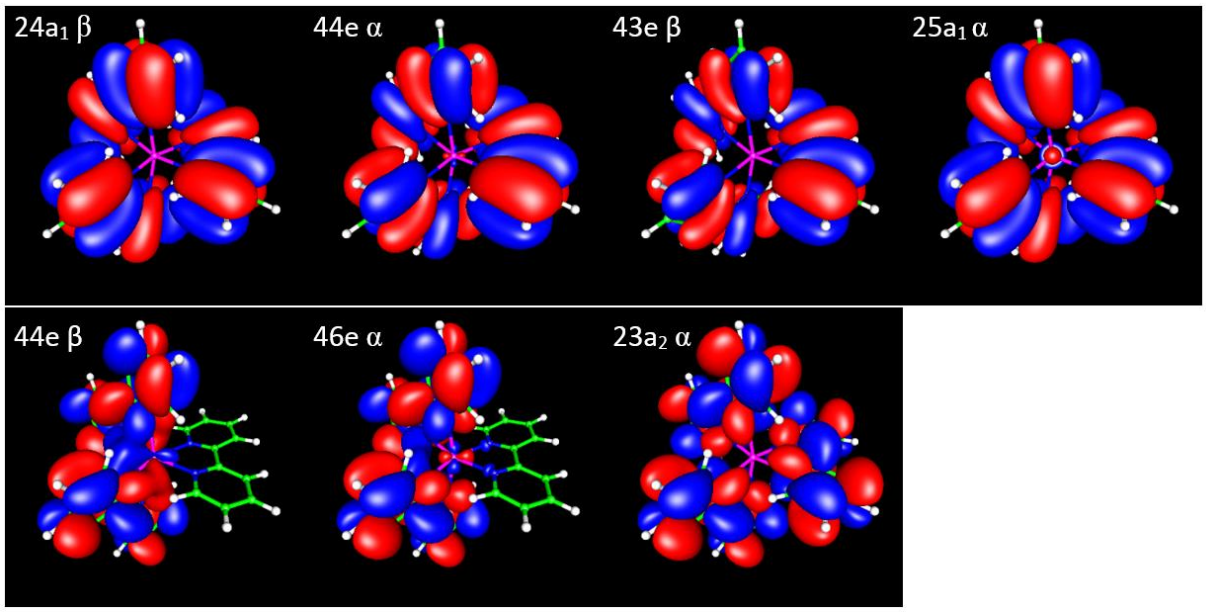

Figure 4.10 Molecular orbitals of $[Mn(bpy)_3]^{2+}$ involved in the transitions listed in **Table 4.8**.

Table 4.9 Calculated (B3LYP/def2-tzvp) energies (E) and oscillator strengths (f) of some of the intense electronic transitions of $[Fe(bpy)_3]^{2+}$ in the region of our spectrum. Only orbitals with contribution greater than 10% are shown (see **Figure 4.11**).

Transition	E [cm^{-1}] / f [10^{-2}]	orbitals
11E	34037 / 8.2	44e → 47e (78.9%)
14E	35811 / 35.6	$24a_1$ → 45e (28.8%) 43e → $23a_2$ (27.3%) 44e → 47e (13.5%) 43e → 45e (13.4%)
$8A_2$	36779 / 64.1	$24a_1$ → $23a_2$ (40.6%) 43e → 45e (28.0%) 44e → 47e (18.7%)

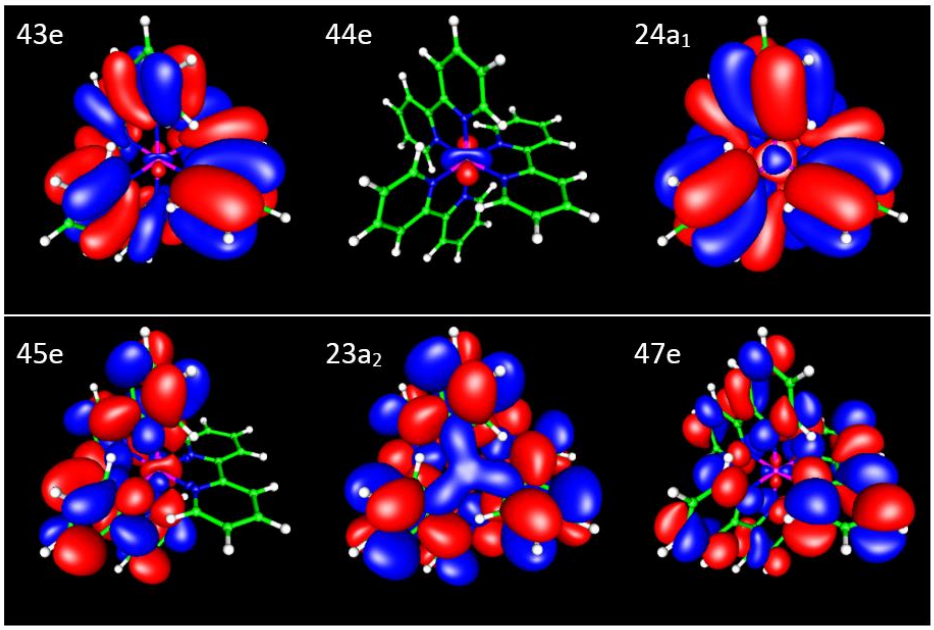

Figure 4.11 Molecular orbitals of $[Fe(bpy)_3]^{2+}$ involved in the transitions listed in **Table 4.9**.

Table 4.10 Calculated energies (E) and oscillator strengths (f) of some of the intense electronic transitions of $[Co(bpy)_3]^{2+}$ in the region of our spectrum. Only orbitals with contribution greater than 10% are shown (see **Figure 4.12**).

Transition	E [cm^{-1}] / f [10^{-2}]	orbitals
12E	34521 / 5.1	43e β → 45e β (45.4%) 44e β → 45e β (22.9%) 25a_1 α → 46e α (15.1%)
13E	34601 / 9.8	24a_1 β → 45e β (60.4%) 25a_1 α → 46e α (19.5%) 44e α → 46e α (11.4%)
$6A_2$	34763 / 13.9	44e α → 46e (41.8%) 43e β → 45e β (28.7%) 44e β → 45e β (11.4%)
16E	35569 / 18.3	43e β → 23a_2 β (38.9%) 44e α → 23a_2 α (32.5%) 44e β → 23a_2 β (16.4%)
$9A_2$	35972 / 34.4	24a_1 β → 23a_2 β (48.4%) 25a_1 α → 23a_2 α (31.9%)

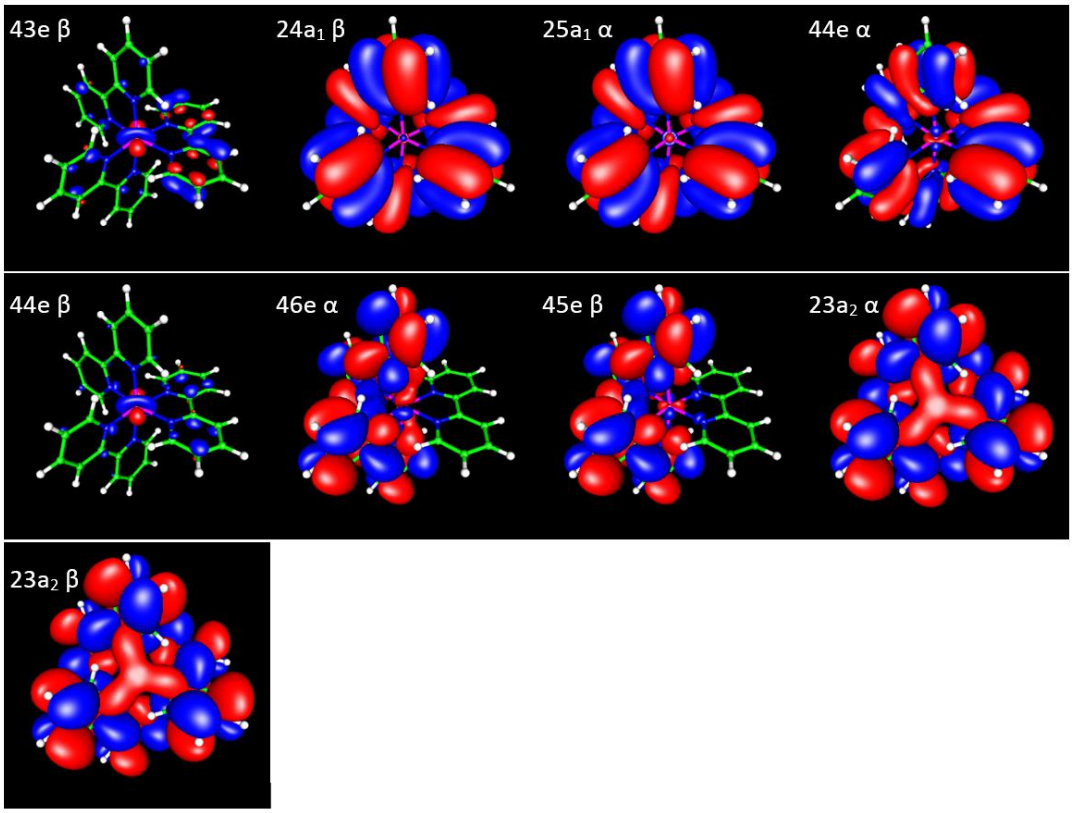

Figure 4.12 Molecular orbitals of $[Co(bpy)_3]^{2+}$ involved in the transitions listed in **Table 4.10**.

Table 4.11 Calculated energies (E) and oscillator strengths (f) of some of the intense electronic transitions of $[Ni(bpy)_3]^{2+}$ in the region of our spectrum. Only orbitals with contribution greater than 10% are shown (see **Figure 4.13**).

Transition	E [cm^{-1}] / f [10^{-2}]	orbitals
8E	34309 / 3.7	44e α → 46e α (63.9%) $25a_1$ α → 46e α (14.3%)
10E	34524 / 6.9	$25a_1$ β → 45e β (45.6%) $25a_1$ α → 46e α (42.4%)
$5A_2$	34635 / 13.7	44e β → 45e β (40.5%) 44e α → 46e α (40.0%)
14E	35515 / 17.1	44e β → $23a_2$ β (56.8%) 44e α → $23a_2$ α (29.4%)
$8A_2$	35985 / 37.5	$25a_1$ β → $23a_2$ β (43.5%) $25a_1$ α → $23a_2$ α (35.4%)

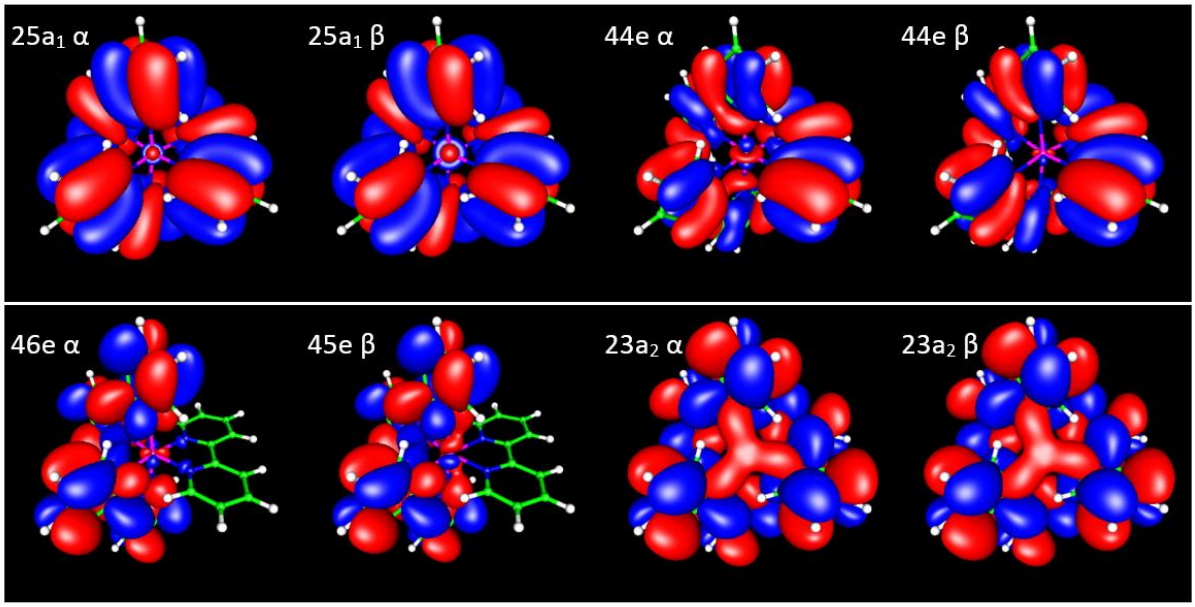

Figure 4.13 Molecular orbitals of $[Ni(bpy)_3]^{2+}$ involved in the transitions listed in **Table 4.11**.

Table 4.12 Calculated energies (E) and oscillator strengths (f) of some of the intense electronic transitions of $[Cu(bpy)_3]^{2+}$ in the region of our spectrum. Only orbitals with contribution greater than 10% are shown (see **Figure 4.14**).

Transition	E [cm^{-1}] / f [10^{-2}]	orbitals
18B	34037 / 8.1	66b α → 71a α (34.1%) 66b β → 71a β (29.0%) 59b β → 70a β (12.0%)
22A	35004 / 14.7	66b β → 68b β (26.3%) 64a β → 70a β (17.2%) 69a α → 71a α (11.5%) 66a α → 68b α (11.3%)
25B	35730 / 7.4	62b β → 70a β (17.7%) 58b β → 70a β (13.4%) 61b β → 70a β (10.8%)
27B	36134 / 23.5	69a β → 69b β (37.9%) 70a α → 69b α (33.1%)
30B	37102 / 10.8	60b β → 70a β (46.2%)
31B	37182 / 9.7	59b β → 70a β (31.6%) 60b β → 70a β (30.5%)
34B	37989 / 10.6	68a β → 69b β (67.2%) 69a α → 69b α (17.1%)

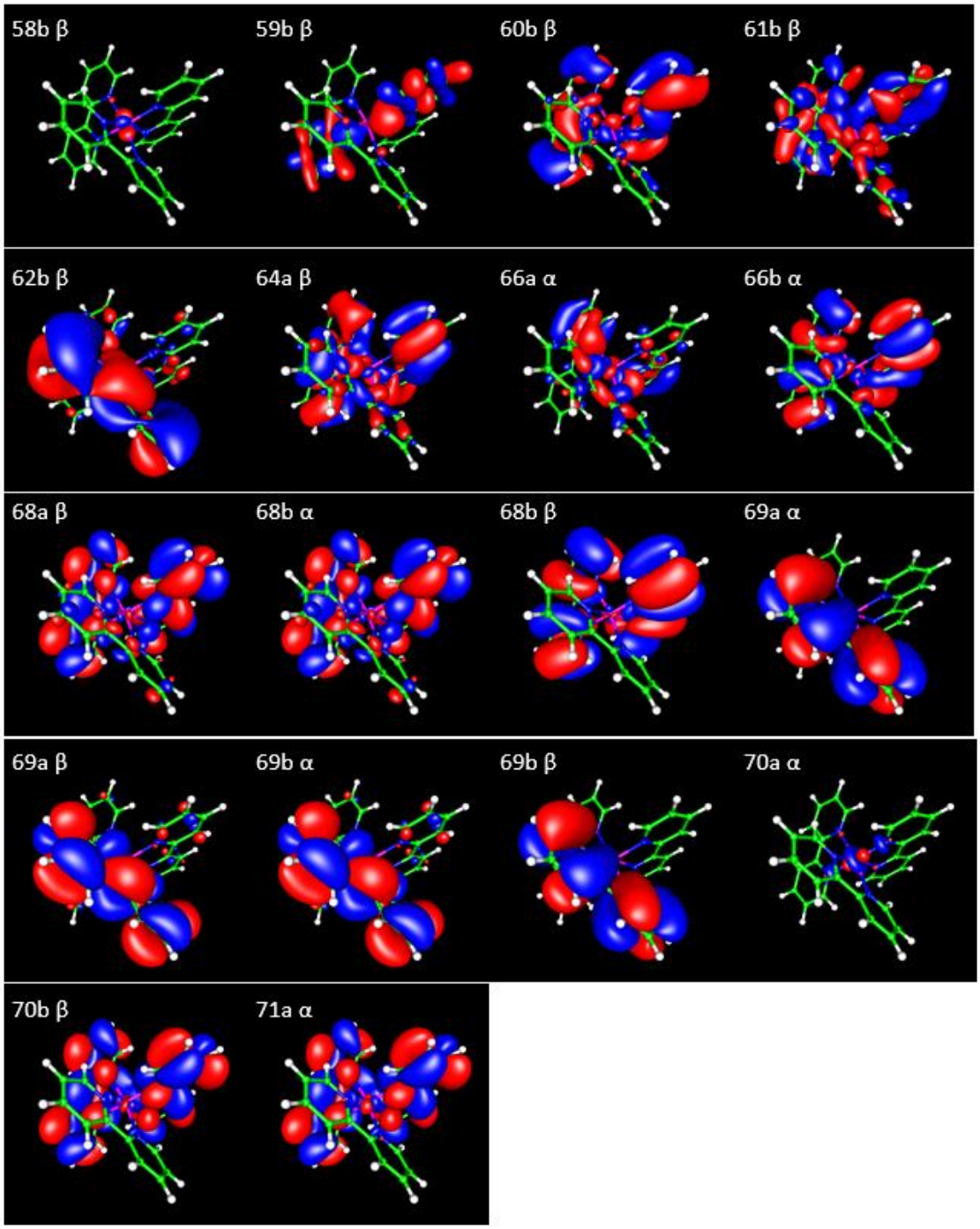

Figure 4.14 Molecular orbitals of $[Cu(bpy)_3]^{2+}$ involved in the transitions listed in **Table 4.12**.

Table 4.13 Calculated energies (E) and oscillator strengths (f) of some of the intense electronic transitions of $[Zn(bpy)_3]^{2+}$ in the region of our spectrum. Only orbitals with contribution greater than 10% are shown (see **Figure 4.15**).

Transition	E [cm^{-1}] / f [10^{-2}]	orbitals
1E	34521 / 7.6	45e → 46e (94.7%)
2E	34763 / 9.3	$25a_1$ → 46e (93.3%)
$1A_2$	34843 / 18.2	45e → 46e (85.2%) $25a_1$ → $23a_2$ (11.1%)
3E	35650 / 15.3	45e → $23a_2$ (91.3%)
$2A_2$	36214 / 35.3	$25a_1$ → $23a_2$ (83.1%) 45e → 46e (7.1%)

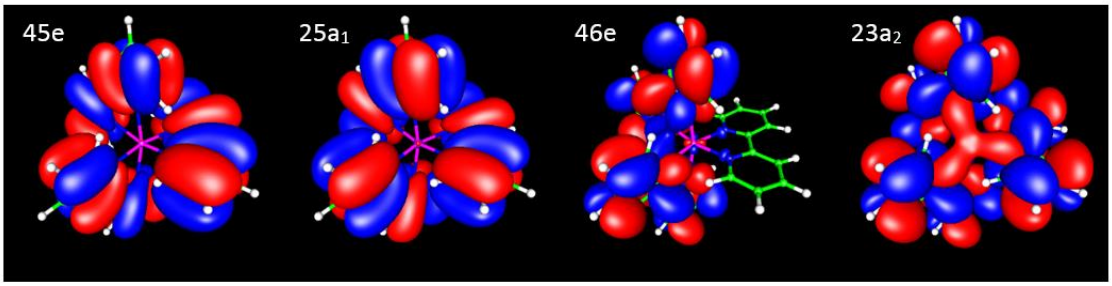

Figure 4.15 Molecular orbitals of $[Zn(bpy)_3]^{2+}$ involved in the transitions listed in **Table 4.13**.

Table 4.14 Calculated (B3LYP/ecp-10-mdf) energies (E) and oscillator strengths (f) of some of the intense electronic transitions of $[Fe(bpy)_3]^{2+}$ in the region of our spectrum. Only orbitals with contribution greater than 10% are shown (see **Figure 4.16**)

Transition	E [cm^{-1}] / f [10^{-2}]	orbitals
1E	17885 / 0.03	$23a_1 \rightarrow 47e$ (52.3%) $43\ e \rightarrow 47e$ (39.4%)
$1A_2$	18585 / 0.007	$43\ e \rightarrow 47e$ (93.3%)
3E	24548 / 4.0	$43e \rightarrow 44e$ (70.0%) $23a_1 \rightarrow 44e$ (18.2%)
4E	25792 / 7.3	$43e \rightarrow 22a_2$ (96.1%)
6E	31143 / 1.6	$43e \rightarrow 23a_2$ (98.3%)
13E	35053 / 19.1	$43e \rightarrow 46e$ (53.0%) $23a_1 \rightarrow 46e$ (14.8%)
14E	36181 / 27.7	$43e \rightarrow 46e$ (35.9%) $42e \rightarrow 22a_2$ (20.1%) $22a_1 \rightarrow 44e$ (17.7%)
$8A_2$	37045 / 58.2	$43e \rightarrow 46e$ (33.1%) $22a_1 \rightarrow 22a_2$ (31.8%) $42e \rightarrow 44e$ (22.6%)

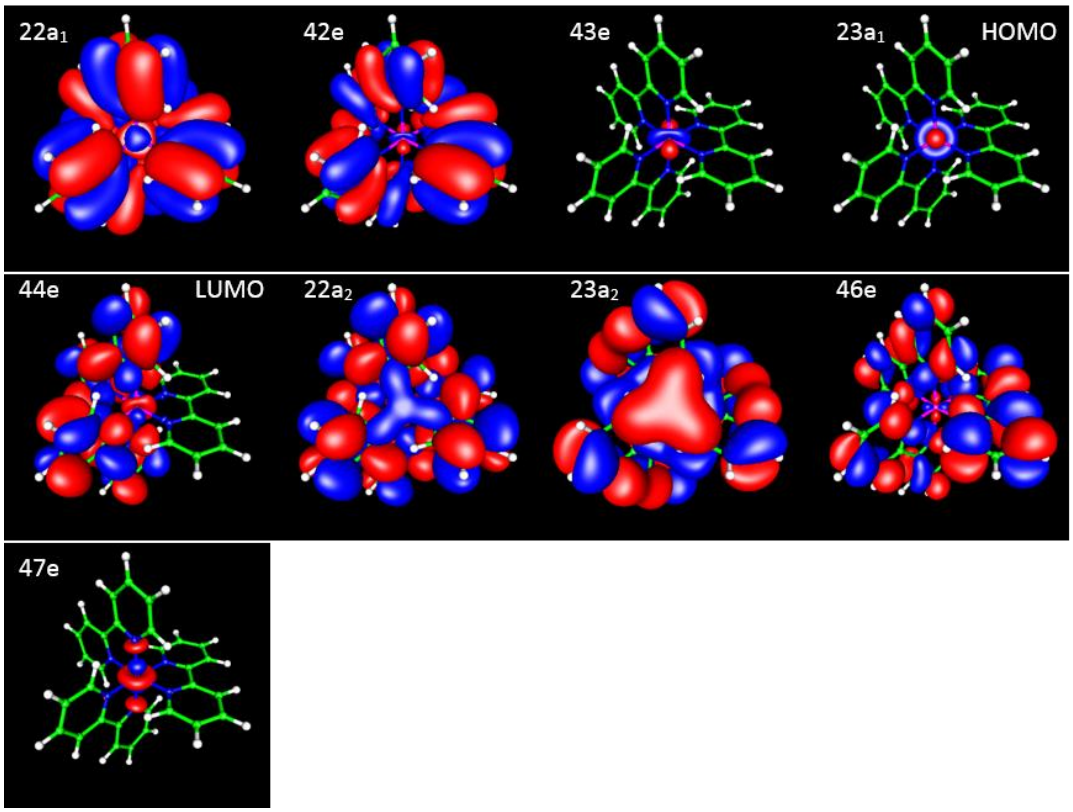

Figure 4.16 Molecular orbitals of $[Fe(bpy)_3]^{2+}$ involved in the transitions listed in **Table 4.14**.

Table 4.15 Calculated energies (E) and oscillator strengths (f) of some of the intense electronic transitions of $[Ru(bpy)_3]^{2+}$ in the region of our spectrum. Only orbitals with contribution greater than 10% are shown (see **Figure 4.17**).

Transition	E [cm^{-1}] / f [10^{-2}]	orbitals
$1A_2$	20850 / 0.12	$23a_1 \rightarrow 22a_2$ (99.3%)
1E	20883 / 0.01	$23a_1 \rightarrow 44e$ (97.9%)
2E	22429 / 1.7	$43e \rightarrow 22a_2$ (77.5%) $43e \rightarrow 44e$ (21.5%)
3E	23507 / 20	$43e \rightarrow 44e$ (76.0%) $43e \rightarrow 22a_2$ (21.6%)
4E	28516 / 2	$43e \rightarrow 23a_2$ (98.5%)
6E	30799 / 0.4	$23a_1 \rightarrow 48e$ (28.8%) $23a_1 \rightarrow 47e$ (20.7%) $43e \rightarrow 45e$ (18.4%) $43e \rightarrow 48e$ (14.2%) $43e \rightarrow 47e$ (10.0%)
9E	31659 / 15	$43e \rightarrow 45e$ (46.4%) $23a_1 \rightarrow 46e$ (20.2%) $43e \rightarrow 24a_1$ (17.2%)
14E	36066 / 42	$22a_1 \rightarrow 44e$ (44.1%) $42e \rightarrow 44e$ (23.6%)
$8A_2$	36783 / 76	$42e \rightarrow 44e$ (52.0%) $22a_1 \rightarrow 22a_2$ (21.4%) $43e \rightarrow 46e$ (10.2%)

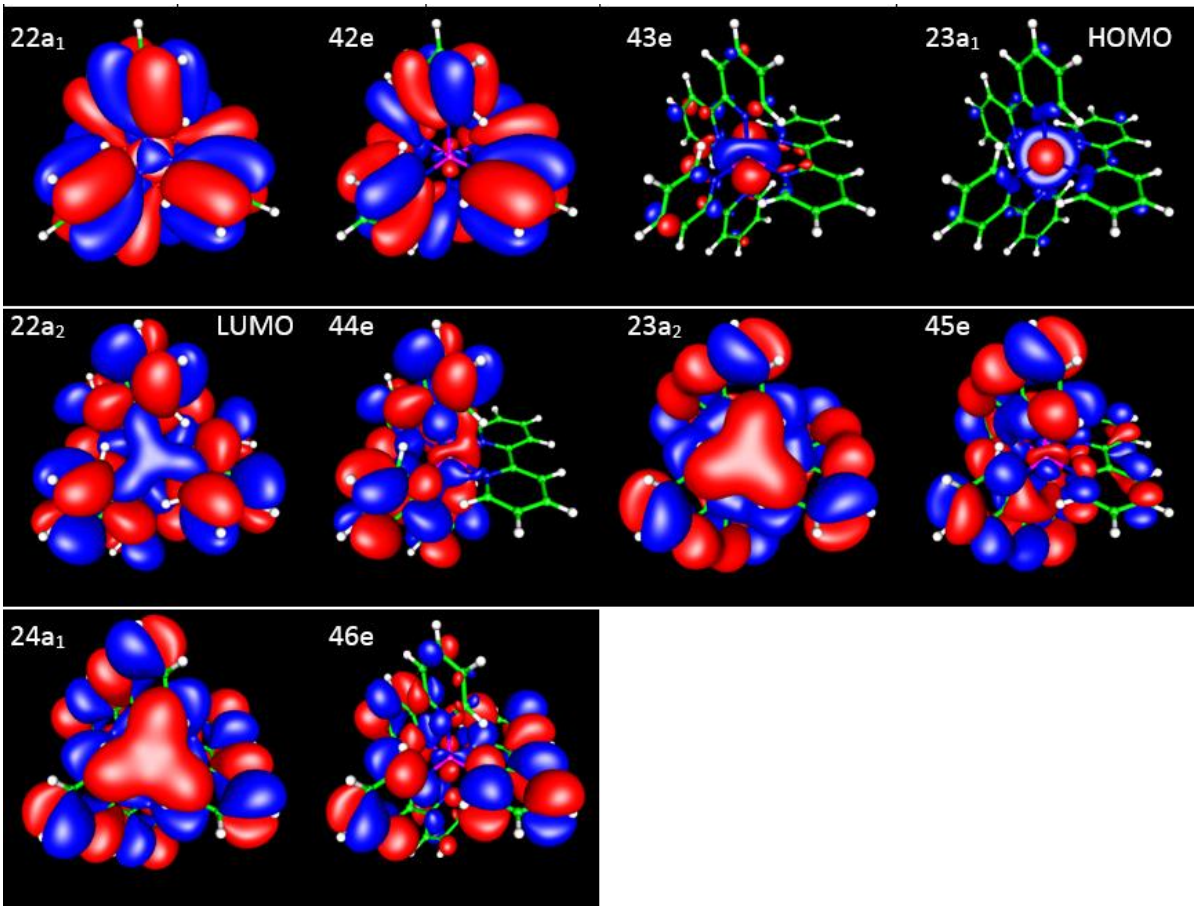

Figure 4.17 Molecular orbitals of $[Ru(bpy)_3]^{2+}$ involved in the transitions listed in **Table 4.15**.

Table 4.16 Calculated energies (E) and oscillator strengths (f) of some of the intense electronic transitions of $[Os(bpy)_3]^{2+}$ in the region of our spectrum. Only orbitals with contribution greater than 10% are shown (see **Figure 4.18**).

Transition	E [cm^{-1}] / f [10^{-2}]	orbitals
$1A_2$	18015 / 0.27	$23a_1 \rightarrow 22a_2$ (99.5%)
1E	18708 / 0.01	$23a_1 \rightarrow 44e$ (98.3%)
2E	20268 / 4.2	$43e \rightarrow 22a_2$ (85.7%) $43e \rightarrow 44e$ (13.5%)
3E	22094 / 21.2	$43e \rightarrow 44e$ (83.9%) $43e \rightarrow 22a_2$ (13.0%)
4E	26579 / 1.8	$43e \rightarrow 23a_2$ (97.2%)
6E	28654 / 4.7	$23a_1 \rightarrow 46e$ (81.2%) $43e \rightarrow 24a_1$ (9.3%)
8E	29838 / 22.7	$43e \rightarrow 45e$ (44.2%) $43e \rightarrow 24a_1$ (36.2%) $23a_1 \rightarrow 46e$ (14.1%)
12E	36110 / 38.2	$22a_1 \rightarrow 44e$ (49.9%) $42e \rightarrow 44e$ (26.4%)
$7A_2$	36709/ 73.2	$42e \rightarrow 44e$ (65.3%) $22a_1 \rightarrow 22a_2$ (13.1%)

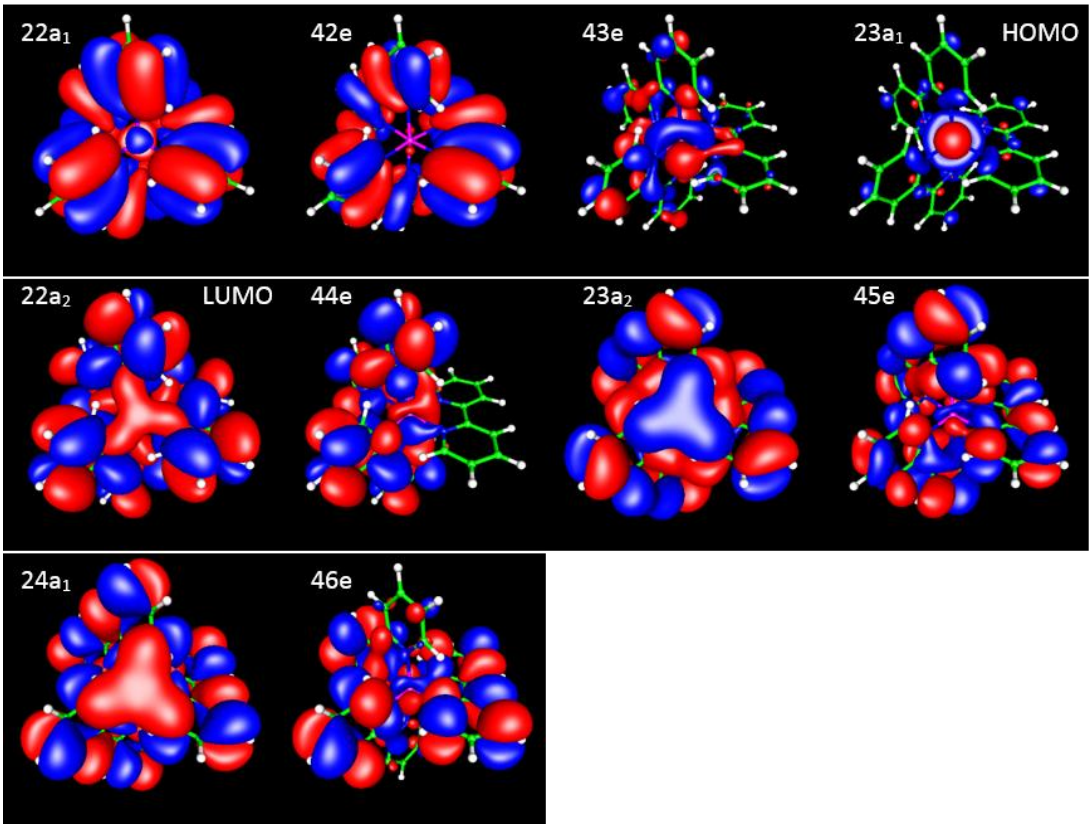

Figure 4.18 Molecular orbitals of $[Os(bpy)_3]^{2+}$ involved in the transitions listed in **Table 4.16**.

4.6 References

1. Xu, S., Smith, J. E. T. & Weber, J. M. The electronic spectrum of cryogenic ruthenium-tris-bipyridine dications in vacuo. *J. Chem. Phys.* **145,** 024034 (2016).

2. McWhinnie, W. R. & Miller, J. D. The chemistry of complexes containing 2,2'-bipyridyl, 1,10-phenanthroline, or 2,2',6',2"-terpyridyl as ligands. *Adv. Inorg. Radiochem.* **12,** 135–215 (1970).

3. Constable, E. C. Homoleptic complexes of 2,2'-bipyridine. *Adv. Inorg. Chem.* **34,** 1–63 (1989).

4. Krausz, E. & Riesen, H. Developement in laser selective spectroscopy and photophysis of d^6 metal-(di-imine) complexes. *Coord. Chem. Rev.* **159,** 9–40 (1997).

5. Kober, E. M. & Meyer, T. J. Concerning the absorption spectra of the ions $M(bpy)_3^{2+}$ (M = Fe, Ru, Os; bpy = 2,2'-bipyridine). *Inorg. Chem.* **21,** 3967–3977 (1982).

6. Decurtins, S., Felix, F., Fergusson, J. E., Güdel, H. U. & Ludi, A. The electronic spectrum of $Fe(bpy)_3^{2+}$ and $Os(bpy)_3^{2+}$. *J. Am. Chem. Soc.* **102,** 4102–4106 (1980).

7. Felix, F., Fergusson, J. E., Güdel, H. U. & Ludi, A. Electronic spectra of $M(bipy)_3^{2+}$ complex ions (M = Fe, Ru and Os). *Chem. Phys. Lett.* **62,** 153–157 (1979).

8. Lay, P. A. & Sasse, W. H. F. Mechanism of the water-mediated reduction of tris(2,2'-bipyridine-N,N')iron(III), -ruthenium(III), and -osmium(III) complexes. *Inorg. Chem.* **24,** 4707–4710 (1985).

9. Ohsawa, Y., DeArmond, M. K., Hanck, K. W. & Moreland, C. G. A ^1H NMR study of reduced paramagnetic tris(2,2'-bipyridine) complexes of iron(II), ruthenium (II), and osmium(II). *J. Am. Chem. Soc.* **107,** 5383–5386 (1985).

10. Zakeeruddin, S. M., Fraser, D. M., Nazeeruddin, M. K. & Grätzel, M. Towards mediator design: Characterization of tris-(4,4'-substituted-2,2'-bipyridine) complexes of iron(II), ruthenium(II) and osmium(II) as mediators for glucose oxidase of Aspergillus niger and other redox proteins. *J. Electroanal. Chem.* **337,** 253–283 (1992).

11. McCaffery, A. J., Mason, S. F. & Norman, B. J. Optical rotatory power of co-ordination compounds. Part XII. Spectroscopic and configurational assignments for the tris-bipyridyl and -phenanthroline complexes of the di- and tri-valent iron-group metal ions. *J. Chem. Soc. A* 1428–1441 (1969).

12. Mason, S. F. The electronic spectra and optical activity of phenanthroline and dipyridyl metal complexes. *Inorganica Chim. Acta Rev.* **2,** 89–109 (1968).

13. Felix, F., Fergusson, J. E., Güdel, H. U. & Ludi, A. The electronic spectrum of $Ru(bpy)_3^{2+}$. *J. Am. Chem. Soc.* **102,** 4096–4102 (1980).

14. Damrauer, N. H. *et al.* Femtosecond dynamics of excited-state evolution in $[Ru(bpy)_3]^{2+}$. *Science* **275,** 54–57 (1997).

15. Kirketerp, M.-B. S. & Nielsen, S. B. Absorption spectrum of isolated tris(2,2'-bipyridine)ruthenium(II) dications in vacuo. *Int. J. Mass Spectrom.* **297,** 63–66 (2010).

16. Demas, J. N. & Adamson, A. W. A New photosensitizer. Tris(2,2'-bipyridine)ruthenium(II) chloride. *J. Am. Chem. Soc.* **93,** 1800–1801 (1971).

17. Daul, C., Baerends, E. J. & Vernooijs, P. A Density functional study of the MLCT states of $[Ru(bpy)_3]^{2+}$ in D_3 symmetry. *Inorg. Chem.* **33,** 3538–3543 (1994).

18. Lytle, F. E. & Hercules, D. M. The Luminescence of tri(2,2'-bipyridine)ruthenium(II) dichloride. *J. Am. Chem. Soc.* **587,** 253–257 (1969).

19. Yeh, A. T., Shank, C. V & McCusker, J. K. Dynamics following photo-induced charge transfer. *Science* **289,** 935–938 (2000).

20. Durham, B., Caspar, J. V, Nagle, J. K. & Meyer, T. J. Photochemistry of $Ru(bpy)_3^{2+}$. *J. Am. Chem. Soc.* **104,** 4803–4810 (1982).

21. Caspar, J. V. & Meyer, T. J. Photochemistry of $Ru(bpy)_3^{2+}$. Solvent effects. *J. Am. Chem. Soc.* **105,** 5583–5590 (1983).

22. Bhasikuttan, A. C., Suzuki, M., Nakashima, S. & Okada, T. Ultrafast fluorescence detection in tris (2,2'-bipyridine)ruthenium(II) complex in solution: relaxation dynamics involving higher excited states. *J. Am. Chem. Soc.* **124,** 8398–8405 (2002).

23. Balzani, V., Juris, A., Ciamician, C. G. & Bologna, I. Photochemistry and photophysics of Ru(II) polypyridine complexes in the Bologna group. From early studies to recent developments. *Coord. Chem. Rev.* **211,** 97–115 (2001).

24. Auböck, G. & Chergui, M. Sub-50-fs photoinduced spin crossover in $[Fe(bpy)_3]^{2+}$. *Nat. Chem.* **7,** 629–633 (2015).

25. Carter, M. T., Rodriguez, M. & Bard, A. J. Voltammetric studies of the interaction of metal chelates with DNA. 2. Tris-chelated complexes of cobalt(III) and iron(II) with 1,10-phenanthroline and 2,2'-bipyridine. *J. Am. Chem. Soc.* **111,** 8901–8911 (1989).

26. Björemark, P. M., Jönsson, J. & Håkansson, M. Absolute asymmetric synthesis: Viedma ripening of $[Co(bpy)_3]^{2+}$ and solvent-free oxidation to $[Co(bpy)_3]^{3+}$. *Chem. - A Eur. J.* **21,**

10630–10633 (2015).

27. Bozic-Weber, B. *et al.* Copper(I) dye-sensitized solar cells with $[Co(bpy)_3]^{2+/3+}$ electrolyte. *Chem. Commun.* **49,** 7222 (2013).

28. Coronado, E., Galán-Mascarós, J. R., Gómez-García, C. J. & Martínez-Agudo, J. M. Molecule-based magnets formed by bimetallic three-dimensional oxalate networks and chiral tris(bipyridyl) complex cations. The series $[Z^{II}(bpy)_3][ClO_4][M^{II}Cr^{III}(ox)_3]$ (Z^{II} = Ru, Fe, Co, and Ni; M^{II} = Mn, Fe, Co, Ni, Cu, and Zn; ox = oxalate dianion). *Inorg. Chem.* **40,** 113–120 (2001).

29. Fleisher, M. B., Waterman, K. C., Turro, N. J. & Barton, J. K. Light induced cleavage of DNA by metal complexes. *Inorg. Chem.* **25,** 3551–3552 (1986).

30. Baffert, C. *et al.* Photoinduced oxidation of $[Mn(L)_3]^{2+}$ and $[Mn_2O_2(L)_4]^{3+}$ (L = 2,2'-bipyridine and 4,4'-dimethyl-2,2'-bipyridine) with the $[Ru(bpy)_3]^{2+}$/-aryl diazonium salt system. *Phys. Chem. Chem. Phys.* **7,** 202–210 (2005).

31. Wang, M., England, J., Weyhermüller, T. & Wieghardt, K. Molecular and electronic structures of the members of the electron transfer series $[Mn(bpy)_3]^n$ (n=2+, 1+, 0, 1-) and $[Mn(tpy)_2]^m$ (m=4+, 3+, 2+, 1+, 0). An experimental and density functional theory study. *Inorg. Chem.* **53,** 2276–87 (2014).

32. Ohno, T. & Kato, S. Ligand-ligand interaction in $[Zn(1,10\text{-phenanthroline})_2(H_2O)_2](NO_3)_2$ and $[Zn(2,2'\text{-bipyridyl})_3](NO_3)_2$. *Bull. Chem. Soc. Jpn.* **47,** 2953–2957 (1974).

33. Mori, Y., Szalda, D. J., Brundschwig, B. S., Schwarz, H. A. & Fujita, E. Toward the Photoreduction of CO_2 with $Ni(2,2'\text{-bipyridine})_n^{2+}$ complexes. *Photochem. Radiat. Chemsitry* **254,** 279–292 (1998).

34. Palanisami, N., Senthilkumar, K., Gopalakrishnan, M. & Moon, I.-S. A mixed Ni(II) ionic complex containing V-shaped water trimer: Synthesis, spectral, structural and thermal properties of $\{[Ni(2,2'\text{-bpy})_3][Ni(2\text{-cpida})(2,2'\text{ -bpy})]\}\ (ClO_4)\cdot 3H_2O$. *J. Chem. Sci.* **127,** 873–878 (2015).

35. Bray, R. G., Fergusson, J. E. & Hawkins, C. J. Ultraviolet absorption spectra and circular dichroism of divalent metal complexes containing 1,10-phenanthroline and 2,2'-bipyridine. *Aust. J. Chem.* **22,** 2091–2103 (1969).

36. Mason, S. F., Peart, B. J. & Waddell, R. E. Optical rotatory power of co-ordination compounds. Part XVI. Intermediate exciton coupling in the circular dichroism of trisbipyridyl complexes. *J. Chem. Soc. Dalt. Trans.* 944–949 (1973).

37. Yamasaki, K. Absorptionsspektren von Metallkomplexsalzen des 2,2'-Dipyridyls. I. *Bull. Chem. Soc. Jpn.* **12,** 390–394 (1937).

38. Schläfer, H. L. Über die UV-Absorptionsspektren von Komplexionen mit π-Elektronensystemen als Liganden. *Zeitschrift fur Anorg. und Allg. Chemie* **8,** 373–386 (1956).

39. Palmer, R. A. & Piper, T. S. 2,2'-Bipyridine Complexes. I. Polarized crystal spectra of tris(2,2' -bipyridine)copper(II), -nickel(II), -cobalt(II), iron(II), and -ruthenium(II). *Inorg. Chem.* **5,** 864–878 (1966).

40. Fergusson, J. E., Hawkins, C. J., Kane-Maguire, L. A. P. & Lip, H. Absolute configurations of 1,10-phenanthroline and 2,2'-bipyridine metal complexes. *Inorg. Chem.* **8,** 771–779 (1969).

41. Mason, S. F. & Norman, B. J. Exciton splittings in the ligand ultraviolet bands of coordination complexes. *Chem. Phys. Lett.* **2,** 22–24 (1968).

42. Orgel, L. E. 715. Double bonding in chelated metal complexes. *J. Chem. Soc.* 3683–3686 (1961).

43. Perrin, M. H. & Gouterman, M. Vibronic coupling. IV. Trimers and trigonal molecules. *J. Chem. Phys.* **46,** 1019 (1967).

44. Creutz, C., Chou, M., Netzel, T. L., Okumura, M. & Sutin, N. Lifetimes, spectra, and quenching of the excited states of polypyridine complexes of iron(II), ruthenium(II), and osmium(II). *J. Am. Chem. Soc.* **102,** 1309–1319 (1980).

45. Parr, R. G. & Yang, W. *Density-Functional Theory of Atoms and Molecules*. *Oxford University Press: New York* (1989).

46. Weigend, F. & Ahlrichs, R. Balanced basis sets of split valence, triple zeta valence and quadruple zeta valence quality for H to Rn: Design and assessment of accuracy. *Phys. Chem. Chem. Phys.* **7,** 3297–3305 (2005).

47. Lee, C., Yang, W. & Parr, R. G. Development of the Colle-Salvetti correlation-energy formula into a functional of the electron density. *Phys. Rev. B* **37,** 785–789 (1988).

48. Becke, A. D. Density-functional exchange-energy approximation with correct asymptotic behavior. *Phys. Rev. A* **38,** 3098–3100 (1988).

49. Furche, F. On the density matrix based approach to time-dependent density functional response theory. *J. Chem. Phys.* **114,** 5982–5992 (2001).

50. Bauernschmitt, R. & Ahlrichs, R. Treatment of electronic excitations within the adiabatic approximation of time dependent density functional theory. *Chem. Phys. Lett.* **256,** 454–464 (1996).

51. Bauernschmitt, R., Häser, M., Treutler, O. & Ahlrichs, R. Calculation of excitation energies within time-dependent density functional theory using auxiliary basis set expansions. *Chem. Phys. Lett.* **264,** 573–578 (1997).

52. Reed, A. E., Weinstock, R. B. & Weinhold, F. Natural population analysis. *J. Chem. Phys.* **83,** 735–746 (1985).

53. Weigend, F., Häser, M., Patzelt, H. & Ahlrichs, R. RI-MP2: optimized auxiliary basis sets and demonstration of efficiency. *Chem. Phys. Lett.* **294,** 143–152 (1998).

54. Ahlrichs, R., Bär, M., Häser, M., Horn, H. & Kölmel, C. Electronic structure calculations on workstation computers: The program system turbomole. *Chem. Phys. Lett.* **162,** 165–169 (1989).

55. Hathaway, B. J., Hodgson, P. G. & Power, P. C. Single-crystal electronic and electron spin resonance spectra of three tris-chelate copper(II) complexes. *Inorg. Chem.* **13,** 2009–2013 (1974).

56. Burstall, F. H. & Nyholm, R. S. Studies in Co-ordination Chemistry. Part XIII. Magnetic moments and bond types of transition-metal complexes. *J. Chem. Soc.* 3570–3579 (1952).

57. Xu, S., Gozem, S., Krylov, A. I., Christopher, C. R. & Weber, J. M. Ligand influence on the electronic spectra of monocationic copper-bipyridine complexes. *Phys. Chem. Chem. Phys.* **17,** 31938–31946 (2015).

58. Juris, A. *et al.* Ru(II) polypyridine complexes: photophysics, photochemistry, eletrochemistry and chemiluminescence. *Coord. Chem. Rev.* **84,** 85–277 (1988).

59. Heully, J.-L., Alary, F. & Boggio-Pasqua, M. Spin-orbit effects on the photophysical properties of $Ru(bpy)_3^{2+}$. *J. Chem. Phys.* **131,** 184308 (2009).

60. Stockett, M. H. & Brøndsted Nielsen, S. Communication: Does a single CH_3CN molecule attached to $Ru(bipy)_3^{2+}$ affect its absorption spectrum? *J. Chem. Phys.* **142,** 171102 (2015).

61. Shaw, G. B., Styers-Barnett, D. D. J., Gannon, E. Z., Granger, J. C. & Papanikolas, J. M. Interligand electron transfer dynamics in $[Os(bpy)_3]^{2+}$: exploring the excited state potential surfaces with femtosecond spectroscopy. *J. Phys. Chem. A* **108,** 4998–5006 (2004).

62. Ronca, E., De Angelis, F. & Fantacci, S. Time-dependent density functional theory modeling of spin–orbit coupling in ruthenium and osmium solar cell sensitizers. *J. Phys. Chem. C* **118,** 17067-17078 (2014).

63. Yamasaki, K. & Sone, K. Stability of complex salts of bivalent metals. *Nature* **166,** 998 (1950).

64. Mellor, D. P. & Maley, L. E. Stability of some metal complexes of histidine. *Nature* **165,** 453 (1950).

65. Irving, H. & Williams, R. J. P. The stability of transition-metal complexes. *J. Chem. Soc.* 3192-3210 (1953).

5 The role of the solvent

This chapter has been reproduced in part with permission from Shuang Xu, James E. T. Smith, J. Mathias Weber, *Hydration of a Binding Site with Restricted Solvent Access – Solvatochromic Shift of the Electronic Spectrum of a Ruthenium Polypyridine Complex, One Molecule at a Time*, The Journal of Physical Chemistry A **2016**, 120 (39), pp.7650–7658. Copyright 2016, American Chemical Society.[1]

5.1 Introduction

While experiments *in vacuo* allow the investigation of intrinsic properties of ions, there is often a lack of connection between isolated systems that are computationally easier to treat and systems in an environment (*e.g.* solutions), where additional chemistry occurs via interaction between solute and solvent. For instance, when studying homogeneous catalysts, even though probing important intermediates in the catalytic cycle *in vacuo* has, undoubtedly, potential for yielding important results, one may still find it difficult to use such information to gauge how electronic modification changes performance in catalysis, because homogeneous catalysts work *in solution* after all, and the effects of solvation may eventually need to be taken into account to properly understand the mechanism. Recent work by Garand and coworkers has shown that solvation of a ruthenium catalyst by a number of water molecules indeed induces oxidation of the *aqua* ligand in the complex.[2] In this sense, the isolated ions may be too simple to address the relevant mechanisms in catalysis. However, solvation effects can be studied in an unprecedentedly clear fashion by using solvated cluster ions, *i.e.* employing photodissociation spectroscopy of ions solvated with a well-defined number of solvent molecules.

One of the important solvation effects is the solvatochromic shift, which is the shift of absorption peak of a compound in solution compared to that of the bare compound. The shift is usually dependent on the nature of the solvent and is typically measured as a relative shift in different solvents. The "absolute" shift is unattainable unless the spectrum of the unsolvated compound (*e.g.* gas phase) is available. There are some interesting questions in this regard, for example: What is the role of individual solvent molecules and solvation shells? What is their contribution to the total solvatochromic shift?

Theorists have designed several approaches to model the solvation process and to compute the solvatochromic shift. One approach that reflects the collective influence of solvent is to treat the solvent as a continuum with given dielectric permittivity ("COnductor-like Screening MOdel", COSMO)[3] or polarizability (as in "Dielectric Polarizable Continuum Model", D-PCM).[4,5] This approach (implicit models) circumvents the high computational cost that would incur if individual solvent molecules were considered (explicit models). Sometimes, the latter approach is necessary. Intuitively, as the number of solvent molecule incorporated in the calculation grows, the accuracy improves but the computational cost quickly becomes prohibitive. Then the question is, how many solvent molecules should be taken into account, if needed, to yield a result with reasonable accuracy?

To answer this question, one needs to compare the performance of calculations to the results from experiments. However, the control of the microsolvation environment, particularly, of the number of solvent molecules present is impossible in solution. In gas-phase experiments, it is possible to produce solvated cluster ions by condensing solvent molecules on the solute ions in an ion trap.[2,6–10] Furthermore, combination of mass spectrometry with spectroscopy allows

selectively studying the properties of ionic species surrounded by well-defined number of solvent molecules. This development opens the possibility of capturing an "intermediate" state of molecular ions between the condensed phase and the gas phase. Experimental results of ions solvated by a defined number of solvent molecules then become available to benchmark theoretical computations on exactly the same systems.

5.2 $[(tpy)(bpy)Ru^{II}\text{-}OH_2]^{2+}$ solvated by 0 - 4 H_2O molecules

5.2.1 Background

In §3.3 we presented our study of a series of ruthenium polypyridine complexes, one of which is $[(tpy)(bpy)Ru^{II}\text{-}OH_2]^{2+}$ (bpy = 2,2'-bipyridine, tpy = 2,2':6'2"-terpyridine), denoted as $[\mathbf{Ru}\text{-}OH_2]^{2+}$. It is believed to be the starting point in the catalytic cycle of water oxidation driven by the catalyst $\mathbf{Ru}^{2+}$. By comparing our photodissociation spectrum of $[\mathbf{Ru}\text{-}OH_2]^{2+}$ *in vacuo*[11] and its spectrum in aqueous solution,[12] we were able to measure the absolute solvatochromic shift of the visible MLCT band. However, as pointed out in §5.1, it remains unknown how water molecules contribute to the overall solvatochromic shift.

The solvatochromic behavior of the ^{1}MLCT band in aqueous solution is a very interesting problem. One can construct a simple picture by considering the following. The MLCT transitions involve the Ru^{2+} ion as well as the hydrophobic bpy and tpy ligands. Solvent access to Ru^{2+} is restricted to a single coordination site, which is occupied by an *aqua* ligand in aqueous solution. The polypyridine ligands have a small amount of positive charge in the ground state.[13] Upon excitation, they gain partial negative charge, making them more hydrophobic. Hydration can destabilize a proton on the *aqua* ligand, as observed in infrared spectroscopic studies,[2] which

offers the possibility of "launching" proton transfer into the solvent environment. As a consequence, a change in the electronic structure of the complex is introduced and the ^{1}MLCT band can be expected to report on this change.

One way to follow how the electronic structure evolves with hydration is to measure electronic spectra of stepwise hydrated species. Previously, Garand and coworkers[2] have probed the vibrational structure of mass selected $[\mathbf{Ru}\text{-}OH_2]^{2+}\cdot(H_2O)_n$ clusters (n = 0 – 4) and showed that the interaction between the *aqua* ligand and the Ru center is strongly affected by the presence of solvent molecules. In particular, the presence of H-bonded networks serves to assist in charge transfer into the Ru-OH_2 bond, anticipating proton transfer into the microhydration environment in the first step of the water oxidation reaction. To study the electronic structure, we measured the electronic spectra in the MLCT region of mass selected $[\mathbf{Ru}\text{-}OH_2]^{2+}\cdot(H_2O)_n$ clusters (n = 0 – 4). As found earlier by Garand and coworkers, the first few solvent water molecules form a network anchored on the *aqua* ligand[2] so we can selectively probe the solvatochromic shift induced by solvent effects on the Ru^{2+} environment, one solvent molecule at a time. The experimental results can be used to compare with computations to show whether and to what extent theoretical predictions are accurate.

5.2.2 Methods

The instrumentation for the experiment has been described in detail in Chapter 2 and the method of generating $[\mathbf{Ru}\text{-}OH_2]^{2+}$ has been reported in §3.3. To produce $[\mathbf{Ru}\text{-}OH_2]^{2+}\cdot(H_2O)_n$ clusters the temperature of the ion trap was set between 160-180 K and water vapor was introduced as the buffer gas to condense water molecules onto the ions in the trap. The use of

water vapor as buffer gas was found to be crucial to the formation of larger clusters, but the high partial pressure of water vapor in the trap results in condensation on the trap electrodes and causes unstable ion signal after a certain amount of experiment time. As a result, the trap temperature had to be raised to defrost about every 5 hours. An example of mass spectrum is shown in **Figure 3.1** with instrument parameters optimizing larger clusters.

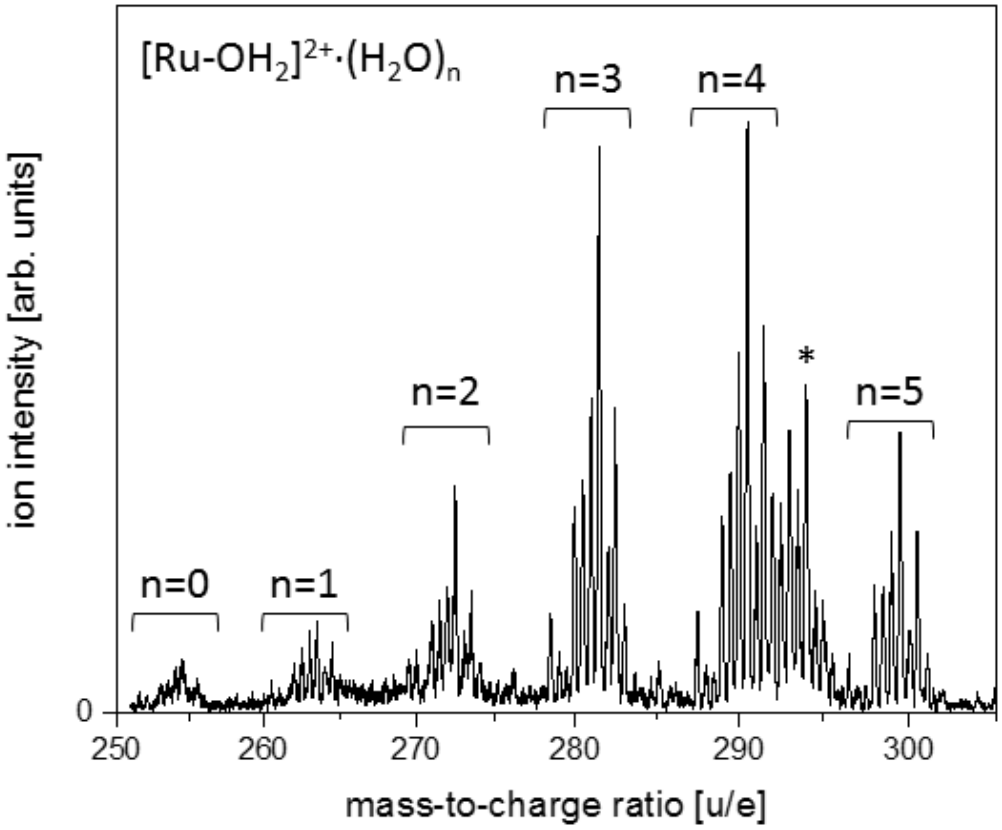

Figure 5.1 Mass spectrum showing the formation of [**Ru**-OH_2]$^{2+}$·$(H_2O)_n$ with instrument parameters optimized for n = 3. Mass peaks marked with asterisk are unidentified.

We measured the photodissociation spectra of all [**Ru**-OH_2]$^{2+}$·$(H_2O)_n$ clusters. Since the clusters exhibit multiple dissociation pathways and thus different photofragments (see §5.2.4),

as mentioned in §2.4.2, the full absorption spectrum is better represented by the depletion spectrum rather than fragment action spectra. However, because the absorption cross section of $[\mathbf{Ru}\text{-}OH_2]^{2+}$ is very high (the maximum extinction is 15000 $M^{-1}cm^{-1}$ at 476 nm[12]) and the OPO output in this wavelength region is very intense, up to 30% loss of parent ions in each ion packet was observed with radiation near 476 nm. Since this is cannot be justified as a small factional loss, we must adopt the modified Lambert-Beer's law to calculate the absorption cross section according to §2.6.3.[14]

For computations we used the Turbomole suite[15,16] of programs to perform geometry optimization, population analysis and excited state calculations. Ground state structures for $[\mathbf{Ru}\text{-}OH_2]^{2+}\cdot(H_2O)_n$ (n = 0 – 4, multiple isomers) and related species were optimized employing density functional theory[17] using the B3LYP[17,18] functional and def2-TZVP basis sets for all atoms. Electronic excitation spectra were calculated using time-dependent DFT with the same functional in two different sets of calculations. In one series, we used def2-TZVP basis sets again for all atoms. This approach yields a qualitative description of the bare complex,[13] and we therefore judge it to be an appropriate tool for the clusters under study. All calculated excitation energies in this series reported here are shifted by -1210 cm^{-1} to improve agreement with the experimental spectrum for n = 0. However, with our resources these calculations were only possible up to n = 3. In order to obtain calculated values for the solvatochromic shifts of all cluster sizes, we repeated the calculations starting from the same optimized ground state structures, but with def2-SV(P) basis sets for all atoms. The latter series was shifted by +2420 cm^{-1} to improve agreement with the experimental spectrum for n = 0.

5.2.3 Bare complex and calculations

The photodissociation spectrum of [**Ru**-OH_2]$^{2+}$ at room temperature and at 180 K (**Figure 5.2**) has been discussed in detail in §3.3.3. We will briefly repeat the main observations regarding the bare ion here in order to help understand the spectra of the solvated ion.

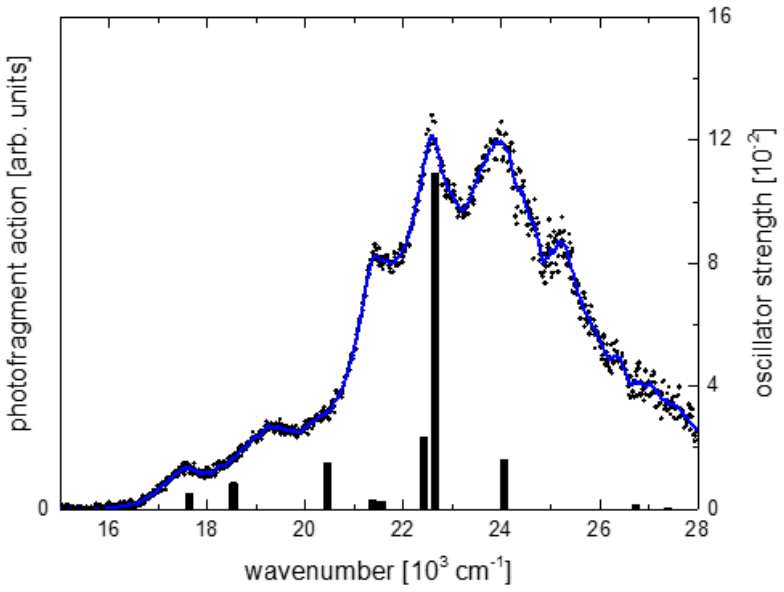

Figure 5.2 Photodissociation action spectrum of [**Ru**-OH_2]$^{2+}$ at 180 K trap temperature. Circles are raw data; the line is a 15-point sliding average. Vertical bars are calculated transition energies (B3LYP/def2-TZVP), shifted by -1210 cm^{-1}.

The ^{1}MLCT band, which is a mostly featureless broad band at 21010 cm^{-1} (476 nm) in solution,[12] reveals rich, partially resolved substructure *in vacuo*, even at room temperature.[11] At 180 K,[13] a signature corresponding to the first excited singlet state (S_1) is observed at 17300 cm^{-1}, followed by two discernible bands at 19300 cm^{-1} and 21400 cm^{-1}, which we assign to the S_2 and S_3 excited states. The two most intense signatures are peaks at 22600 cm^{-1} and 23900 cm^{-1}. TDDFT calculations qualitatively reproduce the experimentally observed pattern.

Several weak bands predicted by the calculations near 22000 cm^{-1} are likely obscured by the envelope of the stronger electronic bands in the region. The band envelope of the ^{1}MLCT band extracted from the gas phase spectrum is found at 23390 cm^{-1}, resulting in a total solvatochromic shift of -2380 cm^{-1} in aqueous solution. No resolved vibrational structure was observed in the electronic bands. The singlet excited states are thought to decay on ultrashort timescales via intersystem crossing to the triplet manifold[19] due to the large spin-orbit interaction typical for Ru compounds. The width of the observed bands is most likely caused by a combination of lifetime broadening and spectral congestion from the Franck-Condon envelopes of the excited electronic bands as well as hot bands.[11]

When [**Ru**-OH_2]$^{2+}$ is solvated by water, a water network is expected to form around the *aqua* ligand, as confirmed by our calculations of the ground state geometry for all clusters in this study, which are summarized in **Figure 5.3**.

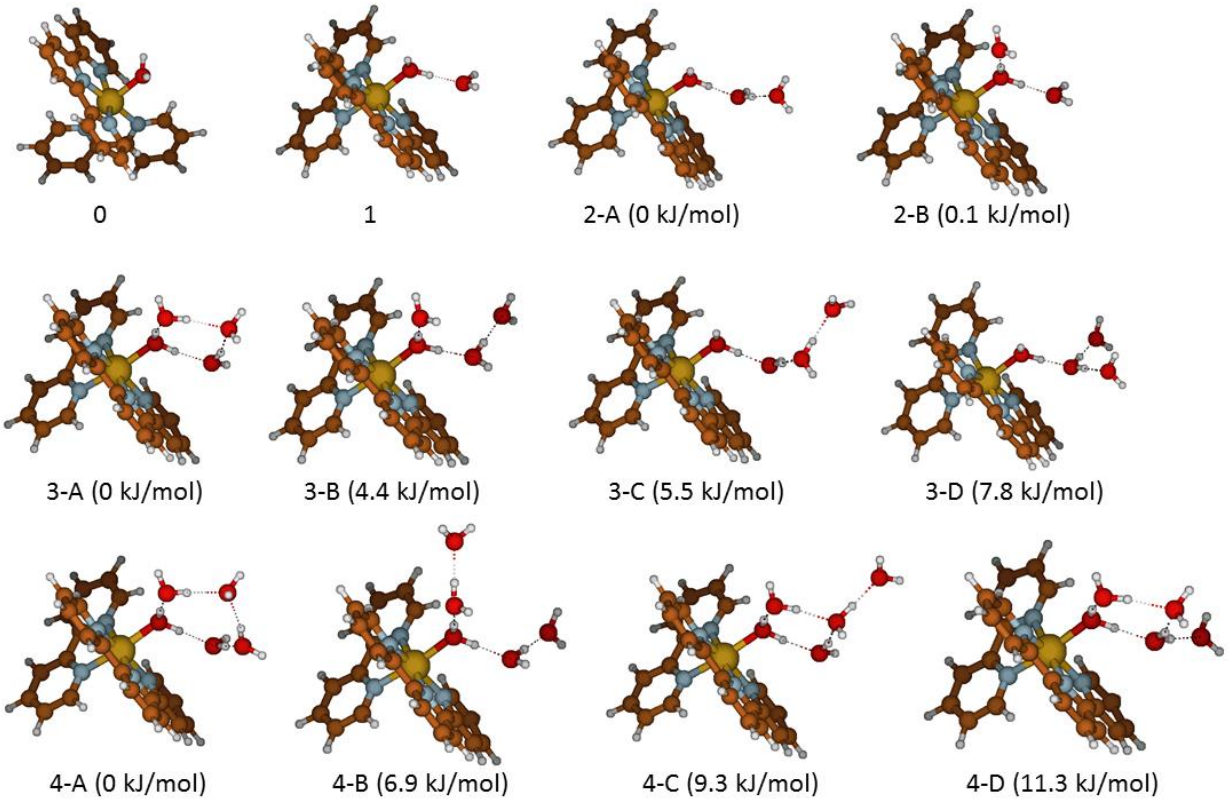

Figure 5.3 Calculated minimum energy structures of $[\mathbf{Ru}\text{-}OH_2]^{2+}\cdot(H_2O)_n$ showing the lowest energy structure for n = 0 and 1 and several low-energy structures for n ≥ 2. Their energies relative to the lowest energy conformer at 0 K are shown in the brackets. Carbon atoms are shown in brown, nitrogen in blue, ruthenium in gold, oxygen in red, and hydrogen in white.

The calculated structure of the monohydrate, $[\mathbf{Ru}\text{-}OH_2]^{2+}\cdot H_2O$ is consistent with work by Garand and coworkers.[2] Only one low-lying stable isomer is found, and the solvent molecule binds directly to the *aqua* ligand. Structures where the water ligand binds to one of the polypyridine ligands are *ca.* 29 kJ/mol and more above this low-lying geometry. There are two low lying structural motifs for the dihydrate, $[\mathbf{Ru}\text{-}OH_2]^{2+}\cdot(H_2O)_2$. In one motif (2-A), the *aqua* ligand and the two solvent molecules form a chain, where the second solvent molecule can be viewed as the onset of the second solvation shell. This isomer is lowest in energy at both 0 K and 180 K. In the other isomer (2-B), the two solvent molecules are equivalent, both acting as H-bond

acceptors from the *aqua* ligand. The 2-B isomer is 0.1 kJ/mol higher in energy (zero-point corrected) at 0 K and 0.7 kJ/mol higher at 180 K. The threshold energies for loss of the "second" water molecule are very similar for both isomers, and the two isomers can be viewed as isoenergetic. Some of the structural motifs of the tri- and tetrahydrates have also been discussed in Ref.[2] The additional water molecules continue to build the H bonding network anchored at the *aqua* ligand. The calculated lowest energy structures have four membered rings (isomers 3-A and 4-A). These structures are calculated to be significantly lower in energy than the others we found (*ca.* 7.8 kJ/mol for n = 3 and 11.3 kJ/mol for n = 4). Hydration around the polypyridine ligands is possible with greater n values but is less favorable than at the *aqua* ligand. According to exploratory calculations, a probable conformer of this type is at least 29 kJ/mol higher in energy than those with hydration around the *aqua* ligand. Therefore, we believe the conformers in **Figure 5.3** are the main contributors to the population in our experiment.

The binding energy of additional water molecules decreases with the size of clusters, which is also expected (see **Table 5.1** Zero-point corrected binding energies of water molecules in $[\mathbf{Ru}\text{-}OH_2]^{2+}\cdot(H_2O)_n$ clusters. The binding energy for n =2 is the same for both conformers. The values for n = 3 and 4 are upper limits, based on the most strongly bound isomers found for these cluster sizes.**Table 5.1**). Note that the binding of the *aqua* ligand is significantly higher than the solvent water molecules, reflecting the direct interaction with the metal ion.

Table 5.1 Zero-point corrected binding energies of water molecules in $[\mathbf{Ru}\text{-}OH_2]^{2+}\cdot(H_2O)_n$ clusters. The binding energy for n =2 is the same for both conformers. The values for n = 3 and 4 are upper limits, based on the most strongly bound isomers found for these cluster sizes.

water molecule	binding energy [kJ/mol]
aqua ligand	90
solvent, n = 1	58
solvent, n = 2	50
solvent, n = 3	47
solvent, n = 4	49

Since [**Ru**-OH_2]$^{2+}$ has its absorption maximum at 442 nm, absorption of a photon at this wavelength (equivalent to *ca.* 270 kJ/mol energy input) will suffice to "evaporate" more than one solvent molecule, if existent, which results in the presence of multiple dissociation pathways and photofragments for n ≠ 0. Indeed, we did observe two dominant decay channels: the loss of all *solvent* molecules at lower energies within the ^{1}MLCT band and the loss of all *water* molecules (solvent and *aqua* ligand) at higher energies. In addition to the fragment action spectra, we also measured the photodepletion spectra of all cluster sizes. This study illustrates the issue raised in §2.4.2 - the connection and difference between absorption, photodissociation action and depletion spectra.

As pointed out in §2.4.2, for photodissociation spectroscopy to faithfully represent the absorption spectrum, the primary condition is that any non-dissociative fate after photoexcitation during the observation window of the experiment should be negligible. For the present case, photon emission from [**Ru**-OH_2]$^{2+}$ has been found to be very weak,[12] which fulfills the requirement. Photodissociation of the parent ion on must occur in the time scale of the experiment (*ca.* 15 μs), and this condition is of particular importance at low photon energies. To verify that this condition is also met, we recorded the photodissociation spectrum of [**Ru**-OH_2]$^{2+}$ with a slower ion beam, allowing more time of flight after photoexcitation (20 μs versus 16 μs), and detected no difference compared to the result from the faster beam (see **Figure 5.4**).

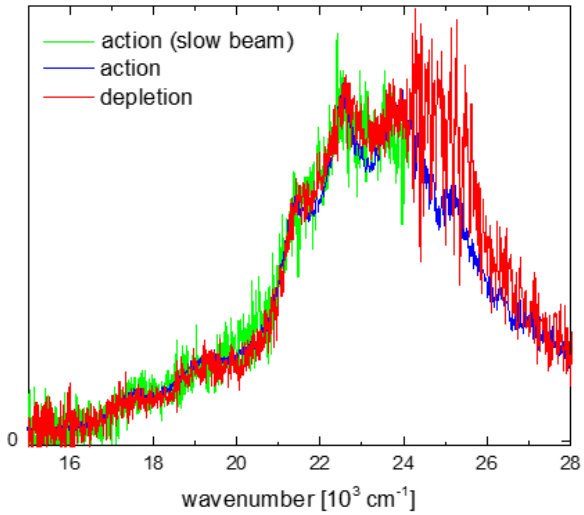

Figure 5.4 The photodissociation action (observation time: green - 16 μs; blue - 20 μs) and depletion spectra (red) of the bare *aqua* complex [**Ru**-OH_2]$^{2+}$. Slow beam action spectrum shows up to 24000 cm^{-1}. All three spectra can be considered to be equivalent within the signal-to-noise ratio of the experiment.

For the bare *aqua* complex [**Ru**-OH_2]$^{2+}$, which has only one photodissociation pathway, photodissociation action and depletion spectra are identical. However, this is not true for solvated species. For the latter, adding the action spectra of all photodissociation pathways should in principle yield the absorption spectrum. However, in this experiment, the fragments may have different detection efficiencies and backgrounds so the signals in different action spectra may not be comparable. Moreover, strong and different kinetic shift effects in the action spectra were observed for different photofragments (see §5.2.4). We will therefore use photodepletion data to present the absorption spectrum. Because the spectrum of bare [**Ru**-OH_2]$^{2+}$ shows no kinetic shift effects, and the calculated binding energies of solvent water molecules in [**Ru**-OH_2]$^{2+}$·$(H_2O)_n$ clusters are substantially lower than that of the *aqua* ligand (see

Table 5.1), it can be assumed that photodissociation of the clusters upon photoexcitation is faster than for the bare *aqua* complex. Consequently, the photodepletion spectra of the clusters should also be free of kinetic shift effects and are therefore representative of the absorption spectra.

In this experiment, each laser pulse depletes up to 30% of the parent ion in a single shot, the approximate linear relationship between the depletion ratio and the absorption cross no longer holds. To calculate the absorption cross section, one needs to use the modified Lambert-Beer law introduced in §2.6.3[14]

$$\frac{Y_P(\lambda)}{P} = 1 - \alpha + \alpha e^{-\sigma(\lambda)F(\lambda)}$$

where α is a parameter indicating the overlap between laser and ion packet, and $F(\lambda)$ is the photon fluence. The overlap parameter α can be extracted from the fluence dependence of the depletion. We set the laser at 442 nm where the absorption of [**Ru**-OH_2]$^{2+}$ peaks and measured the ratio of surviving parent ion and the total parent ion $Y_P\ (\lambda = 442\ \mathrm{nm})/P$. Then we varied the photon fluence F by inserting neutral density filters and plotted $Y_P\ (\lambda = 442\ \mathrm{nm})/P$ as a function of $e^{-\sigma(\lambda=442\ \mathrm{nm})F}$ (see **Figure 5.5**).

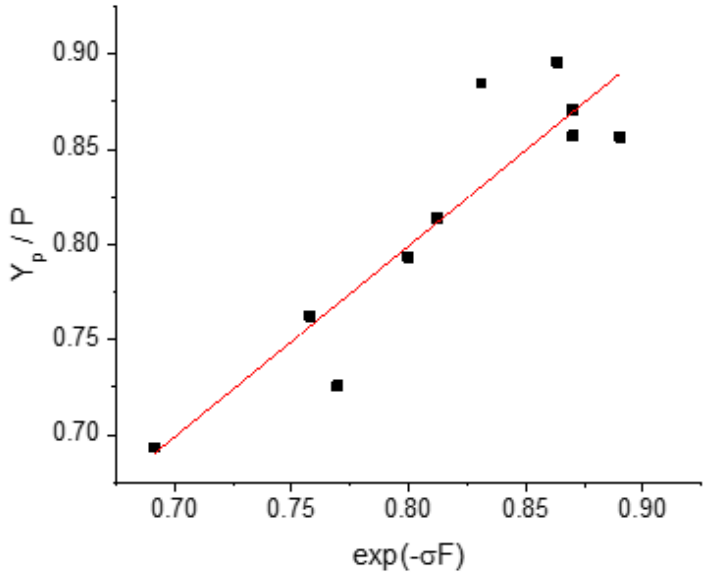

Figure 5.5 Data points are $Y_P\ (\lambda = 442\ \mathrm{nm})/P$ as a function of $e^{-\sigma(\lambda=442\ \mathrm{nm})F}$. Linear fitting (red) returned $\alpha = 1.00$.

Using the data from Ref.[12] the maximum absorption cross section can be calculated to be $5.7 \times 10^{-17}\mathrm{cm}^2$. Here $\sigma(\lambda = 442\ \mathrm{nm})$ is taken as this number, which should have a value that is sufficiently accurate for extracting the overlap parameter α in this step. Fitting of the data using the function $\mathrm{f(x)} = 1 - \alpha + \alpha\mathrm{x}$ yielded an almost 100% overlap between laser and ion packet ($\alpha = 1.00$, standard error 0.05). As a result, the absorption cross section $\sigma(\lambda)$ can be linked to the observed signal via

$$\sigma(\lambda) = -\ln\left(\frac{Y_P(\lambda)}{P}\right)/F(\lambda)$$

This equation will be used in lieu of the linear approximation for representing the absorption spectra processed from our photodepletion data in this chapter.

5.2.4 The hydrated clusters

Figure 5.6 shows the depletion and action spectra for the monohydrate and the dihydrate clusters (n = 1 and 2). The depletion spectrum appears to have less substructure in the ^{1}MLCT band, while the action spectra demonstrate similar substructure as in the bare *aqua* complex. This is due to the inherently lower signal-to-noise ratio for depletion spectra. The lower panel contains the action spectra of both photofragments: **Ru**$^{2+}$and [**Ru**-OH_2]$^{2+}$, the inset being the latter.

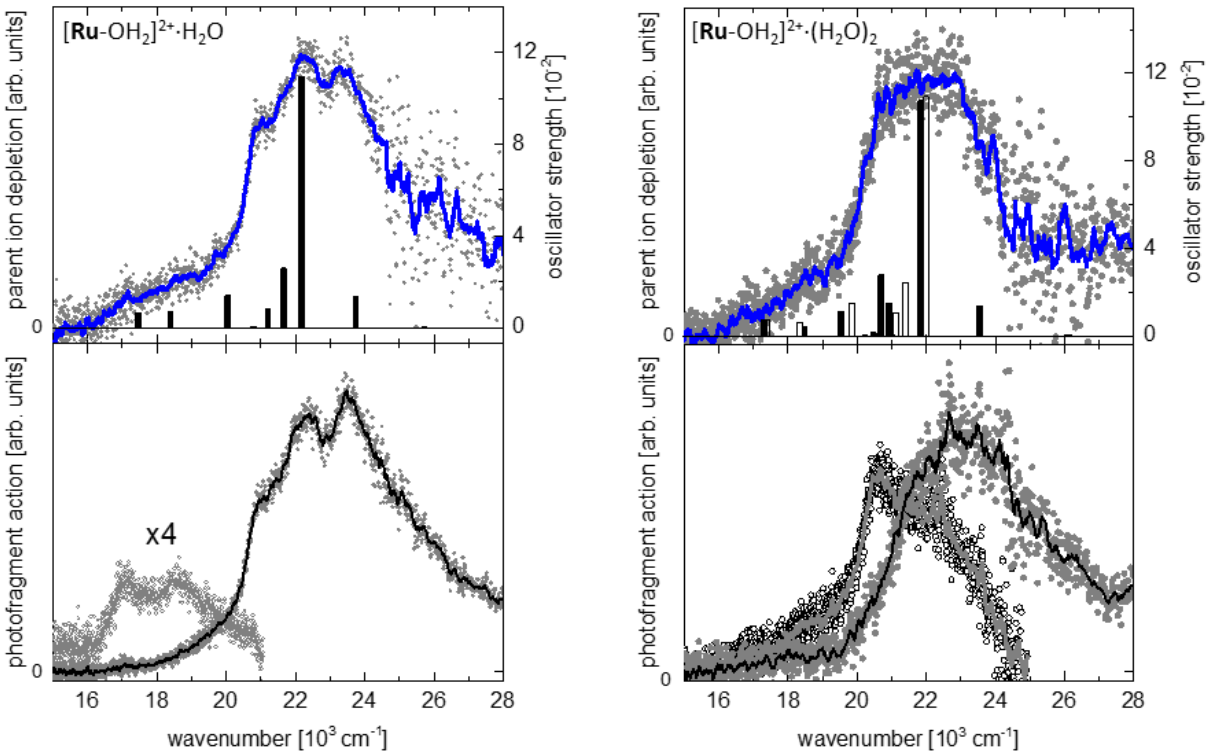

Figure 5.6 Photodissociation spectra for [**Ru**-OH_2]$^{2+}$·H_2O (left) and [**Ru**-OH_2]$^{2+}$·$(H_2O)_2$. Upper panels: photodepletion spectra and calculated vertical excitation spectra (B3LYP/def2-TZVP, columns, shifted by -1210 cm^{-1}). For [**Ru**-OH_2]$^{2+}$·$(H_2O)_2$, the open columns represent the 2-A isomer and the filled columns represent the 2-B isomer. Lower panels: photodissociation action spectra monitoring the yield of [**Ru**-OH_2]$^{2+}$ (open circles, grey full lines) and **Ru**$^{2+}$ (filled circles, black full lines). Circles are raw data points; the full lines are 15-point sliding averages.

It is clear that the action spectra depend on the photofragment formation efficiencies. The fragment channel corresponding to the loss of a single water molecule (presumably the solvent, calculated threshold energy 57.9 kJ/mol) clearly shows the low energy onset (S_1 and S_2 states). The fragment channel corresponding to the loss of two water molecules – albeit detectable – is significantly suppressed at low photon energies, but this channel (calculated threshold energy 147.6 kJ/mol) takes over and dominates the shape of the spectrum above 19400 cm^{-1}. This can be explained by interpreting the loss of the water molecules as a sequential process, with an energy-dependent change in survival probability of the [**Ru**-OH_2]$^{2+}$ intermediate fragment ion (*i.e.*, after the solvent molecule has been lost). With sufficient energy input, this ion will also lose the *aqua* ligand, leading to the observed increase of the branching ratio into in the **Ru**$^{2+}$ fragment channel for higher photon energies.

By comparing with the bare *aqua* complex, we find that all discernible electronic bands of [**Ru**-OH_2]$^{2+}$·H_2O are red-shifted by *ca.* 320 cm^{-1}. This can be interpreted as the solvatochromic shift of each electronic band caused by the presence of a *single* solvent water molecule. The center of gravity and the envelope of the ^{1}MLCT band exhibit a much stronger red-shift of *ca.* 570 cm^{-1}. This may be due to a shortening of the Franck-Condon progressions on the high energy side of each band, which exacerbates the red-shift of the overall envelope. The TDDFT calculations qualitatively reflect the observed red-shift of the individual bands, but they show no drastic changes in oscillator strengths.

The substructure in the ^{1}MLCT region of the dihydrate spectra is less distinct than that of the monohydrate. The ^{1}MLCT band center of gravity and envelope shift by -720 cm^{-1} and -800 cm^{-1}, respectively. The two isomers of the dihydrate result in similar calculated TDDFT

spectra, and the differences between the calculated spectra are not sufficient to unambiguously assign the experimental spectrum to one particular isomer. Similar to the monohydrate, $\mathbf{Ru}^{2+}$ and $[\mathbf{Ru}\text{-}OH_2]^{2+}$ were the only observable photofragments. Again, the yields of the two fragments show different photon energy dependence, but the $\mathbf{Ru}^{2+}$ channel becomes dominant occurs at *ca.* 21000 cm^{-1}, higher in energy than in the case of the monohydrate. This is not surprising because the loss the two or three water molecules demands higher energy input. The S_1 and S_2 states are not resolved in any of the dihydrate spectra. Monitoring the generation of $[\mathbf{Ru}\text{-}OH_2]^{2+}\cdot H_2O$ did not yield any significant signal in the entire spectral region, which means that the survival probability of the $[\mathbf{Ru}\text{-}OH_2]^{2+}\cdot H_2O$ intermediate fragment ion is vanishingly small on the time scale of our experiment. While TDDFT calculations qualitatively predict the red-shift of the dihydrate, the magnitude of the shift is underestimated.

Parent ion intensities for clusters with n = 3 and 4 were at the edge of the sensitivity of our photodissociation spectrometer, resulting in a low signal-to-noise ratio, but the spectra for these species can still be observed (see **Figure 5.7**).

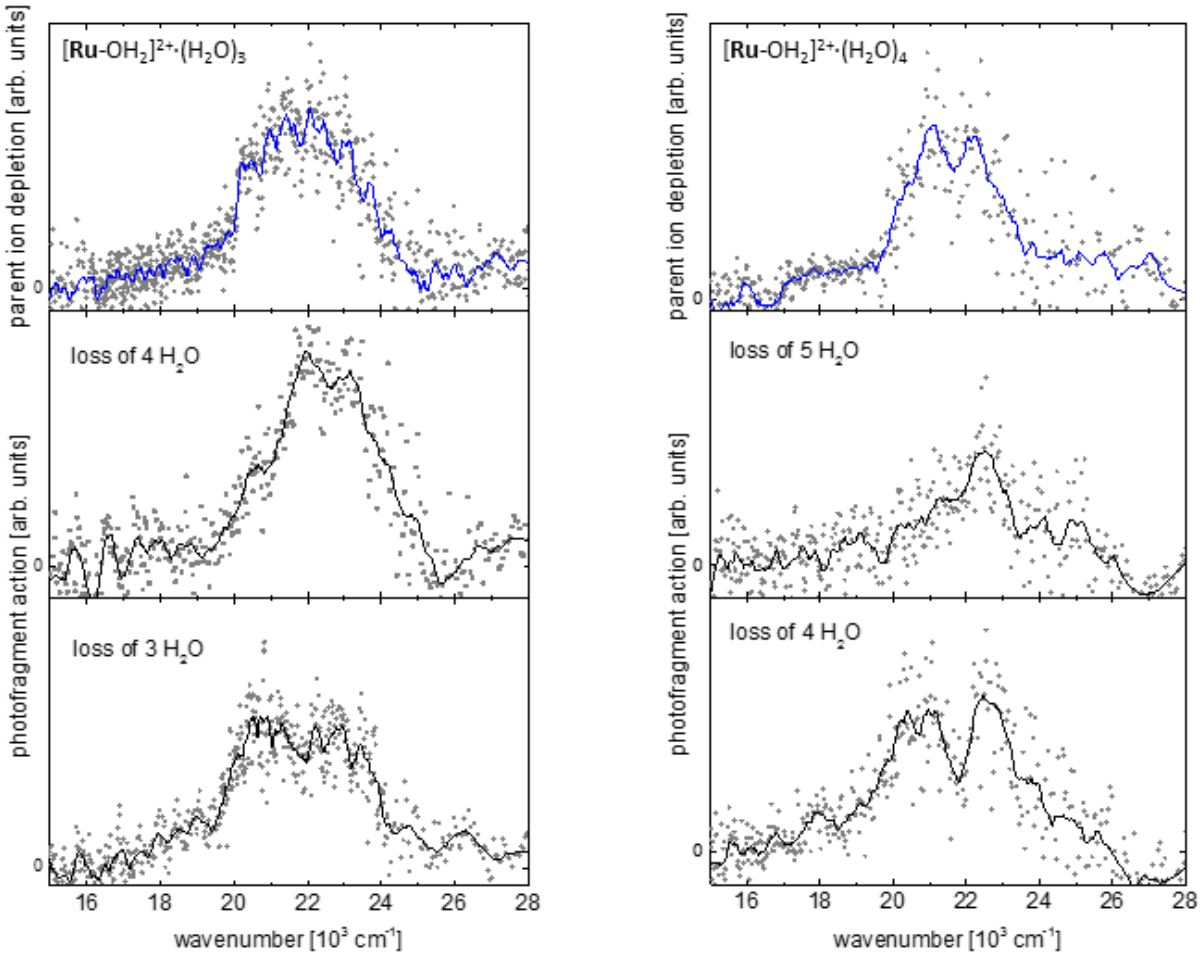

Figure 5.7 Photodissociation spectra for $[\mathbf{Ru}\text{-}OH_2]^{2+}\cdot(H_2O)_3$ (left) and $[\mathbf{Ru}\text{-}OH_2]^{2+}\cdot(H_2O)_4$ (right). The top panels contain the photodepletion spectra and the lower panels show the action spectra monitoring different photofragments as labeled. The dots are raw data points; the full lines are 30-point sliding averages.

The depletion spectra show further red-shifts of the ^{1}MLCT band center of gravity and envelope. As seen in the smaller clusters, $\mathbf{Ru}^{2+}$ and $[\mathbf{Ru}\text{-}OH_2]^{2+}$ are still the dominating photofragments and the yield of $\mathbf{Ru}^{2+}$ is suppressed in the lower energy region. Note that the action spectra are scaled to fit the panel, therefore, the visual intensities are not comparable.

5.2.5 Solvatochromic behavior

Figure 5.8 shows all the depletion spectra obtained in this study together with the solution spectrum adapted from Ref.[12] From the spectra of the solute at different stages of hydration it is possible to determine the solvatochromic shift for each cluster and to compare with the solution spectrum. However, because the spectra have very different shapes and they progressively lose spectroscopic detail as solvation increases (see **Figure 5.8**), they cannot be directly compared to the solution spectrum. Therefore, a reference point that can be used for all spectra needs to be determined in order to quantitatively evaluate the spectral shifts at different stages of solvation. A good numerical measure for the solvatochromic shift would be the peak shift of the envelope of each spectrum. We applied two approaches to fulfill this task. In one approach, the center of gravity of the ^{1}MLCT band for each spectrum was determined by first integrating the curve underneath the experimental ^{1}MLCT band. Integration limits were the low-energy end of the experimental data and the point where the 200-point sliding average (100-point for n = 4) went through a minimum on the high energy side of the band. The center of gravity is at the energy where the area under the experimental data reaches half the value of the full integral (arrows shown under the smoothed curves in **Figure 5.8**). Uncertainties are estimated from the sensitivity of the procedure to the choice of integration interval.

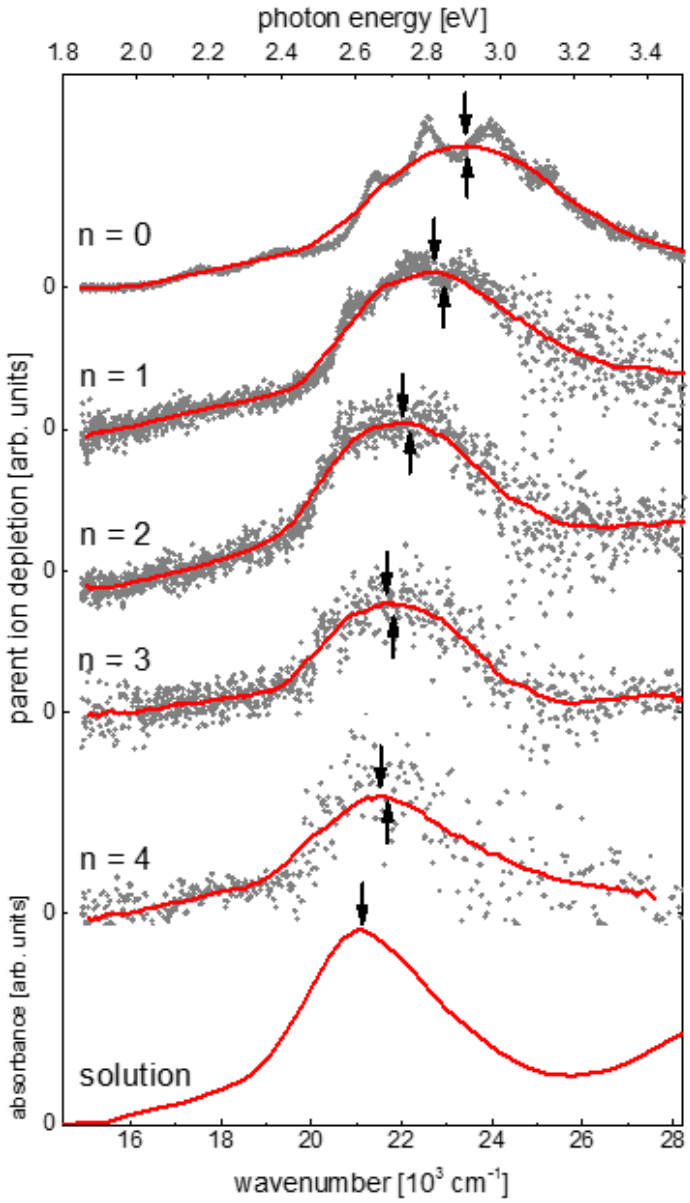

Figure 5.8 Band envelopes of all clusters. Experimental data (data points) were smoothed (red curves) with 200-point sliding average (100 points for n = 4). The smoothed curves were interpreted as band envelopes. Arrows above the smoothed curves are the band envelope peaks; arrows under the curves point at the center of gravity (both values are listed in **Table 5.2**). Error bars are estimated from small variations in the peak position when using different gliding averages. The solution spectrum is adapted from Ref.[12]

Table 5.2 Experimental and calculated energies (in cm^{-1}) of selected spectroscopic features of $[\mathbf{Ru}\text{-}OH_2]^{2+}\cdot(H_2O)_n$ clusters at 180 K trap temperature.

n	E_{COG} [cm^{-1}] [a]	E_{env} [cm^{-1}] [b]	E_{S8} [cm^{-1}] [c]	
			def2-SV(P)	def2-TZVP
0	23470 (80)	23390 (100)	22390	22850
1	22900 (80)	22820 (100)	22000	22530
2	22180 (80)	22020 (100)	21710	22350
3	21780 (160)	21940 (160)	21490	22120
4	21610 (240)	21530 (240)	21340	
bulk		21010 (100)		

[a] Center of gravity of the ^{1}MLCT band for each cluster size.

[b] Peak of band envelope. The bulk value was extracted from the data in Ref.[12]

[c] Calculated values for the most intense transition (S_8) using the B3LYP functional with the basis sets for all atoms as listed. Values are rounded to 10-cm^{-1} accuracy. For cluster sizes with more than one isomer, an average of all values is reported. All def2-TZVP results were shifted by -1210 cm^{-1}. All def2-SV(P) values were shifted by +2420 cm^{-1}.

In the other approach, we employed a sufficiently broad smoothing function to determine the peak of the envelope of the spectrum. A 200-point sliding average was used on the curves shown in **Figure 5.8**, except for n = 4, where the smaller number of data points made 100-point sliding average necessary. Error bars are estimated from small variations in the peak position when using different sliding averages. Note that while the center of gravity is not necessarily the same as the peak position, the results yielded from both methods lie well within the error bars of each other. Therefore, the solvatochromic shifts determined using the two procedures are consistent with each other and we define the overall solvatochromic shift by using the difference between the peak of the band envelope and the peak of the solution spectrum[12] (-2380 cm^{-1}, 0.295 eV).

We performed TDDFT calculations using two different basis sets - def2-TZVP and def2-SV(P) – for all cluster sizes and all the isomers in **Figure 5.3**. Both basis sets were able to qualitatively reproduce the spectral envelope for all cluster sizes up to n = 3. For n =4, only B3LYP/def2-SV(P) yielded converged results, which are shown as stick spectra in **Figure 5.9**.

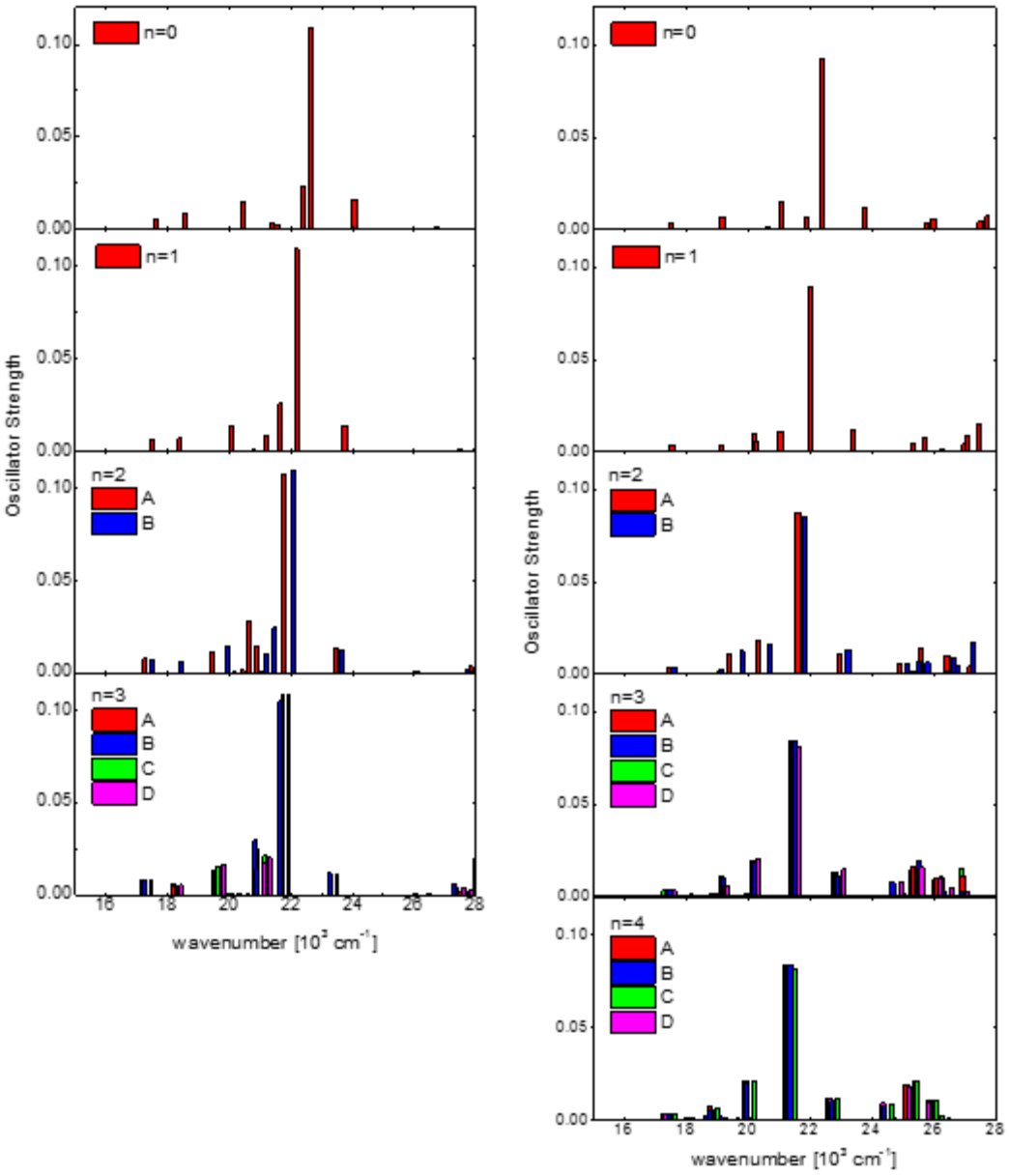

Figure 5.9 Overview of TDDFT spectra for all isomers. Left: B3LYP/def2-TZVP; right: B3LYP/def2-SV(P).

The electronic structures for the different isomers of the clusters are very similar. Although the calculations correctly predicted increasing red-shift as more solvent molecules are present, the magnitudes of the red-shift are all underestimated. The description does not improve with increasing basis set size from def2-SV(P) to def2-TZVP (see **Figure 5.10**).

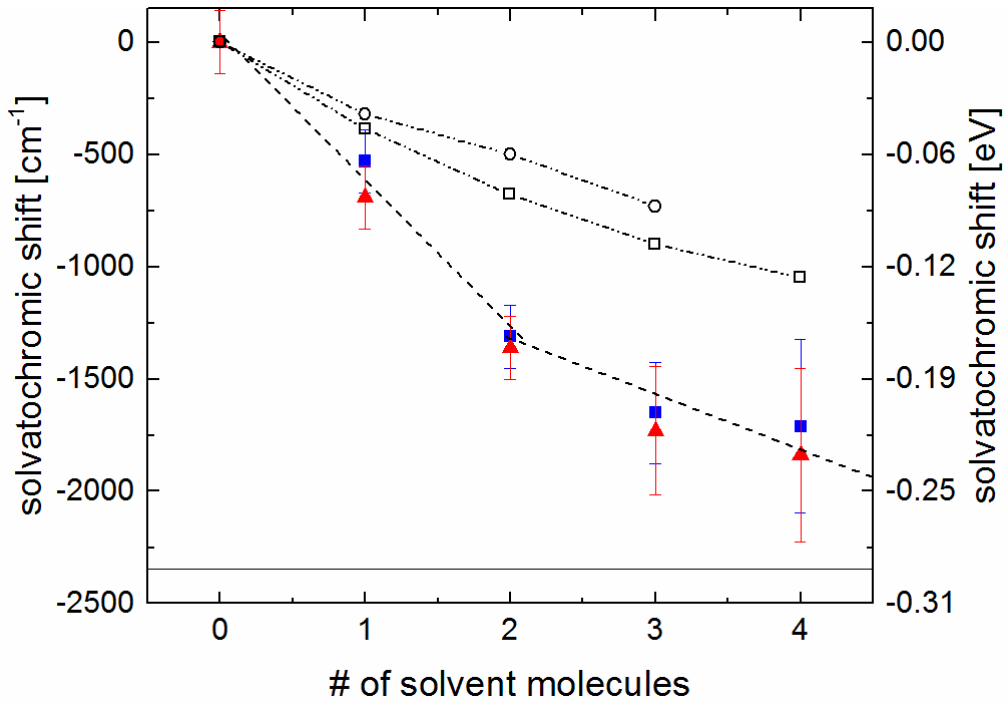

Figure 5.10 Summary of solvatochromic behavior of [**Ru**-OH_2]$^{2+}$·$(H_2O)_n$ compared to bulk aqueous solution[12] (horizontal line). The center of gravity positions of the MLCT bands are shown as filled blue squares, the envelope peaks as filled red triangles. Results from TDDFT calculations are shown as open circles (def2-TZVP) and open squares (def2-SV(P)). The dashed lines are meant to guide the eye. Numerical values are listed in **Table 5.2**, and error bars (where given) are determined from Gaussian error propagation of the errors listed in **Table 5.2**.

The experimental and theoretical descriptions of the solvatochromic behavior of [**Ru**-OH_2]$^{2+}$ are summarized in **Figure 5.10**, from the bare *aqua* complex through the first four water adducts to bulk hydration. The overall envelope shifts to *ca.* 78% of the full bulk

solvatochromic shift with four solvent water molecules present, which highlights the importance of the water network that incorporates the *aqua* ligand. It is clear that the solvatochromic shift induced by each additional solvent molecule is not monotonic from n = 0 – 4. For the first two solvent molecules, the solvatochromic shifts are *ca.* -650 cm^{-1} after each added solvent molecule, while for n > 2, the sequential shift slows to *ca.* -280 cm^{-1} per added solvent molecule. Geometry optimization reveals that the water network of the first solvation "shell" is filled at n = 2, which coincides with the turning point of the curve in **Figure 5.10**. This may suggest that the slower red-shift with progressive solvation reflects saturation of the *aqua* ligand with H-bonds. Here the term "shell" refers to the water network building around the *aqua* ligand only and neglects the possible solvation sites around the polypyridine ligands.

One may predict the solvatochromic behavior beyond this point, assuming the effects of continuing addition of solvent water molecules follows a linear extrapolation of the data for n = 2 – 4. In this very simple picture, it can be estimated that the bulk solvatochromic shift is reached after addition of *ca.* 6 solvent water molecules. T This extrapolation is almost certainly too simple, because it is entirely conceivable that the shift per added solvent molecule will continue to diminish as the number of solvent molecules grows. Moreover, the water network may spread beyond the vicinity of the *aqua* ligand and begin to interact with the organic ligands when the cluster size exceeds a certain point. Despite the obvious shortcomings of the extrapolation, it is instructive to compare the solvated ion $[\mathbf{Ru}\text{-}OH_2]^{+}\cdot(H_2O)_n$ at $n \approx 6$ with the microsolvation environment of a Ru^{2+} ion (without organic ligands) in bulk aqueous solution. The solid angle on the Ru^{2+} ion in the complex that is accessible to hydration only amounts to *ca.* 15% of a full sphere and there are 7 water molecules (including the *aqua* ligand) in this space. This is comparable to

a solution in which an uncoordinated Ru^{2+} ion is surrounded by *ca.* 50 water molecules, which corresponds to roughly 1 M solution of an atomic ion. It is also in line with results by Williams and collaborators[20,21] on the behavior of large hydrated clusters in terms of water binding energy and vibrational spectroscopy.

5.3 Summary

To study the role of solvent, we applied photodissociation spectroscopy on mass-selected water-solvated $[\mathbf{Ru}\text{-}OH_2]^{2+}$ ions *in vacuo*. Upon photoexcitation, $[\mathbf{Ru}\text{-}OH_2]^{2+}\cdot(H_2O)_n$ clusters sequentially lose water molecules, likely by unimolecular decay of a vibrationally hot molecule in its electronic ground state. Kinetic shift effects are obvious in action spectra but negligible for the photodepletion spectra of all ions under study. We measured the electronic spectrum of $[\mathbf{Ru}\text{-}OH_2]^{2+}$ solvated by up to 4 water molecules. The ^{1}MLCT band of the complex shifts towards lower energies upon addition of solvent water molecules at a rate of -650 cm^{-1} per added solvent at first and then -280 cm^{-1}. The rate changes at n = 2 where the *aqua* ligand is saturated with H-bonds and the first solvation "shell" is closed. In the dihydrate (n = 2), this shift recovers 55% of the solvatochromic shift in bulk aqueous solutions of $[\mathbf{Ru}\text{-}OH_2]^{2+}$, while the tetrahydrate spectrum shows 78% of the bulk solvatochromic shift. This observation highlights the importance of the first few solvent molecules for the electronic structure of this complex.

To further study this topic, larger clusters and colder ion temperatures may be interesting to investigate. The current restriction in our setup is the optimal temperature for cluster formation, which forces the ion trap temperature to be 180 K and prevents us from cooling the clusters down to lower temperatures. Therefore, inspired by Garand and coworkers[22], we will

implement an additional ion trap specifically for cluster formation and then transport the clusters to the main trap and cool them.

5.4 References

1. Xu, S., Smith, J. E. T. & Weber, J. M. Hydration of a binding site with restricted solvent access: solvatochromic shift of the electronic spectrum of a ruthenium polypyridine complex, one molecule at a time. *J. Phys. Chem. A* **120,** 7650–7658 (2016).

2. Duffy, E. M., Marsh, B. M. & Garand, E. Probing the hydrogen-bonded water network at the active site of a water oxidation catalyst: $[Ru(bpy)(tpy)(H_2O)]_{2+}\cdot(H_2O)_{0–4}$. *J. Phys. Chem. A* **119,** 6326–6332 (2015).

3. Klamt, A. & Schüürmann, G. Cosmo - a new approach to dielectric screening in solvents with explicit expressions for the screening energy and its gradient. *J. Chem. Soc. Perkin Trans. 2* 799–805 (1993).

4. Skyner, R. E., McDonagh, J. L., Groom, C. R., Van, M. T. & Mitchell, J. B. O. A review of methods for the calculation of solution free energies and the modelling of systems in solution. *Phys. Chem. Chem. Phys.* **17,** 6174–6191 (2015).

5. Cramer, C. J. & Truhlar, D. G. Implicit solvation models: equilibria, structure, spectra, and dynamics. *Chem. Rev.* **99,** 2161–2200 (1999).

6. Spence, T. G., Burns, T. D., Guckenberger, G. B. & Posey, L. A. Wavelength-dependent photodissociation of $[Fe(bpy)_3\cdot(CH_3OH)_n]^{2+}$ clusters, n=2-6, triggered by excitation of the metal-to-ligand charge-transfer transition. *J. Phys. Chem. A* **101,** 1081–1092 (1997).

7. Stockett, M. H. & Brøndsted Nielsen, S. Communication: Does a single CH_3CN molecule attached to $Ru(bipy)_3^{2+}$ affect its absorption spectrum? *J. Chem. Phys.* **142,** 171102 (2015).

8. Houmøller, J. *et al.* On the photoabsorption by permanganate ions in vacuo and the role of a single water molecule. New experimental benchmarks for electronic structure theory. *Chemphyschem* **14,** 1133–7 (2013).

9. Wang, X.-B., Nicholas, J. B. & Wang, L.-S. Electronic instability of isolated SO_4^{2-} and its solvation stabilization. *J. Chem. Phys.* **113,** 10837 (2000).

10. Weber, J. M., Kelly, J. A., Nielsen, S. B., Ayotte, P. & Johnson, M. A. Isolating the spectroscopic signature of a hydration shell with the use of clusters: superoxide tetrahydrate. *Science* **287,** 2461–2463 (2000).

11. Xu, S. & Weber, J. M. Absorption spectrum of a Ru(II)-aquo complex in vacuo: resolving individual charge-transfer transitions. *J. Phys. Chem. A* **119,** 11509–11513 (2015).

12. Jakubikova, E. *et al.* Electronic structure and spectroscopy of $[Ru(tpy)_2]^{2+}$, $[Ru(tpy)(bpy)(H_2O)]^{2+}$, and $[Ru(tpy)(bpy)Cl]^{+}$. *Inorg. Chem.* **48,** 10720–10725 (2009).

13. Xu, S., Smith, J. E. T. & Weber, J. M. Ligand influence on the electronic spectra of dicationic ruthenium- bipyridine-terpyridine complexes. *J. Phys. Chem. A* **120,** 2350–2356 (2016).

14. Schweizer, A. *et al.* Electronic photodissociation spectroscopy of $Au^{4+}{\cdot}Ar_n$, n=0-4: experiment and theory. *J. Chem. Phys.* **119,** 3699–3710 (2003).

15. Weigend, F. & Ahlrichs, R. Balanced basis sets of split valence, triple zeta valence and quadruple zeta valence quality for H to Rn: Design and assessment of accuracy. *Phys. Chem. Chem. Phys.* **7,** 3297–3305 (2005).

16. Weigend, F., Häser, M., Patzelt, H. & Ahlrichs, R. RI-MP2: optimized auxiliary basis sets and demonstration of efficiency. *Chem. Phys. Lett.* **294,** 143–152 (1998).

17. Parr, R. G. & Yang, W. *Density-Functional Theory of Atoms and Molecules*. *Oxford University Press: New York* (1989).

18. Lee, C., Yang, W. & Parr, R. G. Development of the Colle-Salvetti correlation-energy formula into a functional of the electron density. *Phys. Rev. B* **37,** 785–789 (1988).

19. Yoon, S., Kukura, P., Stuart, C. M. & Mathies, R. A. Direct observation of the ultrafast intersystem crossing in tris(2,2'-bipyridine)ruthenium(II) using femtosecond stimulated Raman spectroscopy. *Mol. Phys.* **104,** 1275–1282 (2006).

20. Prell, J. S., Obrien, J. T. & Williams, E. R. Structural and electric field effects of ions in aqueous nanodrops. *J. Am. Chem. Soc.* **133,** 4810–4818 (2011).

21. Donald, W. A. *et al.* Average sequential water molecule binding enthalpies of $M(H_2O)_{19\text{-}124}^{2+}$ (M = Co, Fe, Mn, and Cu) measured with ultraviolet photodissociation at 193 and 248 nm. *J. Phys. Chem. A* **115,** 2–12 (2011).

22. Marsh, B. M., Voss, J. M. & Garand, E. A dual cryogenic ion trap spectrometer for the formation and characterization of solvated ionic clusters. *J. Chem. Phys.* **143**, 204201 (2015).

6 Summary and conclusions

This thesis summarizes my doctoral work on photodissociation spectroscopy of metal-polypyridine complex ions. I investigated the influence of ligands on electronic structure using two series of complexes, $[Cu(bpy)\text{-}L]^{+}$ and $[Ru(bpy)(tpy)\text{-}L]^{2+}$, where L is a variable ligand. The photophysical properties of the complexes are found to be critically dependent on the ligand L, and influence of the ligand is characterized within each series. The role of the metal is studied in a series of $[M^{II}(bpy)_3]^{2+}$ ions, where M stands for a transitional metal. Different metal cores lead to distinct spectral properties. The excited-state lifetime, absorption maxima and absorption cross sections are all dictated by the nature of the metal and differ for different metals. There is no clear trend based on the position of the metal in the periodic table. Lastly, I studied solvation effects on the MLCT band of a water oxidation catalyst, $[Ru(bpy)(tpy)\text{-}OH_2]^{2+}$, by measuring the photodissociation spectrum of its solvated form with up to four solvent water molecules. It is the first time to experimentally observe the evolution of solvatochromic shift of an organometallic complex with addition of one solvent molecule at a time. In this case, the first four solvent molecules already bring about more than 75% of the bulk solvatochromic shift of this complex. In addition to experimental investigations, I also performed quantum chemistry calculations based on (time-dependent) density functional theory and used the computational results to assist the interpretation of the experimental data. The experiments also serve to provide benchmarks for theory so that theoretical methods can be compared and tested.

The experiment has room for improvement. First, our method relies on photodissociation, and the resulting photodissociation spectra are not always representative of the underlying absorption spectra, and sometimes this method is even unfeasible. As a result, we

may resort to messenger tagging. However, no tag is completely innocent. It demands more effort to study the impact of tagging on electronic spectra, although it is probably small. Second, despite mass-selection, it is impossible to distinguish isomers, which may exist and contribute to the observed spectrum simultaneously, particularly for clusters. Infrared spectroscopy can serve to contribute additional information on the structure of the complex under study. Therefore, an infrared system is being implemented and will be used to identify different bonding motifs inside possible isomers. Third, the actual temperature or the internal energy of the ions is difficult to determine quantitatively, and we are investigating candidate molecules to be used as molecular thermometers. Improvements along those lines will allow to extract additional information on molecular ionic systems from their spectra and to further push the frontier of understanding the fundamental properties of these systems.

7 Bibliography

Addison, A.W. & Rao, T.N., 1984. Synthesis, structure, and spectroscopic properties of Cu(II) compounds. *Journal of Chemistry Society Dalton Transactions*, pp.1349–1356.

Ahlrichs, R. et al., 1989. Electronic structure calculations on workstation computers: The program system turbomole. *Chemical Physics Letters*, **162**, pp.165–169.

Allen, A.D. & Bottomley, F., 1968. Inorganic nitrogen fixation. Nitrogen compounds of the transition metals. *Accounts of Chemical Research*, **1**, pp.360–365.

Anonymous, 2015. Cobra-Stretch dye laser datasheet.
Available at: http://www.sirah.com/wp-content/uploads/pdfs/CobraStretch.pdf.

Auböck, G. & Chergui, M., 2015. Sub-50-fs photoinduced spin crossover in $[Fe(bpy)_3]^{2+}$. *Nature Chemistry*, **7**, pp.629–633.

Baer, R. & Neuhauser, D., 2005. Density functional theory with correct long-range asymptotic behavior. *Physical Review Letters*, **94**, pp.2–5.

Baffert, C. et al., 2005. Photoinduced oxidation of $[Mn(L)_3]^{2+}$ and $[Mn_2O_2(L)_4]^{3+}$ (L = 2,2'-bipyridine and 4,4'-dimethyl-2,2'-bipyridine) with the $[Ru(bpy)_3]^{2+}$/-aryl diazonium salt system. *Phys. Chem. Chem. Phys.*, **7,** pp.202–210.

Balzani, V. et al., 2001. Photochemistry and photophysics of Ru(II) polypyridine complexes in the Bologna group . From early studies to recent developments. *Coordination Chemistry Reviews*, **211**, pp.97–115.

Bargawi, K.R., Llobet, A. & Meyer, T.J., 1988. Synthetic design of MLCT excited states. Ligand-substituted, mono-2,2'-bipyridine complexes of ruthenium(II). *Journal of the American Chemical Society*, **110**, pp.7751–7759.

Barnett, S.M., Goldberg, K.I. & Mayer, J.M., 2012. A soluble copper-bipyridine water-oxidation electrocatalyst. *Nature chemistry*, **4**, pp.498–502.

Bartlett, R.J., 2012. Coupled-cluster theory and its equation-of-motion extensions. *Wiley Interdisciplinary Reviews: Computational Molecular Science*, **2**, pp.126–138.

Bauernschmitt, R. et al., 1997. Calculation of excitation energies within time-dependent density functional theory using auxiliary basis set expansions. *Chemical Physics Letters*, **264**, pp.573–578.

Bauernschmitt, R. & Ahlrichs, R., 1996. Treatment of electronic excitations within the adiabatic

approximation of time dependent density functional theory. *Chemical Physics Letters*, **256**, pp.454–464.

Becke, A.D., 1988. Density-functional exchange-energy approximation with correct asymptotic behavior. *Physical Review A*, **38**, pp.3098–3100.

Benjamin J. Knurr, 2015. Structures and charge distributions of cluster anions studied by infrared photodissociation spectroscopy. University of Colorado, Boulder.

Bhasikuttan, A.C. et al., 2002. Ultrafast fluorescence detection in tris(2,2'-bipyridine) ruthenium(II) complex in solution : relaxation dynamics involving higher excited states. *Journal of the American Chemical Society*, **124**, pp.8398–8405.

Björemark, P.M., Jönsson, J. & Håkansson, M., 2015. Absolute asymmetric synthesis: Viedma ripening of $[Co(bpy)_3]^{2+}$ and solvent-free oxidation to $[Co(bpy)_3]^{3+}$. *Chemistry - A European Journal*, **21**, pp.10630–10633.

Blades, A.T., Ikonomou, M.G. & Kebarle, P., 1991. Mechanism of electrospray mass spectrometry. Electrospray as an electrolysis cell. *Analytical Chemistry*, **63**, pp.2109–2114.

Blake, A.J. et al., 1998. Copper(I) chelated by 2,9-dimethyl-1,10-phenanthroline and bridged by 4,4'-bipyridine or trans-1,2-bis(pyridin-4-yl)ethene to give discrete dinuclear and polymeric cations. *Dalton transactions*, **2**, pp.909–915.

Blakemore, J.D., Crabtree, R.H. & Brudvig, G.W., 2015. Molecular catalysts for water oxidation. *Chemical Reviews*, **115**, pp.12974–13005.

Blaskie, M.W. & McMillin, D.R., 1980. Photostudies of copper(I) systems. 6. Room-temperature emission and quenching studies of bis(2,9-dimethyl-1,10- phenanthroline)copper(I). *Inorganic Chemistry*, **19**, pp.3519–22.

Bomben, P.G., Koivisto, B.D. & Berlinguette, C.P., 2010. Cyclometalated Ru complexes of type $[Ru(II)(N^N)_2(C^N)]^z$: physicochemical response to substituents installed on the anionic ligand. *Inorganic Chemistry*, **49**, pp.4960–71.

Bozic-Weber, B. et al., 2013. Copper(I) dye-sensitized solar cells with $[Co(bpy)_3]^{2+/3+}$ electrolyte. *Chemical Communications*, **49**(65), p.7222.

Bray, R.G., Fergusson, J.E. & Hawkins, C.J., 1969. Ultraviolet absorption spectra and circular dichroism of divalent metal complexes containing 1,10-phenanthroline and 2,2'-bipyridine. *Australian journal of chemistry*, **22**, pp.2091–2103.

Burstall, F.H. & Nyholm, R.S., 1952. Studies in Co-ordination Chemistry. Part XIII. Magnetic Moments and Bond Types of Transition-metal Complexes. *Journal of the Chemical Society*,

pp.3570–3579.

Carter, M.T., Rodriguez, M. & Bard, A.J., 1989. Voltammetric Studies of the Interaction of Metal Chelates with DNA. 2. Tris-Chelated complexes of cobalt(III) and iron(II) with 1,10-phenanthroline and 2,2'-bipyridine. *Journal of American Chemical Society*, **111**, pp.8901–8911.

Caspar, J. V. & Meyer, T.J., 1983. Photochemistry of $Ru(bpy)_3^{2+}$. Solvent effects. *Journal of the American Chemical Society*, **105**, pp.5583–5590.

Castellucci, E., Salvi, P.R. & Foggi, P., 1982. Two-photon exictation spectra of the lowest electronic states of 2,2'-bipyridine. *Chemical Physics*, **66**, pp.281–291.

Chen, C. et al., 2006. A ruthenium complex with superhigh light-harvesting capacity for dye-sensitized solar cells. *Angewandte Chemie - International Edition*, **118**, pp.5954–5957.

Chen, Y.J. et al., 2006. Influence of the "innocent" ligands on the MLCT excited-state behavior of mono(bipyridine)ruthenium(II) complexes: A comparison of X-ray structures and 77 K luminescence properties. *Inorganic Chemistry*, **45**, pp.6282–6297.

Chen, Z. et al., 2011. Electrocatalytic reduction of CO_2 to CO by polypyridyl ruthenium complexes. *Chemical Communications*, **47**, pp.12607–12609.

Chen, Z. & Meyer, T.J., 2013. Copper(II) catalysis of water oxidation. *Angewandte Chemie - International Edition*, **52**, pp.700–703.

Concepcion, J.J. et al., 2009. Making oxygen with ruthenium complexes. *Accounts of chemical research*, **42**, pp.1954–1965.

Concepcion, J.J. et al., 2010. Mechanism of water oxidation by single-site ruthenium complex catalysts. *Journal of the American Chemical Society*, **132**, pp.1545–1557.

Concepcion, J.J. et al., 2008. One site is enough. Catalytic water oxidation by $[Ru(tpy)(bpm)(OH_2)]^{2+}$ and $[Ru(tpy)(bpz)(OH_2)]^{2+}$. *Journal of the American Chemical Society*, **130**, pp.16462–16463.

Constable, E.C., 1989. Homoleptic complexes of 2,2'-bipyridine. *Advances in inorganic chemistry*, **34**, pp.1–63.

Coronado, E. et al., 2001. Molecule-based magnets formed by bimetallic three-dimensional oxalate networks and chiral tris(bipyridyl) complex cations. The series $[Z^{II}(bpy)_3][ClO_4][M^{II}Cr^{III}(ox)_3]$ (Z^{II} = Ru, Fe, Co, and Ni; M^{II} = Mn, Fe, Co, Ni, Cu, and Zn; ox = oxalate dianion). *Inorganic Chemistry*, **40**, pp.113–120.

Cramer, C.J. & Truhlar, D.G., 1999. Implicit solvation models: equilibria, structure, spectra, and dynamics. *Chemical Reviews*, **99**, pp.2161–2200.

Creutz, C. et al., 1980. Lifetimes, spectra, and quenching of the excited states of polypyridine complexes of iron(ii), ruthenium(ii), and osmium(II). *Journal of the American Chemical Society*, **102**, pp.1309–1319.

Crutchley, R.J. & Lever, A.B.P., 1982. Comparative chemistry of bipyrazyl and bipyridyl metal complexes: spectroscopy, electrochemistry and photoanation. *Inorganic Chemistry*, **21**, pp.2276–2282.

Damrauer, N.H. et al., 1997. Femtosecond Dynamics of Excited-State Evolution in $[Ru(bpy)_3]^{2+}$. *Science*, **275**, pp.54–57.

Daul, C., Baerends, E.J. & Vernooijs, P., 1994. A Density Functional Study of the MLCT States of $[Ru(bpy)_3]^{2+}$ in D_3 Symmetry. *Inorganic Chemistry*, **33**, pp.3538–3543.

Dawson, P.H., 1968. Ion Storage in Three-dimensional, rotationally symmetric, quadrupole fields. I. Theoretical treatment. *Journal of Vacuum Science and Technology*, **5**, p.1.

Decurtins, S. et al., 1980. The Electronic Spectrum of $Fe(bpy)_3^{2+}$ and $Os(bpy)_3^{2+}$. *Journal of the American Chemical Society*, **102**, pp.4102–4106.

Demas, J.N. & Adamson, A.W., 1971. A New Photosensitizer. Tris(2,2'-bipyridine)ruthenium(II) chloride. *Journal of the American Chemical Society*, **93**, pp.1800–1801.

Dhanya, S. & Bhattacharyya, P.K., 1992. Fluorescence behaviour of 2,2'-bipyridine in aqueous solution. *Journal of Photochemistry and Photobiology A: Chemistry*, **63**, pp.179–185.

Dole, M. et al., 1968. Molecular beams of macroions. *The Journal of Chemical Physics*, **49**, p.2240.

Donald, W.A. et al., 2011. Average sequential water molecule binding enthalpies of $M(H_2O)_{19\text{-}124}^{2+}$ (M = Co, Fe, Mn, and Cu) measured with ultraviolet photodissociation at 193 and 248 nm. *Journal of Physical Chemistry A*, **115**, pp.2–12.

Duffy, E.M., Marsh, B.M. & Garand, E., 2015. Probing the hydrogen-bonded water network at the active site of a water oxidation catalyst: $[Ru(bpy)(tpy)(H_2O)]^{2+}\cdot(H_2O)_{0–4}$. *The Journal of Physical Chemistry A*, **119**, pp.6326–6332.

Durham, B. et al., 1982. Photochemistry of $Ru(bpy)_3^{2+}$. *Journal of the American Chemical Society*, **104**, pp.4803–4810.

Dwyer, F.P., Gyarfas, H.A. & Goodwin, E.C., 1963. Mono- and bis-(2,2'-bipyridine) and (1,10-phenanthroline) chelates of ruthenium and osmium. I. Monochelates of bivalent,

tervalent, and quadrivalent ruthenium. *Australian journal of chemistry*, **16**, pp.42–50.

Ernst, S.D. & Kaim, W., 1989. Energy level tailoring in ruthenium(II) polyazine complexes based on calculated and experimental ligand properties. *Inorganic Chemistry*, **28**, pp.1520–1528.

Felix, F. et al., 1979. Electronic spectra of $M(bipy)_3^{2+}$ complex ions (M = Fe, Ru and Os). *Chemical Physics Letters*, **62**, pp.153–157.

Felix, F. et al., 1980. The electronic spectrum of $Ru(bpy)_3^{2+}$. *Journal of the American Chemical Society*, **102**, pp.4096–4102.

Fenn, J.B. et al., 1989. Electrospray ionization for mass spectrometry of large biomolecules. *Science*, **246**, pp.64–71.

Fergusson, J.E. et al., 1969. Absolute configurations of 1,10-phenanthroline and 2,2'-bipyridine metal complexes. *Inorganic Chemistry*, **8**, pp.771–779.

Fleisher, M.B. et al., 1986. Light induced cleavage of DNA by metal complexes. *Inorganic Chemistry*, **25**, pp.3551–3552.

Furche, F., 2001. On the density matrix based approach to time-dependent density functional response theory. *Journal of Chemical Physics*, **114**, pp.5982–5992.

Gao, F. et al., 2008. A new heteroleptic ruthenium sensitizer enhances the absorptivity of mesoporous titania film for a high efficiency dye-sensitized solar cell. *Chemical Communications*, pp.2635–2637.

Garand, E., Stipdonk, M.J. Van & Johnson, M.A., 2012. Isomer-specific IR-IR double resonance spectroscopy of D_2-tagged protonated dipeptides prepared in a cryogenic ion trap. *The Journal of Physical Chemistry Letters*, **3**, pp.1099-1105.

Gerlich, D., 1992. Inhomogeneous RF fields : a versatile tool for the study of processes with slow ions. *Advances in Chemical Physics: State-Selected and State-To-State Ion-Molecule Reaction Dynamics, Part 1. Experiment*, **82**.

Gersten, S.W., Samuels, G.J. & Meyer, T.J., 1982. Catalytic oxidation of water by an oxo-bridged ruthenium dimer. *Journal of the American Chemical Society*, **104**, pp.4029–4030.

Geusic, J.E., Marcos, H.M. & Van Uitert, L.G., 1964. Laser oscillations in nd-doped yttrium aluminum, yttrium gallium and gadolinium garnets. *Applied Physics Letters*, **4**, pp.182–184.

Gondo, Y. & Kanda, Y., 1965. The Phosphorescence 2,2'- and 4,4'-bipyridyls. *Bulletin of the chemical society of Japan*, **38**, pp.1187–1190.

Guilhaus, M., 1995. Principles and instrumentation in time-of-flight mass spectrometry. *Journal of Mass Spectrometry*, **30**, pp.1519–1532.

Harriman, A., 1978. Photophysics of 2,2'-bipyridyl. *Journal of Photochemistry*, **8**, pp.205–209.

Hathaway, B.J., Hodgson, P.G. & Power, P.C., 1974. Single-crystal electronic and electron spin resonance spectra of three tris-chelate copper (II) complexes. *Inorganic Chemistry*, **13**, pp.2009–2013.

Heully, J.-L., Alary, F. & Boggio-Pasqua, M., 2009. Spin-orbit effects on the photophysical properties of $Ru(bpy)_3^{2+}$. *The Journal of Chemical Physics*, **131**, 184308.

Hoffmann, E. & Stroobant, V., 2006. *Mass Spectrometry: Principles and Applications* Second ed., West Sussex: John Wiley & Sons, Ltd.

Horvath, O., 1994. Photochemistry of copper(I) complexes. *Coordination Chemistry Reviews*, **135/136**, pp.303–324.

Houmøller, J. et al., 2013. On the photoabsorption by permanganate ions in vacuo and the role of a single water molecule. New experimental benchmarks for electronic structure theory. *Chemphyschem : a European journal of chemical physics and physical chemistry*, **14**, pp.1133–1137.

Ichinaga, A.K. et al., 1987. Charge-transer absorption and emission of $Cu(NN)^{2+}$ systems. *Inorganic Chemistry*, **26**, pp.4290–4292.

Ikonomou, M.G., Blades, A.T. & Kebarle, P., 1991. Electrospray-ion spray: a comparison of mechanisms and performance. *Analytical Chemistry*, **63**, pp.1989–1998.

Irving, H. & Williams, R.J.P., 1953. The stability of transition-metal complexes. *Journal of Chemistry Society*, pp.3192-3210.

Ishida, H. et al., 1990. Ligand effects of ruthenium 2,2'-bipyridine and 1,10-phenanthroline complexes on the electrochemical reduction of CO_2. *Journal of the Chemical Society, Dalton Transactions*, **2**, p.2155.

Ishida, H., Tanaka, K. & Tanaka, T., 1987. Electrochemical CO_2 Reduction Catalyzed by $[Ru(bpy)_2(CO)_2]^{2+}$ and $[Ru(bpy)_2(CO)Cl]^{+}$. The Effect of pH on the Formation of CO and $HCOO^{-}$. *Organometallics*, **6**, pp.181–186.

Jakubikova, E. et al., 2009. Electronic structure and spectroscopy of $[Ru(tpy)_2]^{2+}$, $[Ru(tpy)(bpy)(H_2O)]^{2+}$, and $[Ru(tpy)(bpy)Cl]^{+}$. *Inorganic Chemistry*, **48**, pp.10720–10725.

Ji, L.-N., Zou, X.-H. & Liu, J.-G., 2001. Shape- and enantioselective interaction of Ru(II)/Co(III) polypyridyl complexes with DNA. *Coordination Chemistry Reviews*, **216–217**, pp.513–536.

Jones, R.M. & Gerlich, D., 1997. Simple radio-frequency power source for ion guides and ion traps. *Review of Scientific Instruments*, **68**, pp.3357–3362.

Juris, A. et al., 1988. Ru(II) polypyridine complexes: photophysics, photochemistry, eletrochemistry and chemiluminescence. *Coordination Chemistry Reviews*, **84**, pp.85–277.

Kalyanasundaram, K., 1982. Photophysics, photochemistry and solar energy conversion with tris(bipyridyl)ruthenium(ii) and its analogues. *Coordination Chemistry Reviews*, **46**, pp.159–244.

Kebarle, P. & Tang, L., 1993. From ions in solution to ions in the gas phase. *Analytical chemistry*, **65**, p.972A–986A.

Kebarle, P. & Verkerk, U.H., 2009. Electrospray: from ions in solution to ions in the gas phase, what we know now. *Mass Spectrometry Reviews*, **28**, pp.898–917.

Kirketerp, M.-B.S. & Nielsen, S.B., 2010. Absorption spectrum of isolated tris(2,2'-bipyridine)ruthenium(II) dications in vacuo. *International Journal of Mass Spectrometry*, **297**, pp.63–66.

Klamt, A. & Schüürmann, G., 1993. Cosmo - a new approach to dielectric screening in solvents with explicit expressions for the screening energy and its gradient. *Journal of Chemistry Society Perkin Transactions 2*, pp.799–805.

Knoll, J.D. et al., 2014. Unusually efficient pyridine photodissociation from Ru(II) complexes with sterically bulky bidentate ancillary ligands. *The Journal of Physical Chemistry A*, **118**, pp.10603–10610.

Knoll, J.D., Albani, B.A. & Turro, C., 2015. New Ru(II) complexes for dual photoreactivity: ligand exchange and $^1O_2$ generation. *Accounts of Chemical Research*, **48**, pp.2280–2287.

Kober, E.M. & Meyer, T.J., 1982. Concerning the absorption spectra of the ions $M(bpy)_3^{2+}$ (M = Fe, Ru, Os; bpy = 2,2'-bipyridine). *Inorganic Chemistry*, **21**, pp.3967–3977.

Kotlicka, J. & Grabowski, Z.R., 1979. The flueorescence of 2,2'-bipyridyl. *Journal of Photochemistry*, **11**, pp.413–418.

Krausz, E. & Riesen, H., 1997. Developement in laser selective spectroscopy and photophysis of d^6 metal-(di-imine) complexes. *Coordination Chemistry Reviews*, **159**, pp.9–40.

Krylov, A.I., 2008. Equation-of-motion coupled-cluster methods for open-shell and electronically excited species: the Hitchhiker's guide to Fock space. *Annual review of physical chemistry*, **59**, pp.433–462.

Lay, P.A. & Sasse, W.H.F., 1985. Mechanism of the water-mediated reduction of tris(2,2'-bipyridine-N,N')iron(III), -ruthenium(III), and -osmium(III) Complexes. *Inorganic Chemistry*, **24**, pp.4707–4710.

Lazorski, M.S. & Castellano, F.N., 2014. Advances in the light conversion properties of Cu(I)-based photosensitizers. *Polyhedron*, **82**, pp.57–70.

Lee, C., Yang, W. & Parr, R.G., 1988. Development of the Colle-Salvetti correlation-energy formula into a functional of the electron density. *Physical Review B*, **37**, pp.785–789.

Liu, F. et al., 2008. Mechanisms of Water Oxidation from the Blue Dimer to Photosystem II. *Inorganic Chemistry*, **47**, pp.1727–1752.

Livshits, E. & Baer, R., 2007. A well-tempered density functional theory of electrons in molecules. *Phys. Chem. Chem. Phys.*, **9**, pp.2932–2941.

Lytle, F.E. & Hercules, D.M., 1969. The luminescence of tri(2,2'-bipyridine)ruthenium(II) dichloride. *Journal of the American Chemical Society*, **587**, pp.253–257.

Madeja, K. & Konig, E., 1963. Zur Frage der Bindungsverhältnisse in Komplexverbindungen des Eisen(II) mit 1,10-Phenanthrolin. *Journal of Inorganic and Nuclear Chemistry*, **25**, pp.377–385.

Mara, M.W., Fransted, K. a. & Chen, L.X., 2014. Interplays of excited state structures and dynamics in copper(I) diimine complexes: Implications and perspectives. *Coordination Chemistry Reviews*, **282–283**, pp.2–18.

March, R.E., 1997. An introduction to quadrupole ion trap mass spectrometry. *Journal of Mass Spectrometry*, **32**, pp.351–369.

Marcum, J.C., 2011. *Electronic Photodissociation Spectroscopy of Electrosprayed Anions*. University of Colorado, Boulder.

Marsh, B.M., Voss, J.M. & Garand, E., 2015. A dual cryogenic ion trap spectrometer for the formation and characterization of solvated ionic clusters. *Journal of Chemical Physics*, **143**, 204201.

Mason, S.F., 1968. The electronic spectra and optical activity of phenanthroline and dipyridyl metal complexes. *Inorganica Chimica Acta Reviews*, **2**, pp.89–109.

Mason, S.F. & Norman, B.J., 1968. Exciton splittings in the ligand ultraviolet bands of coordination complexes. *Chemical Physics Letters*, **2**, pp.22–24.

Mason, S.F., Peart, B.J. & Waddell, R.E., 1973. Optical rotatory power of co-ordination compounds. Part XVI. Intermediate exciton coupling in the circular dichroism of trisbipyridyl complexes. *Journal of the Chemical Society, Dalton Transactions*, pp.944–949.

McCaffery, A.J., Mason, S.F. & Norman, B.J., 1969. Optical rotatory power of co-ordination compounds. Part XII. Spectroscopic and configurational assignments for the tris-bipyridyl and -phenanthroline complexes of the di- and tri-valent iron-group metal ions. *Journal of the Chemical Society A*, pp.1428–1441.

McGarvey, J.J., Bell, S.E.J. & Bechara, J.N., 1986. Resonance Raman spectra of charge-transfer excited states of copper(I) complexes. *Inorganic Chemistry*, **25**, pp.4325–7.

McWhinnie, W.R. & Miller, J.D., 1970. The chemistry of complexes containing 2,2'-bipyridyl, 1,10-phenanthroline, or 2,2',6',2"-terpyridyl as ligands. *Advances in Inorganic Chemistry and Radiochemistry*, **12**, pp.135–215.

Mellor, D.P. & Maley, L.E., 1950. Stability of some metal complexes of histidine. *Nature*, **165**, p.453.

Mori, Y. et al., 1998. Toward the photoreduction of CO_2 with Ni(2,2'-bipyridine)$_n^{2+}$ Complexes. *Photochemistry and Radiation Chemsitry*, **254**, pp.279–292.

Nagao, H., Mizukawa, T. & Tanaka, K., 1994. Carbon-carbon bond formation in the electrochemical reduction of carbon dioxide catalyzed by a ruthenium complex. *Inorganic Chemistry*, **33**, pp.3415–3420.

Nielsen, I.M.B. & Janssen, C.L., 1999. Double-substitution-based diagnostics for coupled-cluster and Møller–Plesset perturbation theory. *Chemical Physics Letters*, **310**, pp.568–576.

Niven, M.L. & Percy, G.C., 1978. The infrared spectra of the 2,2'-bipyridine. *Transition Metal Chemistry*, **3**, pp.267–271.

Ohno, T. & Kato, S., 1974. Ligand-ligand Interaction in [Zn(1,10-phenanthroline)$_2$(H_2O)$_2$](NO_3)$_2$ and [Zn(2,2'-bipyridyl)$_3$](NO_3)$_2$. *Bulletin of the chemical society of Japan*, **47**, pp.2953–2957.

Ohsawa, Y. et al., 1985. A ^{1}H NMR study of reduced paramagnetic tris(2,2'-bipyridine) complexes of iron(II), ruthenium (II), and osmium(II). *Journal of the American Chemical Society*, **107**, pp.5383–5386.

Orgel, L.E., 1961. 715. Double bonding in chelated metal complexes. *Journal of the Chemical Society*, pp.3683–3686.

Palanisami, N. et al., 2015. A mixed Ni(II) ionic complex containing V-shaped water trimer: Synthesis, spectral, structural and thermal properties of {[Ni(2,2′-bpy)$_3$][Ni(2-cpida)(2,2′ -bpy)]}(ClO_4)·3H_2O. *Journal of Chemical Sciences*, **127**, pp.873–878.

Palmer, R.A. & Piper, T.S., 1966. 2,2′-Bipyridine complexes. I. Polarized crystal spectra of tris(2,2′-bipyridine)copper(II), -nickel(II), -cobalt(II), iron(II), and -ruthenium(II). *Inorganic Chemistry*, **5**, pp.864–878.

Parr, R.G. & Yang, W., 1989. *Density-Functional Theory of Atoms and Molecules*, Oxford University Press.

Pelikán, P. & Boča, R., 1984. Geometric and electronic factors of dinitrogen activation on transition metal complexes. *Coordination Chemistry Reviews*, **55**, pp.55–112.

Perdew, J.P., Burke, K. & Ernzerhof, M., 1996. Generalized gradient approximation made simple. *Physical Review Letters*, **77**, pp.3865–3868.

Perrin, M.H. & Gouterman, M., 1967. Vibronic coupling. IV. Trimers and trigonal molecules. *The Journal of Chemical Physics*, **46**, p.1019.

Prell, J.S., Obrien, J.T. & Williams, E.R., 2011. Structural and electric field effects of ions in aqueous nanodrops. *Journal of the American Chemical Society*, **133**, pp.4810–4818.

Pugh, J.R. et al., 1991. Formation of a metal-hydride bond and the insertion. Key steps in the electrocatalytic reduction of carbon dioxide to formate anion. *Inorganic Chemistry*, **30**, pp.86–91.

Rayleigh, F.R.S., 1882. On the equilibrium of liquid conducting masses charged with electricity. *Philosophical Magazine Series 5*, **14**, pp.184–186.

Reed, A.E., Weinstock, R.B. & Weinhold, F., 1985. Natural population analysis. *Journal of Chemical Physics*, **83**, pp.735–746.

Renouard, T. et al., 1999. Tetrahedral bipyridyl copper(I) complexes: a new class of non-dipolar chromophore for nonlinear optics. *Chemical Communications*, pp.871–872.

Rillema, D.P., Meyer, T.J. & Conrad, D., 1983. Redox properties of ruthenium(II) tris chelate complexes containing the ligands 2,2′-bipyrazine, 2,2′-bipyridine, and 2,2′-bipyrimidine. *Inorganic Chemistry*, **22**, pp.1617–1622.

Ronca, E., De Angelis, F. & Fantacci, S., 2014. Time-dependent density functional theory modeling

of spin–orbit coupling in ruthenium and osmium solar cell sensitizers. *The Journal of Physical Chemistry C*, **118**, pp.17067–17078.

Schläfer, H.L., 1956. Über die UV-Absorptionsspektren von Komplexionen mit π-Elektronensystemen als Liganden. *Zeitschrift fur anorganische und allgemeine Chemie*, **8**, pp.373–386.

Schweizer, A. et al., 2003. Electronic photodissociation spectroscopy of $Au^{4+}{\cdot}Ar_n$, n=0-4: Experiment and theory. *Journal of Chemical Physics*, **119**, pp.3699–3710.

Shaw, G.B. et al., 2004. Interligand electron transfer dynamics in $[Os(bpy)_3]^{2+}$: exploring the excited state potential surfaces with femtosecond spectroscopy. *The Journal of Physical Chemistry A*, **108**, pp.4998–5006.

Siddique, Z.A. et al., 2003. Structure-dependent photophysical properties of singlet and triplet metal-to-ligand charge transfer states in copper(I) bis(diimine) compounds. *Inorganic Chemistry*, **42**, pp.6366–6378.

Skyner, R.E. et al., 2015. A review of methods for the calculation of solution free energies and the modelling of systems in solution. *Physical Chemistry Chemical* Physics, **17**, pp.6174–6191.

Sone, K., Krumholz, P. & Stammereich, H., 1955. Studies on the coördinate bond. III. Absorption spectra of mono-α,α'-dipyridyl and mono-o-phenanthroline complexes. *Journal of the American Chemical Society*, **77**, pp.777–780.

Spence, T.G. et al., 1997. Wavelength-dependent photodissociation of $[Fe(bpy)_3{\cdot}(CH_3OH)_n]^{2+}$ clusters, n=2-6, triggered by excitation of the metal-to-ligand charge-transfer transition. *The Journal of Physical Chemistry A*, **101**, pp.1081–1092.

Spettel, K.E. & Damrauer, N.H., 2014. Synthesis, electrochemical characterization, and photophysical studies of structurally tuned aryl-substituted terpyridyl ruthenium(ii) complexes. *The Journal of Physical Chemistry A*, **118**, pp.10649–10662.

Stockett, M.H. & Brøndsted Nielsen, S., 2015. Communication: Does a single CH_3CN molecule attached to $Ru(bipy)_3^{2+}$ affect its absorption spectrum? *The Journal of Chemical Physics*, **142**, p.171102.

Stoermer, C.W. et al., 1998. A high resolution dual mass gate for ion separation in laser desorption/ionization time of flight mass spectrometry. *Review of Scientific Instruments*, **69**, p.1661.

Sun, Y. et al., 2010. Unusual photophysical properties of a ruthenium(II) complex related to $[Ru(bpy)_2(dppz)]^{2+}$. *Inorganic Chemistry*, **49**, pp.4257–4262.

Takeuchi, K.J. et al., 1984. Redox and spectral properties of monooxo polypyridyl complexes of ruthenium and osmium in aqueous media. *Inorganic Chemistry*, **23**, pp.1845–1851.

Tanaka, K. & Ooyama, D., 2002. Multi-electron reduction of CO_2 via Ru-CO_2, -C(O)OH, -CO, -CHO, and -CH_2OH species. *Coordination Chemistry Reviews*, **226**, pp.211–218.

Taylor, G., 1964. Disintegration of water drops in an electric field. *Proceedings of the Royal Society A: Mathematical, Physical and Engineering Sciences*, **280**, pp.383–397.

Thompson, M.C. et al., 2015. Heavy atom vibrational modes and low-energy vibrational autodetachment in nitromethane anions. *The Journal of Chemical Physics*, **142**, 234304.

Tosi, P. et al., 1989. Transport of an ion beam through an octopole guide operating in the r.f.-only mode. *International Journal of Mass Spectrometry and Ion Processes*, **93**, pp.95–105.

Tsuboyama, A. et al., 2007. Photophysical properties of highly luminescent copper(I) halide complexes chelated with 1,2-bis(diphenylphosphino)benzene. *Inorganic Chemistry*, **46**, pp.1992–2001.

De Waele, V. et al., 2005. Asymmetric structure for the excited S1 state of 2,2'-bipyridine evidenced by picosecond time-resolved resonance Raman experiments and ab initio calculation. *International Journal of Quantum Chemistry*, **104**, pp.794–807.

Wang, M. et al., 2014. Molecular and electronic structures of the members of the electron transfer series $[Mn(bpy)_3]^n$ (n = 2+, 1+, 0, 1-) and $[Mn(tpy)_2]^m$ (m = 4+, 3+, 2+, 1+, 0). An experimental and density functional theory study. *Inorganic Chemistry*, **53**, pp.2276–87.

Wang, P. et al., 2003. A stable quasi-solid-state dye-sensitized solar cell with an amphiphilic ruthenium sensitizer and polymer gel electrolyte. *Nature Materials*, **2**, pp.402–407.

Wang, X.-B., Nicholas, J.B. & Wang, L.-S., 2000. Electronic instability of isolated SO_4^{2-} and its solvation stabilization. *The Journal of Chemical Physics*, **113**, 10837.

Wasylenko, D.J. et al., 2010. Insight into water oxidation by mononuclear polypyridyl Ru catalysts. *Inorganic Chemistry*, **49**, pp.2202–2209.

Weber, J.M. et al., 2000. Isolating the spectroscopic signature of a hydration shell with the use of clusters: superoxide tetrahydrate. *Science*, **287**, pp.2461–2463.

Weigend, F. et al., 1998. RI-MP2: optimized auxiliary basis sets and demonstration of efficiency. *Chemical Physics Letters*, **294**, pp.143–152.

Weigend, F. & Ahlrichs, R., 2005. Balanced basis sets of split valence, triple zeta valence and quadruple zeta valence quality for H to Rn: Design and assessment of accuracy. *Physical*

Chemistry Chemical Physics, **7**, pp.3297–3305.

Wilde, R.E., Srinivasan, T.K.K. & Ghosh, S.N., 1973. Mono complexes of 2,2'-bipyridine and 1,10-phenanthroline with transition metals. *Journal of Inorganic and Nuclear Chemistry*, **35**, pp.1017–1021.

Wiley, W.C. & McLaren, I.H., 1955. Time-of-flight mass spectrometer with improved resolution. *Review of Scientific Instruments*, **26**, 1150.

Xu, S. et al., 2015. Ligand influence on the electronic spectra of monocationic copper-bipyridine complexes. *Physical Chemistry Chemical Physics*, **17**, pp.31938–31946.

Xu, S., Smith, J.E.T. & Weber, J.M., 2016. Hydration of a binding site with restricted solvent access: solvatochromic shift of the electronic spectrum of a ruthenium polypyridine complex, one molecule at a time. *The Journal of Physical Chemistry A*, **120**, pp.7650–7658.

Xu, S., Smith, J.E.T. & Weber, J.M., 2016a. Ligand influence on the electronic spectra of dicationic ruthenium- bipyridine-terpyridine complexes. *The Journal of Physical Chemistry A*, **120**, pp.2350–2356.

Xu, S., Smith, J.E.T. & Weber, J.M., 2016b. The electronic spectrum of cryogenic ruthenium-tris-bipyridine dications in vacuo. *The Journal of Chemical Physics*, **145**, 24034.

Xu, S. & Weber, J.M., 2015. Absorption spectrum of a Ru(II)-aquo complex in vacuo: resolving individual charge-transfer transitions. *The Journal of Physical Chemistry A*, **119**, pp.11509–11513.

Yagi, M. & Kaneko, M., 2001. Molecular catalysts for water oxidation. *Chemical Reviews*, **101**, pp.21–35.

Yamasaki, K., 1937. Absorptionsspektren von Metallkomplexsalzen des 2,2'-Dipyridyls. I. *Bulletin of the Chemical Society of Japan*, **12**, pp.390–394.

Yamasaki, K. & Sone, K., 1950. Stability of Complex Salts of Bivalent Metals. *Nature*, **166**, p.998.

Yamashita, M. & Fenn, J.B., 1984. Electrospray ion source. Another variation on the free-jet theme. *The Journal of Physical Chemistry*, **88**, pp.4451–4459.

Yeh, A.T., Shank, C. V & McCusker, J.K., 2000. dynamics following photo-induced charge transfer. *Science*, **289**, pp.935–938.

Yoon, S. et al., 2006. Direct observation of the ultrafast intersystem crossing in tris(2,2'-bipyridine)ruthenium(II) using femtosecond stimulated Raman spectroscopy. *Molecular Physics*, **104**, pp.1275–1282.

Zakeeruddin, S.M. et al., 1992. Towards mediator design: characterization of tris-(4,4'-substituted-2,2'-bipyridine) complexes of iron(II), ruthenium(II) and osmium(II) as mediators for glucose oxidase of Aspergillus niger and other redox proteins. *Journal of Electroanalytical Chemistry*, **337**, pp.253–283.

Zong, R. & Thummel, R.P., 2005. A new family of Ru complexes for water oxidation. *Journal of the American Chemical Society*, **127**, pp.12802–12803.